Analysis and Control of High-Speed Wheeled Vehicles

A Dissertation

Presented to the Academic Faculty

by

Efstathios Velenis

In partial fulfillment

of the requirements for the degree of

Doctor of Philosophy

School of Aerospace Engineering

Atlanta, Georgia 30332-0150 U.S.A.

May, 2006

Analysis and Control of High-Speed Wheeled Vehicles

Approved by:

Dr. Panagiotis Tsiotras (Advisor)
Aerospace Engineering
Georgia Institute of Technology

Dr. Amy Pritchett
Aerospace Engineering
Georgia Institute of Technology

Dr. Olivier Bauchau
Aerospace Engineering
Georgia Institute of Technology

Dr. David Taylor
Electrical and Computer Engineering
Georgia Institute of Technology

Dr. Wassim Haddad
Aerospace Engineering
Georgia Institute of Technology

Date Approved: October 26, 2005

To Dimitris, Giorgos, Nota and Panorea

Acknowledgements

It is with great pleasure that I am welcoming the opportunity to give thanks, and rightfully acknowledge all of you who have guided me through out my academic years at Georgia Tech.

First and foremost, I would like to express my appreciation and deep respect towards my advisor Dr. Panagiotis Tsiotras. Your constant guidance and encouragement propelled me to reach my outmost potential as of yet, and for this I am grateful to you. Your genuine concern over my well-being and future, speaks volumes of you as an advisor.

Moreover, I would like to extend my appreciation to my committee, Dr. Olivier Bauchau, Dr. Wassim Haddad, Dr. Amy Pritchett and Dr. David Taylor for their willingness to participate in my thesis defense and devote time from their already loaded schedules. I especially feel greatly indebted to Dr. Haddad and Dr. Taylor for their kind efforts and sincere concern in regards to my future plans. I greatly appreciate you going out of your way to provide me with guidance, and supporting me with carrier advise.

I would also like to extend my gratitude to Dr. Carlos Canudas de Wit of the Laboratoire d' Automatique de Grenoble for the opportunity to work with his group in the fall of 2001 and complete part of this work under his co-advisement.

Furthermore, I would like to acknowledge all of my lab-mates of the Dynamics and Control Systems Lab, especially Dongwon "Thomas" Jung and Brian Wilson for the hours of productive discussion, advise and moral support.

At this point I would like to thank all of my close fiends who have supported me morally during these past few years. You heard all of my challenges and endeavors,

and in times of need you stood by me, as well as celebrated with me in times of success. Vivi, Hrisa, Andrea, Yianni G., Yianni K., Eugenie and Niko, thank you for staying as close and true as when we were neighbors in Athens. Fonta, Maria, Nikita, Panagioti and my fellow musicians from "Erasis Techne", Amira, Andrea and Costa thank you for making Atlanta my new home.

Last but certainly not least, I would like to give an enormous "Thank you" to my beloved family. Your love and care, even from thousands of miles away, have given me the strength I needed to complete this task. To my beloved mother, Nota, and father, Giorgos, I could not have asked for more loving and nurturing parents. To my dear brother, Dimitris, you have been a source of inspiration to me. Thank you for always being by my side, making even the most stressful of days brighter. Finally to my beloved aunt, Panorea, your name says it all: most beautiful, in every sense. I truly thank you for everything each and everyone has ever done for me. I love you all, dearly.

Stathis Velenis
September 2005

Table of Contents

List of Tables

List of Figures

Summary

In this work we reproduce driving techniques used by expert race drivers and obtain the open-loop control signals that may be used by auto-pilot agents driving autonomous ground wheeled vehicles.

Race drivers operate their vehicles at the limits of the acceleration envelope. An accurate characterization of the acceleration capacity of the vehicle is required. Understanding and reproduction of such complex maneuvers also require a physics-based mathematical description of the vehicle dynamics. Most of the modeling issues of ground-vehicles/automobiles are addressed using classical mechanics and are already well established in the literature. On the other hand, lack of understanding of the physics associated with friction generation results in ad-hoc approaches to tire friction modeling. In this work we revisit this aspect of the overall vehicle modeling in order to gain experience and insight into the dominant characteristics of tire friction generation and to develop a tire friction model that provides physical interpretation of the tire forces. The new model is free of those singularities at low vehicle speed and wheel angular rate that are inherent in the widely used empirical static models. In addition, the dynamic nature of the tire model proposed herein allows the study of dynamic effects such as transients and hysteresis.

The trajectory planning problem for an autonomous ground wheeled vehicle is formulated in an optimal control framework aiming to minimize the time of travel and maximize the use of the available acceleration capacity. The first approach to solve the optimal control problem is using numerical techniques. Numerical optimization allows incorporation of a vehicle model of high fidelity and generates realistic solutions. Such an optimization scheme provides an ideal platform to study the limit operation of the

vehicle which would not be possible via straightforward simulation.

In this work we emphasize the importance of online applicability of the proposed methodologies. This underlines the need for optimal solutions that require little computational cost and are able to incorporate real, unpredictably-changing environments. A semi-analytic methodology is developed to generate the optimal velocity profile for minimum time travel along a prescribed path. The semi-analytic nature ensures minimal computational cost while a receding horizon implementation allows application of the methodology in uncertain environments. Extensions to increase fidelity of the vehicle model are finally provided.

This thesis consists of three parts. In the first part we develop a new dynamic tire friction model by extension of the LuGre friction model for point contact of two bodies. The point contact model is applied on the contact patch of the tire, resulting in a distributed model of infinite dimension. The steady-state characteristics of the distributed model are derived for comparison with existing empirical static models and identification of the distributed model's parameters. Finite order expressions of the dynamics of the new tire friction model are derived in order to study its dynamic behavior. Validation of the dynamic behavior of the proposed model is provided via comparison with experimental data. In the second part of this thesis we introduce the optimal control formulation of the trajectory planning problem and pursue the solution using numerical optimization. Convergence of the optimization algorithm depends on the complexity of the problem and the accuracy of the initial guess provided. We obtain the optimal solution by progressively increasing the complexity of the vehicle model used. Several optimization scenarios are presented for different road formations and different optimization cost functions, revealing different racing styles. In the third part of this thesis finally we provide rigorous proof of optimality of a semi-analytic methodology to generate optimal velocity profiles along prescribed paths using optimal control theory. A receding horizon implementation is designed introducing a dynamic scheme to determine planning and execution horizons. An extension of the semi-analytic methodology to the half-car model with yaw stability considerations is finally presented.

Chapter 1

Introduction

1.1 Motivation

The need to reduce the risk for human lives as well as eliminate the effects of human error in operating vehicles in hostile and hazardous environments (Fig. 1.1) has motivated the development of unmanned and autonomous ground, air and underwater vehicles. Research in the area of mobile robots has led to great advances in navigation of autonomous ground vehicles addressing problems such as position regulation and path tracking [12, 13, 14, 15] as well as obstacle/collision avoidance [16, 17, 18, 19, 20].

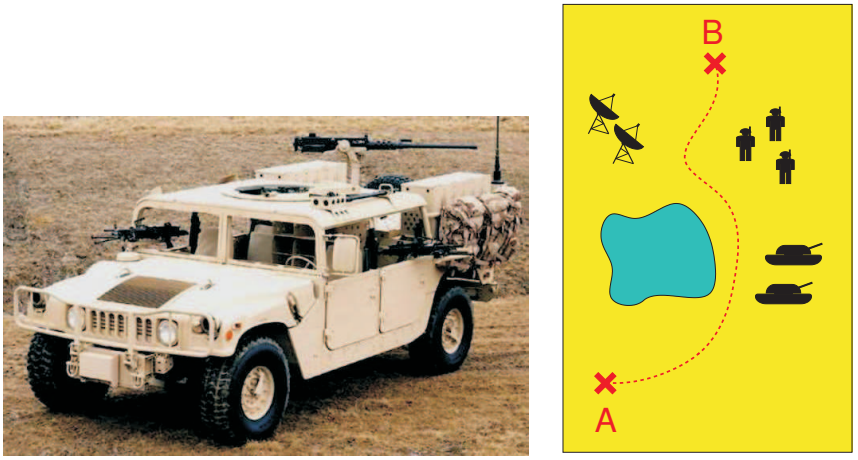

Figure 1.1: *Autonomous unmanned vehicles are envisioned to eliminate the risk for human lives in hazardous environments; Military off-road vehicle and mission map.*

A common assumption to date has been that the vehicle is moving relatively

slow and a no-slipping/no-sliding condition is imposed to simplify the vehicle/ground interaction (Fig. 1.2). Under such conditions a nonholonomic constraint is introduced and a kinematic model is adequate to describe the equations of motion of the vehicle. The vehicle is operating in the range of validity of the linearized dynamics away from the adhesion limits of the vehicle/ground interface (e.g. tires) resembling the way average drivers operate their automobiles (Fig. 1.3). It is envisioned that the next generation of auto-pilot agents for autonomous ground vehicles will take advantage of more of the available acceleration capacity of the vehicle, driving through each mission as fast as possible, minimizing the exposure to danger. The ultimate goal is to develop autonomous systems that mimic the behavior of expert race drivers that operate at the limits of the vehicle's handling capacity (Fig. 1.3) and intentionally violate the no-slipping/no-sliding constraints to maximize the vehicle's acceleration through a course (Fig. 1.4). In such a mode of operation of a vehicle a kinematic model is not adequate to describe the equations of motion.

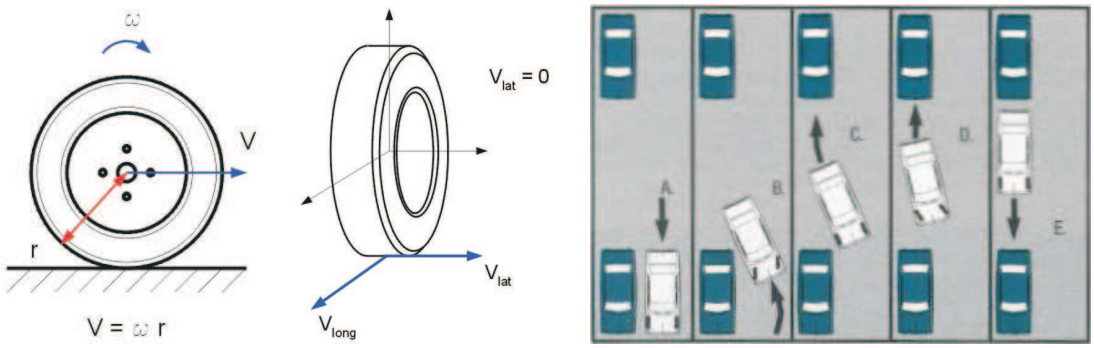

(a) (b) (c)

Figure 1.2: *(a) Pure rolling of the tire (No-slip condition); (b) No lateral velocity component (No-slide condition); (c) The parallel parking maneuver is a typical example of a vehicle mode of operation where we have low speed and the no-slip, no-slide conditions hold imposing a non-holonomic constraint. The non-integrable (non-holonomic) velocity constraint implies that the vehicle may not move sideways which makes this maneuver somewhat difficult.*

The goal of this work is to reproduce driving techniques used by expert race drivers and obtain the reference signals (open-loop controls) for an auto-pilot agent. As already mentioned we wish to take advantage of the whole acceleration capacity of

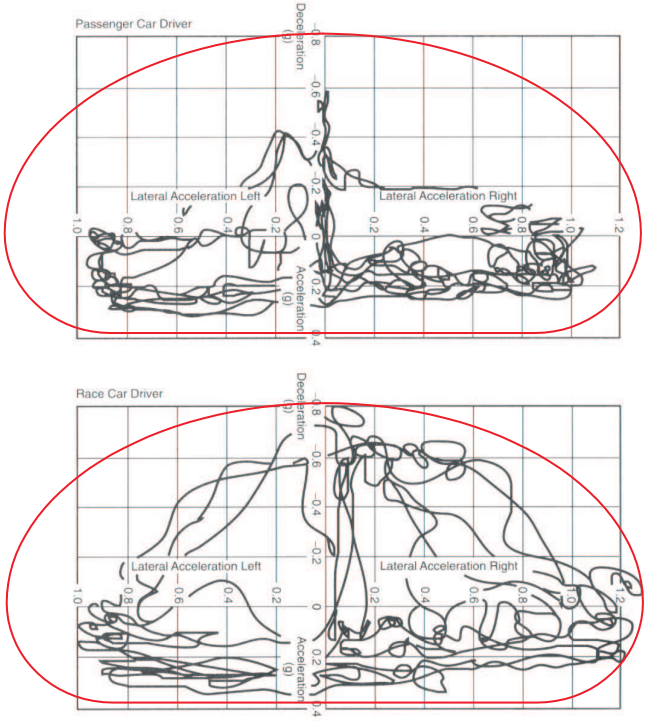

Figure 1.3: *The average driver (top) operates away from the acceleration limits of the vehicle denoted by the elliptic envelope. A race-driver (bottom) takes advantage of the whole acceleration capacity and a linear model is not appropriate anymore to describe the vehicle dynamics.*

the vehicle and thus an accurate characterization of the acceleration envelope of the vehicle is required. While most of the modeling issues of ground-vehicles/automobiles are well established in the literature there still remain a few unresolved problems. Most important is a lack of understanding of the physics associated with friction generation, which results in ad-hoc approaches to tire friction modeling. We are thus motivated to revisit this aspect of the overall vehicle modeling in order to gain experience and insight on the dominant characteristics of tire friction generation.

The trajectory planning problem then needs to be formulated in an optimal control framework aiming to minimize the time of travel and maximize the use of the available acceleration capacity. A linear approximation of the vehicle dynamics incorporating the simplifying assumption of no-slipping/no-sliding is obviously inappropriate when trying to reproduce race-car drivers behavior. On the other hand, increasing the fidelity of the vehicle model used results in increasing the complexity of the optimal

control problem. Care must be taken such that the proposed algorithms are efficient for online applications. This underlines the need for optimal solutions that require little computational cost and are able to incorporate real, unpredictably changing environments.

Figure 1.4: *Navigation of mobile robots approaches (left) assume low speeds and negligible slipping/sliding. Race drivers (right) intentionally induce slipping/sliding of the vehicle to minimize time of travel during a race. In this work we reproduce such techniques and obtain the open-loop controls for auto-pilot agents that will drive autonomous vehicles.*

1.2 Current State of Knowledge

Modeling for simulation and control of automotive systems has been a subject of intense research in the literature. This research has led to several methodologies for simulating vehicle dynamics in order to evaluate the performance of vehicles, develop new systems to enhance safety and performance as well as to automate several tasks during driving. Certain results can also be used to fully automate the operation of ground vehicles and develop autonomous systems to carry out missions in hazardous environments.

Control design requires first the development of an accurate mathematical model that describes the dynamics of the system. Most of the modeling issues regarding vehicle dynamics have been resolved [21, 22, 2] using classical mechanics. However, the physics of tire friction generation are not yet completely understood and currently a great deal of research is focused on modeling the tire forces.

1.2.1 Tire Friction Modeling

The problem of predicting the friction force between the tire and the ground for wheeled vehicles is of enormous importance to the automotive industry. Since friction is the major mechanism for generating forces on the vehicle, it is extremely important to have an accurate characterization of the magnitude and direction of the friction force generated at the tire/ground interface. However, accurate tire/ground friction models are difficult to obtain analytically. Subsequently, in the past several years, the problem of modeling and predicting tire friction has become an area of intense research in the automotive community. In particular, anti-lock braking systems (ABS) and traction control systems rely on knowledge of the friction characteristics. Such systems have enhanced safety and maneuverability to such an extent, that they have become almost mandatory for all future passenger vehicles.

The most common class of tire fiction models in research and applications are the so-called "static" models [23, 24, 25, 1, 26]. These models predict the friction force (magnitude and direction) for constant vehicle and tire angular velocity as a static map of the relative velocity of the tire to tire friction force. The major representative of this class of models is Pacejka's "Magic Formula" [1, 26]. This is a semi-empirical model using a set of parameters to fit a mathematical formula to experimental data. This data corresponds to steady-state (i.e., constant linear and angular velocity) tire friction measurements in a highly controlled laboratory environment or using specially designed test vehicles. Under such steady-state conditions, experimental data seem to support the force vs. slip predictions of these static models. In reality, the linear and angular velocities can never be controlled independently, and hence, such idealized steady-state conditions are not reached except during the rather uninteresting case of cruising with constant speed. The development of the friction force at the tire/road interface is very much a dynamic phenomenon. In other words, the friction force does not reach its steady-state value instantaneously, but rather exhibits transient behavior which may differ significantly from its steady-state value. Experiments performed in commercial vehicles have shown that the tire/road forces do not necessarily vary

along the steady-state force versus slip curves, but rather "jump" from one steady-state curve to the other [27]. In addition, in realistic situations, these variations are most likely to exhibit hysteresis loops, clearly indicating the dynamic nature of friction. Slip based static tire friction models also have inherent singularities at low speeds/wheel angular rates due to the definitions of the slip quantities and thus caution is required when they are applied to vehicle motion simulations.

Recently, a second class of tire friction models has been developed that capture the dynamic behavior of friction forces – the so-called "dynamic tire friction models" [28, 29, 30, 31, 5, 32, 33, 34]. In [28] dynamic models were proposed to handle the rate-independent hysteresis phenomena observed in practice. As an application to this work, a dynamic elastoplastic friction model was developed in [35]. This friction model was then applied to the longitudinal motion of a tire in [29] and extended to the longitudinal/lateral motion in [30, 31]. Slightly different in spirit is the work in [5] where a static map of relative velocity to friction and the dynamics of slip and slip angle were used to predict tire friction forces by taking into consideration the effects of length relaxation.

A significant amount of research has been conducted towards extending the low-order dynamic friction model of [36], namely the LuGre dynamic model for point contact, to the motion of a tire. The model of [36] is a dynamic visco-elastoplastic friction model that accurately captures the dynamic behavior of the friction generation mechanism in the presence of relative motion between two surfaces. The LuGre tire friction model was initially introduced in [37] and was later corrected and improved upon in [34, 38] taking into consideration longitudinal-only relative motion at the contact patch of a tire. Further extension of the longitudinal tire model of [34, 37, 38] to the plane (longitudinal and lateral) motion of the tire has appeared in [30, 32, 33]. In [33], the coupling of the forces in different directions has been neglected, resulting in a set of two independent ordinary differential equations describing the deflection of the bristles at the contact patch in the longitudinal and lateral directions. In [32], the coupling of the forces in the longitudinal and lateral directions was taken into consideration in accordance to an extension of the static

friction model for longitudinal/lateral motion in [1]. In [32], however, the anisotropy of the friction characteristics in steady-state and the rotation of the wheel rim about the vertical axis were neglected. In [39, 40] the LuGre point contact friction model was first extended to the planar motion of a surface including rotation and then to a tire model that captures the effects of the wheel rim rotation, using the simplifying assumption of a uniform normal load distribution. A more complete dynamic model is presented in [30]. This reference takes into consideration both the coupling of the friction forces in different directions and the anisotropy of the friction characteristics in steady-state, as well as the effects of the wheel rim rotation about the vertical axis. In [30] a discretization of the contact patch has been used in order to achieve a finite order expression of the dynamics, leading potentially, however, to a large number of states. Similarly, finite order expressions of the LuGre tire model were proposed in [30, 32, 33, 34, 37, 38] introducing approximations that, however, do not hurt the accuracy of the model in steady-state, to obtain lumped models with as a small number of ordinary differential equations (i.e., states) as possible. Such low-dimensional, lumped models are necessary for the development and implementation of *on-line* estimation and control algorithms [41, 42]. In particular, in the context of this work we reserve the term "lumped model" for the mathematical description via a single ordinary differential equation along each direction, in lieu of a distributed model with an infinite number of states or a discretized distributed model with a large number of states.

1.2.2 Vehicle Modeling and Control

Next, we demonstrate the current trend in research on ground vehicle (automobile) modeling and control towards simulation for performance evaluation/enhancement as well as development of control systems to assist the driver with or completely automate certain tasks during driving. A few results, mainly in open-loop control, concentrate on limit-operation of the vehicle, i.e., taking advantage of the total acceleration capacity of the vehicle to perform a maneuver.

In [43] a linear model of the lateral half-car dynamics with linear friction is used

to solve the "inverse dynamics" problem. Using as input a lateral acceleration profile which describes a path of the lateral dynamic states, yaw rate and sideslip angle are calculated. The steering angle, which is the actual control input, is calculated analytically from the lateral states, while the longitudinal velocity is considered constant.

In [44] the linear lateral dynamics of a "half-car" model (with linear tire friction) is used to design sliding steering controllers for automatic path tracking using robust estimators with vehicle position and yaw rate measurements. Nonlinearities are introduced into the problem arising from saturation constraints on the steering angle. The longitudinal dynamics are not taken into consideration and the vehicle velocity is treated as a constant parameter. In [45] linear and nonlinear controllers are designed for the same problem using a linear model with linear tire friction. Once again, the velocity of the car is considered as a constant, but uncertain, parameter. In [46] yaw rate feedback is used to make the yaw rate dynamics unobservable from the lateral motion dynamics. The controller makes the yaw dynamics stable and the human driver is left to deal with the lateral position dynamics. In this work the lateral tire forces are treated as unknown parameters. An alternative method for decoupling yaw motion from lateral motion is presented in [47]. Instead of yaw rate feedback, a measurement of the position error of a look ahead point at some distance in front of the vehicle along the path is used. The car model is assumed to be linear with linear tire friction. In [48] and [49] a definition similar to [47] of a "look ahead offset" is used with linear feedback to design a steering controller to achieve tracking. A nonlinear model with linear tire friction is used. The linearized model is considered to prove local stability. Still, in this work the longitudinal dynamics are not taken into consideration. In [50] another path tracking controller is designed using 4-wheel steering (4WS) and direct yaw control (DYC). In [51] digital optimal control with road preview is used to design a steering controller for path tracking minimizing the tracking error. A linearized "half-car" model with linear friction is used while the longitudinal dynamics are neglected and the longitudinal velocity is treated as a parameter. In [52] an open-loop and a closed-loop controller are presented for the problem of path tracking of a "half-car" model (linear with linear friction, no longi-

tudinal dynamics) through a lane change maneuver. The form of the control input (steering angle) is pre-specified and contains parameters optimized for travel time minimization. The closed loop controller is based on a single preview point feedback which provides the deviation from the path generated by the open loop controller. A nonlinear, four-wheel car model is used in [53] to design a steering controller for heading angle and combined heading angle - yaw rate tracking. The model and the controllers are written in terms of the friction forces. It is suggested that the friction forces can be estimated. The nonlinear lateral vehicle dynamics with linear friction are used in [54] to design a steering controller for the C.G. of the vehicle to track the centerline of the road.

Several references can be found in the literature that deal with the combined longitudinal and lateral control of an autonomous vehicle. In [55, 56, 57, 58] a half-car model with linear tire friction is considered and a combined longitudinal and lateral motion controller for regulation and path tracking is designed based on a Lyapunov approach. In [59] a numerical optimization problem is solved to obtain the open-loop control inputs (longitudinal and lateral) for the case of path tracking. Using a singular perturbation context, the longitudinal control input is considered to be the longitudinal slip of the wheels. A controller is then proposed for the torque input to track the desired longitudinal slip history. In [60] combined longitudinal and lateral control design is presented for the problem of target following in a truck convoy. The longitudinal controller guarantees that a safety distance is kept between the controlled (following) and the leading (target) vehicle. The steering (lateral) controller eliminates the offset angle between the velocity vector of the following vehicle and the longitudinal axis of the target. Nonlinear dynamics for the truck vehicles are used, however linear friction model is adopted. Another result on combined lateral and longitudinal control for the target following problem of a vehicle in an Automated Highway System is presented in [61]. A nonlinear bicycle model using Pacejka's "Magic Formula" for the tire forces, including aerodynamic forces and longitudinal weight transfer is introduced. Sliding controllers are designed to regulate the longitudinal spacing between follower and target and the lateral deviation of the center of

the front bumper of the follower from the road centerline. The control inputs are first considered to be the friction forces and then by solution of the associated inverse dynamics the real control inputs (steering angle and engine torque) are calculated. The combined control problem is taken into consideration in [62]. A complete nonlinear car model is used and a nonlinear steering controller using state and "look-ahead" measurement feedback is proposed for path following. At the same time a second controller is proposed for the longitudinal control in order to track a specified velocity profile generated by means of numerical optimization.

Next we present results in open-loop control of automobiles in the literature. Expert race-car drivers operate the vehicles at the limits of their stability envelope, which makes the role of the different vehicle parameters involved extremely difficult to investigate solely by means of numerical simulation. To this end, numerical optimization techniques have been used in the literature in order to reproduce trajectories and driving techniques similar to those of expert race-car drivers. In [63] numerical optimization for a car performing a "lane change" maneuver is presented. The inverse dynamics are solved by an optimization algorithm which provides the open-loop control history. The car model used in [63] is rich in the sense that it includes a nonlinear tire model, load transfer effects and both lateral and longitudinal control inputs. The task of path tracking is attacked by including the position error from the specified path in the cost function; this way one avoids the use of state constraints. In [64] the Newton-Raphson algorithm is used in order to calculate steering and braking/accelerating inputs for a car to perform a specific maneuver, defined by lateral and longitudinal acceleration profiles, within some tolerances. The vehicle model is a comprehensive multi-body dynamics model which includes suspension dynamics and nonlinear tire friction model. There are no optimization considerations in [64] and the main use of the approach is to compare the response of different vehicles performing the same maneuver.

In [65] numerical solutions of the optimal control problem of a car performing a "lane change" maneuver are presented in order to compare different approaches for rear wheel steering. The path to the followed by the vehicle is included in the

cost function, as in [63]. More recently, in [66] the numerical solution of the optimal time problem for a car driving through a segment of the Suzuka F1 circuit has been presented. An accurate 3D description of the road is used which even includes bank. The car model used in that reference is over-simplified, however, as the vehicle is regarded as a particle. Another approach for the numerical optimization problem is presented in [67]. The constraint of the road is included as an additional term in the cost function, while a comprehensive 4-wheel car model, including nonlinear tire friction, load transfer, aerodynamic forces and driveline constraints is used. In [68] the authors have solved a similar optimization problem as in [67] using an equally rich car model and a more efficient optimization algorithm. In addition, the role of yaw inertia was studied in that reference. In [69] the authors presented the optimal time solution for the Suzuka and Barcelona F1 circuits and studied the influence of vehicle mass to the optimal trajectory. A change of the independent variable from time to distance travelled in the path is common in the above numerical optimization approaches and makes the optimization problem one of fixed final "time" which is easier to converge. At the same time, this change of independent variable introduces a singularity at high vehicle slip angles. High vehicle slip angles are not typically encountered in F1 race driving; they are, however, often noticed in off-road rally racing (Fig. 1.4).

Numerical optimization techniques, as presented above, incorporate accurate, high order dynamical models in the optimization process and thus produce quite realistic results. However, these numerical optimization approaches are computationally costly and may not be appropriate for real-time implementation. In order to develop a scheme for fast autonomous vehicle operation that can be applied in real time, we need a method that produces optimal or near optimal solutions with low computational cost. Such methods have been proposed, for instance, in [70, 71] and [72]. The path in these references is designed using geometric principles, and an "intuitively optimal" velocity profile is generated using a semi-analytical approach, by taking into consideration the maximum acceleration available to the vehicle at each point on the path.

These open-loop control approaches have been used by researchers to gain intuition on the governing dynamics of ground vehicles as well as study the role of several vehicle parameters in the vehicle's handling characteristics. It is envisioned that efficient methods to generate optimal open loop control inputs and reference trajectories for autonomous vehicles may be developed.

1.3 Objectives

In what follows we define the objectives of this work keeping in mind the motivation and limitations of current results as presented above.

- The first step, before we can even start studying racing techniques and obtaining reference signals for auto-pilot agents, is to gain experience and intuition on the vehicle dynamics. That requires the development of a vehicle model that provides physical interpretation of the phenomena taking place and enough fidelity to incorporate all dominant characteristics of the dynamics.

  Tire modeling is our first concern since there exists no established theory to explain the physics of tire friction generation. We follow a different path than the one usually followed in the literature. Since the physics are not understood, researchers typically use semi-empirical models based on experimental observations. In this work we aim to develop a tire model starting from point-contact friction models that provide a physical interpretation of the friction forces as a result of elastic deformation of the surfaces in contact. The dynamics of the friction generation mechanism is then applied to the contact patch of a tire on the road leading to a dynamic tire friction model. Features neglected in related results [30, 33, 32], such as coupling of the friction components in longitudinal/lateral directions, non-homogeneous static and dynamic friction characteristics and rotation of the wheel rim about a vertical (steering) axis, are now taken in consideration. The dynamic nature of the new tire model makes it more appropriate for simulations and control design since several singularities

and discrepancies of existing static tire models will be avoided. Low order expressions of the distributed tire model need to be derived for control/estimation applications. In this work we pursue the derivation of finite order expressions that not only capture the steady-state behavior of the distributed model but also its exact dynamic behavior. This allows us to validate existing low-order approximations.

Overall vehicle modeling is visited next. Most of the issues of automobile systems modeling have been resolved using classical mechanics. The problem is to establish a model which is rich and accurate enough to allow us to identify and interpret race driving techniques in simulations and, on the other hand, simple enough to make numerical simulations and optimization feasible.

- The problem of trajectory planning is addressed next. In this work we choose an optimal control formulation seeking the solution to the minimum time problem in order to investigate the driving techniques of expert race drivers. Our first optimization approach is the use of numerical techniques in accordance to existing results in the literature. However in this work we do not allow singularities at high vehicle slip angles by choosing time to be the independent variable. We also choose appropriate control inputs such that racing techniques that violate the coupling of controls (e.g. "handbrake cornering" and "left foot braking" for independent braking/acceleration of the wheels of each axle) may be reproduced.

  The advantage of this approach is that it provides freedom to choose the fidelity of the vehicle model in order to generate realistic solutions and study higher order effects such as load transfer and suspension dynamics. On the other hand, we expect increasing computational cost with the increase of the vehicle model's level of detail. Unpredictable environments cannot be incorporated (Fig. 1.5) and the numerical optimization scheme seems to show little promise of applicability in real-time. In addition, convergence of the optimization algorithm depends on the accuracy of an initial guess of the optimal solution that needs to

be provided by the user. To this end we perform a study with increasing level of detail of the dynamical model. We also consider several optimization scenarios with different optimization costs in order to reproduce several racing styles. The numerical optimization scheme still remains a powerful tool for off-line applications, such as experimentation with vehicle dynamics, vehicle parameter tuning and optimization, as well as reference signal generation for trajectory planning in unchanging environments.

- In order to overcome the major limitation of the numerical optimization schemes (high computational cost) we next seek analytic solutions of the trajectory optimization problem. Initially we provide a rigorous proof of optimality of the semi-analytical method of [70, 71] and [72], and address problematic cases where loss of controllability occurs, neglected in these references.

  Apart from the low computational cost, the optimization approach has to satisfy the requirement of applicability in unpredictably changing environments for on-line implementation (Fig. 1.5). We design a receding horizon optimization scheme, where the optimal solution is executed up to a finite horizon and then recalculated from the current position, allowing changes in the environment in the mean time to be taken into consideration. We have to ensure that at the end of each executed subarc the vehicle can reach a "safe state" (for example complete stop) no matter the changes in the environment outside the planning horizon. Such robustness guaranties are provided by design of a dynamic scheme that determines planning and execution horizons.

  An analytic approach to a complex optimization problem such as the maneuvering of a wheeled vehicle subject to saturation constraints is very likely to compromise the fidelity of the dynamical model used. Care is taken and the necessary extensions are provided such that no important feature of the vehicle dynamics is left out from the formulation of the optimal control problem.

  Finally, the analytic solution approach, except from satisfying the requirements for on-line applications, also provides a useful tool to generate "good" initial

guesses for the numerical optimization scheme using higher fidelity vehicle models.

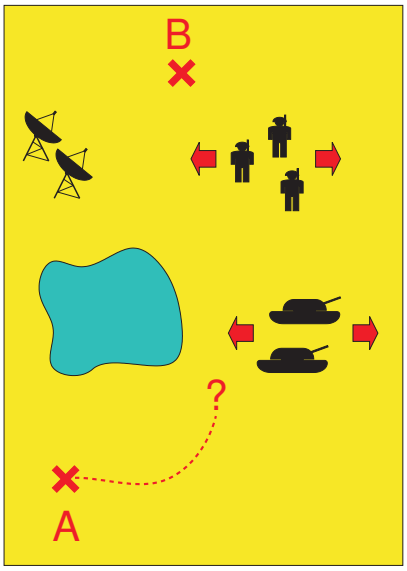

Figure 1.5: *In a fast changing environment we cannot determine the whole trajectory before hand.*

Part I

Tire Friction Modeling

Chapter 2

The LuGre Tire Friction Model: Derivation and Steady-State Characteristics

Lack of understanding of the physics of the dry friction generation mechanism poses a major challenge in developing mathematical models to predict tire friction. The automotive community currently copes with this challenge through collection of characteristics and properties of the tire friction by means of experimental observation and the development of empirical models.

In order to isolate and quantify the role of a specific parameter in the tire friction generation mechanism several experiments for different values of this parameter are necessary under fixed overall tire operating conditions. Such ideal operating conditions may only be achieved in a highly controllable experimental facility as in Fig. 2.1. The collected friction force data corresponds to steady-state conditions of constant vehicle speed v, wheel angular velocity ω and slip angle α (refer to Fig.2.2), normal load, road condition, tire temperature, inflation pressure etc.

The automotive community has reached an agreement as far as the component decomposition of the total friction force developed at the contact patch of a tire (Fig. 2.10). These components are the longitudinal tire force f_x, also referred to as accelerating/braking force, and the lateral tire force f_y, also referred to as cornering

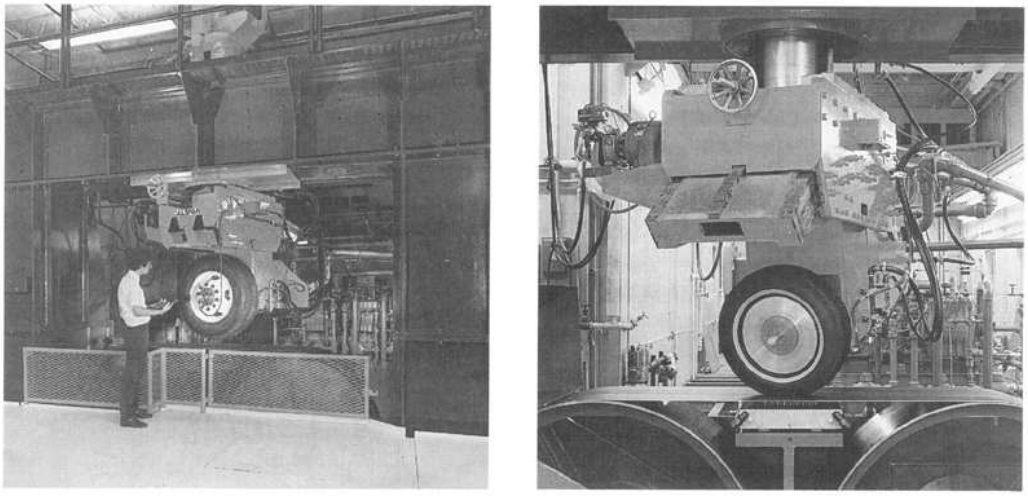

Figure 2.1: *Laboratory tire test machine for the characterization of tire friction properties [2].*

force. It is observed that, along with the longitudinal and lateral friction force components at the center of the contact patch, a moment M_z about the vertical axis is required to complete the overall tire friction force decomposition. Such a moment appears during cornering and opposes the increase of the slip angle α. This moment is referred to as "aligning torque" and is a result of the fact that the total force acts on a point on the contact patch away from the center by a distance that is called the "pneumatic trail".

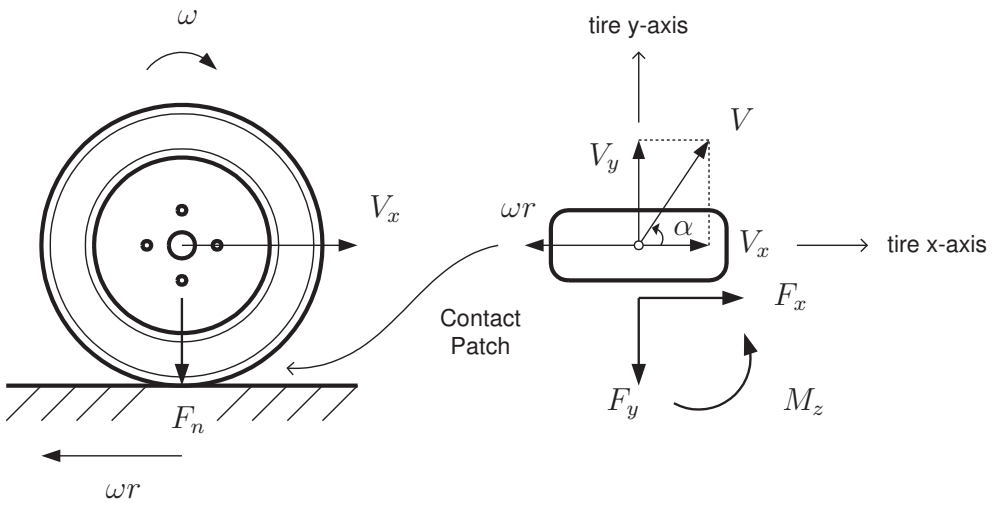

Figure 2.2: *Force and velocity components at the contact patch between the tire and the ground*

Experimental observation of the tire behavior under different operating conditions led to several major conclusions about the tire friction generation mechanism. Most important is the dependence of the generated friction force on the relative velocity between the tire and the road. The relative velocity at the contact patch is typically quantified by the non-dimensional slip quantities, longitudinal slip s_x and lateral slip s_y as follows (refer to Fig. 2.10):

$$s_x = \begin{cases} 1 - \frac{V_x}{\omega r} & \text{for} \quad \omega r \geq V_x \quad \text{(acceleration)} \\ -1 + \frac{\omega r}{V_x} & \text{for} \quad V_x \geq \omega r \quad \text{(braking)} \end{cases} \tag{2.1}$$

$$s_y = -\tan\alpha = -\frac{V_y}{V_x} \tag{2.2}$$

In all tire force characteristics with respect to a slip quantity, as in Fig. 2.3, we observe a distinct maximum at the end of an approximately linear region (adhesion region).

Other observations on tire friction come to agreement with what is already established by experience in dry (Coulomb) friction. For example, it is observed that the friction force is approximately a linear function of the normal load applied on the tire (Figures 2.3(a),(b)). In this work we will use the notation of the friction coefficient:

$$\mu_i = \frac{F_i}{F_n}, \quad i = x, y \tag{2.3}$$

In addition, an eminent dependence of the tire friction forces on the type and/or condition of the contact surface (Fig. 2.3(c)) exists. It is clear, even to the average driver, that the tire capacity to generate friction is reduced on a wet or icy road. Figure 2.3(d) shows the dependence of tire friction to the vehicle (tire translation) speed. We observe that the friction force capacity of the tire is reduced with increasing vehicle speed.

Finally, Fig. 2.4 reveals the coupling of the longitudinal and lateral components of the tire friction force. As mentioned above the tire's capacity to generate friction is limited by a distinct maximum for the longitudinal (Fig. 2.3(c),(d)) and lateral (Fig. 2.3(a)) directions. The experimental plot of Fig. 2.4 shows that the limited tire capacity translates to an elliptic (or circular) envelope in the $f_x - f_y$ plane which provides coupling between longitudinal and lateral components. For example, let that

the tire operates such that the maximum braking force is produced. That is a point on the friction envelope and no lateral (cornering) force is available.

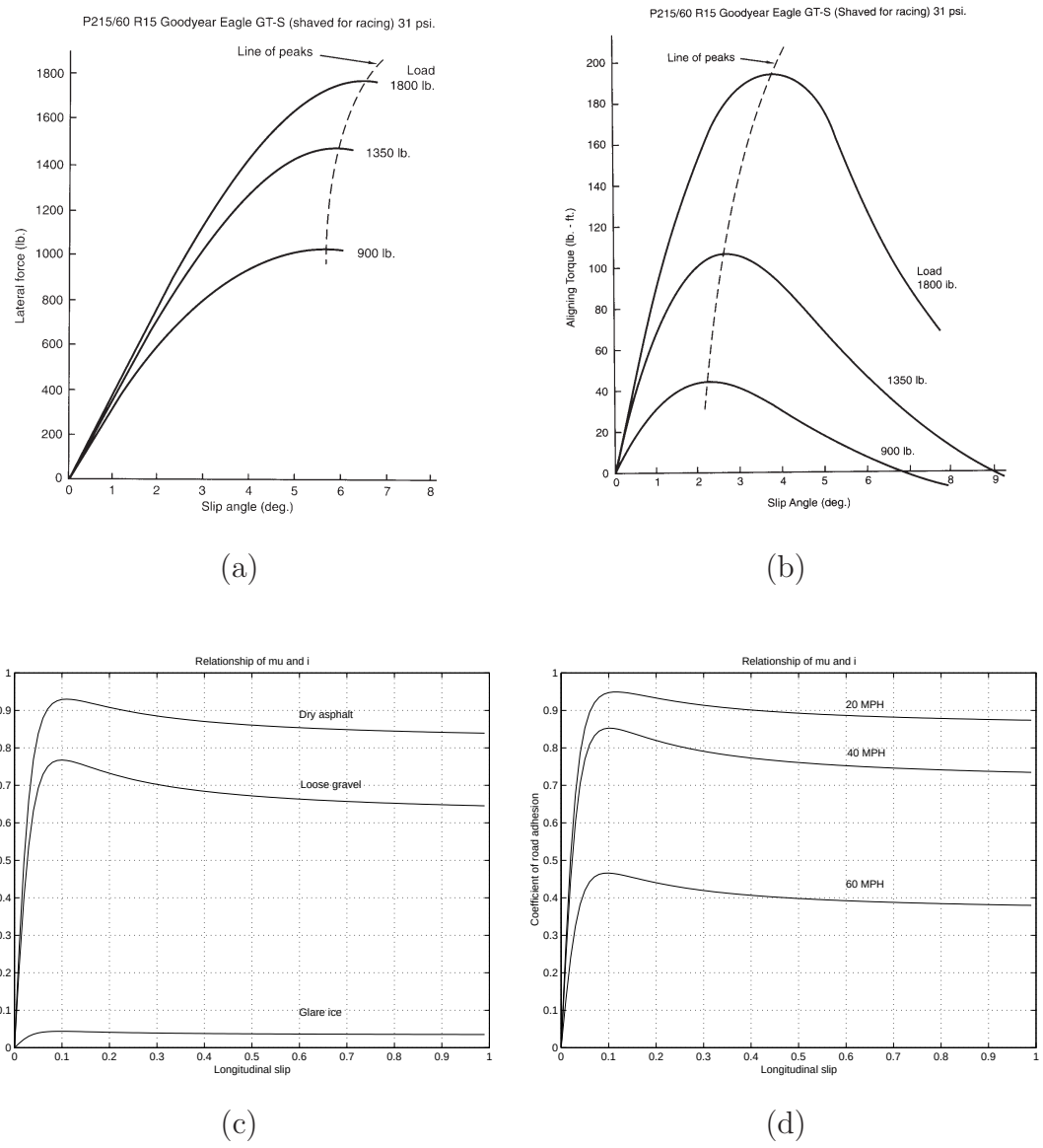

Figure 2.3: *Lateral friction force (a) and aligning moment (b) with respect to slip angle α for different normal loads [2]; Tire friction characteristics for different contact surfaces (c) and different vehicle speeds (d) [3].*

The discussion above cannot do justice to the amount of effort put to research in tire friction. It is just an introduction to the methodologies currently used by the industry to overcome the challenges associated with tire friction modeling and a few only of the major conclusions of this research. In this chapter we describe the

development of a new dynamic tire friction model from first principles, aiming to introduce physical interpretation to the modeling process. This is in contrast to the empirical models that are widely used in research of vehicle dynamics. The major representative of this class of models, Pacejka's "Magic Formula" is briefly described in the next session. The limitations of the steady-state empirical class of models provide additional motivation for a new approach in tire friction modeling.

2.1 Pacejka's 'Magic Formula'

A typical example of an empirical tire friction model is Pacejka's 'Magic Formula' (MF) [1, 26, 73]. In this model a mathematical formula is proposed to generate friction forces and moments characteristics versus longitudinal and lateral slip quantities to fit experimental data. The experimental data in this case correspond to steady-state operation of a tire, that is constant speed, angular rate and slip angle. Such conditions are practically realizable only in highly controllable experimental environments (Fig. 2.1).

The 'Magic Formula' is as follows

$$\begin{aligned} y &= D\sin(\mathrm{Carctan}(\mathrm{B}\phi)) \\ \phi &= (1-E)x + (E/B)\arctan(\mathrm{Bx}) \end{aligned} \tag{2.4}$$

or in a simplified version

$$y = D\sin(C\mathrm{atan}(Bx)) \tag{2.5}$$

In these formulas y is either the longitudinal and lateral tire friction forces F_x and F_y respectively, or the aligning torque M_z and the input x is either the longitudinal slip s_x or the slip angle α. The parameters B, C, D and E are identified such that the characteristics generated by the MF fit experimental data. There is no physical interpretation of the friction generation mechanism and thus the name 'Magic Formula'. The same formula (2.5) with different sets of parameters is used to produce F_x vs. s_x, F_y vs. α and M_z vs. α plots. Each set of parameters corresponds to the

specific steady-state velocity, normal load, contact surface, temperature, pressure etc conditions under which the experiment was conducted. As we can see in Fig. 2.5 [1] we can achieve excellent data fitting with (2.5) in cases of pure acceleration/braking or pure cornering.

For the combined longitudinal and lateral motion of the tire there is an extension of the 'Magic Formula' to include the 'friction circle property' discussed in the previous section. To this end in [1] the total slip quantity is defined as

$$s = \sqrt{s_x^2 + s_y^2} \tag{2.6}$$

The total friction force $F(s)$ on the tire is then computed using the 'Magic Formula' (2.5) where x is substituted by the total slip s. The longitudinal and lateral components are then calculated as

$$F_i = -\frac{s_i}{s} F(s), \quad i = x, y \tag{2.7}$$

Obviously

$$F(s) = \sqrt{F_x^2 + F_y^2} \tag{2.8}$$

and the total friction $F(s)$ is limited in a circle of radius equal to the maximum given by the 'Magic Formula' (2.3).

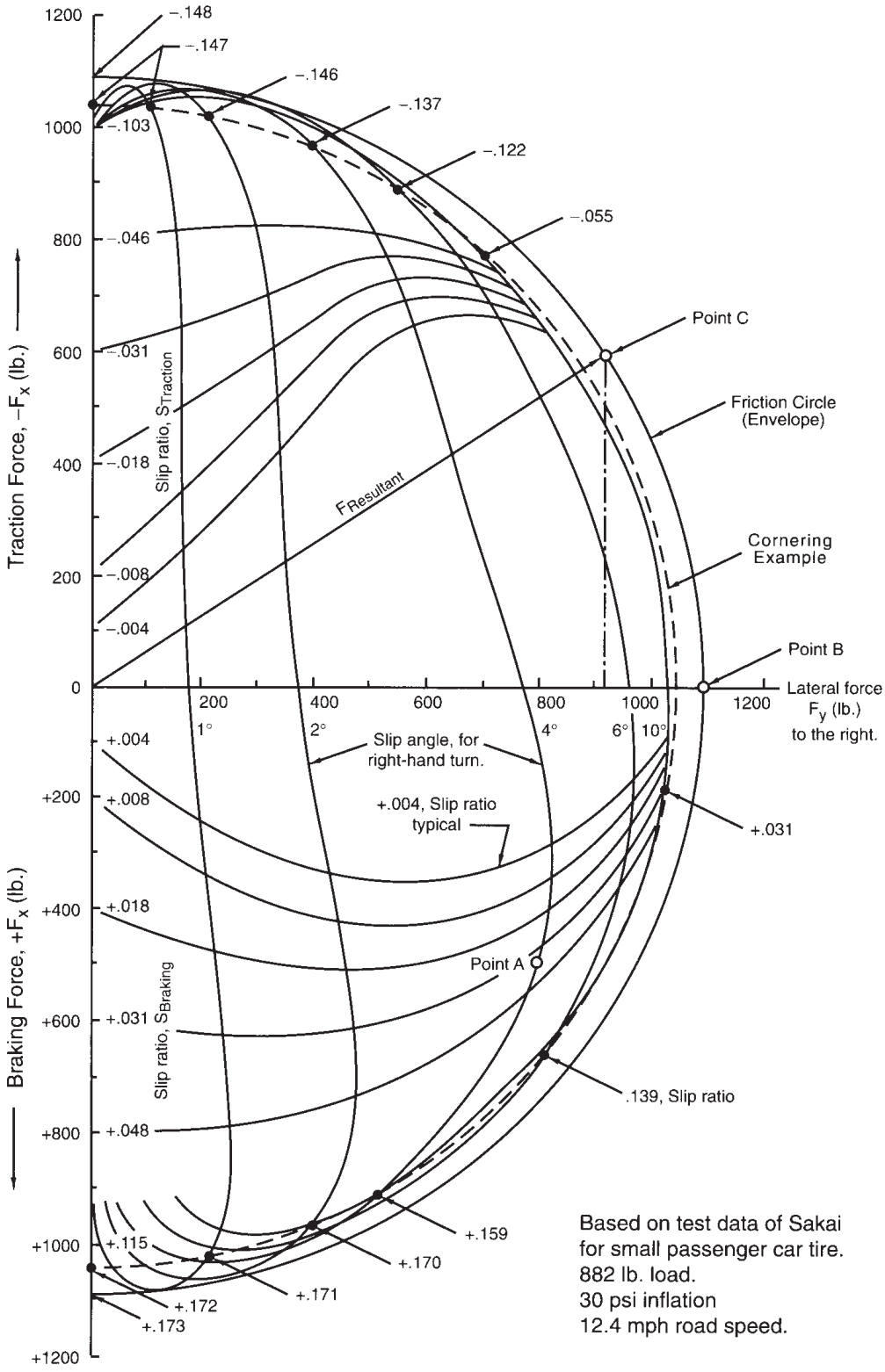

Figure 2.4: *Experimental friction circle diagram [2].*

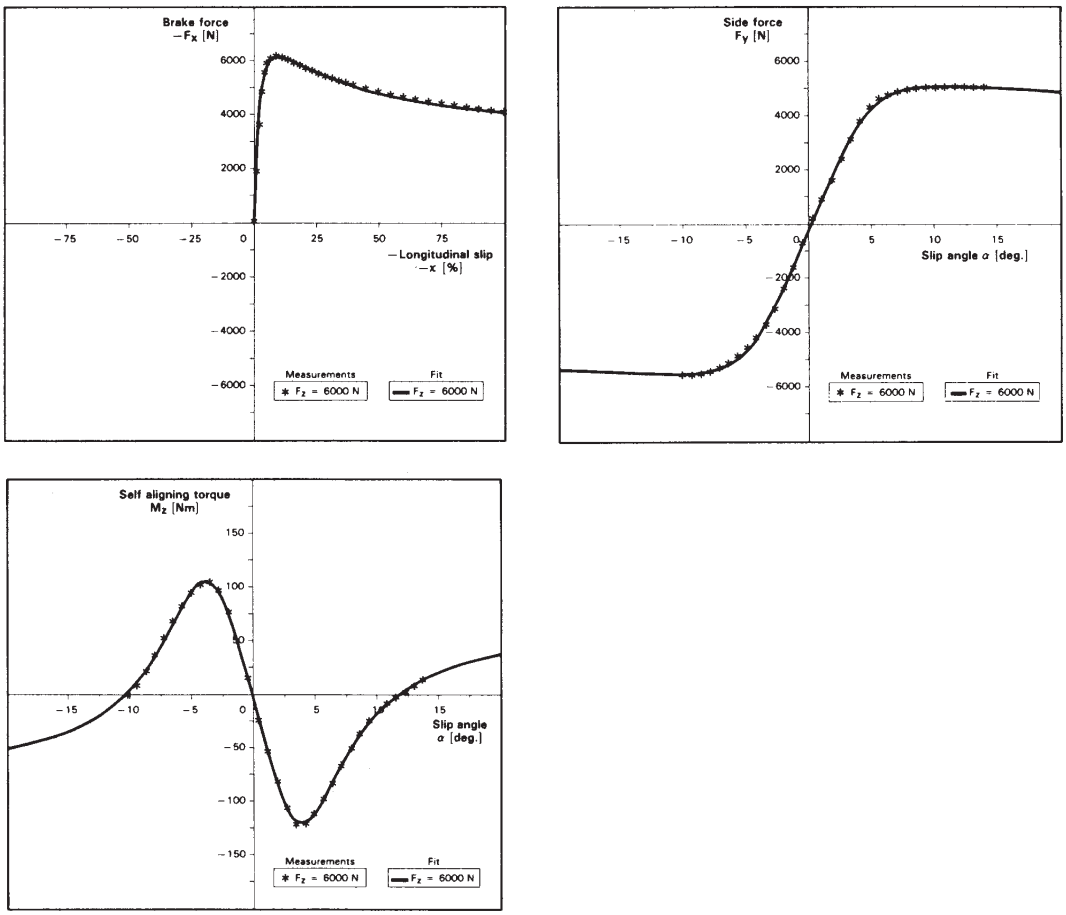

Figure 2.5: *F_x vs s_x, F_y vs α and M_z vs α 'Magic Formula' plots fitted to experimental data from [1].*

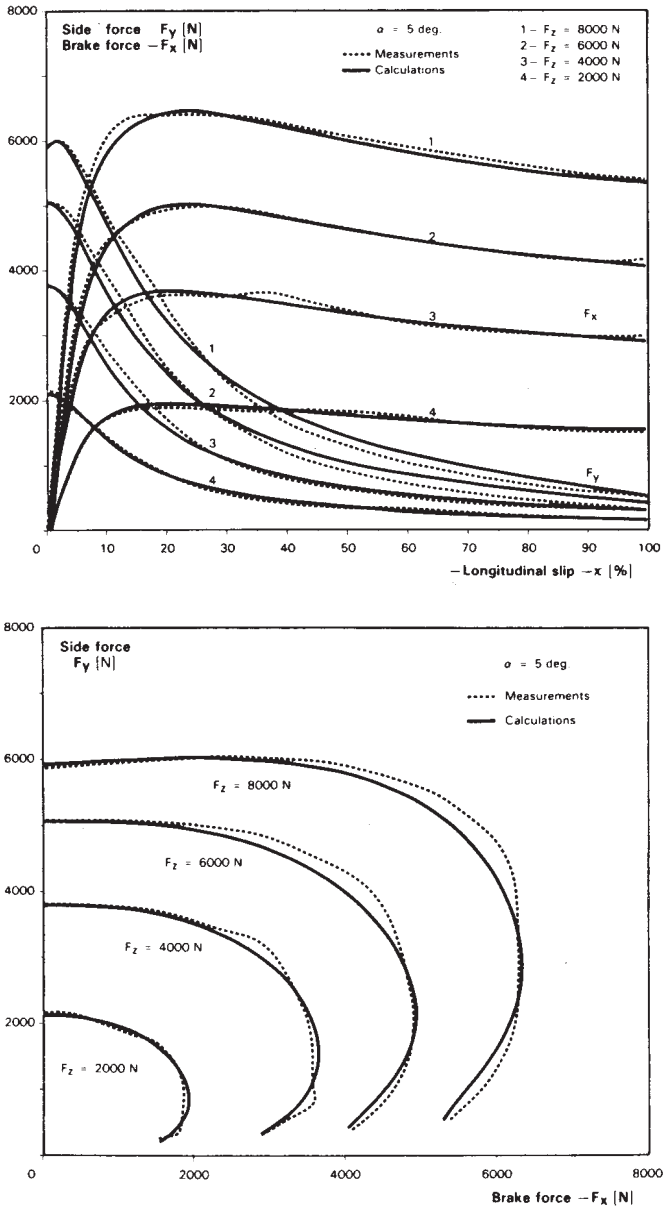

Figure 2.6: *f_x and f_y 'Magic Formula' plots for combined longitudinal and lateral tire motion from [1].*

2.2 Derivation of the LuGre Dynamic Tire Friction Model

The widely used class of steady-state empirical models, such as Pacejka's MF of the previous section, provide a useful approach to tire friction modeling. Such models, however, provide no information about the transient behavior of the tire friction forces and they are designed to capture only the steady-state operation of a tire. In addition, they provide friction force predictions as functions of the slip quantities (2.1) and (2.2) which are ill-defined in low speeds. Singularities of the slip quantities are directly transferred to the predicted friction forces through a static map (such as the MF).

A new approach to tire friction modeling is presented next. A physics-based dynamic friction model for point contact, the LuGre friction model [36], is applied to the contact patch of a tire and a new tire friction model is developed from first principles. The new model provides physical interpretation of the friction forces as a result of elastic deformation of the surfaces in contact. Its dynamic nature allows the study of the transient behavior of tire friction while the singularities associated with slip quantities are avoided.

In particular, in what follows we first present a methodology that allows one to derive a static friction model for combined 2D (longitudinal and lateral) motion. Using this methodology, we obtain a whole class of dynamic friction models. As a special case, we present the LuGre friction model for 2D motion which reduces nicely to the longitudinal motion model in the 1D (longitudinal) case [36]. Next, we derive a distributed tire friction model for the longitudinal/lateral motion of the tire by discretization of the contact patch and application of the point-contact friction model. We finally calculate the steady-state expression of the distributed tire model and compare it with Pacejka's MF model to determine a set of realistic parameters for the former.

2.2.1 Two-Dimensional Coulomb Friction Model

Recall that the Coulomb friction model for the linear translation of a body, with velocity v_r relative to the contact surface, provides the friction force coefficient by

$$\mu(v_r) = \begin{cases} -\mu_k & \text{for } v_r > 0, \\ [-\mu_s, \mu_s] & \text{for } v_r = 0, \\ \mu_k & \text{for } v_r < 0 \end{cases} \tag{2.9}$$

where μ_k is the kinetic and μ_s is the static friction coefficient. The friction force is given by $F = \mu F_n$ where F_n is the normal load. Typically, $\mu_s \geq \mu_k > 0$.

Consider now the simple case where $\mu_s = \mu_k$. We can derive the same model as in (2.9) by applying the Maximal Dissipation Rate Principle [74] to the following set of admissible friction coefficients

$$\mathcal{C} = \{\mu \in \mathbb{R} : |\mu_k^{-1}\mu| \leq 1\}. \tag{2.10}$$

Notice that if $\mu_k = \mu_s$ then $\mu \in [-\mu_k, \mu_k]$ is equivalent to the condition $\mu \in \mathcal{C}$. The dissipation rate is the product of the friction force with the relative velocity

$$D(v_r, \mu) := -\mu F_n v_r$$

The Coulomb friction force coefficient μ^* is the one in the admissible set that maximizes the dissipation rate, i.e.,

$$\mu^* = \text{argmax}_{\mu \in \mathcal{C}}[-\mu F_n v_r(t)], \quad \forall v_r, \forall t > 0 \tag{2.11}$$

Theorem 1 ([30]) The solution to (2.10), (2.11) is given by

$$\mu^* = -\text{sign}(v_r)\mu_k \tag{2.12}$$

and the maximum dissipation rate is

$$D(v_r, \mu^*) = -\mu^* F_n v_r = \mu_k F_n |v_r| \tag{2.13}$$

Proof For $\mu \in \mathcal{C}$ the following holds

$$-\mu\mu_k^{-1}\mu_k v_r \leq |\mu\mu_k^{-1}\mu_k v_r| = |\mu\mu_k^{-1}||\mu_k v_r| \leq |\mu_k v_r| = \mu_k |v_r|$$

which implies,

$$\begin{aligned} \mu_k|v_r| &\geq -\mu\mu_k^{-1}\mu_k v_r \\ \mu_k|v_r| &\geq -\mu v_r \\ \text{sign}(v_r)\mu_k F_n v_r &\geq -\mu F_n v_r \\ -\mu^* F_n v_r &\geq -\mu F_n v_r, \quad \forall \mu \in \mathcal{C} \end{aligned}$$

Thus, we have $D(v_r, \mu^*) = -\mu^* F_n v_r = \mu_k F_n |v_r| \geq D(v_r, \mu), \quad \forall \mu \in \mathcal{C}$. □

Next, consider the case of plane (2D) translation of a body with velocities v_{rx}, v_{ry} relative to the contact surface along the longitudinal and lateral directions, respectively. Let the velocity vector $v_r := [v_{rx}\ v_{ry}]^T$ and let

$$M_k := \begin{bmatrix} \mu_{kx} & 0 \\ 0 & \mu_{ky} \end{bmatrix} > 0 \tag{2.14}$$

be the matrix of kinetic friction coefficients, with μ_{kx} and μ_{ky} the friction coefficients for longitudinal motion along the x and y directions, respectively. In general μ_{kx} and μ_{ky} are different [30].

In analogy to (2.10), the set of admissible friction coefficient vectors $\mu = [\mu_x\ \mu_y]^T$ may now be defined as

$$\mathcal{C} = \{\mu \in \mathbb{R}^2 : \|M_k^{-1}\mu\| \leq 1\}, \tag{2.15}$$

where $\|.\|$ denotes the Euclidean norm. The Coulomb friction force coefficient will again be the one from the admissible set that maximizes the dissipation rate. Thus,

$$\mu^* = \text{argmax}_{\mu \in \mathcal{C}}[-F_n \mu^T v_r(t)], \quad \forall v_r, \forall t > 0 \tag{2.16}$$

Theorem 2 ([30]) The solution to (2.15), (2.16) is given by

$$\mu^* = -\frac{M_k^2 v_r}{\|M_k v_r\|} \tag{2.17}$$

and the maximum dissipation rate is

$$D(v_r, \mu^*) = -F_n \mu^{*T} v_r = F_n \|M_k v_r\| \tag{2.18}$$

Proof For $\mu \in \mathcal{C}$ and by the Cauchy - Schwarz inequality the following holds

$$-\mu^T M_k^{-1} M_k v_r \leq |\mu^T M_k^{-1} M_k v_r| \leq \|\mu^T M_k^{-1}\| \|M_k v_r\| \leq \|M_k v_r\|$$

which implies

$$\begin{aligned} \|M_k v_r\| &\geq -\mu^T M_k^{-1} M_k v_r \\ \frac{1}{\|M_k v_r\|} v_r^T M_k^T M_k v_r &\geq -\mu^T v_r \\ \frac{F_n}{\|M_k v_r\|} v_r^T M_k^2 v_r &\geq -F_n \mu^T v_r \\ -F_n \mu^{*T} v_r &\geq -F_n \mu^T v_r, \quad \forall \mu \in \mathcal{C} \end{aligned}$$

Thus, we have that $D(v_r, \mu^*) = -F_n \mu^{*T} v_r = F_n \|M_k v_r\| \geq D(v_r, \mu)$ for all $\mu \in \mathcal{C}$. $\square$

Observe that $\mu \in \mathcal{C}$ does not imply dissipativity of the friction force. Actually, $\mu \in \mathcal{C}$ implies $-\mu \in \mathcal{C}$ and if $F_n \mu^T v_r \geq 0$ then $-F_n \mu^T v_r \leq 0$. On the other hand, conditions (2.10), (2.11) or (2.15), (2.16) together imply dissipativity of the friction force. Since $0 \in \mathcal{C}$, it follows that $F_n \mu^{*T} v_r \leq 0$. The set $\mathcal{C}$ provides bounds for the friction forces and also coupling between the forces in different directions; see Fig. 2.7. In the case where $\mu_{kx} = \mu_{ky} = \mu_k$ then $\mu \in \mathcal{C} \Leftrightarrow \|\mu\| \leq \mu_k$ which is a circle in the $\mu_x - \mu_y$ plane. Observe that for μ^* from (2.17) we have that $\|M_k^{-1} \mu^*\| = 1$ which means that the predicted Coulomb friction coefficient μ^* always lies on the boundary of the friction ellipse (Fig 2.7). Thus, the set of admissible friction coefficients can be rewritten as

$$\mathcal{C} = \{\mu \in \mathbb{R}^2 : \|M_k^{-1} \mu\| \leq \|M_k^{-1} \mu^*\|\} \ . \tag{2.19}$$

Finally, observe that the maximization of the dissipation rate was done for the case where $v_r \neq 0$. Obviously when $v_r = 0$ the dissipation rate $D(v_r, \mu) = 0$ regardless of the value of μ. In this case the friction coefficient is bounded by the static friction coefficients $\|M_s^{-1} \mu\| \leq 1$ where

$$M_s = \begin{bmatrix} \mu_{sx} & 0 \\ 0 & \mu_{sy} \end{bmatrix} > 0 \ , \tag{2.20}$$

is the matrix of static friction coefficients.

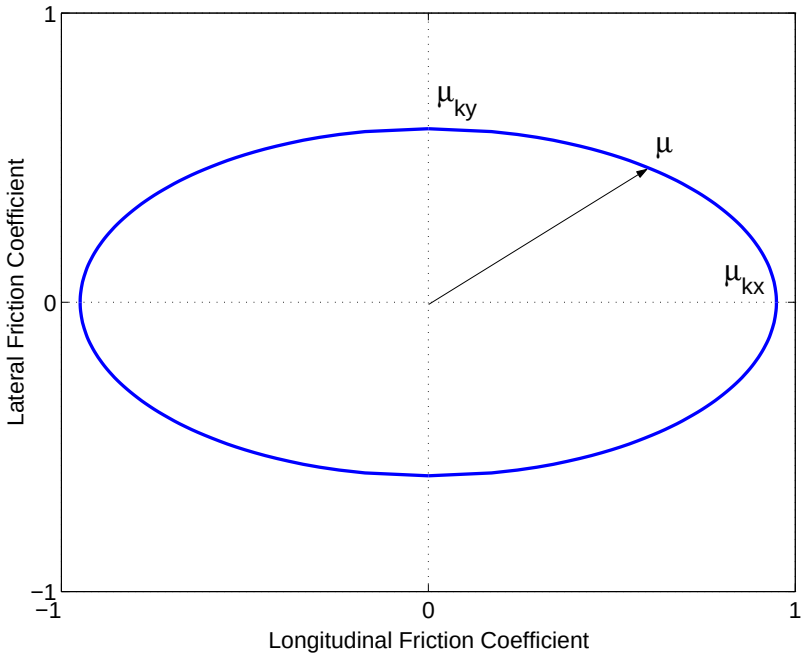

Figure 2.7: *Set $\mathcal{C}$ of admissible coefficients for the two-dimensional Coulomb case.*

2.2.2 A Class of Two-Dimensional Dynamic Friction Models

Using the set $\mathcal{C}$ of admissible friction coefficients and the Maximal Dissipation Rate Principle in [30, 74] dynamic friction models for the 2D motion of a body are derived. In this section we summarize the results of [30, 74] which will be useful in our developments. Dynamic models assume that friction is generated due to the interaction forces between microscopic bristles at the contact area; see Fig. 2.9. Most importantly, dynamic friction models can capture the Stribeck effect [36], according to which the steady-state friction coefficient decreases monotonically with v_r and the kinetic friction coefficients μ_{kx} and μ_{ky} provide bounds for the friction coefficient components only asymptotically, i.e. as $\|v_r\| \to \infty$ (Fig. 2.8). To this end, let M_k as in (2.14) be the matrix of asymptotic friction coefficients and let

$$K = F_n \begin{bmatrix} \sigma_{0x} & 0 \\ 0 & \sigma_{0y} \end{bmatrix} > 0 \tag{2.21}$$

be the matrix of stiffnesses of the bristles. Denote by u the relative deformation of a bristle at the contact area of the body and by $F = \mu F_n$ the associated force. Consider the elastic and plastic deformations $u_e = -F_n K^{-1}\mu$ and $u_p = u - u_e$ respectively, as

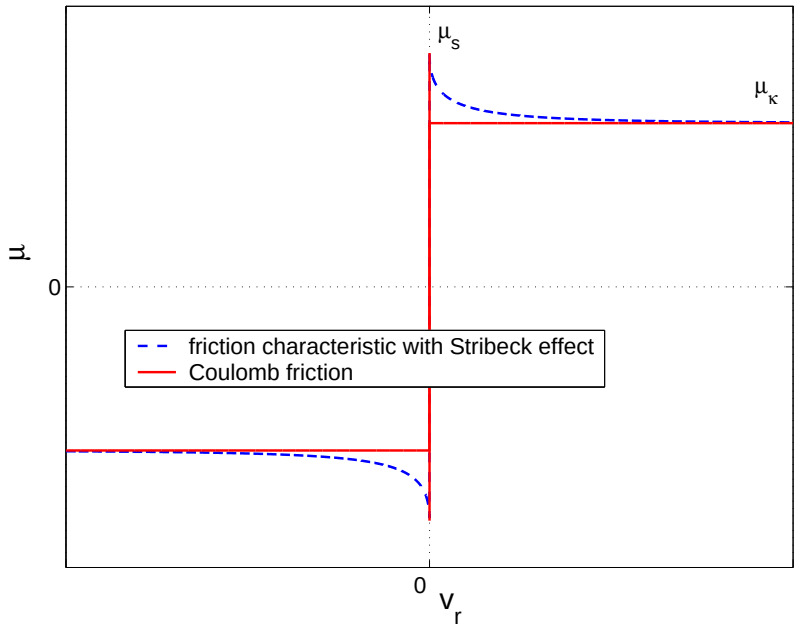

Figure 2.8: *The Stribeck effect.*

shown in Fig. 2.9. Dissipation depends only on the plastic deformation. Therefore, $D(\dot{u}_p, \mu) = -F_n \mu^T \dot{u}_p$ is the dissipation rate that must be positive and maximal. The friction coefficient μ^* is then given by the following Quasi-Variational Inequality (QVI) [30]

$$D(\dot{u}_p, \mu^*) \geq D(\dot{u}_p, \mu) \Rightarrow -(\dot{u} + F_n K^{-1} \dot{\mu^*})^T (\mu^* - \mu) \geq 0 \tag{2.22}$$

$$\forall\ \mu \in \mathcal{C} = \{\mu \in \mathbb{R}^2 : \|M_k^{-1}\mu\| \leq \|M_k^{-1}\mu^*\|\} \tag{2.23}$$

Observe that, in analogy to the Coulomb model of the previous section, the solution μ^* of the friction model is the one in the admissible set $\mathcal{C}$ that maximizes the dissipation rate. Observe also that we use the expression (2.19) for the set $\mathcal{C}$ which provides the coupling between the friction coefficient components. One cannot use here (2.15) because this expression, in addition to the coupling of the components, implies that the friction coefficient components are bounded by the Coulomb friction coefficients at all time, which contradicts the Stribeck effect (see previous discussion).

The QVI (2.22)-(2.23) has many solutions. In [30, 74] a class of solutions is proposed, generating a class of dynamic friction models as follows

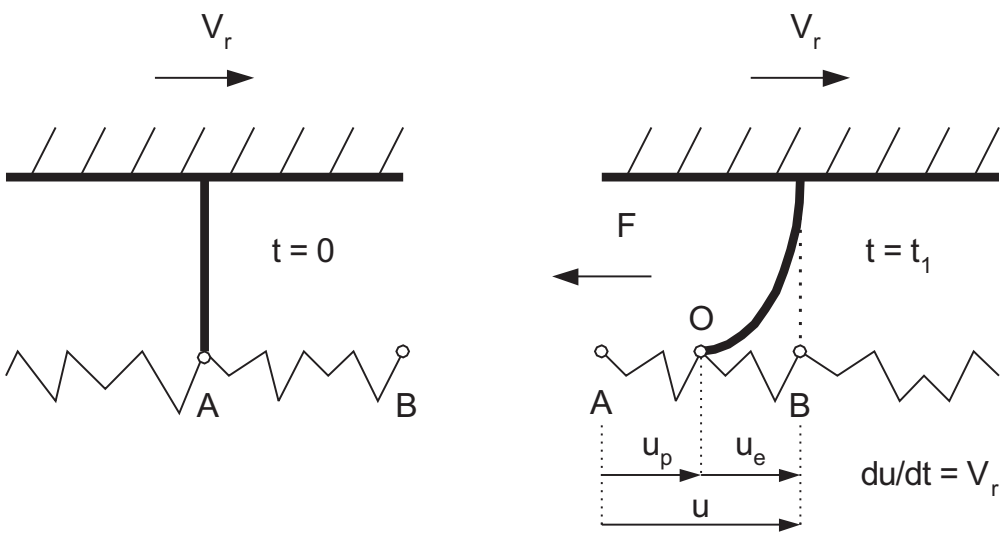

Figure 2.9: *Microscopic view of dynamics of friction.*

Theorem 3 ([30]) Any solution μ^* of

$$-F_n K^{-1}\dot{\mu^*} - \lambda(u, \dot{u}, \mu^*)M_k^{-2}\mu^* = \dot{u} \tag{2.24}$$

where $\mu^*(0) = \mu_0$, satisfies (2.22)-(2.23) for all $\lambda(u, \dot{u}, \mu^*) \geq 0$.

Proof Denote $\dot{u}_p = \dot{u} - F_n K^{-1}\dot{\mu}$. For $\mu \in \mathcal{C}$ and by the Cauchy-Schwarz inequality the following holds

$$-\dot{u}_p^T\mu \leq |\dot{u}_p^T M_k M_k^{-1}\mu| \leq \|M_k\dot{u}_p\|\|M_k^{-1}\mu\| \leq \|M_k\dot{u}_p\|\|M_k^{-1}\mu^*\| \tag{2.25}$$

Note that (2.24) implies that

$$\begin{aligned} -F_n K^{-1}\dot{\mu^*} - \lambda(u, \dot{u}, \mu^*)M_k^{-2}\mu^* &= \dot{u} \\ \dot{u} + F_n K^{-1}\dot{\mu^*} &= -\lambda(u, \dot{u}, \mu^*)M_k^{-2}\mu^* \\ M_k\dot{u}_p &= -\lambda(u, \dot{u}, \mu^*)M_k^{-1}\mu^* \end{aligned}$$

with $\lambda(u, \dot{u}, \mu^*) \geq 0$. It follows that (2.25) implies that

$$-\dot{u}_p^T\mu \leq -\dot{u}_p^T M_k M_k^{-1}\mu^* = -\dot{u}_p^T\mu^*$$

Thus we have that $D(\dot{u}_p, \mu^*) \geq D(\dot{u}_p, \mu)$ for all $\mu \in \mathcal{C}$. □

Several multi-dimensional dynamic friction models can be derived using (2.24) by choosing different scalar functions $\lambda(u, \dot{u}, \mu^*)$. The LuGre model [74] corresponds to the specific choice

$$\lambda(u, \dot{u}, \mu^*) \;=\; \lambda(\dot{u}) := \frac{\|M_k^2 \dot{u}\|}{g(\dot{u})} \tag{2.26}$$

with

$$g(\dot{u}) \;:=\; \frac{\|M_k^2 \dot{u}\|}{\|M_k \dot{u}\|} + \tilde{g}(\|M_k \dot{u}\|) \tag{2.27}$$

where $\tilde{g}(\|M_k \dot{u}\|) \to 0$ when $\dot{u} \to +\infty$. Note that we wish a model which asymptotically (as $\dot{u} \to +\infty$) approaches the Coulomb model (2.17) presented in the previous section. Therefore, the function $g(\dot{u})$ characterizes the steady-state of our dynamic model. In particular, for $\dot{u} \to +\infty$, (2.26) and (2.27) lead to

$$g(\dot{u}) \to \frac{\|M_k^2 \dot{u}\|}{\|M_k \dot{u}\|} \quad \text{and} \quad \lambda(\dot{u}) \to \|M_k \dot{u}\| \tag{2.28}$$

The steady-state friction coefficient is found by setting $\dot{\mu}^* = 0$ in (2.24)

$$\mu^{*\text{ss}} \to -\frac{M_k^2 \dot{u}}{\lambda(\dot{u})} = -\frac{M_k^2 \dot{u}}{\|M_k \dot{u}\|} \tag{2.29}$$

exactly as in (2.17). This justifies the choice of the particular $\lambda(u, \dot{u}, \mu^*)$ in (2.26).

2.2.3 LuGre Friction Model for 2D Motion

The LuGre friction model proposed in the previous section assumes that the friction is proportional only to the deflection (elastic deformation u_e) of the bristles at the contact point. Henceforth, we will refer to u_e as the internal friction state and we will denote it by z. In fact, it has already been assumed that $\mu = -(K/F_n)z$ and thus $\dot{\mu} = -(K/F_n)\dot{z}$. In order to include the dependence of the friction on the rate of z and the relative velocity at the point of contact $\dot{u}$, i.e., in order to include the damping and the viscous friction effects, we rewrite equation (2.24) in terms of the internal friction state z. We then have [36]

$$\dot{z} = \dot{u} - \lambda(u, \dot{u}, z) M_k^{-2} \frac{K}{F_n} z \tag{2.30}$$

where for the LuGre model the function $\lambda(u, \dot{u}, z)$ is given in (2.26). Finally, we choose $g(\dot{u})$ and $\tilde{g}(\dot{u})$ to be able to recover the LuGre friction model of [36] for longitudinal motion. To this end, we choose

$$g(\dot{u}) = \frac{\|M_k^2 \dot{u}\|}{\|M_k \dot{u}\|} + \left(\frac{\|M_s^2 \dot{u}\|}{\|M_s \dot{u}\|} - \frac{\|M_k^2 \dot{u}\|}{\|M_k \dot{u}\|} \right) e^{-\left(\frac{\|\dot{u}\|}{v_s}\right)^{\gamma}} \tag{2.31}$$

where M_s is the matrix of static friction coefficients as in (2.20) and v_s and γ are parameters used to achieve desirable steady-state behavior [34, 36]. Finally, the friction coefficient vector, including damping for z and a viscous friction component, is given by

$$\mu = - \begin{bmatrix} \sigma_{0x} & 0 \\ 0 & \sigma_{0y} \end{bmatrix} z - \begin{bmatrix} \sigma_{1x} & 0 \\ 0 & \sigma_{1y} \end{bmatrix} \dot{z} - \begin{bmatrix} \sigma_{2x} & 0 \\ 0 & \sigma_{2y} \end{bmatrix} \dot{u}. \tag{2.32}$$

Equations (2.26), (2.30), (2.31) and (2.32) represent the LuGre friction model for combined longitudinal/lateral motion. This model reduces to the longitudinal motion model of [36] in the 1D case.

To write the previous equations in terms of the x and y components let

$$z = \begin{bmatrix} z_x \\ z_y \end{bmatrix}, \quad \mu = \begin{bmatrix} \mu_x \\ \mu_y \end{bmatrix} \quad \text{and} \quad \dot{u} = v_r = \begin{bmatrix} v_{rx} \\ v_{ry} \end{bmatrix} \tag{2.33}$$

The proposed friction model is then written as follows

$$\dot{z}_i = v_{ri} - C_{0i}(v_r) z_i \tag{2.34a}$$

$$\mu_i = -\sigma_{0i} z_i - \sigma_{1i} \dot{z}_i - \sigma_{2i} v_{ri} \tag{2.34b}$$

where,

$$C_{0i}(v_r) = \frac{\lambda(v_r)\sigma_{0i}}{\mu_{ki}^2}, \qquad i = x, y \tag{2.35}$$

The scalar function $\lambda(v_r)$ is given by (2.26) and the function $g(v_r)$ by (2.31). Observe that the forces in the x and y directions are coupled due to $\lambda(v_r)$. This is consistent with the two-dimensional Coulomb friction model in (2.17) and Fig. 2.7.

2.2.4 Two-Dimensional LuGre Tire Friction Model

In this section we apply the LuGre friction model for 2D motion at the contact patch of a tire in order to derive a model for the tire-road contact forces and moments. We follow an approach similar to that in [37, 34]. To this end, we assume that the contact patch of the tire (the area of contact with the road) is approximately rectangular (Fig. 2.10). We divide the contact patch into infinitesimal elements. For each element we apply the point LuGre model for 2D motion of equations (2.34)-(2.35). In order to find the total forces and moments we then integrate the forces of each element along the patch. It should be mentioned that although we will keep referring to this friction model as 2D model, it will be in fact a 3-dof model since not only the longitudinal and lateral forces but the aligning moment will be captured as well.

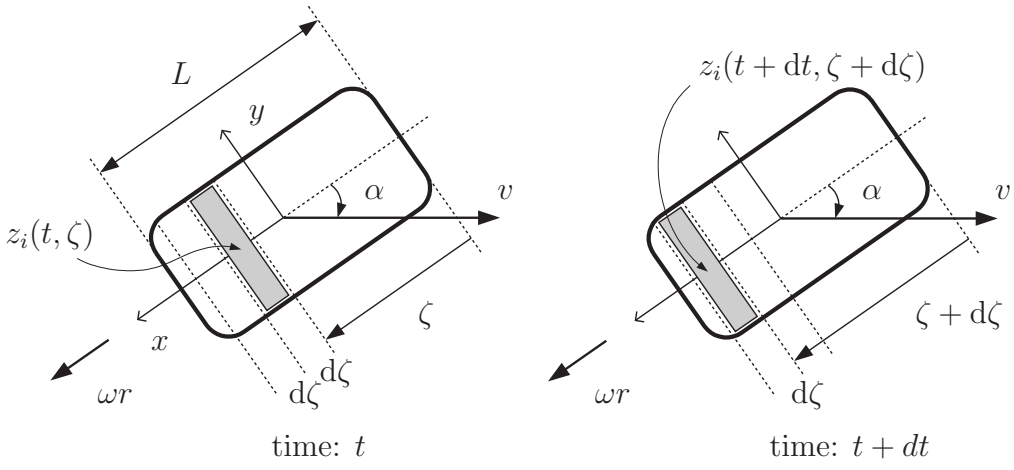

Figure 2.10: *Frame of reference and velocities at the contact patch. Derivation of the distributed tire model.*

To this end, let v denote the velocity of the vehicle and let ω denote the angular velocity of the wheel of radius r. Let α be the side slip angle of the wheel, that is, the angle between the velocity vector and the x (longitudinal) body axis of the tire. Let us also assume, for the time being, that the wheel rim is not rotating with respect to the vertical axis, i.e., the steering angle is constant. In general, the velocity of the tire has components in both x and y axes. The relative velocity components of the

elements in the contact patch with respect to the ground are

$$v_{rx} = \omega r - v\cos(\alpha) \tag{2.36a}$$

$$v_{ry} = -v\sin(\alpha) \tag{2.36b}$$

Considering a frame fixed on the contact patch, we observe that the tire elements move only along the length of the patch (ζ direction). For each tire element on the patch we can compute the friction using the LuGre model of the previous section. The internal friction states z_i $(i = x, y)$ now become functions of both time t and the position of the element on the patch ζ.

Let $z_i(t, \zeta)$ denote the deflections of the patch element along x and y directions respectively, located at the point ζ with respect to the patch frame at a certain time t. Consider the total deflection of this element between two time instances t and $t + \mathrm{d}t$. Since during the time interval $\mathrm{d}t$ the element has moved to the location $\zeta + \mathrm{d}\zeta$, and using (2.34) we have that the total deflections $\mathrm{d}z_i$ are

$$\mathrm{d}z_i = z_i(t + \mathrm{d}t, \zeta + \mathrm{d}\zeta) - z_i(t, \zeta) = (v_{ri} - C_{0i}(v_r)z_i(t, \zeta))\mathrm{d}t, \quad i = x, y$$

Since $\mathrm{d}z_i = \frac{\partial z_i}{\partial \zeta}\mathrm{d}\zeta + \frac{\partial z_i}{\partial t}\mathrm{d}t$ and using the fact that $\mathrm{d}\zeta/\mathrm{d}t = |\omega r|$, the friction model is summarized by the following equations

$$\frac{\mathrm{d}z_i(t, \zeta)}{\mathrm{d}t} = \frac{\partial z_i(t, \zeta)}{\partial t} + \frac{\partial z_i(t, \zeta)}{\partial \zeta}|\omega r| = v_{ri} - C_{0i}(v_r)z_i(t, \zeta) \tag{2.37a}$$

$$\mu_i(t, \zeta) = -\sigma_{0i}z_i(t, \zeta) - \sigma_{1i}\frac{\partial z_i(t, \zeta)}{\partial t} - \sigma_{2i}v_{ri}, \tag{2.37b}$$

where $i = x, y$. The total forces along the x and y directions are computed from

$$F_i(t) = \int_0^L \mu_i(t, \zeta)f_n(\zeta)\mathrm{d}\zeta, \quad i = x, y \tag{2.38}$$

where $f_n(\zeta)$ is the normal load distribution (force per unit length) along the contact patch and L is the length of the patch. The force distribution along the y direction also results into a moment about the center of the patch (aligning torque) given by

$$M_z(t) = -\int_0^L \mu_y(t, \zeta)f_n(\zeta)\left(\frac{L}{2} - \zeta\right)\mathrm{d}\zeta \tag{2.39}$$

For $\omega = 0$ equation (2.37a) reduces to equation (2.34a) of the point contact LuGre model for $\omega = 0$. This is in agreement with the physics of the problem, as in this case the tire is a body in pure translation and its dynamics should coincide with those of a point-contact dry friction model, which are given by equation (2.34a).

To evaluate this distributed model we compare it against other tire models. In the following we compare the forces predicted by the previous distributed model, in steady-state, with the MF model.

2.3 Static Behavior of the LuGre Tire Model

2.3.1 Steady-State Conditions

The steady-state characteristics of the model (2.37) are obtained by setting $\frac{\partial z(t,\zeta)}{\partial t} = 0$, and by imposing that the velocities v and ω (and hence v_r) are constant. In this case, the pde in (2.37a) becomes

$$\frac{\partial z_i(t,\zeta)}{\partial \zeta} = \frac{1}{|\omega r|}\left(v_{ri} - C_{0i}(v_r) z_i(t,\zeta)\right), \quad i = x, y, \quad \omega \neq 0 \tag{2.40}$$

Enforcing the boundary condition $z_i(t,0) = 0$ (no deflection at the entry point of the patch) and the steady-state conditions of constant v and ω, we may integrate (2.40) to obtain

$$z_i^{\text{ss}}(\zeta) = C_{1i}\left(1 - e^{-\frac{\zeta}{C_{2i}}}\right), \quad i = x, y \tag{2.41}$$

where,

$$C_{1i} := \frac{v_{ri}\mu_{ki}^2}{\lambda(v_r)\sigma_{0i}}, \quad C_{2i} := \frac{|\omega r|}{C_{0i}(v_r)}, \quad i = x, y \tag{2.42}$$

We can now compute the steady-state expressions for the forces and the alignment torque using (2.38) and (2.39). In particular, we have

$$F_i^{\text{ss}} = -\int_0^L \left(\sigma_{0i} z_i^{\text{ss}}(\zeta) + \sigma_{2i} v_{ri}\right) f_n(\zeta) \mathrm{d}\zeta\ , \quad i = x, y \tag{2.43}$$

$$M_z^{\text{ss}} = \int_0^L \left(\sigma_{0y} z_y^{\text{ss}}(\zeta) + \sigma_{2y} v_{ry}\right) f_n(\zeta) \left(\frac{L}{2} - \zeta\right) \mathrm{d}\zeta \tag{2.44}$$

Before we proceed with our analysis, a few words about the normal load distribution f_n are in order. One may be tempted to assume uniform load distribution i.e. $f_n = \text{const}$. This is not a realistic assumption, because the uniform load distribution does not satisfy the natural boundary conditions of zero normal load at the edges of the patch. In addition, the uniform load distribution would lead to an aligning torque that does not change sign at higher lateral slip angles, as observed in practice. An empirical plot of the normal load distribution along the contact patch, taken from [4] is shown in Fig. 2.11(a). Several possible approximations of the normal load distribution are shown in Fig. 2.11(b). At this point, we adopt a trapezoidal distribution, as proposed by Deur et al in [32]. In this case, the function f_n is given by

$$f_n(\zeta) = \begin{cases} \alpha_1 \zeta & \text{for } \; 0 \leq \zeta \leq a, \\ f_{\max} & \text{for } \; a \leq \zeta \leq b, \\ \alpha_2 \zeta + \beta_2 & \text{for } \; b \leq \zeta \leq L \end{cases} \tag{2.45}$$

with $f_{\max}$ being the maximum value of the normal load distribution. Here a and b are parameters which determine the position of the linear and constant portions of the distribution, and

$$\alpha_1 = \frac{f_{\max}}{a}, \quad \alpha_2 = -\frac{f_{\max}}{L-b}, \quad \beta_2 = \frac{L f_{\max}}{L-b} \; . \tag{2.46}$$

The total normal force is therefore,

$$F_n = \int_0^L f_n(\zeta) \mathrm{d}\zeta = \frac{L+b-a}{2} f_{\max} \; . \tag{2.47}$$

Note that the trapezoidal normal load distribution satisfies the associated boundary conditions and allows the effects of the pneumatic trail to appear (sign change in the aligning torque characteristic). It is quite simple to integrate leading to a relatively simple average lumped model that we discuss later on. A more realistic expression for the normal load can of course be used in equations (2.38) and (2.39), thus resulting in a higher fidelity model. However, such higher order normal distributions would necessarily increase the complexity of the model.

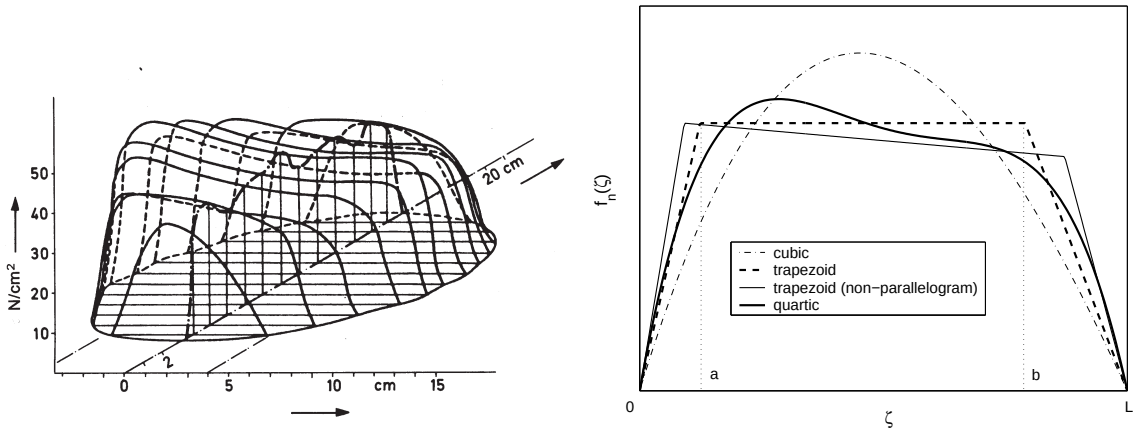

(a) (b)

Figure 2.11: *(a) Empirical plots of normal load distribution taken from [4]; (b) Possible choices of* $f_n(\zeta)$

Using the solution $z_i^{\text{ss}}(\zeta)$ of the internal friction state $z_i(t,\zeta)$ in steady-state from (2.41), along with the expressions (2.43) and (2.44) for the steady-state forces and moment and equation (2.45) for the normal load distribution, the following expressions for the distributed steady-state forces and moment of the distributed model can be calculated.

The steady-state forces are:

$$\begin{aligned}
F_i^{\text{ss}} &= -\sigma_{0i}C_{1i}\alpha_1\left(\frac{a^2}{2} + C_{2i}ae^{-\frac{a}{C_{2i}}} - C_{2i}^2\left(1 - e^{-\frac{a}{C_{2i}}}\right)\right) \\
&- \sigma_{0i}C_{1i}f_{\max}\left((b-a) + C_{2i}\left(e^{-\frac{b}{C_{2i}}} - e^{-\frac{a}{C_{2i}}}\right)\right) \\
&- \frac{1}{2}\sigma_{0i}C_{1i}\alpha_2\left(L^2 - b^2\right) - \sigma_{0i}C_{1i}\beta_2\left(L - b\right) \\
&- \sigma_{0i}C_{1i}\alpha_2C_{2i}\left(Le^{-\frac{L}{C_{2i}}} - be^{-\frac{b}{C_{2i}}}\right) \\
&- \sigma_{0i}C_{1i}C_{2i}\left(\beta_2 + \alpha_2C_{2i}\right)\left(e^{-\frac{L}{C_{2i}}} - e^{-\frac{b}{C_{2i}}}\right) \\
&- \sigma_{2i}v_{ri}\left(\frac{1}{2}\alpha_1a^2 + f_{\max}\left(b-a\right) + \frac{1}{2}\alpha_2\left(L^2 - b^2\right) + \beta_2\left(L - b\right)\right), \qquad i = x, y
\end{aligned}$$

The steady-state aligning torque is:

$$
\begin{aligned}
M_z^{\text{ss}} &= \sigma_{0y}C_{1y}\alpha_1 a^2\left(\frac{L}{4}-\frac{a}{3}\right)+\frac{1}{2}\sigma_{0y}C_{1y}\alpha_1 LC_{2y}\left(ae^{-\frac{a}{C_{2y}}}+C_{2y}e^{-\frac{a}{C_{2y}}}-C_{2y}\right)\\
&+ \sigma_{0y}C_{1y}\alpha_1 C_{2y}\left(-a^2e^{-\frac{a}{C_{2y}}}-2C_{2y}ae^{-\frac{a}{C_{2y}}}-2C_{2y}^2\left(e^{-\frac{a}{C_{2y}}}-1\right)\right)\\
&+ \sigma_{0y}C_{1y}f_{\max}\left(\frac{L}{2}(b-a)-\frac{1}{2}\left(b^2-a^2\right)+\frac{L}{2}C_{2y}\left(e^{-\frac{b}{C_{2y}}}-e^{-\frac{a}{C_{2y}}}\right)\right)\\
&+ \sigma_{0y}C_{1y}f_{\max}C_{2y}\left(-be^{-\frac{b}{C_{2y}}}+ae^{-\frac{a}{C_{2y}}}-C_{2y}\left(e^{-\frac{b}{C_{2y}}}-e^{-\frac{a}{C_{2y}}}\right)\right)\\
&+ \sigma_{0y}C_{1y}\alpha_2\left(\frac{L}{4}\left(L^2-b^2\right)-\frac{1}{3}\left(L^3-b^3\right)\right)\\
&+ \sigma_{0y}C_{1y}\beta_2\left(\frac{L}{2}(L-b)-\frac{1}{2}\left(L^2-b^2\right)\right)\\
&+ \frac{1}{2}\sigma_{0y}C_{1y}\alpha_2 LC_{2y}\left(Le^{-\frac{L}{C_{2y}}}-be^{-\frac{b}{C_{2y}}}+C_{2y}\left(e^{-\frac{L}{C_{2y}}}-e^{-\frac{b}{C_{2y}}}\right)\right)\\
&+ \sigma_{0y}C_{1y}\beta_2 C_{2y}\left(-Le^{-\frac{L}{C_{2y}}}+be^{-\frac{b}{C_{2y}}}-C_{2y}\left(e^{-\frac{L}{C_{2y}}}-e^{-\frac{b}{C_{2y}}}\right)\right)\\
&+ \frac{1}{2}\sigma_{0y}C_{1y}\beta_2 LC_{2y}\left(e^{-\frac{L}{C_{2y}}}-e^{-\frac{b}{C_{2y}}}\right)+\sigma_{0y}C_{1y}\alpha_2 C_{2y}\left(-L^2e^{-\frac{L}{C_{2y}}}+b^2e^{-\frac{b}{C_{2y}}}\right)\\
&+ 2\sigma_{0y}C_{1y}\alpha_2 C_{2y}^2\left(-Le^{-\frac{L}{C_{2y}}}+be^{-\frac{b}{C_{2y}}}-C_{2y}\left(e^{-\frac{L}{C_{2y}}}-e^{-\frac{b}{C_{2y}}}\right)\right)\\
&+ \sigma_{2y}v_{ry}\alpha_1 a^2\left(\frac{L}{4}-\frac{a}{3}\right)+\frac{1}{2}\sigma_{2y}v_{ry}f_{\max}\left(Lb-La-b^2+a^2\right)\\
&+ \sigma_{2y}v_{ry}\alpha_2\left(\frac{L}{4}\left(L^2-b^2\right)-\frac{1}{3}\left(L^3-b^3\right)\right)\\
&+ \sigma_{2y}v_{ry}\beta_2\left(\frac{L}{2}(L-b)-\frac{1}{2}\left(L^2-b^2\right)\right)
\end{aligned}
$$

Using the definitions of the longitudinal and lateral slip we construct the steady-state s_x–F_x^{ss}, F_y^{ss} and α–M_z^{ss} plots shown in Fig. 2.12. Steady-state plots of longitudinal and lateral forces with longitudinal slip rate, and for different constant values of lateral slip α, plots of longitudinal and lateral forces with lateral slip and for different constant values of longitudinal slip, as well as the friction ellipse plots are shown in Fig. 2.13 and Fig. 2.14. These figures are in qualitative agreement with similar curves found in the literature [1, 21].

2.3.2 Parameter Identification

In this section, we propose a method to identify the unknown parameters in (2.37) by comparing the steady-state characteristics of the model to steady-state data. Such

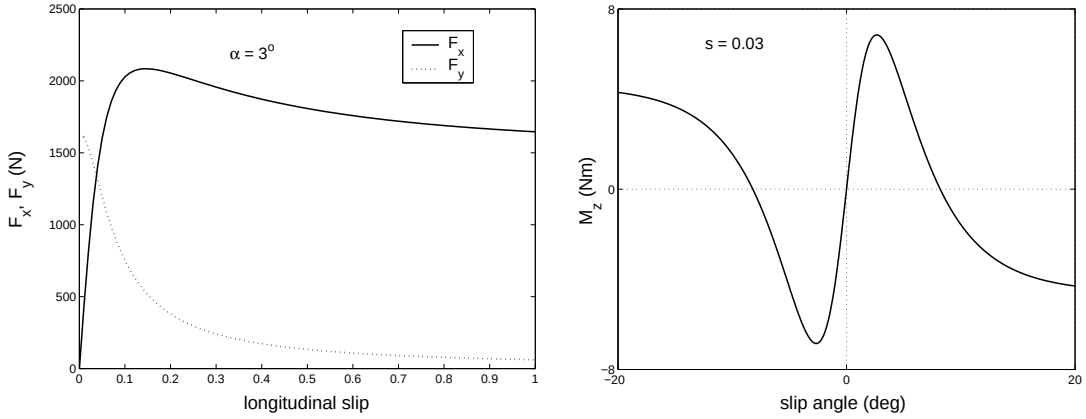

Figure 2.12: *Steady-state forces* $F_x^{\text{ss}}, F_y^{\text{ss}}$ *and aligning moment* M_z^{ss} *(*$F_n = 2000\text{Nt}$*).*

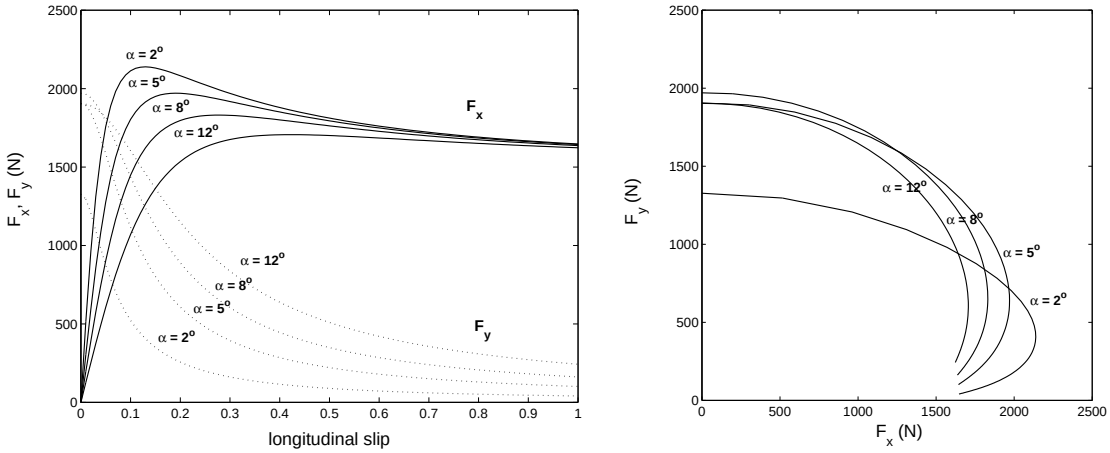

Figure 2.13: *Steady-state forces for several constant values of the slip angle (*$F_n = 2000\text{Nt}$*).*

steady-state data are easily obtainable by experiments and can be readily found in the literature [1]. In particular, we compare the forces and aligning moment predicted by the steady-state expressions (2.41)-(2.44) to the forces and moment generate by the MF using the MF parameters shown in Table 2.1. These parameters have been identified in [1] to fit experimental data.

The identification of the parameters for the LuGre tire model was done by fitting the plots generated by the steady-state expressions (2.43) and (2.44) to the MF plots with the above parameters. The curve fitting was done using the `lsqnonlin` command in MATLAB which solves an associated nonlinear least squares problem. The data used in generating the plots for the MF corresponded to cases of pure

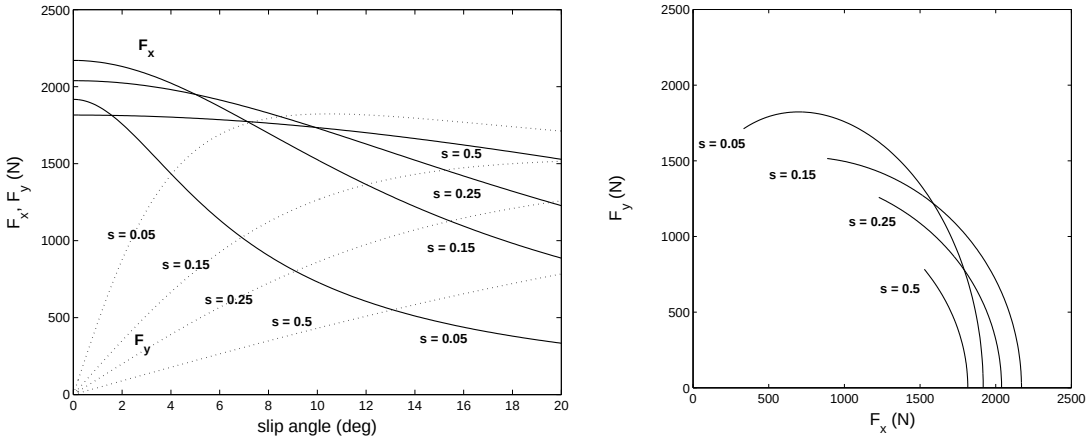

Figure 2.14: *Steady-State forces for several constant values of the longitudinal slip ($F_n = 2000$Nt).*

Table 2.1: *Parameters for the Magic Formula; taken from [1].*

Parameters	B	C	D	E
F_x	0.178	1.55	2193	0.432
F_y	0.244	1.5	1936	-0.132
M_z	0.247	2.56	-15.53	-3.92

braking and pure cornering, i.e. there were no lateral forces and aligning moment during braking and no longitudinal forces during cornering. Thus, the parameters $\sigma_{0x}, \mu_{kx}, \mu_{sx}, \sigma_{2x}$ were identified by fitting the longitudinal friction forces plots, the parameters $\sigma_{0y}, \mu_{ky}, \mu_{sy}, \sigma_{2y}$ were identified by fitting the lateral friction forces and aligning moment plots simultaneously while the parameters γ, L, a, b and v_s were identified by trial and error in order to achieve best overall fitting of all longitudinal/lateral forces and aligning moment plots.

The identified parameters are given in Table 2.2. The results are shown in Fig. 2.15. The F_x plot shown at the top of Fig. 2.15 is for pure braking i.e., longitudinal motion with $\alpha = 0$ and vehicle speed 60 km/h. The F_y and M_z plots are for pure cornering i.e., $s = 0$, $\alpha = 5^0$ and vehicle speed 70 km/h. In all cases the normal load was $F_n = 2000$ N. Even for the relatively simple trapezoidal load distribution the agreement between the curves in Fig. 2.15 is very good, especially for the forces. Some discrepancy exists in the plot of the aligning moment. This can be explained as

follows: the MF model for pure cornering provides two independent equations for the lateral forces and aligning moment and has thus enough freedom to fit both sets of experimental data. This is somewhat artificial, since it is clear from the physics of the problem that the lateral forces and the aligning moment are related. The LuGre dynamic model naturally captures this coupling. The reason for the slight discrepancy between the aligning moments at the bottom of Fig. 2.15 is due to the simple normal load distribution used in this example. A more realistic normal force distribution can be used if a better fitting for the aligning moment is desired.

The identified parameters a/L and b/L from table 2.2 result in a value for the rolling resistance coefficient (distance of the total normal load acting point from the midpoint of the contact patch, normalized by the patch length) of 0.04, which is realistic in accordance to the discussion on rolling resistance moment in [2].

Table 2.2: *Identified Parameters.*

Parameter	**Value**	**Parameter**	**Value**
σ_{0x} (1/m)	555	σ_{0y} (1/m)	470
μ_{kx}	0.75	μ_{ky}	0.75
μ_{sx}	1.35	μ_{sy}	1.40
$\sigma_{2x,y}$ (sec/m)	0	v_s (m/sec)	3.96
L (m)	0.15	γ	1
a/L	0.02	b/L	0.77

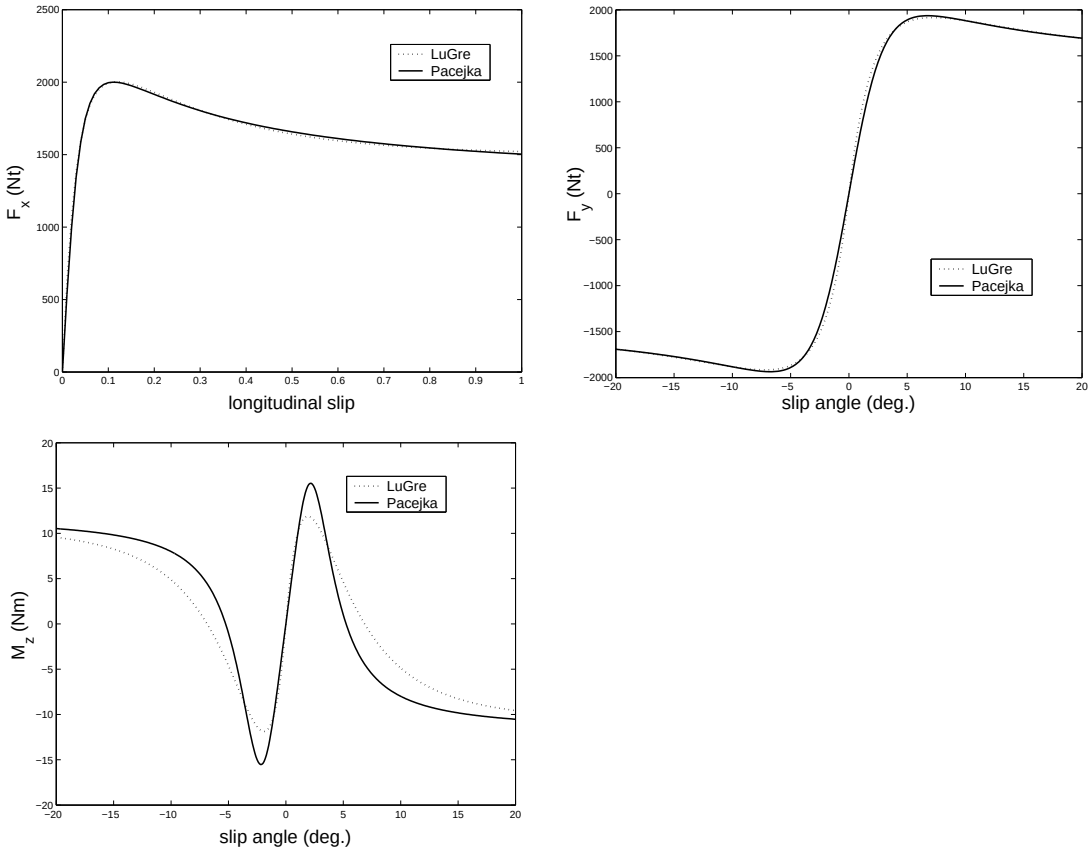

Figure 2.15: *Comparison between LuGre and Pacejka (Magic Formula) models. The values of the parameters for the Magic Formula were taken from [1] and correspond to experimental data.*

Chapter 3

The LuGre Tire Friction Model: Dynamic Behavior

In the previous chapter we derived a physics based dynamic tire friction model with static characteristics that nicely match widely used empirical models. The dynamic model of the previous section is a distributed one of infinite dimension. In this chapter we develop finite order expressions of the dynamics of the distributed LuGre tire model. In particular, approximate low order expressions, which are useful for control/estimation applications, are developed by definition of a set of mean states. The Method of Moments is used to derive an exact finite order expression which is used to validate the low order approximations. Next, we investigate the effect of the wheel rim rotation on both the distributed and the low order models. Finally, we provide experimental validation of the transient behavior of the longitudinal tire friction model as well as an account of the transient properties of the combined motion model.

3.1 Approximate Finite Order Expressions

The distributed model (2.37) may not be easy to use for analysis and – most importantly – control design. In this section, we develop lumped models, described by a system of ordinary differential equation of low order, which captures the "average"

behavior of the internal friction states. It is used to approximate the longitudinal and lateral forces as well as the aligning torque as a function of these "average states," at least at steady-state. The approach used in this section mimics the one used in Refs. [37, 34] for the longitudinal case.

3.1.1 Approximate Average Lumped Model

Recall the expressions for the longitudinal and lateral forces at the contact patch. According to (2.38) we have

$$F_i(t) = -\int_0^L \left(\sigma_{0i} z_i(t,\zeta) + \sigma_{1i}\frac{\partial z_i(t,\zeta)}{\partial t} + \sigma_{2i} v_{ri}\right) f_n(\zeta)\mathrm{d}\zeta \ , \qquad i = x, y.$$

Define now, as in [34], the weighted mean internal friction states $\bar{z}_i$ along the x and y directions as follows

$$\bar{z}_i(t) := \frac{1}{F_n}\int_0^L z_i(t,\zeta) f_n(\zeta)\mathrm{d}\zeta, \qquad i = x, y. \tag{3.1}$$

We thus we have that

$$\frac{\mathrm{d}\bar{z}_i(t)}{\mathrm{d}t} = \frac{1}{F_n}\int_0^L \frac{\partial z_i(t,\zeta)}{\partial t} f_n(\zeta)\mathrm{d}\zeta, \qquad i = x, y. \tag{3.2}$$

The total friction force can then be written in terms of the mean states $\bar{z}_i$ as follows,

$$F_i(t) = -F_n\left(\sigma_{0i}\bar{z}_i(t) + \sigma_{1i}\dot{\bar{z}}_i(t) + \sigma_{2i} v_{ri}\right). \tag{3.3}$$

To complete the model we need to determine the dynamics of the mean states. To this end, from (3.2) and (2.37a) we have that

$$\begin{aligned}
\dot{\bar{z}}_i(t) &= \frac{1}{F_n}\int_0^L \left(v_{ri} - C_{0i}(v_r) z_i(t,\zeta) - \frac{\partial z_i(t,\zeta)}{\partial \zeta}|\omega r|\right) f_n(\zeta)\mathrm{d}\zeta \\
&= v_{ri} - C_{0i}(v_r)\bar{z}_i(t) - \frac{|\omega r|}{F_n}\left[z_i(t,\zeta) f_n(\zeta)\right]_0^L + \frac{|\omega r|}{F_n}\int_0^L z_i(t,\zeta)\frac{\partial f_n(\zeta)}{\partial \zeta}\mathrm{d}\zeta \\
&= v_{ri} - C_{0i}(v_r)\bar{z}_i(t) - \kappa_i(t)|\omega r|\bar{z}_i(t) \ , \qquad i = x, y
\end{aligned} \tag{3.4}$$

where,

$$\kappa_i(t) := -\frac{\int_0^L z_i(t,\zeta) f_n'(\zeta)\mathrm{d}\zeta}{\int_0^L z_i(t,\zeta) f_n(\zeta)\mathrm{d}\zeta} \ , \qquad i = x, y \tag{3.5}$$

and where $(|\omega r|/F_n)\big[z_i(t,\zeta)f_n(\zeta)\big]_0^L = 0$ considering a normal load distribution that satisfies the boundary conditions at the edges of the contact patch (Fig. 2.11). Thus, the average lumped model for the friction forces is summarized by the following equations.

$$\dot{\bar{z}}_i(t) = v_{ri} - C_{0i}(v_r)\bar{z}_i(t) - \kappa_i(t)|\omega r|\bar{z}_i(t) \tag{3.6}$$

$$\bar{F}_i(t) = -F_n(\sigma_{0i}\bar{z}_i(t) + \sigma_{1i}\dot{\bar{z}}_i(t) + \sigma_{2i}v_{ri}), \quad i = x, y. \tag{3.7}$$

Using the definition for $\kappa_i(t)$ from (3.5) the friction forces of the lumped model $\bar{F}_i$ from (3.7) are equal to the forces F_i calculated from the distributed model (2.38). However, the calculation of $\kappa_i(t)$ from (3.5) requires the solution $z_i(t,\zeta)$ from the partial differential equation (2.37a) of the distributed model. In order to derive a lumped model which is independent from the distributed model we approximate $\kappa_i(t)$ in such a way that the *steady-state* solution of the lumped model $\bar{F}_i^{\text{ss}}$ is the same with the *steady-state* solution of the distributed model F_i^{ss}, as it was done in [38, 34, 32].

For constant ω and v, the steady-state of the lumped model is found by setting $\dot{\bar{z}}_i(t) = 0$ in (3.6). Hence,

$$\bar{z}_i^{\text{ss}} = \frac{v_{ri}}{C_{0i}(v_r) + \kappa_i^{\text{ss}}|\omega r|}, \quad i = x, y \tag{3.8}$$

where κ_i^{ss} is defined by

$$\kappa_i^{\text{ss}} = -\frac{\int_0^L z_i^{\text{ss}}(\zeta)f_n'(\zeta)\mathrm{d}\zeta}{\int_0^L z_i^{\text{ss}}(\zeta)f_n(\zeta)\mathrm{d}\zeta}, \quad i = x, y \tag{3.9}$$

and where z_i^{ss} from (2.41). Calculation of κ_i^{ss} is not easy using directly the definition (3.9). Instead, we calculate κ_i^{ss} so that the distributed and the lumped models produce the same steady-state forces. Enforcing $F_i^{\text{ss}} = \bar{F}_i^{\text{ss}}$ $(i = x, y)$, yields

$$\bar{z}_i^{\text{ss}} = \frac{1}{F_n}\int_0^L z_i^{\text{ss}}(\zeta)f_n(\zeta)\mathrm{d}\zeta, \quad i = x, y \tag{3.10}$$

The explicit expression for $\bar{z}_i^{\text{ss}}$ for a trapezoidal normal load distribution (2.45) is

given below.

$$\begin{aligned}
\bar{z}_i^{\text{ss}} &= \frac{1}{F_n} C_{1i}\alpha_1 \left(\frac{a^2}{2} + C_{2i} a e^{-\frac{a}{C_{2i}}} - C_{2i}^2 \left(1 - e^{-\frac{a}{C_{2i}}} \right) \right) \\
&+ \frac{1}{F_n} C_{1i} f_{\max} \left((b-a) + C_{2i} \left(e^{-\frac{b}{C_{2i}}} - e^{-\frac{a}{C_{2i}}} \right) \right) \\
&+ \frac{1}{2}\frac{1}{F_n} C_{1i}\alpha_2 \left(L^2 - b^2 \right) + \frac{1}{F_n} C_{1i}\beta_2 \left(L - b \right) \\
&+ \frac{1}{F_n} C_{1i}\alpha_2 C_{2i} \left(L e^{-\frac{L}{C_{2i}}} - b e^{-\frac{b}{C_{2i}}} \right) \\
&+ \frac{1}{F_n} C_{1i} C_{2i} \left(\beta_2 + \alpha_2 C_{2i} \right) \left(e^{-\frac{L}{C_{2i}}} - e^{-\frac{b}{C_{2i}}} \right), \qquad i = x, y
\end{aligned}$$

The term $\kappa(t)$ in (3.6) is approximated by solving (3.8) for κ_i^{ss}, yielding

$$\kappa_i^{\text{ss}} = \frac{1}{|\omega r|} \left(\frac{v_{ri}}{\bar{z}_i^{\text{ss}}} - C_{0i}(v_r) \right), \qquad i = x, y. \tag{3.11}$$

To calculate a lumped model for the aligning torque, recall first that the expression for the aligning torque along the contact patch is given from (2.39) and (2.37). Using the definition of the mean internal fiction state $\bar{z}_y$ from in (3.1), the expression for $M_z(t)$ can be written as follows

$$\begin{aligned}
M_z(t) = &\frac{L}{2} \left(\sigma_{0y} \bar{z}_y(t) + \sigma_{1y} \dot{\bar{z}}_y(t) + \sigma_{2y} v_{ry} \right) - \sigma_{0y} \int_0^L z_y(t,\zeta) f_n(\zeta) \zeta \mathrm{d}\zeta \\
&+ \sigma_{1y} \int_0^L \frac{\partial z_y(t,\zeta)}{\partial t} f_n(\zeta) \zeta \mathrm{d}\zeta + \sigma_{2y} v_{ry} \int_0^L f_n(\zeta) \zeta \mathrm{d}\zeta
\end{aligned} \tag{3.12}$$

Define now the weighted mean internal state $\hat{z}_y$ for the aligning torque as follows

$$\hat{z}_y(t) := \frac{1}{F_n L} \int_0^L z_y(t,\zeta) f_n(\zeta) \zeta \mathrm{d}\zeta. \tag{3.13}$$

Thus,

$$\frac{\mathrm{d}\hat{z}_y(t)}{\mathrm{d}t} = \frac{1}{F_n L} \int_0^L \frac{\partial z_y(t,\zeta)}{\partial t} f_n(\zeta) \zeta \mathrm{d}\zeta. \tag{3.14}$$

The total aligning torque can then be written in terms of the mean states $\bar{z}_y$ and $\hat{z}_y$, as follows

$$\frac{M_z(t)}{F_n L} = \sigma_{0y} \left(\tfrac{1}{2} \bar{z}_y(t) - \hat{z}_y(t) \right) + \sigma_{1y} \left(\tfrac{1}{2} \dot{\bar{z}}_y(t) - \dot{\hat{z}}_y(t) \right) + \sigma_{2y} \left(\tfrac{1}{2} v_{ry} - \frac{G}{F_n L} \right) \tag{3.15}$$

where,

$$G = \int_0^L f_n(\zeta) \zeta \mathrm{d}\zeta \tag{3.16}$$

For the case of a trapezoidal normal load distribution as in (2.45) we have

$$G = \frac{\alpha_1}{3}a^3 + \frac{f_{\max}}{2}\left(b^2 - a^2\right) + \frac{\alpha_2}{3}\left(L^3 - b^3\right) + \frac{\beta}{2}\left(L^2 - b^2\right). \tag{3.17}$$

Finally, we need to find the dynamics of the mean state $\hat{z}_y$. Using (3.14) we have that

$$\begin{aligned}
\dot{\hat{z}}_y(t) &= \frac{1}{F_n L}\int_0^L \frac{\partial z_y(t,\zeta)}{\partial t} f_n(\zeta)\zeta \mathrm{d}\zeta \\
&= \frac{1}{F_n L}\int_0^L \left(v_{ry} - C_{0y}(v_r) z_y(t,\zeta) - \frac{\partial z_y(t,\zeta)}{\partial \zeta}|\omega r|\right) f_n(\zeta)\zeta \mathrm{d}\zeta \\
&= \frac{G}{F_n L}v_{ry} - C_{0y}(v_r)\hat{z}_y(t) - \frac{|\omega r|}{F_n L}\int_0^L \frac{\partial z_y(t,\zeta)}{\partial \zeta} f_n(\zeta)\zeta \mathrm{d}\zeta \\
&= \frac{G}{F_n L}v_{ry} - C_{0y}(v_r)\hat{z}_y(t) - \frac{|\omega r|}{F_n L}\left[z_y(t,\zeta) f_n(\zeta)\zeta\right]_0^L \\
&+ \frac{|\omega r|}{F_n L}\int_0^L z_y(t,\zeta)\frac{\partial f_n}{\partial \zeta}\zeta \mathrm{d}\zeta + \frac{|\omega r|}{F_n L}\int_0^L z_y(t,\zeta) f_n(\zeta)\mathrm{d}\zeta \\
&= \frac{G}{F_n L}v_{ry} - C_{0y}(v_r)\hat{z}_y(t) - \nu(t)|\omega r|\hat{z}_y(t) + \frac{|\omega r|}{L}\bar{z}_y(t)
\end{aligned} \tag{3.18}$$

where,

$$\nu(t) := -\frac{\int_0^L z_y(t,\zeta) f_n'(\zeta)\zeta \mathrm{d}\zeta}{\int_0^L z_y(t,\zeta) f_n(\zeta)\zeta \mathrm{d}\zeta} \tag{3.19}$$

where, again $(|\omega r|/(F_n L))\left[z_i(t,\zeta) f_n(\zeta)\zeta\right]_0^L = 0$ because of the assumed normal load distribution in (2.45). Thus, the average lumped model for the aligning torque is summarized by

$$\dot{\hat{z}}_y(t) = \frac{G}{F_n L}v_{ry} - C_{0y}(v_r)\hat{z}_y(t) - \nu(t)|\omega r|\hat{z}_y(t) + \frac{|\omega r|}{L}\bar{z}_y(t) \tag{3.20}$$

$$\frac{\hat{M}_z(t)}{F_n L} = \sigma_{0y}\left(\tfrac{1}{2}\bar{z}_y(t) - \hat{z}_y(t)\right) + \sigma_{1y}\left(\tfrac{1}{2}\dot{\bar{z}}_y(t) - \dot{\hat{z}}_y(t)\right) + \sigma_{2y}\left(\tfrac{1}{2}v_{ry} - \frac{G}{F_n L}\right). \tag{3.21}$$

Notice, that by definition, $\hat{M}_z(t) = M_z(t)$. However, the calculation of $\hat{z}_y(t)$ from (3.20) requires knowledge of $\nu(t)$ from (3.19) which is not easy to obtain. Following the same reasoning as for the case of the lumped model forces, we approximate $\nu(t)$ in (3.20) by an appropriate constant value, ν^{ss} by assuming that, at *steady-state*, the aligning torque predicted by the lumped model $\hat{M}_z^{\mathrm{ss}}$ will be the same with the one predicted by the distributed model M_z^{ss} given in (2.44).

The steady-state of the lumped model is found by setting $\dot{\hat{z}}_y = 0$, $\bar{z}_y = \bar{z}_y^{\text{ss}}$ and $\dot{\bar{z}}_y = 0$ in (3.21). This leads to the following expression for the steady-state $\hat{z}_y^{\text{ss}}$

$$\hat{z}_y^{\text{ss}} = \frac{1}{2\sigma_{0y}} \left(\sigma_{0y} \bar{z}_y^{\text{ss}} + \sigma_2 v_{ry} \right) - \frac{M_z^{\text{ss}}}{F_n L \sigma_{0y}} - \frac{G\sigma_2 v_{ry}}{\sigma_{0y}} \tag{3.22}$$

where $\bar{z}_y^{\text{ss}}$ from (3.10) and M_z^{ss} from (2.44). In order to compute ν^{ss} we let $\dot{\hat{z}}_y = 0$, $\bar{z}_y(t) = \bar{z}_y^{\text{ss}}$ and $\hat{z}_y(t) = \hat{z}_y^{\text{ss}}$ in (3.20) to finally obtain

$$\nu^{\text{ss}} = \frac{1}{|\omega r|} \left(\frac{1}{\hat{z}_y^{\text{ss}}} \left(\frac{G v_{ry}}{F_n L} + \frac{|\omega r| \bar{z}_y^{\text{ss}}}{L} \right) - C_{0y} \right), \tag{3.23}$$

where $\bar{z}_y^{\text{ss}}$ from (3.10) and $\hat{z}_y^{\text{ss}}$ from (3.22).

In summary, we have presented a low order approximation of the distributed model (2.37) that we refer to as the average lumped model. The lumped model is described by equations (3.6), (3.7), (3.20) and (3.21), where the terms $\kappa_i(t)$ and $\nu(t)$ are approximated by κ_i^{ss} and ν^{ss} from equations (3.11) and (3.23) respectively. The average lumped model reproduces exactly the steady-state characteristics of the distributed model (2.37) as in Section 2.3.1 but provides no guarantees on the accuracy of the transient behavior.

3.1.2 Single-State Dynamic Friction Model for 2D Motion

In case we want to simulate the motion of a wheeled vehicle in relatively high velocities, it is common to neglect the self-aligning friction moments. However, these moments are important and may not be neglected in cases where we want to perform steering control. In this section, we propose a simplification to the average lumped model presented in the previous section that uses only a single state (hence a single ordinary differential equation) in order to compute both the longitudinal and lateral components of the friction force. Simulations at the end of this section demonstrate that this simplified model is rich enough to capture the friction force characteristics at steady-state.

Deur et al in [32] proposed an extension for the longitudinal LuGre tire model of [37] to the combined longitudinal and lateral motion of the tire, assuming isotropy of the steady-state friction characteristics, i.e. $\mu_{kx} = \mu_{ky} = \mu_k$ and $\mu_{sx} = \mu_{sy} = \mu_s$.

Under these assumptions the model (2.37) proposed in this work reduces to the one of [32]. In particular, equations (2.37) become

$$\frac{\mathrm{d}z_i(t,\zeta)}{\mathrm{d}t} = \frac{\partial z_i(t,\zeta)}{\partial t} + \frac{\partial z_i(t,\zeta)}{\partial \zeta}|\omega r| = v_{ri} - \frac{\sigma_{0i}\|v_r\|}{g(v_r)} z_i \tag{3.24a}$$

$$\mu_i(t,\zeta) = -\sigma_{0i} z_i(t,\zeta) - \sigma_{1i}\frac{\partial z_i(t,\zeta)}{\partial t} - \sigma_{2i} v_{ri} \tag{3.24b}$$

with

$$g(v_r) = \mu_k + (\mu_s - \mu_k) e^{-(\|v_r\|/v_s)^\theta}. \tag{3.25}$$

By assuming isotropy of both static and dynamic friction characteristics, i.e. $\sigma_{0x} = \sigma_{0y} = \sigma_0$, $\sigma_{1x} = \sigma_{1y} = \sigma_1$, $\sigma_{2x} = \sigma_{2y} = \sigma_2$ as well as $\mu_{kx} = \mu_{ky} = \mu_k$ and $\mu_{sx} = \mu_{sy} = \mu_s$ we observe that the coefficients of equations (2.37) or (3.24) are the same for both $i = x, y$. It is only the inputs v_{ri} that differ and generate the internal friction states z_x and z_y. Using equations (3.24) with the total relative velocity $v_r = \sqrt{v_{rx}^2 + v_{ry}^2}$ we may compute the total friction force using a single friction state z. The equations of the friction model are then written

$$\frac{\mathrm{d}z(t,\zeta)}{\mathrm{d}t} = \frac{\partial z(t,\zeta)}{\partial t} + \frac{\partial z(t,\zeta)}{\partial \zeta}|\omega r| = v_r - \frac{\sigma_0|v_r|}{g(v_r)} z \tag{3.26a}$$

$$\mu(t,\zeta) = -\sigma_0 z(t,\zeta) - \sigma_1\frac{\partial z(t,\zeta)}{\partial t} - \sigma_2 v_r \tag{3.26b}$$

which is exactly the longitudinal model of [38, 34]. At this point we propose the calculation of the components of the friction coefficient along the longitudinal and lateral directions, μ_x and μ_y, in accordance to the static model [1], i.e.

$$\mu_i(t,\zeta) = \frac{v_{ri}}{v_r}\mu(t,\zeta)\ , \qquad i = x, y \tag{3.27}$$

An average lumped model for (3.26) has been computed in [38, 34] as follows

$$\dot{\bar{z}}(t) = v_r - \frac{\sigma_0|v_r|}{g(v_r)} - \frac{\kappa}{L}|\omega r|\bar{z} \tag{3.28a}$$

$$\mu(t) = \sigma_0\bar{z} + \sigma_1\dot{\bar{z}} + \sigma_2 v_r \tag{3.28b}$$

where, for simplicity κ can be taken as constant in the interval $\kappa \in [1.1, 1.4]$. It is shown in [32] that such a choice for κ results in realistic steady-state characteristics

under the assumption of uniform normal load distribution. As mentioned, at this point we neglect the aligning torque and the assumption of uniform normal load distribution is acceptable.

At steady-state (3.28) reduces to

$$\bar{z}^{\text{ss}} = \frac{v_r}{\frac{\sigma_0|v_r|}{g(v_r)} + \frac{\kappa|\omega r|}{L}} \tag{3.29a}$$

$$\mu^{\text{ss}} = \sigma_0 \bar{z}^{\text{ss}} + \sigma_2 v_r \tag{3.29b}$$

Using the steady-state expression of the friction coefficient above and separating the friction components as in (3.27) we demonstrate next that the general static characteristics of the friction are captured by this simplified model. We construct plots of the longitudinal and lateral components of the steady-state friction force with respect to the longitudinal slip rate, and for different constant values of the lateral slip α; plots of the longitudinal and lateral forces with respect to the lateral slip, and for different constant values of the longitudinal slip s_x; as well as the friction ellipses of the longitudinal vs. lateral friction forces.

The results are shown in Fig. 3.1 and Fig. 3.2. These are very close to the ones shown in Fig. 2.13 and Fig. 2.14 generated by the distributed LuGre tire friction model and capture the steady-state characteristics of Pacejka's 'Magic Formula' from experiments [1].

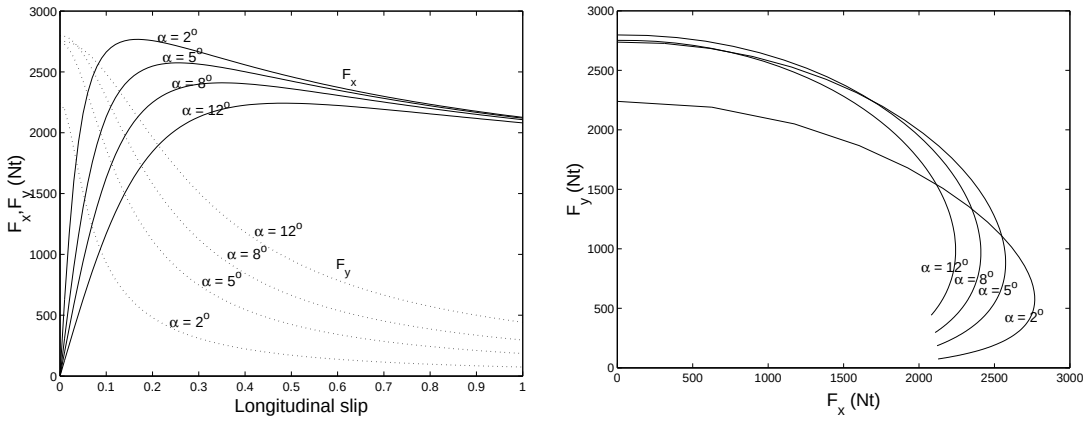

Figure 3.1: *Longitudinal and lateral friction forces for several values of the slip angle; single-state LuGre model.*

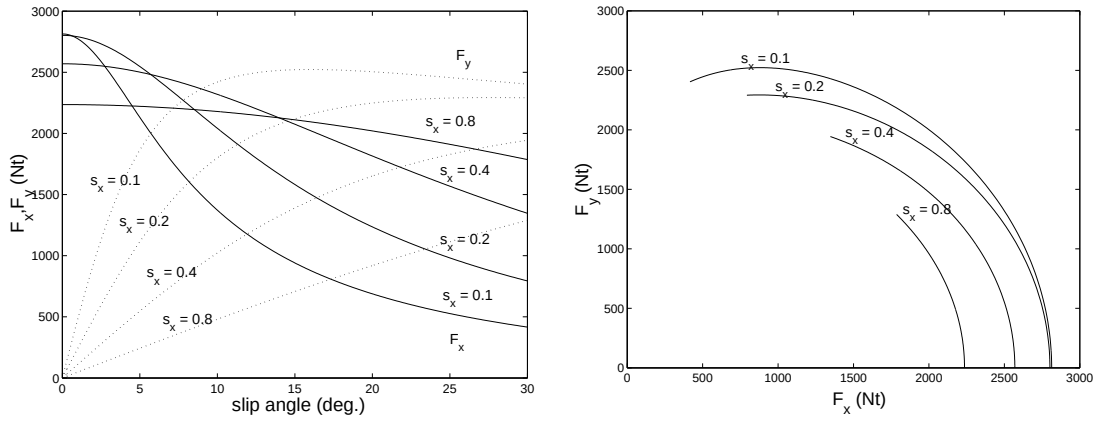

Figure 3.2: *Longitudinal and lateral friction forces for several values of the longitudinal slip; single-state LuGre model.*

3.2 Exact Finite Order Expressions

In the previous section we derived low order approximations of the distributed model (2.37). The approximate model of Section 3.1.1 is described by a set of three ordinary differential equations and produce exactly the same steady-state characteristics as the distributed model. However there are no guarantees that the transient behavior of the approximate model captures the (transient) characteristics of the distributed one. In this section we use the Method of Moments in order to describe the (exact) dynamics of the distributed model by a finite (not necessarily low) number of ordinary differential equations. The exact lumped model will be used to evaluate the dynamic characteristics of the approximate model of Section 3.1.1 as well as other approximations in the literature.

3.2.1 Exact Lumped Model Using the Method of Moments

Define the pth moment of $z_i(t, \zeta)$ for $\zeta \in [a,\, b]$ as follows

$$M_{p,i}^{ab}(t) := \int_a^b z_i(t, \zeta)\zeta^p \mathrm{d}\zeta, \quad i = x, y \tag{3.30}$$

Taking the time derivative of $M_{p,i}^{ab}$ yields,

$$\begin{aligned}\dot{M}_{p,i}^{ab}(t) &= \int_a^b \frac{\partial z_i(t,\zeta)}{\partial t}\zeta^p \mathrm{d}\zeta \\ &= \int_a^b \left(v_{ri} - C_{0i}(v_r) z_i(t,\zeta) - |\omega r| \frac{\partial z_i(t,\zeta)}{\partial \zeta} \right) \zeta^p \mathrm{d}\zeta \\ &= \frac{b^{p+1} - a^{p+1}}{p+1} v_{ri} - C_{0i}(v_r) \int_a^b z_i(t,\zeta)\zeta^p \mathrm{d}\zeta - |\omega r| \int_a^b \frac{\partial z_i(t,\zeta)}{\partial \zeta}\zeta^p \mathrm{d}\zeta. \end{aligned} \tag{3.31}$$

Integrating by parts, (3.31) gives a recursive formula for the calculation of all moments $M_{p,i}^{ab}$ for $p \geq 1$

$$\dot{M}_{p,i}^{ab} = \frac{b^{p+1} - a^{p+1}}{p+1} v_{ri} - C_{0i}(v_r) M_{p,i}^{ab} - |\omega r| z_i(t,\zeta)\zeta^p \Big|_a^b + |\omega r| p M_{p-1,i}^{ab} \tag{3.32}$$

For $p = 0$ equation (3.31) yields

$$\dot{M}_{0,i}^{ab} = (b-a) v_{ri} - C_{0i}(v_r) M_{0,i}^{ab} - |\omega r| \Big(z_i(t,b) - z_i(t,a) \Big) \tag{3.33}$$

Given any sufficiently smooth normal load distribution $f_n(\zeta)$, we can approximate f_n with its Taylor series expansion as follows

$$f_n(\zeta) \simeq \sum_{k=0}^{m} c_k \zeta^k \tag{3.34}$$

for some constants $c_0, c_1, ..., c_m$. Note that the total normal load on the contact patch is given by

$$F_n = \int_0^L f_n(\zeta) \mathrm{d}\zeta. \tag{3.35}$$

Using the definition of the moments $M_{p,i}^{ab}$, and using (3.34) the friction forces $F_i(t),\ i = x, y$ in (2.38) can then be written as follows

$$\begin{aligned} F_i(t) &= -\int_0^L \left(\sigma_{0i} z_i + \sigma_{1i} \frac{\partial z_i}{\partial t} + \sigma_{2i} v_{ri} \right) f_n(\zeta) \mathrm{d}\zeta \\ &= -\sigma_{0i} \sum_{k=0}^{m} c_k M_{k,i}^{0L} - \sigma_{1i} \sum_{k=0}^{m} c_k \dot{M}_{k,i}^{0L} - \sigma_{2i} v_{ri} F_n \end{aligned} \tag{3.36}$$

Finally, the aligning torque $M_z(t)$ in (2.39) can be written in terms of the moments $M_{p,i}^{ab}$ as

$$\begin{aligned} M_z(t) &= -\int_0^L \left(\sigma_{0y} z_y + \sigma_{1y} \frac{\partial z_y}{\partial t} + \sigma_{2y} v_{ry} \right) f_n(\zeta) \left(\frac{L}{2} - \zeta \right) \mathrm{d}\zeta \\ &= -\frac{L}{2} F_y(t) + \sigma_{2y} v_{ry} \int_0^L f_n(\zeta)\zeta \mathrm{d}\zeta + \sigma_{0y} \sum_{k=0}^{m} c_k M_{k+1,y}^{0L} + \sigma_{1y} \sum_{k=0}^{m} c_k \dot{M}_{k+1,y}^{0L} \end{aligned} \tag{3.37}$$

3.2.2 Closure Relationship

Equations (3.32), (3.33) require the time history of the internal friction states $z_i(t, \zeta)$ for fixed positions on the contact patch, namely, $\zeta = a$ and $\zeta = b$. In this section we discuss the calculation of these terms.

Going back to the original partial differential equation (2.37a) let us consider the characteristics given by

$$t = t(s) \ , \qquad \zeta = \zeta(s)$$

with

$$\frac{\partial t}{\partial s} = 1 \ , \qquad \frac{\partial \zeta}{\partial s} = |\omega r|.$$

Let the characteristic $y(s) = \zeta(t(s))$ starting from $\zeta = 0$ at time $t - \tau$ for some (still unknown) τ and ending at $\zeta = \zeta_0$ at time t. Then

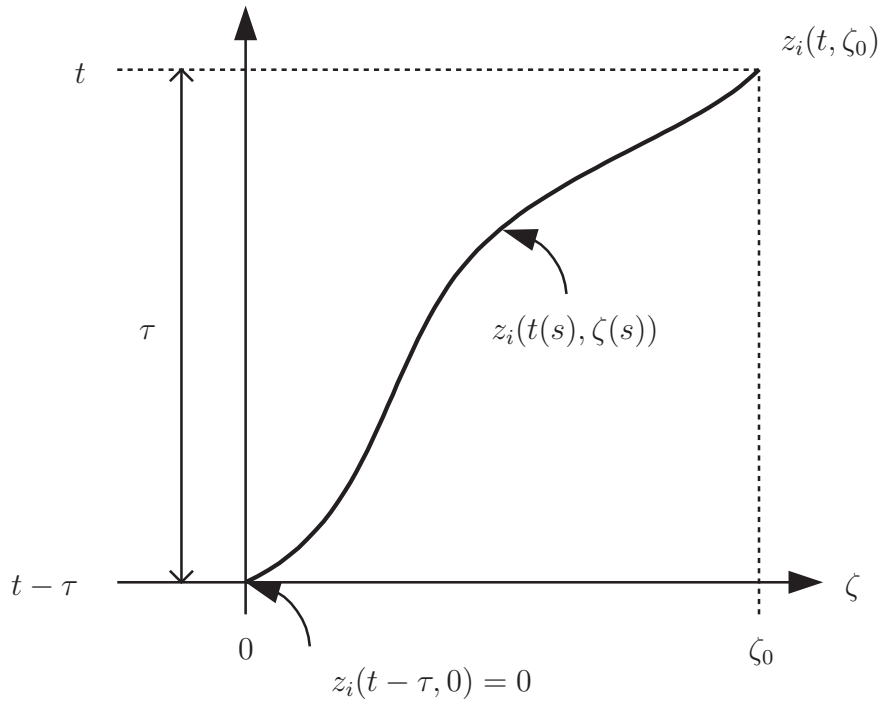

Figure 3.3: *Solution $z_i(t, \zeta)$ along the characteristic $y(s) = \zeta(t(s))$.*

$$y(t') = \int_{t-\tau}^{t'} |\omega r|(\sigma) \mathrm{d}\sigma \tag{3.38}$$

and $y(t) = \zeta_0$. Hence,

$$\zeta_0 = \int_{t-\tau}^{t} |\omega r|(\sigma) \mathrm{d}\sigma \tag{3.39}$$

Let us follow the solution along the characteristic (Fig. 3.3). To this end, define $\xi_i(t) := z_i(t, y(t))$. Thus,

$$\dot{\xi}_i(t) = \frac{\partial z_i}{\partial t} + \frac{\partial z_i}{\partial y}\frac{\partial y}{\partial t} = v_{ri} - C_{0i}(v_r)\xi_i(t) \tag{3.40}$$

with initial condition

$$\xi_i(t-\tau) = z_i(t-\tau, y(t-\tau)) = z_i(t-\tau, 0) = 0 \ .$$

Finally, $z_i(t, \zeta_0) = \xi_i(t)$ and τ is such that (3.39) holds. By setting $\zeta_0 = a$ and $\zeta_0 = b$ we now have an expression for the last term in (3.33).

3.2.3 The Effect of Normal Force Distribution

In this section we derive the exact aggregate LuGre tire friction model for several specific cases of normal force distribution $f_n(\zeta)$. Namely, we provide the moment calculations for several simple load distributions commonly used in the literature (e.g., uniform, trapezoidal) [75, 37, 38, 34, 32, 76], as well as for the more realistic load distribution with quartic dependence. A quartic polynomial produces normal load profiles for f_n which are very close to empirical ones (Fig. 2.11). At any rate, the methodology developed here may be used to incorporate any smooth or piecewise smooth $f_n(\zeta)$ load distribution along the patch.

Exact Lumped Model for Uniform Load Distribution

The uniform load distribution $f_n(\zeta) = c_0$ is derived from (3.34) with $m = 0$ while in equations (3.32) and (3.33) we substitute $a = 0$ and $b = L$. The dynamics of friction are described by five ordinary differential equations with states $M_{0,x}^{0L}$, $M_{0,y}^{0L}$ from equation (3.33), $M_{1,y}^{0L}$ from equation (3.32) with $p = 1$ and $z_x(t, L)$, $z_y(t, L)$ from equation (3.40). A methodology for choosing appropriate initial conditions to integrate these ode's is discussed in Section 3.2.4.

Exact Lumped Model for Trapezoidal Load Distribution

In [32] it was shown that the LuGre tire friction model with uniform load distribution reproduced the longitudinal and lateral forces matching very well other empirical models (at least at steady-state). However, this model failed to reproduce realistic aligning torque characteristics. In order to accurately capture the behavior of the aligning moment one needs to introduce the effects of pneumatic trail. This was achieved in [32] with the introduction of a trapezoidal normal load distribution (Fig. 2.11). Recall that we have introduced the trapezoidal normal load distribution (2.45) to derive the steady-state characteristics of the distributed model in Section 2.3.1 and the approximate average lumped model in Section 3.1.1.

The normal load distribution of equation (2.45) is only piecewise smooth and the approximation (3.34) cannot be used directly. In this case, it is necessary to consider different moments of $z_i(t,\zeta)$ for different parts of the contact patch. To this end let $M_{p,i}^{0a}(t)$ for $\zeta \in [0,\, a]$, $M_{p,i}^{ab}(t)$ for $\zeta \in (a,\, b)$ and $M_{p,i}^{bL}(t)$ for $\zeta \in [b,\, L]$. Thus, the dynamics of friction are described by a set of nineteen ordinary differential equations with states $z_i(t,a)$, $z_i(t,b)$ and $z_i(t,L)$, $M_{0,i}^{0a}$, $M_{0,i}^{ab}$ and $M_{0,i}^{bL}$ from equation (3.33), $M_{1,i}^{0a}$ and $M_{1,i}^{bL}$ from equation (3.32), with $i = x, y$ and finally $M_{2,y}^{0a}$, $M_{1,y}^{ab}$ and $M_{2,y}^{bL}$ again from equation (3.32). The calculation of $z_i(t,a)$, $z_i(t,b)$ and $z_i(t,L)$ is done in accordance to the discussion of Section 3.2.2 using equation (3.40). The choice of initial conditions is discussed in Section 3.2.4.

The forces are given by

$$\begin{aligned} F_i(t) = &-\sigma_{0i}\left(C_1 M_{1,i}^{0a} + f_{\max} M_{0,i}^{ab} + C_2 M_{1,i}^{bL} + C_3 M_{0,i}^{bL}\right) \\ &- \sigma_{1i}\left(C_1 \dot{M}_{1,i}^{0a} + f_{\max} \dot{M}_{0,i}^{ab} + C_2 \dot{M}_{1,i}^{bL} + C_3 \dot{M}_{0,i}^{bL}\right) \\ &- \sigma_{2i} v_{ri} F_n, \qquad i = x, y \end{aligned} \tag{3.41}$$

and the aligning torque by

$$\begin{aligned} M_z(t) = &-\frac{L}{2} F_y + \sigma_{2y} v_{ry} \int_0^L f_n(\zeta)\zeta \mathrm{d}\zeta \\ &+ \sigma_{0y}\left(C_1 M_{2,y}^{0a} + f_{\max} M_{1,y}^{ab} + C_2 M_{2,y}^{bL} + C_3 M_{1,y}^{bL}\right) \\ &+ \sigma_{1y}\left(C_1 \dot{M}_{2,y}^{0a} + f_{\max} \dot{M}_{1,y}^{ab} + C_2 \dot{M}_{2,y}^{bL} + C_3 \dot{M}_{1,y}^{bL}\right). \end{aligned} \tag{3.42}$$

Exact Lumped Model for a Quartic Load Distribution

Next, we introduce yet another approximation for the normal load distribution at the contact patch. The quartic normal load distribution (Fig. 2.11) is derived from (3.34) for $m = 4$:

$$f_n(\zeta) = c_4\zeta^4 + c_3\zeta^3 + c_2\zeta^2 + c_1\zeta + c_0 \tag{3.43}$$

Using this approximation, one is able to incorporate the effects of the pneumatic trail, resulting to realistic aligning torque predictions, as well as the natural boundary conditions of the normal load distribution, i.e. $f_n(\zeta = 0) = f_n(\zeta = L) = 0$. In addition, the proposed expression is smooth along the whole length of the contact patch and the pth moment of $z_i(t, \zeta)$ from $\zeta = 0$ to $\zeta = L$, $M_{p,i}^{0L}$, may be used. Thus, we avoid splitting the integral (3.31) as was done for the trapezoidal distribution. This also results in a smaller number of states (and differential equations).

It can be easily shown that in this case the dynamics of the tire friction are described by a set of thirteen ordinary differential equations with states $z_x(t, L)$ and $z_y(t, L)$ from equation (3.40), $M_{p,x}^{0L}$ and $M_{p,y}^{0L}$ with $p = 0, 1, ..., 4$ from equations (3.32) and (3.33) and $M_{5,y}^{0L}$ from equation (3.32). Once again, the choice of initial conditions is discussed in Section 3.2.4.

3.2.4 Initial Conditions

The initial condition $\xi_i(0) = z_i(0, \zeta_0)$ required in (3.40) can be calculated easily by integrating (3.40) from $t = -\tau$ to $t = 0$, where

$$\tau = \frac{\zeta_0}{|\omega r|}. \tag{3.44}$$

Under the assumption that during this period v, ω and α are constant, one obtains

$$\xi(t = 0) = \frac{v_{ri}}{C_{0i}(v_r)} \left(1 - e^{-C_{0i}(v_r)\tau}\right) \tag{3.45}$$

Substituting τ from (3.44) in (3.45) one obtains

$$\xi(t = 0) = \frac{v_{ri}}{C_{0i}(v_r)} \left(1 - e^{-\frac{C_{0i}(v_r)\zeta_0}{|\omega r|}}\right) = z_i(0, \zeta_0) \tag{3.46}$$

The same result can also be obtained by assuming that the tire is initially at steady-state with constant ω, v and α. To this end, we may enforce $\frac{\partial z_i(t,\zeta)}{\partial t} = 0$ in equation (2.37a) to obtain

$$\frac{\partial z_i(t,\zeta)}{\partial \zeta} = \frac{1}{|\omega r|}\Big(v_{ri} - C_{0i}(v_r) z_i(t,\zeta)\Big), \quad i = x, y \tag{3.47}$$

Taking into consideration the boundary condition $z_i(t,0) = 0$ (no deflection at the entry point of the contact patch) and the steady-state conditions of constant ω, v and α, we may integrate (3.47) to obtain the distribution $z_i^{ss}(\zeta)$ of z_i $(i = x, y)$, along the contact patch length at steady-state, as in [32] and [75].

$$z_i^{ss}(\zeta) = \frac{v_{ri}}{C_{0i}(v_r)} \left(1 - e^{-\frac{C_{0i}(v_r)\zeta}{|\omega r|}}\right) \ , \quad i = x, y \tag{3.48}$$

Note that for $\zeta = \zeta_0$ the previous expression coincides with (3.46).

Using the expression (3.48), equivalently (3.46), in (3.30) we can then calculate the initial conditions $M_{pi}^{ab}(0)$ for all the moment equations (3.32), (3.33).

3.2.5 Numerical Simulations

In this section we present numerical simulations of the previously developed lumped LuGre tire friction models [33, 32, 75] and the approximate average lumped model of Section 3.1.1 and compare the results with the exact lumped model developed in this paper. The tire friction models under consideration are subject to the same excitation, consisting of a linearly decreasing angular rate ω from 32 rad/sec to zero within 2 sec, and constant velocity v and slip angle α (Fig. 2.10). It should be pointed out that this is a controlled excitation that can be achieved only in a laboratory environment. For a wheeled vehicle, reduction in ω is normally accompanied by a reduction in the vehicle speed v as well.

Uniform Normal Load Distribution

In [32] two approximate lumped LuGre tire friction models were developed. These models are summarized in the equations below:

$$\dot{\tilde{z}}_i(t) = v_{ri} - \left(C_{0i}(v_r) + \frac{\kappa_i}{L}|\omega r| \right) \tilde{z}_i(t), \quad i = x, y \tag{3.49}$$

$$F_i(t) = -F_n \left(\sigma_{0i}\tilde{z}_i + \sigma_{1i}\dot{\tilde{z}}_i + \sigma_{2i}v_{ri} \right), \quad i = x, y \tag{3.50}$$

The two different lumped models correspond to different choices (approximations) of κ_i. This term is either approximated as constant, i.e., $\kappa_i \in [1.1 \;\; 1.4]$, or as a function of ω and v_r, i.e., $\kappa_i = \kappa_i^{ss}(v_r, \omega)$, such that the steady-state solution of the lumped model captures exactly the *steady-state* solution of the distributed model. In the latter case the expression for κ_i is given as follows [32]

$$\kappa_i^{ss} = \frac{1 - e^{-L/Z_i}}{1 - \frac{Z_i}{L}\left(1 - e^{-L/Z_i}\right)}, \quad Z_i = \frac{|\omega r|}{C_{0i}(v_r)} \tag{3.51}$$

It is shown in [32] that the approximate lumped model captures the steady-state characteristics of the distributed friction very well, while no guarantees for the accuracy of the model during transient were available. Evaluation of the effect of these transients is now possible via comparison with the exact lumped model presented in Section 3.2.3.

Two cases are investigated in this section. The first case assumes low tire stiffness ($\sigma_{0i} = 150$ m^{-1}, $i = x, y$) while the second case assumes a higher tire stiffness ($\sigma_{0i} = 500$ m^{-1}, $i = x, y$). The time histories of the friction forces (Fig. 3.4) show that the approximations for κ_i made in [32] are more realistic when the stiffness of the tire is higher. In this case the steady-state is reached faster. As already mentioned, the approximate lumped models in [32, 75] were derived having only the accuracy of the steady-state behavior in mind.

Trapezoidal and Quartic Load Distribution

Next, we compare the dynamic behavior of the approximate average lumped model of Section 3.1.1 with the behavior of the exact lumped models with trapezoidal and quartic normal load distribution presented above. In order to make a fair comparison

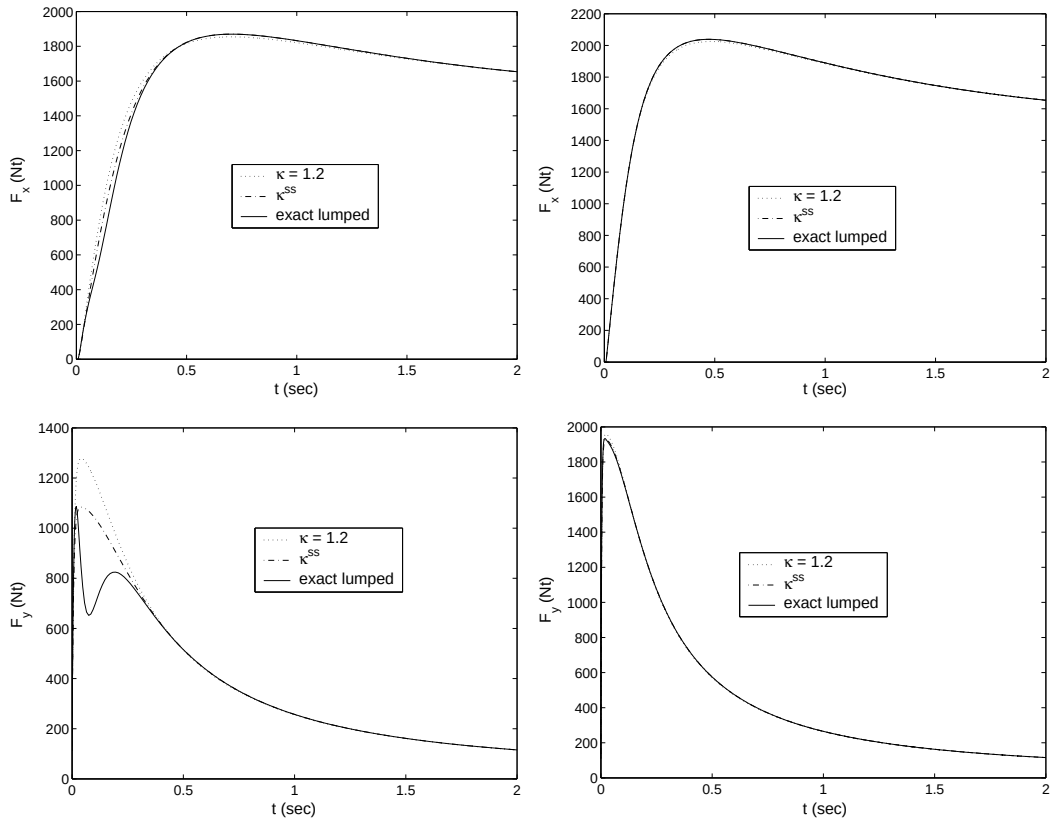

Figure 3.4: *Time histories for longitudinal and lateral forces for uniform load distribution (left column:* $\sigma_{0i} = 150$ m^{-1}*, right column:* $\sigma_{0i} = 500$ m^{-1}*,* $i = x, y$*)*

between the trapezoidal and the quartic normal load distribution models we have selected the parameters of the two expressions (2.45) and (3.43) such that they produce the same total normal force F_n and the same pneumatic trail.

We consider the case of a tire with stiffness $\sigma_{0i} = 500$ m^{-1}, $i = x, y$. The excitation of the system remains the same as before. The results are shown on the left column of Fig. 3.6. In Fig. 3.6 the time histories of the friction forces and the aligning torque are shown. We observe that the three models converge to the same steady-state, as expected. However, significant differences in the transient behavior of the three models are also evident. These differences are more apparent in the lateral force F_y and aligning torque M_z. The discrepancy is due to the fact that the normal load distribution $f_n(\zeta)$, along with the distribution of the contact patch deflection $z_i(t, \zeta)$, determine the amount of the total friction generated by each tire element along the contact patch length (see equations (2.37b), (2.38)) at each time

t. In the case of the approximate lumped model of Section 3.1.1 the use of the states $\tilde{z}_i(t),\ i = x, y$ and $\hat{z}_y(t)$ averages out the individual contribution to the total friction of each tire element, thus resulting in smoother transient behavior of the friction forces and aligning torque. In the case of the exact lumped model on the other hand, the product of the individual contact patch deflection $z_i(t, \zeta)$ with $f_n(\zeta)$ determines the amount of friction generated by each tire element in the contact patch; see equations (2.37b), (2.38). This is true both for the distributed and the exact lumped models. In Fig. 2.11(b) one observes that the trapezoidal normal load distribution weights more the tire elements close to the entry point of the contact patch (especially in the area $\zeta < a$) when compared to the quartic distribution. Similarly, the quartic distribution places more emphasis than the trapezoidal on the part of the patch $\zeta > a$. Observing the initial distribution of z_y^{ss} in Fig. 3.5 we notice that the tire elements close to $\zeta = 0$ are less deformed compared to the tire elements for larger values of ζ. As a result, the quartic distribution gives higher values for F_y than the trapezoidal distribution at the initial time. As the time progresses, and ω is reduced, (for example, $\omega = 20$ rad/sec) the distribution of z_y^{ss} tends to a uniform one. Since the total normal load is the same for both the quartic and the trapezoidal distributions, the two distributions will give similar values after the transients have receded. This is verified from the results shown in Fig. 3.6.

To provide an additional confirmation of these observations, a second set of numerical simulations was performed, using the approximate model in Section 3.1.1 and the exact trapezoidal and quartic models respectively, but with a larger slip angle, namely $\alpha = 15^\circ$. The tire stiffness and the excitation remained the same. The results are shown in the right column of Fig. 3.6. For this case the time histories of the friction forces and the aligning moment are almost identical for all three cases of normal load distributions. The bottom plot in Fig. 3.5 reveals that for $\alpha = 15^\circ$ the distribution of z_y^{ss} is very close to a uniform one, thus corroborating the earlier observations.

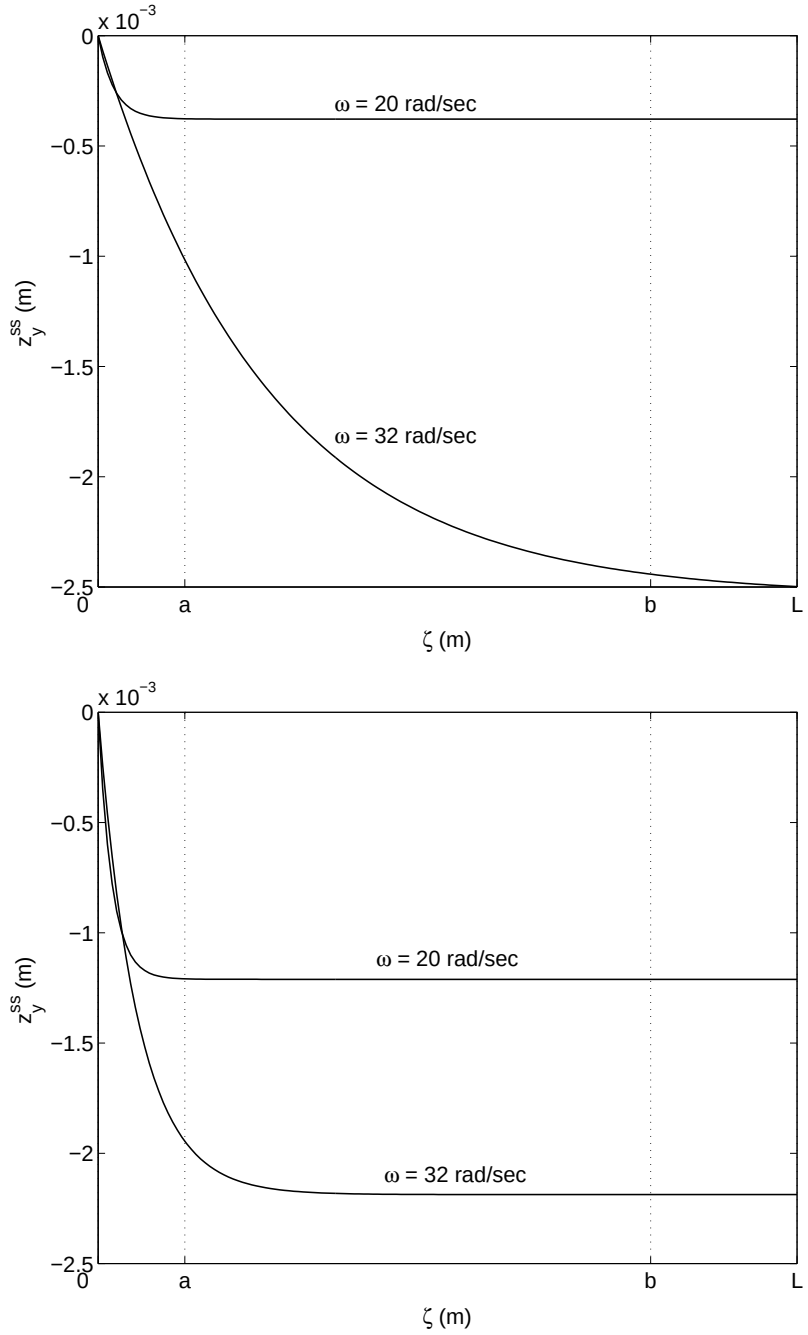

Figure 3.5: *Distribution of* $z_y^{ss}(\zeta)$ *along the contact patch, top:* $\alpha = 4°$*, bottom:* $\alpha = 15°$

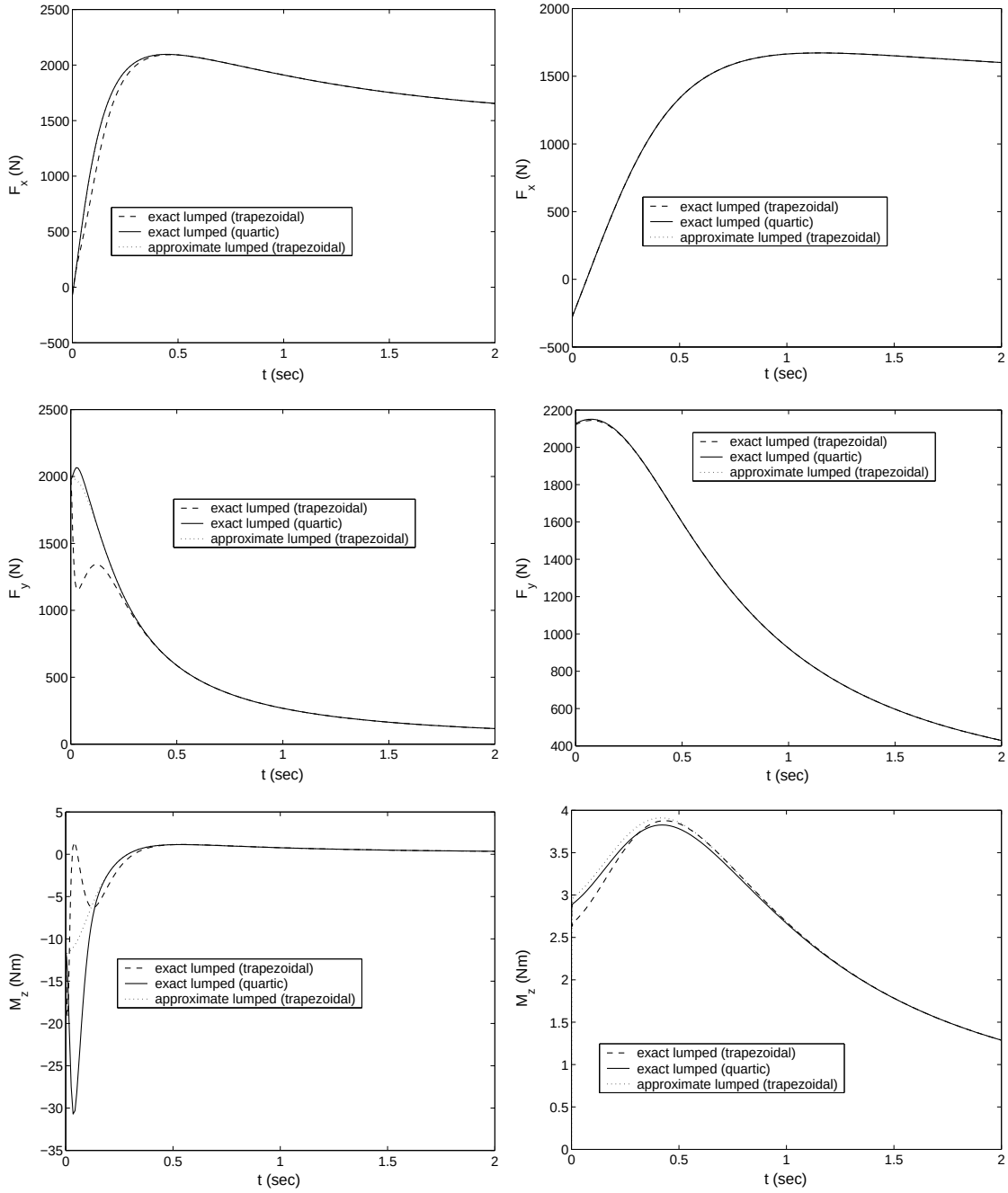

Figure 3.6: *Time histories for longitudinal/lateral forces and aligning torque (trapezoidal and quartic normal load distribution), left column:* $\alpha = 4°$*, right column:* $\alpha = 15°$

3.3 Effect of Steering Angle Rate

Thus far, we have derived models (distributed, approximate and exact lumped) that predict the friction forces and moments at the contact patch of the wheel when the steering angle of the wheel ϕ remains constant. In order to include the effect of the angular velocity $\dot{\phi}$ about the vertical axis of the wheel rim we first rewrite the expression for the relative velocity at the contact patch. We thus have

$$v_{rx} = \omega r - v\cos(\alpha) \tag{3.52a}$$

$$v_{ry}(\zeta) = -v\sin(\alpha) - \left(\frac{L}{2} - \zeta\right)\dot{\phi} \tag{3.52b}$$

Observe that in this case the relative velocity v_{ry} is a function of the position on the contact patch ζ. The new definition of the relative velocity v_{rx} and v_{ry} can be used in the distributed model (2.37)-(2.39) to calculate the friction forces and moments at the contact patch including the effect of $\dot{\phi}$. However, since now v_{ry} depends on ζ the dynamics of the approximate average lumped lumped model (3.4) and (3.18) or the exact lumped model (3.31) are not valid anymore. In order to include the effect of $\dot{\phi}$ on the *average lumped* (approximate or exact) model we propose in this section a LuGre-type dynamic friction model for the angular motion of the wheel about an axis normal to the contact area.

Consider as in Fig. 3.7 the rotation of a wheel about an axis normal to the contact patch. Let, in analogy to Section 2.2.2, assume that the forces developed due to this rotation are due to microscopic *torsional* springs/bristles in the contact patch. Assume also that ϕ_p is the plastic angular deformation and ϕ_e the elastic angular deformation of these bristles. Let $\phi = \phi_p + \phi_e$ be the total angle of rotation. Denote by $M_{z-\text{tor}}$ the friction moment due to the relative rotation of the wheel with respect to the surface and let

$$\mu_{z-\text{tor}} := \frac{M_{z-\text{tor}}}{F_n L} \tag{3.53}$$

the associated torsional friction coefficient. Let also μ_{kz} be the asymptotic (as $\dot{\phi} \to \infty$) friction moment coefficient and $k_z = F_n L \sigma_{0z}$ the torsional stiffness.

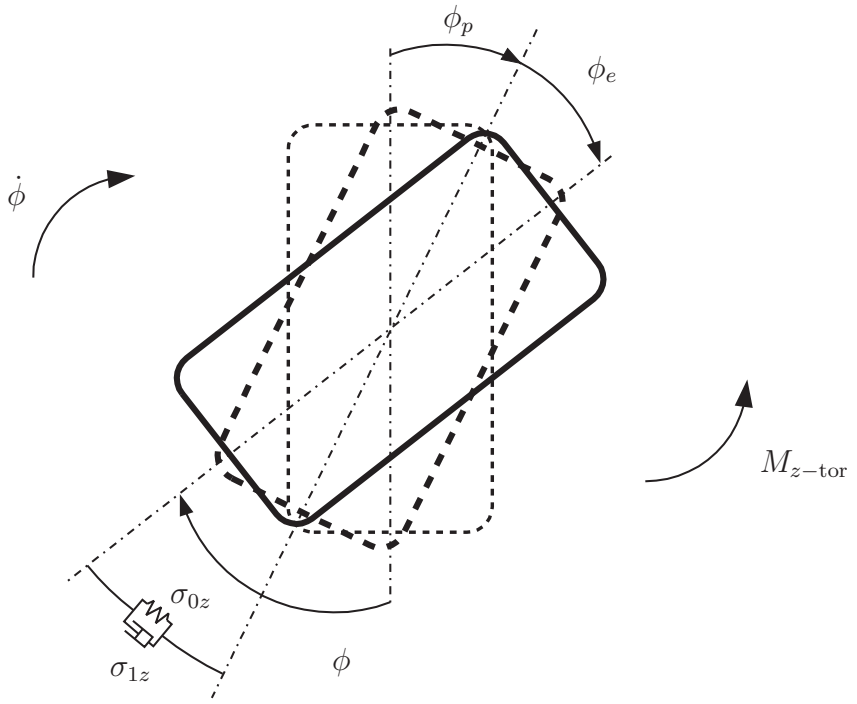

Figure 3.7: *Angular motion of the contact patch.*

The elastic and plastic angular deformations are

$$\phi_e = -k_z^{-1} F_n L \mu_{z-\mathrm{tor}} \quad \text{and} \quad \phi_p = \phi - \phi_e \tag{3.54}$$

respectively. The dissipation rate associated to the friction moment is

$$D(\dot{\phi}_p, \mu_{z-\mathrm{tor}}) = -F_n L \mu_{z-\mathrm{tor}} \dot{\phi}_p. \tag{3.55}$$

Following the same reasoning as in the case of the 2D motion in Sections 2.2.2 and 2.2.3, we find the torsional friction coefficient by solving an associated QVI. We then derive to the following dynamic LuGre-type friction model for the angular relative motion of the wheel with respect to the contact area

$$\dot{z}_z(t) = \dot{\phi} - \frac{\sigma_{0z}|\dot{\phi}|}{g_z(\dot{\phi})} z_z(t) \tag{3.56a}$$

$$g_z(\dot{\phi}) = \mu_{kz} + (\mu_{sz} - \mu_{kz})\, e^{-\left(\frac{\dot{\phi}}{\dot{\phi}_s}\right)^{\beta}} \tag{3.56b}$$

and

$$M_{z-\mathrm{tor}} = -F_n L \left(\sigma_{0z} z_z + \sigma_{1z} \dot{z}_z + \sigma_{2z} \dot{\phi} \right) \tag{3.57}$$

This model can be used to include the effect of $\dot{\phi}$ to the moment predicted by the lumped model (3.4), (3.18) and (3.15). The total moment predicted by the average lumped model will then be the summation of $M_{z-\text{tor}}$ and M_z from (3.15) where the latter is computed using the initial definition of the relative velocity (2.36) without the $\dot{\phi}$ term,

$$M_{z-\text{total}} = M_z + M_{z-\text{tor}}. \tag{3.58}$$

There is a final point that requires further clarification. It is not only the aligning torque that needs adjustment when we include the effects of the wheel rim rotation. Since the expression of v_{ry} depends on ζ, there should be some adjustment to the lateral forces as well. To simplify the model, we have assumed that the rotation of the rim does not affect the longitudinal and lateral friction forces, and that the definition (2.36) can still be used for the relative velocity input to the lateral friction force model. This is a realistic assumption, since in relatively high speeds the term $\left(\frac{L}{2} - \zeta\right)\dot{\phi}$ is much smaller compared to $v\sin(\alpha)$ due to the small length of the patch and the relatively low steering velocity $\dot{\phi}$. Furthermore, in low vehicle velocities the normal load distribution is closer to a symmetric one. Considering only the rotation of the wheel rim $\dot{\phi}$ and the symmetry of the normal load distribution results in cancellation of the lateral friction forces. This is demonstrated in the next section.

In conclusion, we emphasize that the introduction of equations (3.56)-(3.57) to the average lumped tire model has been done rather artificially. As mentioned earlier, the effect of $\dot{\phi}$ is captured by the distributed model (2.37)-(2.39) by introducing the definition (3.52) and without adding any new parameters to the system. In order for the *average lumped* model to capture the effect of $\dot{\phi}$ we introduced equations (3.56)-(3.57) and a new set of parameters σ_{0z}, σ_{1z}, σ_{2z}, μ_{kz}, μ_{sz}, $\dot{\phi}_s$ and β. The coefficients of (3.56)-(3.57) can be identified by comparing the distributed and the lumped models.

Next, we propose a steady-state scenario ($v = 0$, $\omega = 0$ and $\dot{\phi} \neq 0$) in order to predict the torsional torque of the distributed model, and then identify the remaining coefficients in such a way, that the behavior of the lumped model captures the behavior of the distributed one at steady-state. Note that for the case $v = \omega = 0$, $\dot{\phi} \neq 0$ the

self-aligning torque is zero and the only moment acting normal to the patch is the torsional moment.

3.3.1 Identification of the Torsional Equation Parameters

In this section we identify the parameters of the torsional equations (3.56)-(3.57) of the average lumped model by comparing it with the distributed model using a special steady-state case scenario. In particular, consider the case when $\omega, v = 0$ and $\dot{\phi} = \text{const}$. The relative velocity v_r is then

$$\begin{aligned} v_{rx} &= 0 \\ v_{ry} &= -\dot{\phi}\left(\frac{L}{2} - \zeta\right). \end{aligned} \tag{3.59}$$

In this particular case, and since $\omega = 0$, the equations of the internal friction states from the distributed model reduce to

$$\frac{\partial z_i}{\partial t} + \frac{\partial z_i}{\partial \zeta}|\omega r| = \frac{\partial z_i}{\partial t} = v_{ri} - C_{0i}(v_r) z_i \tag{3.60}$$

where $i = x, y$. Also, in steady-state, we have $\frac{\partial z_i}{\partial t} = 0$ which leads to the following steady-state values

$$z_i^{\text{ss}} = \frac{v_{ri}}{C_{0i}(v_r)}, \qquad i = x, y \tag{3.61}$$

Obviously, and since $v_{rx} = 0$, we have $z_x^{\text{ss}} = 0$ and the steady-state longitudinal force is $F_x^{\text{ss}} = 0$.

As far as the value of z_y^{ss} is concerned, imposing $v_{rx} = 0$, we have from (2.26), (2.35) and (3.61),

$$z_y^{\text{ss}} = \text{sign}(v_{ry}) \frac{g(v_{ry})}{\sigma_{0y}}. \tag{3.62}$$

Now observe that for $v_{rx} = 0$ the function $g(v_{ry})$ in (2.31) becomes

$$g(v_{ry}) = \mu_{ky} + (\mu_{sy} - \mu_{ky}) \exp\left[-\left(\frac{|\dot{\phi}|\,|L/2 - \zeta|}{v_s}\right)^{\gamma}\right] \tag{3.63}$$

At this point we make one final assumption. Since $v = 0$, it is necessary to assume a symmetric normal load distribution that will impose symmetry in the friction forces. For simplicity, we choose $f_n = F_n/L = \text{const}$. Recall that

$$\mu_y^{\text{ss}} = -\sigma_{0y} z_y^{\text{ss}} - \sigma_{2y} v_{ry} \tag{3.64}$$

Since z_y^{ss} is symmetric with respect to the center of the patch (Fig. 3.8), and assuming a uniform load distribution, we conclude that the lateral forces cancel each other out, resulting in $F_y^{\text{ss}} = 0$.

The total moment predicted by the distributed model (2.39) in case when $\omega, v = 0$ and $\dot{\phi} = \text{const.}$ is given by

$$M_{z-\text{total}}^{\text{ss}} = -\text{sign}(\dot{\phi})\frac{1}{4}\mu_{ky} f_n L^2 - 2\frac{(\mu_{sy} - \mu_{ky}) f_n v_s}{\dot{\phi}} \left(-\frac{L}{2} e^{-\frac{L|\dot{\phi}|}{2v_s}} + \frac{v_s}{|\dot{\phi}|}(1 - e^{-\frac{L|\dot{\phi}|}{2v_s}}) \right) \tag{3.65}$$

Since there is no self-aligning torque in case when $\omega, v = 0$ this equation gives also the value of the torsional moment in (3.58). Comparing (3.65) with the steady-state torsional component of the lumped model (3.56)-(3.57) given by

$$z_z^{\text{ss}} = \text{sign}(\dot{\phi})\frac{g_z(\dot{\phi})}{\sigma_{0z}} \tag{3.66a}$$

$$M_{z-\text{tor}}^{\text{ss}} = -F_n L \left(\sigma_{0z} z_z^{\text{ss}} + \sigma_{2z} \dot{\phi} \right) \tag{3.66b}$$

we can identify the parameters $\mu_{sz}, \mu_{kz}, \dot{\phi}_s, \sigma_{2z}$ and β. For different values of $\dot{\phi}$ we have identified the parameters $\mu_{sz}, \mu_{kz}, \dot{\phi}_s, \sigma_{2z}$ and β by comparing the plots generated by the distributed model steady state (3.65) with the plots generated by the average lumped model steady state (3.66). The parameters identified using this approach are shown in the following table, and the result of the curve fitting is shown in Fig. 3.8.

Table 3.1: *Identified Parameters*

Parameter	μ_{kz}	μ_{sz}	σ_{2z}	$\dot{\phi}_s$(rad/sec)	β
Value	0.76	0.91	0	74	1

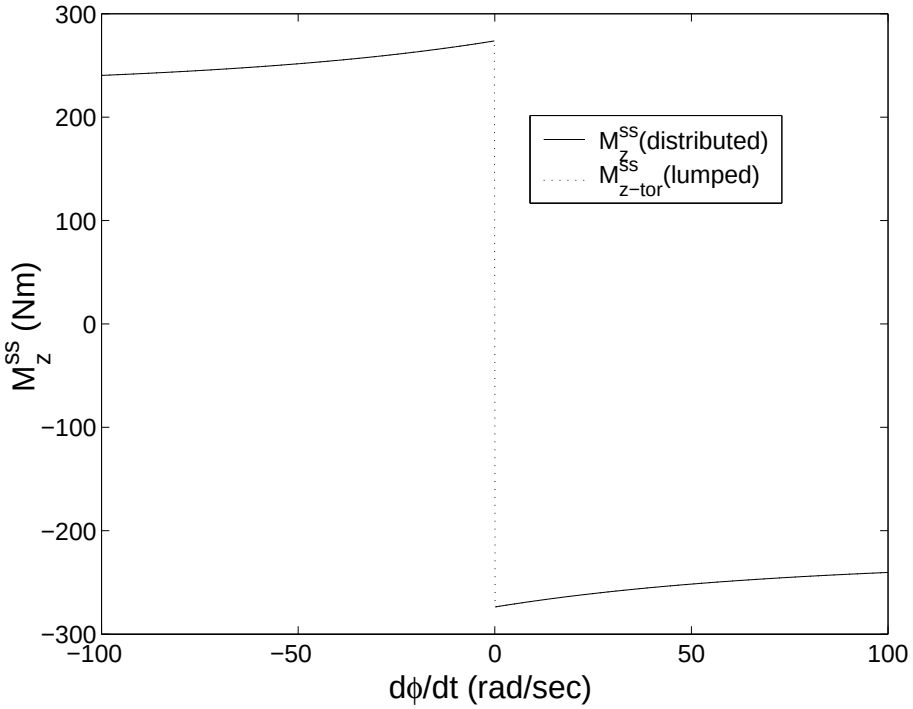

Figure 3.8: *Comparison between* $M^{\rm ss}_{z-{\rm tor}}$ *and* $M^{\rm ss}_{z-{\rm total}}$ *from data fitting; case when* $v = \omega = 0$.

3.4 Experimental Validation of the Longitudinal LuGre Dynamic Tire Friction Model

In this section we use the results of an experiment conducted with a specially equipped test vehicle, provided by Renault, to validate the proposed dynamic friction model. The test vehicle was driven through a straight path and braking was applied three times. Measurements of vehicle speed and acceleration and wheel loads and angular rate were collected and used to calculate the friction coefficients and longitudinal slip quantities during the experiment. These measurements allow us to identify the longitudinal parameters of the approximate average lumped LuGre tire friction model of Section 3.1.1.

3.4.1 Testbed Car Description

The friction data were collected using the "BASIL" car which is a laboratory vehicle based on a Renault Mègane 110 Kw. The car is equipped with several sensors to study the behaviour of the vehicle during braking and traction phases. These sensors are (see Fig. 3.9):

- an optical cross-correlation sensor that measures the transverse and longitudinal vehicle velocities
- a basic inertial measurement unit with a piezoelectric vibrating gyroscope that measures the yaw rate; a separate sensor measures the roll velocity
- a magnetic compass that provides directional information
- two acceleration sensors that measure the longitudinal and lateral accelerations
- an ABS-system used to derive – via suitable signal processing – the wheels' velocities; the ABS system was not enabled during the experiments, it was used only as a wheel velocity sensor

- a differential GPS (DGPS) system used to locate the vehicle and compute its trajectory with great accuracy (less than one centimeter); this allows repeated experiments at the same road location

- other specific purpose sensors (not described herein) used to measure the throttle angle (which reflects the command acceleration) and the collector pressure (which reflects the braking command)

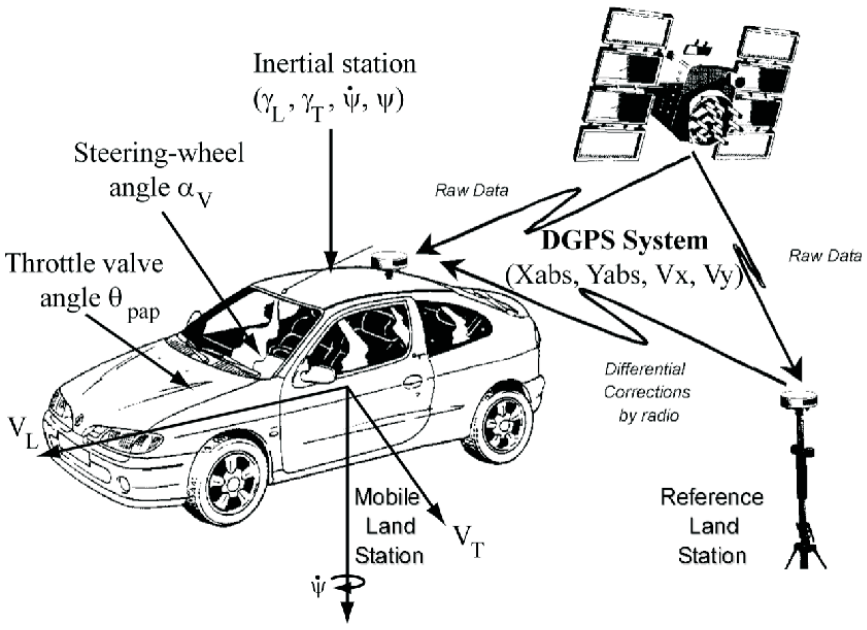

Figure 3.9: *Sensors and measurement parameters.*

For these experiments, a Wheel Force Transducer (WFT) was installed at center of the rim of the front right wheel (FRW) to measure the dynamic forces and moments acting between the road and the vehicle at the wheel center. Its inertial effects are small and hence they were neglected. This sensor gives the complete wrench in real time, namely the forces F_{xc}, F_{yc}, F_{zc} and the moment M_z. These are shown in Fig. 3.10. Although the WFT does not measure directly the friction forces and moments on the tire itself, it is assumed that the rim and tire dynamics can be neglected so that the forces and moments expressed at the contact patch (according to ISO 8855 specifications) can be calculated from the forces and moments at the

wheel center via a simple coordinate transformation; see right drawing of Fig. 3.10. Such additional rim/tire dynamics can be added to the overall model, if desired. Since our main objective is to show the ability of the proposed friction model to capture the overall complex behavior of the friction force and moment characteristics acting on the vehicle, it was not deemed necessary to incorporate such higher order dynamics. Although more accurate, such an approach would unnecessarily dilute from the main results of this work.

A schematic of the completely equipped "BASIL" vehicle, along with the corresponding measurement parameters is given in Fig. 3.9.

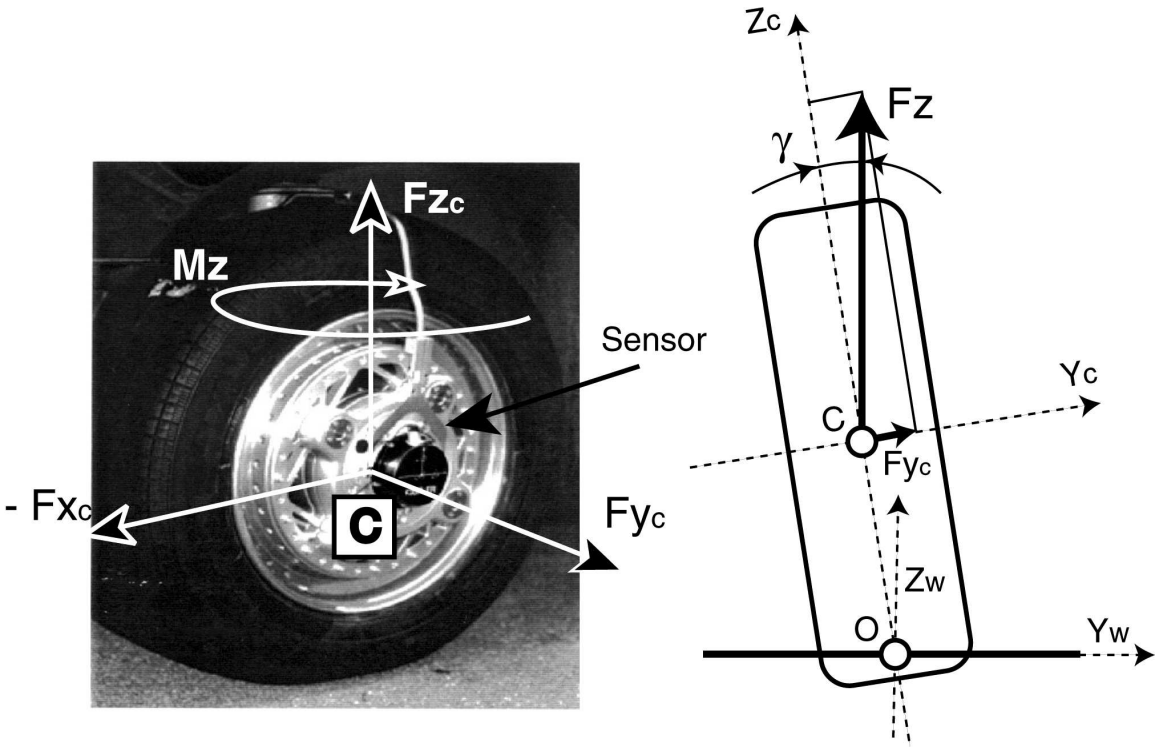

Figure 3.10: *View of the equipped wheel with the Wheel Force Transducer (WFT); variables measured and axis systems used are according to ISO 8855 specifications. Rim and wheel dynamics are neglected so that the FWT forces are related to the actual forces at the contact patch via a simple coordinate transformation.*

Experimental procedure For safety reasons, trials were carried out on a straight, undeformed, flat and dry road. Before the braking phase, the following conditions where met:

- zero vertical load transferred
- slip velocity closed to zero
- steering wheel angle closed to zero
- F_x approximately constant and as small as possible

Most of these conditions may be reached (or approached) by removing the traction torque in the front wheels. For this, the driver releases the clutch for approximately two seconds, until the vehicle's speed decreases to a pre-specified value. Then, the test driver starts the braking phase and brakes strongly until the grip limit of the front wheels is reached. Finally, he releases the brake pedal and the front wheels reach again normal grip conditions (small value of slip velocity). Then, the driver accelerates again to repeat the same sequence several times. Three such braking phases were performed and the results were stored in a file for subsequent analysis.

3.4.2 Collected Data

The collected data obtained from the experiments are shown in Figures 3.11 and 3.12. Figure 3.11 shows a snapshot of the measurements of the braking pressure, the longitudinal speed of the vehicle and the front right wheel (FRW) velocity, for the three braking phases. Figure 3.12 shows the calculated forces F_{xw}, F_{yw}, F_{zw} at the contact patch, the calculated camber angle γ and the lateral acceleration G_t, for the test conditions specified above. The forces F_{xw}, F_{yw}, F_{zw} are derived from the projection of the measured forces F_{xw}, F_{yw}, F_{zw} in the $C-$frame onto the $W-$frame and they account for the camber and toe angle deviations (see Fig. 3.10).

The values of F_{yw} and G_t clearly show the low lateral excitation of the vehicle during braking. The peaks exhibited by these profiles are probably due to the geometrical characteristics of the suspension system that result in nonzero wheel camber angles and, in particular, to the toe angle compliance.

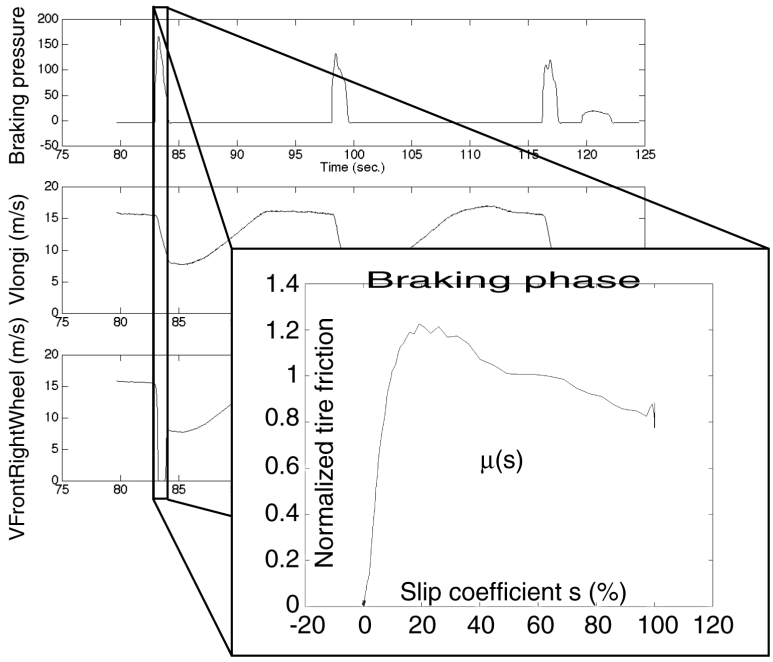

Figure 3.11: *Braking experiments: measurements of the braking pressure, the longitudinal speed of the vehicle and the FRW velocity.*

3.4.3 Parameter Identification

The data collected include three braking maneuvers, shown in Fig. 3.12. Braking #1 consists of all data collected between 80 and 83.5 sec, Braking #2 consists of all data collected between 97 and 100 sec, and Braking #3 consists of the data collected approximately between 115 and 118 sec; see also the top plot of Fig. 3.12. First, we compare the (μ, s, v) steady-state solution of the distributed dynamical LuGre model of Section 2.3.1 with the friction coefficient μ given by the experiments to determine the longitudinal parameters of the model ($\sigma_{0x}, \sigma_{2x}, \mu_{sx}, \mu_{kx}, v_s$ and γ). This is in complete analogy to the method we used in Section 2.3.1 to identify the LuGre model parameters by comparison to the MF. By comparing the time histories of the friction force given by the model of Section 3.1.1, with the ones given by the experiments we can determine the rest of the parameters (e.g., σ_{1x}).

In order to identify the model parameters the `lsqnonlin` command of MATLAB was used by fitting the 3-D (μ,s,v) steady-state solution of the distributed model to the data of Braking #2. In all cases the patch length was chosen as $L = 0.2\,\mathrm{m}$. The

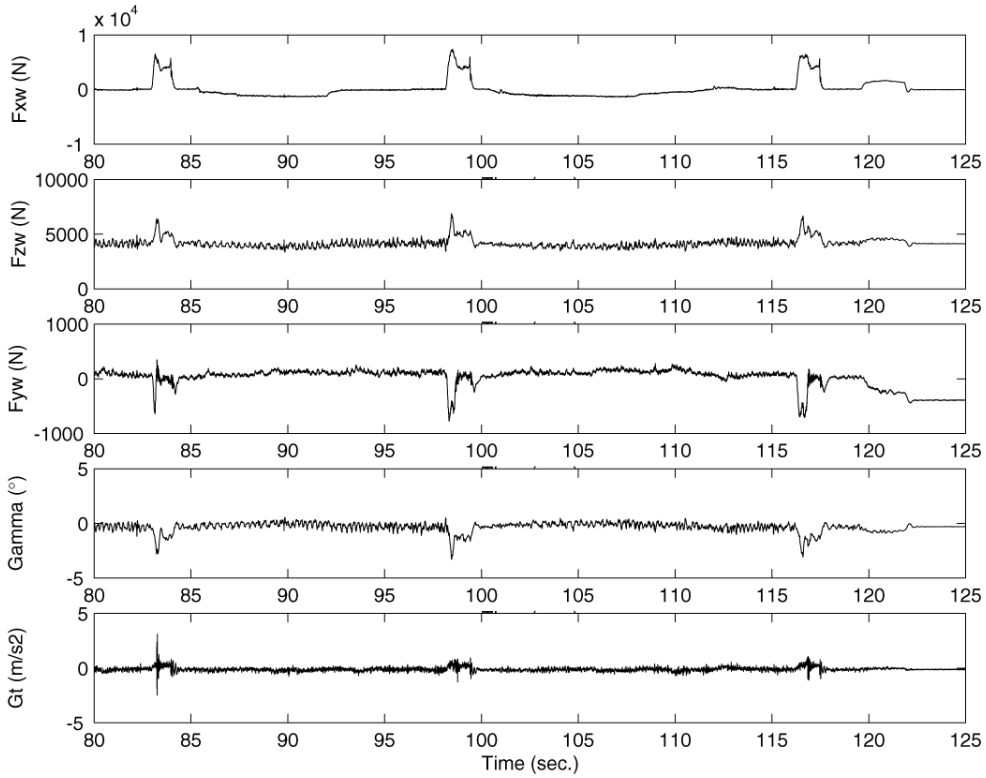

Figure 3.12: *Braking experiments: time-profiles of the forces F_{xw}, F_{yw}, F_{zw}, the camber angle γ and the lateral acceleration G_t.*

results of the identification algorithm are shown in Table 3.2.

Table 3.2: *Data used for the plots in Fig. 3.14.*

Parameter	**Value**
σ_{0x}	178 m^{-1}
σ_{1x}	1 m^{-1}
σ_{2x}	0 sec /m
μ_{kx}	0.8
μ_{sx}	1.5
v_s	5.5 m/ sec
γ	2

The comparison between the experimental results and the simulation results using

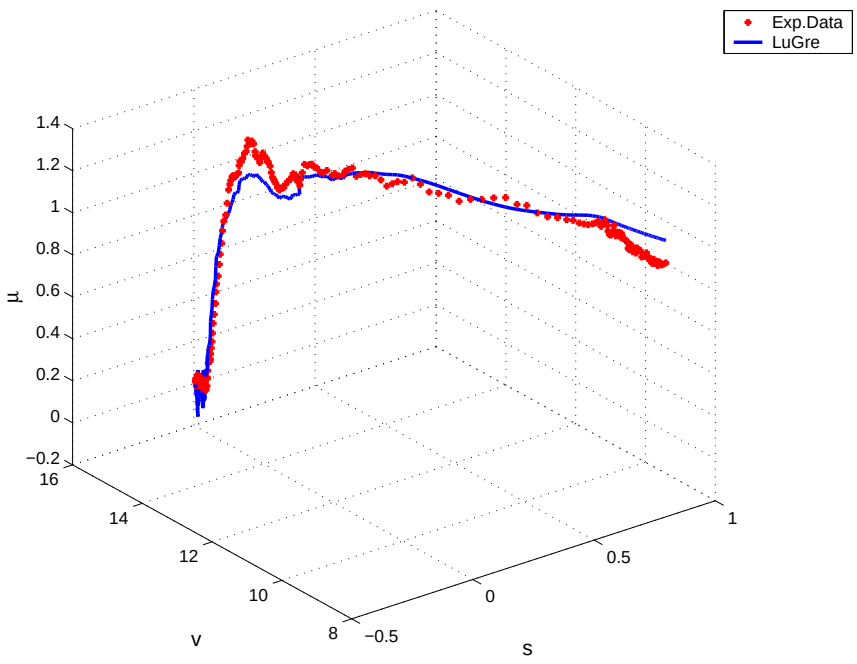

Figure 3.13: *Three-dimensional plots of the corresponding (μ,s,v) curves for the collected data and the estimated predicted steady-state LuGre average lumped model.*

the LuGre dynamic friction model for the three cases are shown in Fig. 3.14. These figures indicate that our proposed model captures very well both steady-state and transient friction force characteristics.

3.5 Dynamic Characteristics of the 2D Model

In the previous section we presented comparison of the transient response of the longitudinal lumped LuGre tire friction model with experimental data. Validating the combined longitudinal/lateral behavior of the model is not as straightforward. In fact, experimental results for combined longitudinal/lateral behavior of tire models under realistic transient conditions are scarce in the literature. In this section we present a qualitative validation of the dynamic response of the tire friction for the combined longitudinal/lateral motion predicted by the proposed model against the results found in [5].

In [5] a static map of relative velocity to friction and the dynamics of slip and slip angle development are used to predict tire friction forces by taking into consid-

eration the effects of relaxation length. Experimental results using a "Mobile Tire Tester" are presented for different braking inputs. The "Mobile Tire Tester" is an experimental test-bed that allows independent control of slip angle, rate of rotation and travel velocity of a tire. Both experimental and simulation results are given in [5] corresponding to a case of constant travel speed and slip angle and with different braking profiles which affect only the wheel's rotation rate.

Similar simulations have been conducted with the model developed in Section 3.1.1 using linearly increasing and "stair-step" increasing braking torques under constant vehicle speed ($v = 8$ m/sec) and wheel slip angle ($\alpha = 4$ deg) as in [5]. The dynamic response of the friction forces (Fig. 3.15) is in complete accordance with the results given in [5]. In particular, it is verified that the longitudinal and lateral force components predicted when longitudinal slip is increasing are considerably different from those predicted when slip is decreasing rapidly (first column of Fig. 3.15, linear increase of braking torque). This implies that dynamic effects may not be neglected. We also observe the same patterns in friction development due to steps in torque (second column of Fig. 3.15, "stair-step" increase of braking torque) as might be introduced by a poor anti-lock braking system or a jerky driver as mentioned in [5]. These results are in agreement with the experimental observations in [5]. Notice in particular the hysteretic loops in bottom two rows of Fig. 3.15. These loops are exclusively a dynamic phenomenon and cannot be reproduced by steady-state models.

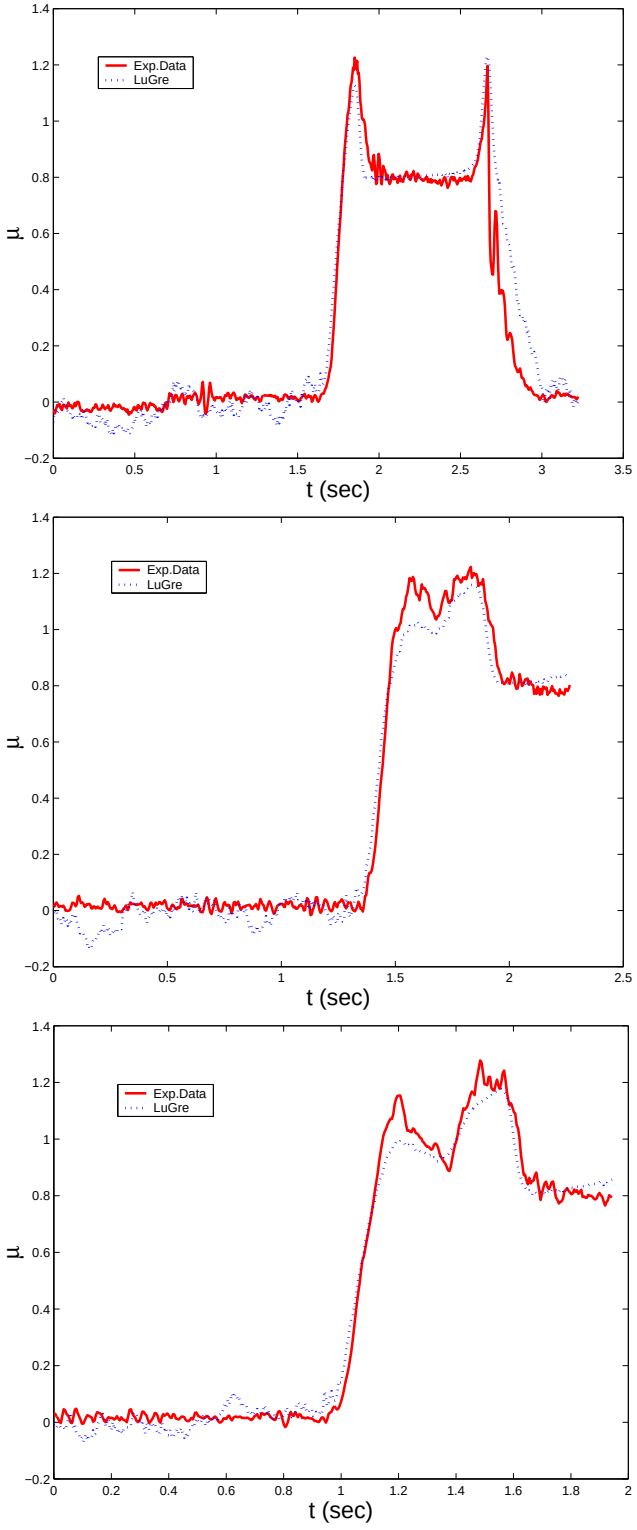

Figure 3.14: *Experimental and simulation results.*

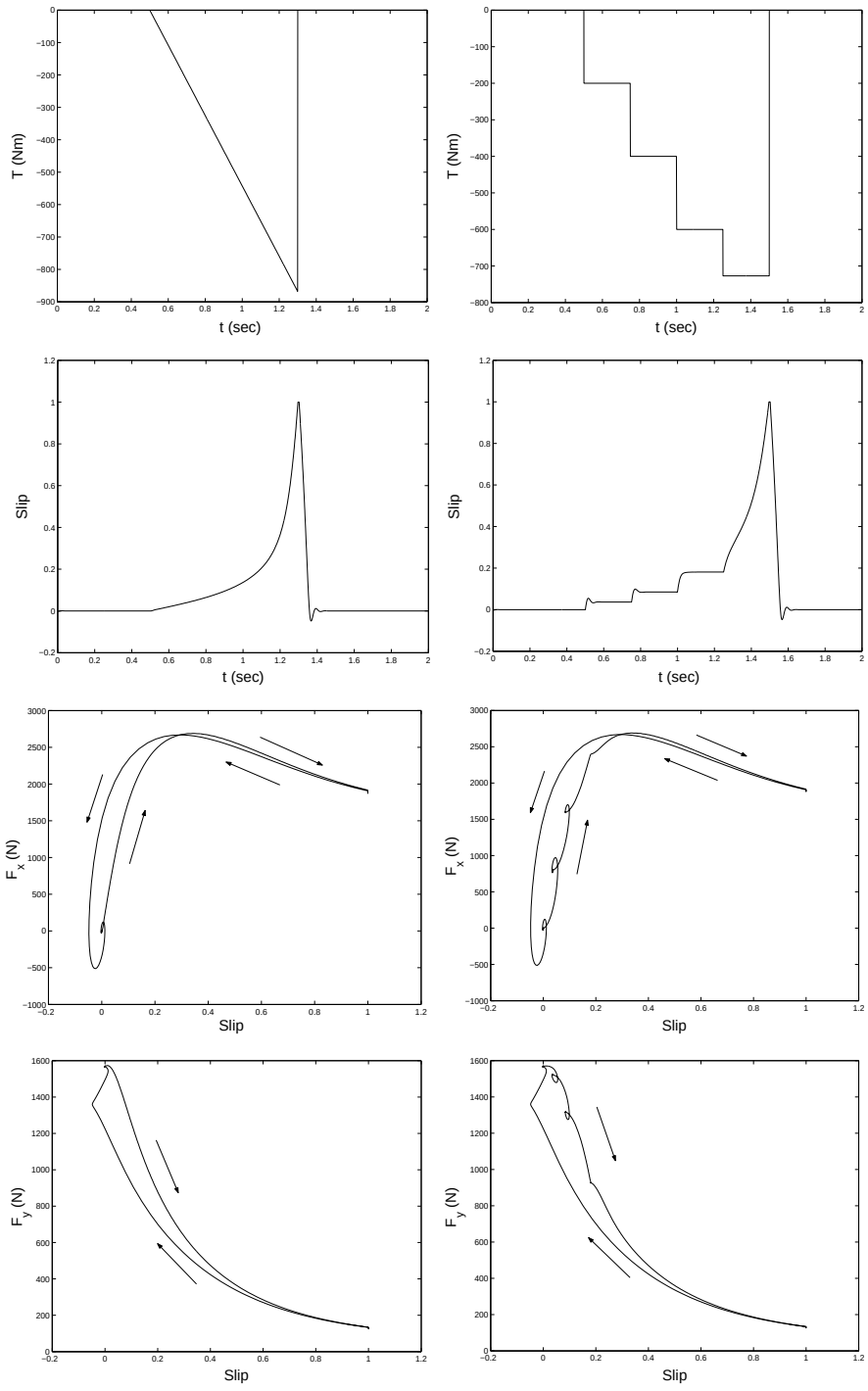

Figure 3.15: *Dynamic response of friction for linear (left column) and "stair-step" increasing (right column) braking torque. The results are in complete agreement with those presented in [5] ($\alpha = 4\text{deg.} = \text{const.}$, $F_n = 2500\text{Nt}$).*

Part II

Vehicle Modeling and Numerical Optimization

Chapter 4

The Half-Car Model and Minimum Time Cornering

Numerical techniques are typically used to address the problem of trajectory optimization for ground wheeled vehicles. Such approaches allow the incorporation of high fidelity vehicle models and generate realistic results. They are extremely powerful tools for off-line applications such as vehicle performance evaluation and optimization, as well as trajectory planning for autonomous vehicles in unchanging environments.

In what follows we first revisit the subject of vehicle dynamics, which is well established in the literature, to adopt a vehicle model for our optimization considerations. The vehicle model that we choose is rich enough to incorporate important effects in vehicle handling such as normal load transfer and suspension dynamics. Convergence of the optimization algorithm depends on the complexity of the problem and the accuracy of the initial guess of the optimal solution. To this end, we also introduce a simplified/low order version of the model which we use to obtain preliminary results in minimum time cornering and gain experience with vehicle dynamics and the optimization algorithm.

4.1 Dynamics of a Half-Car Model

In this section, the assumptions associated with the half-car model are summarized and the equations of motion are derived. Two models are presented. The first one includes wheel and suspension dynamics which allows one to investigate the role of important effects, such as the longitudinal load transfer, in vehicle handling. The second half-car model presented here is based on additional simplifying assumptions, leading to a model of reduced order which is easier to implement in an optimization algorithm and achieve convergence in case no reliable initial guesses of the optimal solution are provided.

4.1.1 Assumptions

A typical ground vehicle consists of the main body (frame, passenger area, engine, transmission) linked to four wheels via the suspension system. Except from translation and yawing motion during travel, the suspended body performs pitching, rolling and vertical translation motions. The vehicle interacts with the environment through tire friction forces, which allow the vehicle to accelerate, decelerate and steer as well as aerodynamic drag and lift forces generated due to relative motion of the body and the atmosphere. Steering of the vehicle is generated typically by the front two wheels, although it is not unusual for steering to be generated by the rear or all four wheels. The power is transmitted from the engine to the wheels through the transmission system. Typically, for an off-road vehicle power is transmitted to all four wheels.

Next, we present a list of assumptions taken into consideration to describe mathematically the motions of a ground vehicle.

- We consider no rear wheel steering. For further simplification we can assume equal steering angles of the front left and front right wheels.

- We assume that the C.G. is located on the longitudinal vehicle axis. The longitudinal position of the C.G. is a parameter of our model. The static vertical load though is equally distributed to the left and right wheels.

- The rolling motion of the suspended mass is neglected. In addition we assume that friction forces and velocities appearing on wheels of the same axle are identical. Taking into consideration all the assumptions above, the model is now equivalent to a 2-wheel vehicle (half-car) as in Figure 4.1, with one front and one rear wheel on the longitudinal x body axis of the vehicle. The friction forces of each wheel of the half-car model is equal to the sum of friction forces of the wheels of the same axle.

- The mass of the wheels is neglected. The vehicle is modelled as a single rigid body. However, equations to describe the rotation of each wheel are necessary in order to calculate the angular speed of each wheel. This allows the calculation of the relative velocity of each wheel with the ground and thus the friction forces generated by each tire by use of a tire friction model. More discussion follows.

- The aligning moment of the tires is neglected for simplicity as it is common in the literature [62], [68], [69] for trajectory following/optimization applications.

- Aerodynamic forces are completely neglected.

- Engine, transmission and brakes dynamics are neglected. We assume that the longitudinal control of the vehicle are two independent torques on each wheel. However, the controls in a real car is one acceleration pedal and one brake pedal. Thus the input torques of each wheel are coupled. On the other hand, several race driving techniques, such as "hand-brake cornering" and "left foot braking" allow some independence on the longitudinal control of each wheel. More discussion follows.

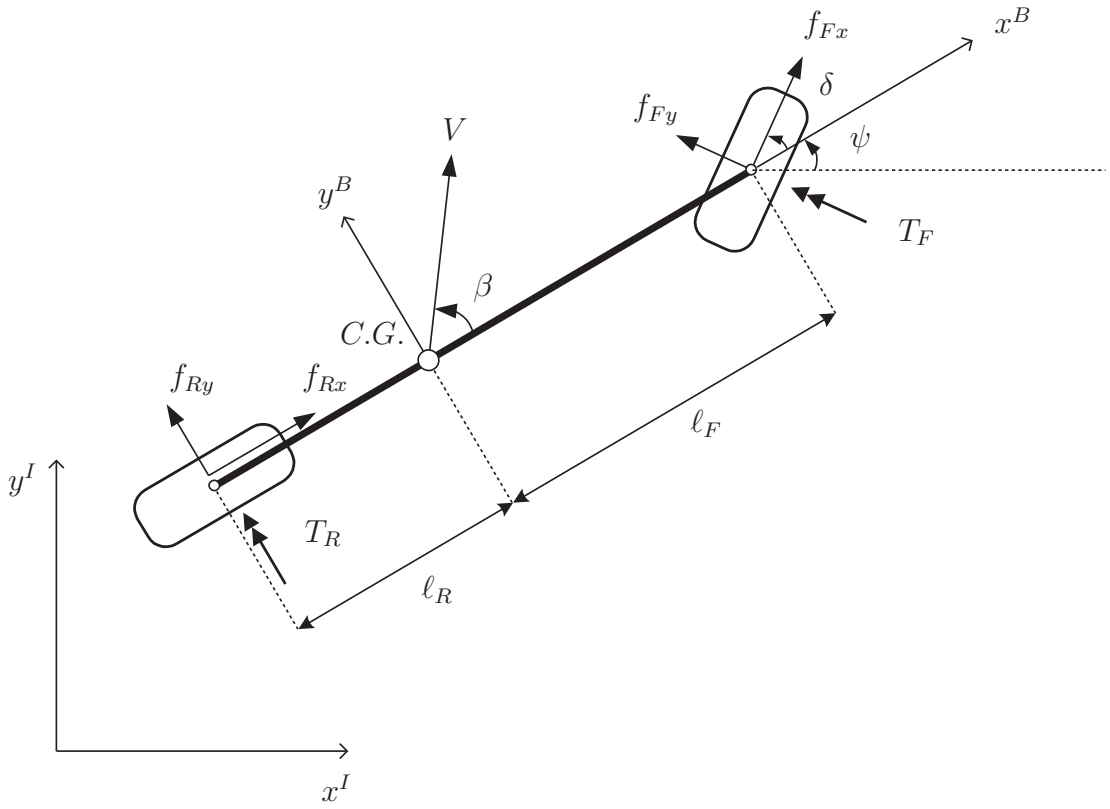

Figure 4.1: *Bicycle Model*

4.1.2 Equations of Motion

The equations of motion of the half-car model, shown in Fig. 4.1, taking into consideration the assumptions of the previous section, are presented below.

$$m\ddot{x} = f_{Fx}\cos(\psi+\delta) - f_{Fy}\sin(\psi+\delta) + f_{Rx}\cos\psi - f_{Ry}\sin\psi \tag{4.1}$$

$$m\ddot{y} = f_{Fx}\sin(\psi+\delta) + f_{Fy}\cos(\psi+\delta) + f_{Rx}\sin\psi + f_{Ry}\cos\psi \tag{4.2}$$

$$I_z\ddot{\psi} = (f_{Fy}\cos\delta + f_{Fx}\sin\delta)\,\ell_F - f_{Ry}\ell_R \tag{4.3}$$

$$I_F\dot{\omega}_F = T_F - f_{Fx}r \tag{4.4}$$

$$I_R\dot{\omega}_R = T_R - f_{Rx}r \tag{4.5}$$

In the equations above m is the vehicle's mass, I_z is the polar moment of inertia of the vehicle, I_i, $i = F, R$ are the moments of inertia of the front and rear wheels about the axis of rotation, r is the radius of each wheel, x and y are the cartesian coordinates of the C.G. in the inertial frame of reference, ψ is the yaw angle of the

vehicle, ω_i, $i = F, R$ is the angular rate of the front and rear wheel. By f_{ij}, $j = x, y$ and $i = F, R$ we denote the longitudinal and lateral friction of the front and rear wheels, respectively. In this model the inputs are the driving/braking torques T_F and T_R at the front and rear wheels respectively, and δ is the steering angle of the front wheel.

The tire friction forces are calculated using Pacejka's MF model of Section 2.1. Equation (2.5) is used to calculate the total friction coefficient of each tire and multiplied by the corresponding normal load provides the total friction force. In particular we have the longitudinal and lateral slip quantities in front and rear axles, in terms of the system (4.1)-(4.5) states and inputs, as follows

$$s_{Rx} = \begin{cases} +1 - \frac{v\cos\beta - \dot{\psi}\ell_R}{\omega_F r} & \text{for acceleration} \\ -1 + \frac{\omega_F r}{v\cos\beta - \dot{\psi}\ell_R} & \text{for deceleration} \end{cases}, \tag{4.6}$$

$$s_{Ry} = \frac{v\sin\beta - \dot{\psi}\ell_R}{v\cos\beta}, \tag{4.7}$$

$$s_{Fx} = \begin{cases} +1 - \frac{v\cos(\beta-\delta) + \dot{\psi}\ell_F\cos\delta}{\omega_F r} & \text{for acceleration} \\ -1 + \frac{\omega_F r}{v\cos(\beta-\delta) + \dot{\psi}\ell_F\cos\delta} & \text{for deceleration} \end{cases}, \tag{4.8}$$

$$s_{Fy} = \frac{v\sin(\beta-\delta) + \dot{\psi}\ell_F\cos\delta}{v\cos(\beta-\delta) + \dot{\psi}\ell_F\sin\delta}, \tag{4.9}$$

where v is the vehicle's speed $v = \sqrt{\dot{x}^2 + \dot{y}^2}$ and β the vehicle slip angle $\beta = \tan^{-1}\left(\frac{\dot{y}}{\dot{x}}\right) - \psi$. Equation 2.6 is used to calculate the total slip in front and rear axles, that is s_F and s_R respectively, which we use to calculate the total friction forces F_F and F_R from the Magic Formula (2.5). The longitudinal and lateral friction components in front and rear tires f_{ij}, $i = F, R$, $j = x, y$ are taken from equation (2.7) as follows

$$f_{ij} = -\frac{s_{ij}}{s_i} F_i(s_i),\ i = F, R,\ j = x, y \tag{4.10}$$

$$F_i(s_i) = f_{iz} D\sin(C\text{atan}(Bs_i)),\ i = F, R \tag{4.11}$$

The normal load on each axle f_{iz}, $i = F, R$ is affected by the suspension dynamics as described in the following.

4.1.3 Suspension Dynamics

The suspension dynamics are essentially added to the overall vehicle model when studying passenger comfort. They also allow one to incorporate to the model the effects of dynamic normal load transfer from one wheel to the others during acceleration/braking and cornering of the vehicle.

Normal load transfer appears as a reaction to inertial forces during acceleration when the vertical distance of the center of gravity of the vehicle is taken into consideration. Normal load transfer may be expressed without introducing the additional suspension dynamics, but in this case it is expressed as a function of the derivatives of states of the vehicle model [2]. In some cases, the load transfer is approximated using the vehicle model's inputs and states, as in [62], [68] and [69]. In this work we propose to describe the dynamic normal load transfer by introducing the suspension dynamics. No approximation is necessary and the effect is completely described by the states of the system making it possible for the dynamic load transfer effect to be taken into consideration in a simulation scheme. Having already assumed a half-car model, we will investigate the normal load transfer in the longitudinal only direction, i.e load transfer from the front to the rear axle and vice versa.

Let z be the vertical displacement of the center of gravity of the vehicle and θ the pitch angle of the suspended mass as in Figure 4.2. The dynamics of the vertical and pitching motion of the suspended mass are described by the following equations.

$$m\ddot{z} = f_{Fz} + f_{Rz} - mg \tag{4.12}$$

$$I_y\ddot{\theta} = f_{Rz}\ell_R\cos\theta - f_{Fz}\ell_F\cos\theta - \Sigma f_{Rx}\big(h+z\big) - \Sigma f_{Fx}\big(h+z\big) \tag{4.13}$$

where, m is the vehicle mass (equal to the suspended mass after neglecting the wheel's mass), I_y is the moment of inertia of the vehicle about the center of gravity and the y body axis. By h we denote the vertical distance of the C.G. from the ground in an equilibrium state where $z = 0$. By $f_{iz}\ \ i = F, R$ we denote the normal load forces at the front and rear axle respectively and by $\Sigma f_{ix}\ \ i = F, R$ we denote the projection of the total friction force of each wheel on the x longitudinal body axis.

$$\Sigma f_{Rx} = f_{Rx} \quad \text{and} \quad \Sigma f_{Fx} = f_{Fx}\cos\delta - f_{Fy}\sin\delta \tag{4.14}$$

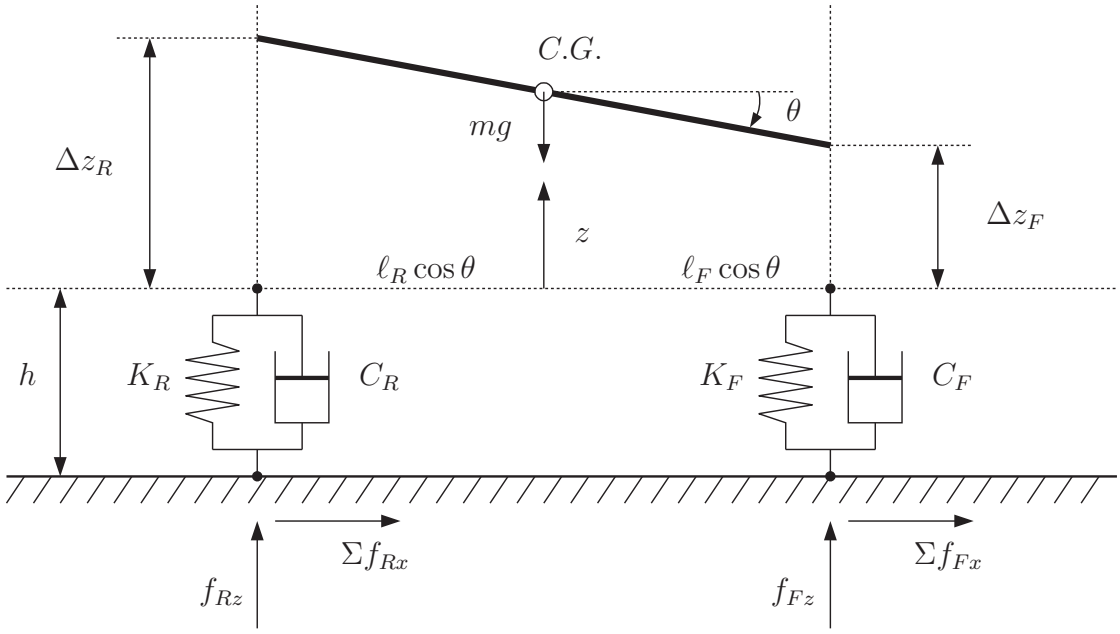

Figure 4.2: *Suspension Dynamics*

Consider now the equilibrium state ($\dot{z},\ \ddot{z},\ \dot{\theta},\ \ddot{\theta} = 0$) where $z = 0$ and $\theta = 0$. The normal load at each wheel is then the static distribution of the suspended weight to the front and rear axles, which depends on the longitudinal offset of the C.G. In particular we have that

$$f_{Fz}^o = mg\frac{\ell_R}{\ell_F + \ell_R} \tag{4.15}$$

$$f_{Rz}^o = mg\frac{\ell_F}{\ell_F + \ell_R} \tag{4.16}$$

Now, given vertical displacement of the C.G. z and pitch angle θ the normal load of each wheel is given by

$$f_{Fz} = f_{Fz}^o - K_F\Delta z_F - C_F\dot{\Delta z}_F \tag{4.17}$$

$$f_{Rz} = f_{Rz}^o - K_R\Delta z_R - C_R\dot{\Delta z}_R \tag{4.18}$$

where

$$\Delta z_R = z + \ell_R \sin\theta \ ,\ \Delta z_F = z - \ell_F \sin\theta$$

$$\dot{\Delta z}_R = \dot{z} + \ell_R \cos\theta\ \dot{\theta} \ ,\ \dot{\Delta z}_F = \dot{z} - \ell_F \cos\theta\ \dot{\theta}$$

Unless stated otherwise, the vehicle parameters that we use in this chapter are summarized in Table 4.1.

Table 4.1: *Vehicle Parameters.*

Parameter	**Value**
m (kgr)	650
I_z (kgr m^2)	1000
ℓ_F (m)	1.5
ℓ_R (m)	1.0
r (m)	0.3
$I_{F,R}$ (kgr m^2)	8
$K_{F,R}$ (N/m)	20000
$C_{F,R}$ (N sec/m)	1700
B	7
C	1.6
D	0.7

4.1.4 Reduced Order Half-Car Model

In order to simplify the calculations during the optimization we make some simplifying assumptions which lead to a model of reduced order. The system as presented in equations (4.1)-(4.5), (4.12) and (4.13) has T_F, T_R and δ as inputs. At this point we make the assumption that we can control the longitudinal slip at each wheel s_{Fx} and s_{Rx} directly. The equations of the system in this case will be

$$m\ddot{x} = f_{Fx}\cos(\psi+\delta) - f_{Fy}\sin(\psi+\delta) + f_{Rx}\cos\psi - f_{Ry}\sin\psi \tag{4.19}$$

$$m\ddot{y} = f_{Fx}\sin(\psi+\delta) + f_{Fy}\cos(\psi+\delta) + f_{Rx}\sin\psi + f_{Ry}\cos\psi \tag{4.20}$$

$$I_z\ddot{\psi} = (f_{Fy}\cos\delta + f_{Fx}\sin\delta)\,\ell_F - f_{Ry}\ell_R \tag{4.21}$$

The inputs of the system are now the longitudinal slip s_{Fx} and s_{Rx} of the front and rear wheel respectively and the steering angle δ of the front wheel. We may still

calculate the "real" inputs T_F and T_R using the definition (2.1) in order to find the angular velocity of each wheel from the known inputs s_{Fx} and s_{Rx}. Differentiating and using equations (4.4) and (4.5) we can then calculate the required torques. We would normally consider coupling between the front and rear wheel accelerating or braking torque (since in a car one pedal controls acceleration of all four wheels; the same for braking) which would result in coupling of the longitudinal slip quantities in the front and rear wheels. Since we are considering race car handling, where brakes and accelerator are sometimes used simultaneously as well as handbrake (which usually apply only on the rear wheels) we can assume that the longitudinal slip of the front and rear wheels can be controlled independently. The order of the model may be further reduced if we assume no dynamic longitudinal load transfer, i.e. f_{Fz} and f_{Rz} are given by (4.15) and (4.16) respectively at all times.

4.2 Optimal Control Formulation

In this section we formulate the problem of minimum time or maximum velocity maneuvering of a vehicle as a problem in optimal control. The system's dynamics are derived in the previous sections and given either by (4.1)-(4.5), (4.12) and (4.13) or by (4.19)-(4.21) depending on the desired level of fidelity of the vehicle model and the acceptable level of complexity of the problem. In order to formulate an optimal control problem, it is necessary to define the cost function to be optimized and specify all state/control constraints and boundary conditions.

In this work we present preliminary optimization results, using the reduced order model of Section 4.1.4, for three different paths: a 90 deg corner, a U-turn and an S-turn (similar to lane change maneuver) that the vehicle has to negotiate in minimum time. The constraint in each case is on the position of the C.G. of the vehicle; this is demonstrated in Figs. 4.3, 4.4 and 4.5. The origin of the frame of reference is located at the center of the corner for the 90 deg corner and the U-turn, while for the S-turn the origin is located at the mid-point of the road segment into consideration.

After gaining experience with the simplified model, we are able to generate initial

guesses that lead to convergence of the optimization algorithm using the comprehensive vehicle model of Sections 4.1.2, 4.1.3. We present a case study, comparing minimum time versus maximum exit velocity cornering strategies.

The cost function for the minimum travel time problem is given by

$$J = \int_o^{t_f} \mathrm{d}t, \tag{4.22}$$

while for the maximum exit velocity problem the cost function is given by

$$J = -\sqrt{\dot{x}_f^2 + \dot{y}_f^2}. \tag{4.23}$$

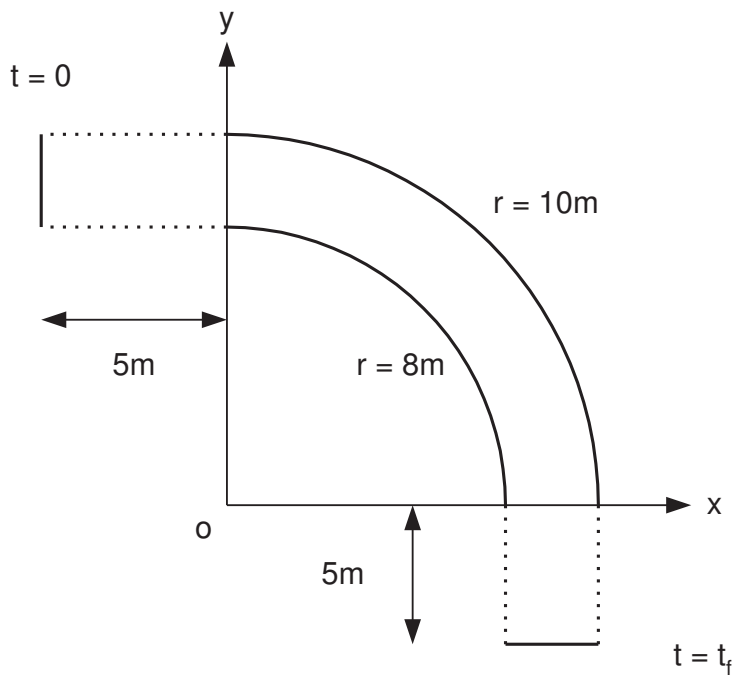

Figure 4.3: *State constraint for the* 90 deg *corner*

4.2.1 State Constraints

The state constraint for the 90 deg corner is shown in Fig. 4.3 and can be mathematically described as follows

$$8 \leq \sqrt{x^2 + y^2} \leq 10 \quad \text{when} \quad x \geq 0 \quad \text{and} \quad y \geq 0 \tag{4.24}$$

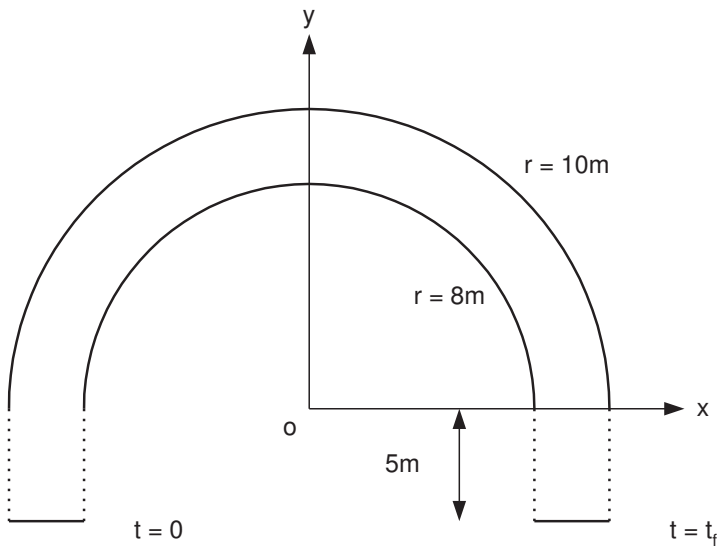

Figure 4.4: *State constraint for the U-turn*

The state constraint for the U-turn is shown in Fig. 4.4 and can be described as follows

$$8 \leq \sqrt{x^2 + y^2} \leq 10 \quad \text{when} \;\; y \geq 0 \tag{4.25}$$

The state constraint for the S-turn is shown in Fig. 4.5 and can be described as follows

$$\begin{aligned} 8 \leq \sqrt{(x+9)^2 + y^2} \leq 10 \quad & \text{when} \;\; x < 0 \;\; \text{and} \;\; y < 0 \\ 8 \leq \sqrt{(x-9)^2 + y^2} \leq 10 \quad & \text{when} \;\; x \geq 0 \;\; \text{and} \;\; y \geq 0 \end{aligned} \tag{4.26}$$

In all cases we have added two straight segments of 5m each before and after the corner so that the car enters the corner after travelling straight and exits the corner in a posture that will lead to straight travel again. The boundaries of the road at the straight segments are not included in the state constraint. However, the boundary conditions as we will see in the next section, take into account the width of the road as well.

4.2.2 Boundary Conditions

The boundary conditions are summarized in Table 4.2. These conditions guarantee

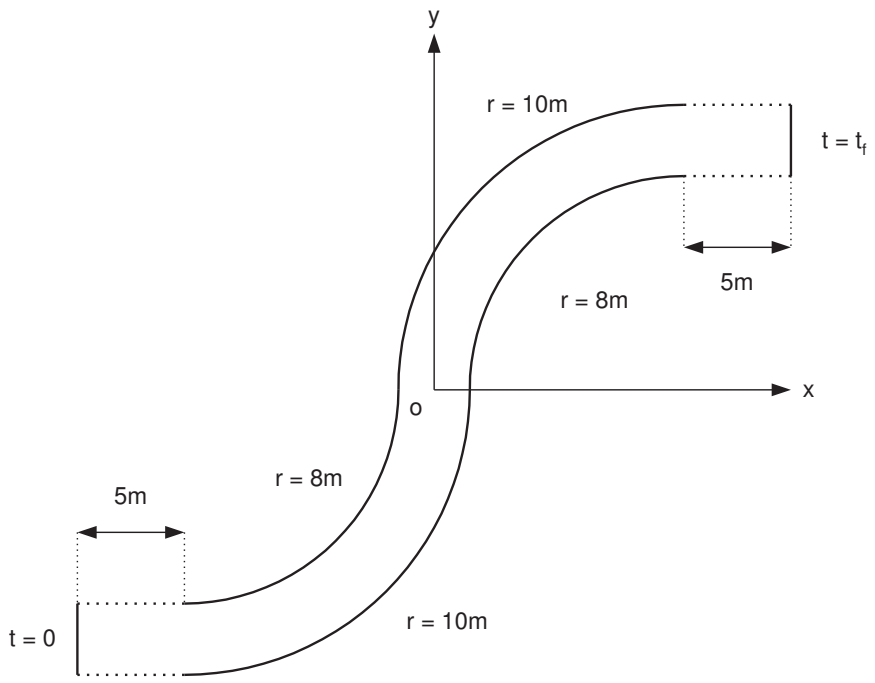

Figure 4.5: *State constraint for the S-turn*

that the car is travelling straight before and after the corner. The initial and final position of the car is within the width of the road. Finally, the longitudinal velocities at the initial and final time and the final time t_f are left free.

Using the comprehensive half-car model (4.1)-(4.5), (4.12) and (4.13) we may need to simplify somehow the problem in order to achieve convergence of the optimization algorithm. This may be done by "fixing" some of the "free" boundary conditions. For example, we may choose fixed value for the initial longitudinal velocity. The value may be taken from the solution using the low order system reduced by a safety factor. It also makes sense to "fix" the initial conditions for vertical position/velocity (z, $\dot{z}$) and pitch angle/rate (θ, $\dot{\theta}$) of the suspended mass. The natural choice would be to consider an initial steady-state where $z = \dot{z} = \theta = \dot{\theta} = 0$.

Table 4.2: *Boundary Conditions*

90 deg corner	U-turn	S-turn
$x(t=0)=-5$	$-10 \leq x(t=0) \leq -8$	$x(t=0)=-14$
$8 \leq y(t=0) \leq 10$	$y(t=0)=-5$	$-10 \leq y(t=0) \leq -8$
$8 \leq x(t=t_f) \leq 10$	$8 \leq x(t=t_f) \leq 10$	$x(t=t_f)=14$
$y(t=t_f)=-5$	$y(t=t_f)=-5$	$8 \leq y(t=t_f) \leq 10$
$\psi(t=0)=0$	$\psi(t=0)=\frac{\pi}{2}$	$\psi(t=0)=0$
$\dot{\psi}(t=0)=0$	$\dot{\psi}(t=0)=0$	$\dot{\psi}(t=0)=0$
$\psi(t=t_f)=-\frac{\pi}{2}$	$\psi(t=t_f)=-\frac{\pi}{2}$	$\psi(t=t_f)=0$
$\dot{\psi}(t=t_f)=0$	$\dot{\psi}(t=t_f)=0$	$\dot{\psi}(t=t_f)=0$
$\dot{y}(t=0)=0$	$\dot{x}(t=0)=0$	$\dot{y}(t=0)=0$
$\dot{x}(t=t_f)=0$	$\dot{x}(t=t_f)=0$	$\dot{y}(t=t_f)=0$

4.2.3 Control Constraints

Recall that, in the case of the low order half car model of Section 4.1.4, the control inputs are the longitudinal slip s_{Fx} and s_{Rx} of each wheel and the steering angle δ. The control constraints (same in all optimization scenarios) are

$$-1 \leq s_{ix} \leq 1, \quad i = F, R \tag{4.27}$$

$$-0.7 \text{ rad} \leq \delta \leq 0.7 \text{ rad} \tag{4.28}$$

The constraint on the longitudinal slip is imposed by the definition of equation (2.1), while in the case of the steering angle, the constraint reflects the physical limits of the steering mechanism.

In the case of the comprehensive half car model of Sections 4.1.2, 4.1.3 the control inputs are the accelerating/braking torques T_F and T_R of each axle and the steering angle δ. The control constraints are

$$-1000 \text{ Nm} \leq T_i \leq 1000 \text{ Nm}, \quad i = F, R \tag{4.29}$$

$$-0.7 \text{ rad} \leq \delta \leq 0.7 \text{ rad} \tag{4.30}$$

The constraints on the accelerating/braking torques reflect the limited power that

may be provided by the engine/transmission and braking systems.

4.2.4 Optimization Algorithm

The optimal control problem is solved numerically using EZOPT, a direct optimization software available by Analytical Mechanics Associates Inc., which uses collocation to transcribe an optimal control problem to a nonlinear programming problem (NLP). It provides a gateway to NPSOL, a nonlinear optimization program (for details see [77]). The optimization algorithm involves discretization of the independent variable (time). The control inputs are approximated with constant functions for each time interval. The user is required to provide the system's dynamics, the cost to be optimized, state constraints, boundary conditions and an initial guess for the optimal control inputs and states time history (Fig. 4.6). The convergence of the algorithm depends on the complexity of the problem and the accuracy of the initial guess.

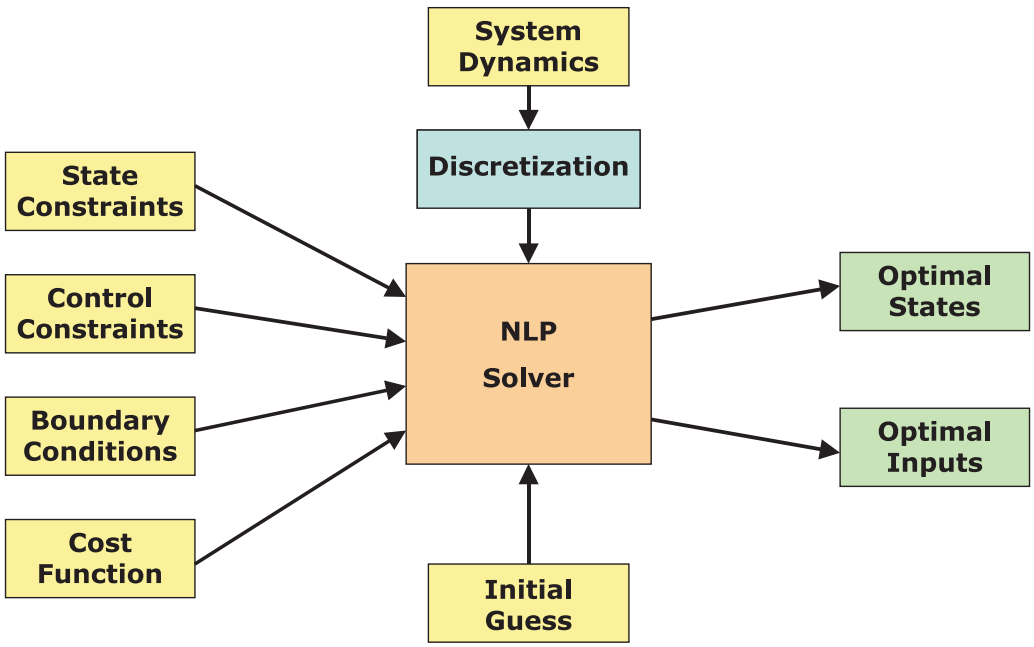

Figure 4.6: *Numerical optimization scheme.*

We have chosen time to be the independent variable resulting in an optimal control problem of free "final time". In [67], [68] and [69] time is replaced by travelled distance as the independent variable resulting in a fixed "final time" optimal control problem,

which is easier to converge numerically to a solution. However this change of variable results in a singularity when the vehicle travels with large slip angles. While such a scenario is never encountered in F1 racing, it is very common in rally-racing where drivers often drift through corners at large slip angles. This justifies the choice of the independent variable in this work.

4.3 Results Using the Low Order Half-Car Model

As already mentioned, convergence of the optimization algorithm depends on the accuracy of the initial guess and the complexity of the problem, including the order of the associated dynamical system. In order to gain experience with this optimization scheme as well as insight on the vehicle dynamics we pursue preliminary results using the simplified half-car vehicle model of Section 4.1.4. In what follows we present the solutions to the minimum time problem along the paths of Figures 4.3, 4.4 and 4.5.

4.3.1 90 deg Corner

Figures 4.7-4.12 completely describe the optimal solution for the minimum time problem along the 90 deg corner. Figure 4.7 shows the time histories of the vehicle's states except from the cartesian coordinates of the C.G. The later can be seen in Fig. 4.11. Figure 4.8 shows the optimal control inputs (longitudinal slip of front and rear axle and steering angle). In Figure 4.9 we can see the development of tire friction in front and rear axles with respect to time. The friction forces plots appear highly non-smooth. Recall that the friction forces are calculated as a static map of the discretized control inputs. Figure 4.10 again shows the friction forces of the tires, only this time on the longitudinal-lateral friction plane. The dotted circle corresponds to the friction circle according to the discussion in Section 2.1. Figure 4.12 finally shows the vehicle's trajectory radius and the vehicle speed with respect to time. The radius of trajectory is calculated using the formula for the centripetal force, $F_c = mv^2/R$ and appears non-smooth due to the discretized states and control involved in the calculation.

Trajectory

The trajectory (Fig. 4.11) for $0.5\,\text{sec} \leq t \leq 1.8\,\text{sec}$ is approximately of constant radius (Fig. 4.12) and the vehicles motion is close to a steady-state turn, as defined in [22] and [2], that is constant speed and yaw rate. There are two transient parts in the trajectory ($t \leq 0.5\,\text{sec}$ and $1.8\,\text{sec} \leq t$), since the boundary conditions enforce that the vehicle enters and exits the corner travelling straight. The bigger the radius of the trajectory the higher is the velocity that the vehicle can drive through the corner for a given maximum centrifugal force (determined by the tire friction limits).

However, observing Fig. 4.7 we notice that the vehicle does *not* enter or exit the corner at the limit of the state constraint. This means that there may exist a possible trajectory of bigger radius. This trajectory would allow the car to drive through the corner with higher speed, but the distance travelled would also be greater. Such a trajectory will not necessarily minimize time.

In conclusion, the optimal trajectory in the case of time minimization approaches a circular arc with such a radius that compromises between the highest possible travel speed and the shortest distance travelled. In fact there exists a distinct minimum in the trajectory radius around 1.5 sec. The vehicle decelerates before and accelerates after this point (Fig. 4.12).

Control History and Response

Figure 4.8 shows the control input history. We observe that the steering angle δ has an initial negative value. This creates immediately a lateral slip on the front wheel which generates lateral friction (see Fig. 4.9). This initial lateral friction serves two purposes. The first is that it operates as a centrifugal force for the vehicle and the second is that it initiates the yawing motion of the car. This yawing motion results to a lateral motion of the rear wheel of the vehicle; thus, a lateral slip and lateral friction (which contributes to the total centripetal force) is also generated at the rear wheel. We observe that the steering angle is gradually being reduced and actually at around 2 sec changes its sign ("opposite lock"). This is done in order to damp

the yawing motion and eventually eliminate it by the time the car exits the corner. We observe that there is some overshoot about the desired final yaw angle and the steering angle changes its sign again at the end.

We observe that the longitudinal slip of the rear wheel is initially ($t < 0.5$ sec) such that a braking friction force is generated in order to regulate the speed of the car to a limit that makes it possible for the car to follow the optimal trajectory. Recall that the trajectory begins from a straight line and gradually increases its curvature and thus the maximum velocity possible through the trajectory is decreasing. The longitudinal slip of the front wheel generates an accelerating friction force which compensates for the braking component of the front wheel lateral friction force. The situation where the front wheel is accelerating while the rear wheel is braking resembles the use of handbrake simultaneously with throttle by expert race drivers of off-road vehicles.

Notice from Fig. 4.9 that the total friction generated by the front tire is equal to the tire's force capacity. In case the front tire is not saturated by lateral force, an accelerating longitudinal force is generated to take advantage of the total force capacity of the tire. As far as the friction generated by the rear tire, observing Fig. 4.9 and Fig. 4.10 we notice that it is also most of the times equal to its maximum. Nonetheless, we observe that friction of the rear tire is not maximum at $t \geq 2.25$ sec. One would expect that since the car is at the exit of the corner there should be maximum acceleration. However, at this point in time the front wheel is saturated with lateral friction in order to stop the yawing motion. More acceleration (which *is* available since the driven rear tire is not saturated) would require more effort from the front tire to stop the yawing motion; such an effort in this case is *not* available, however.

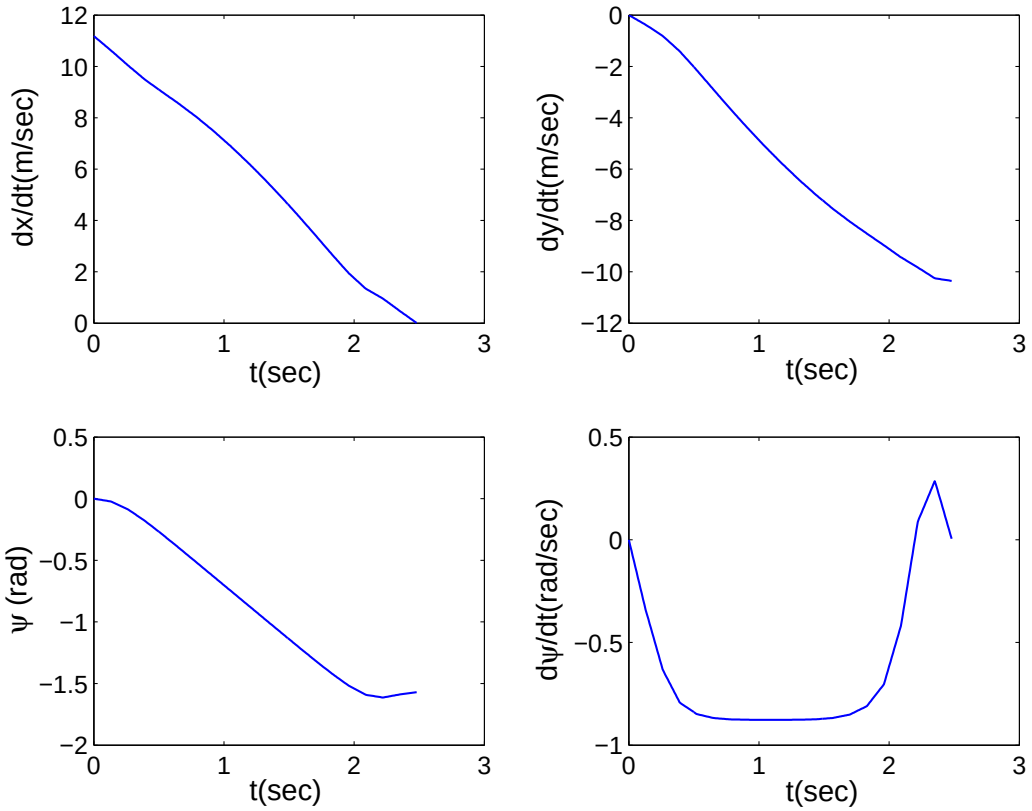

Figure 4.7: 90 deg *corner, minimum time, states*

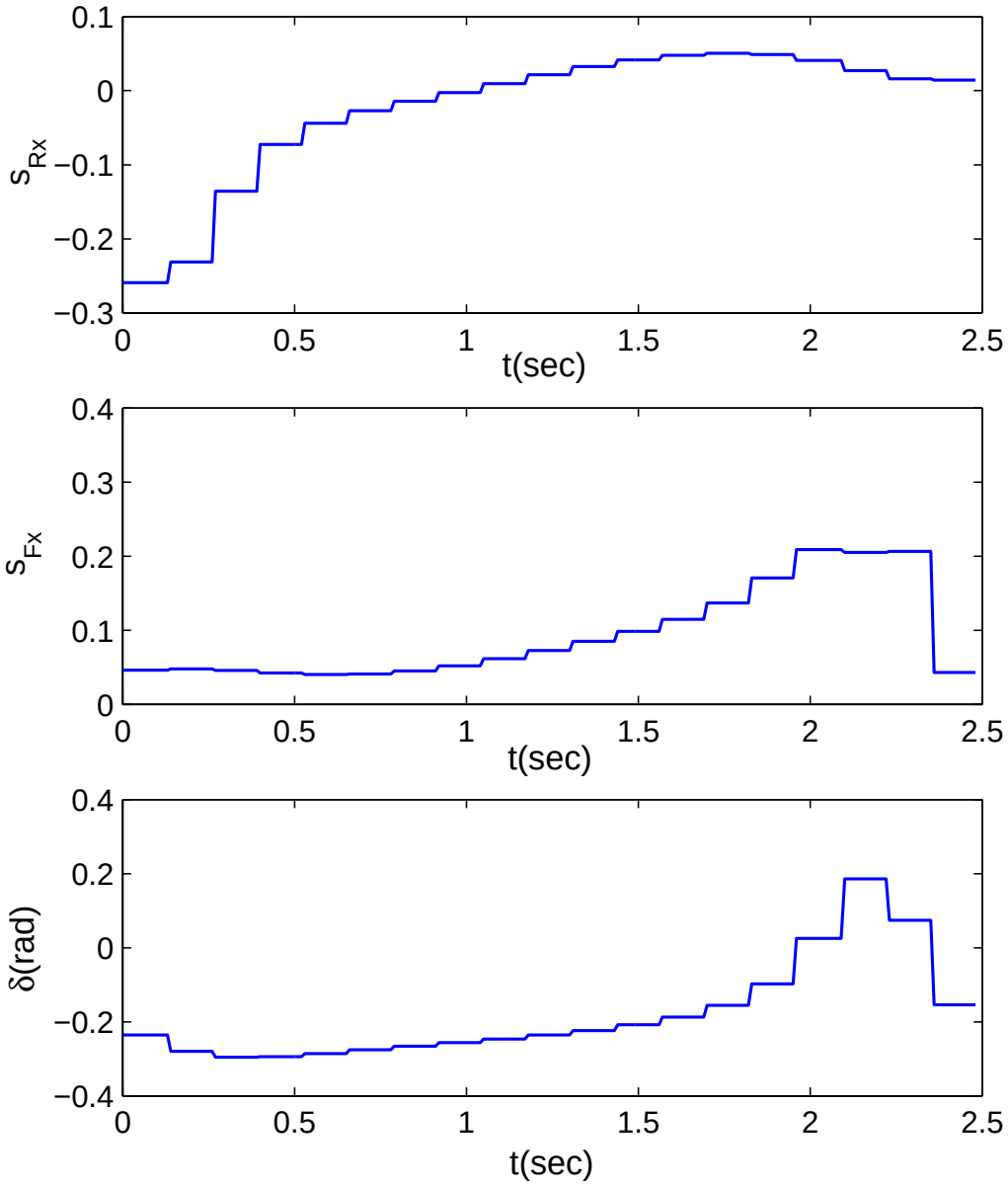

Figure 4.8: 90 deg *corner*, *minimum time*, *control*

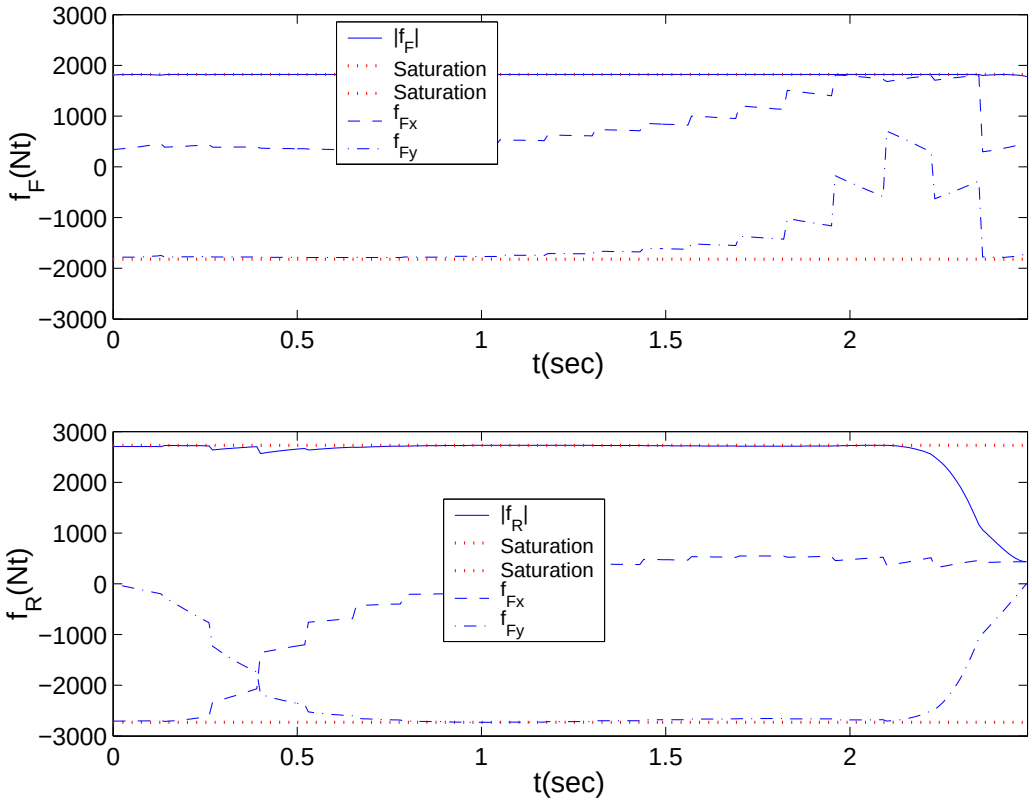

Figure 4.9: 90 deg *corner, minimum time, friction*

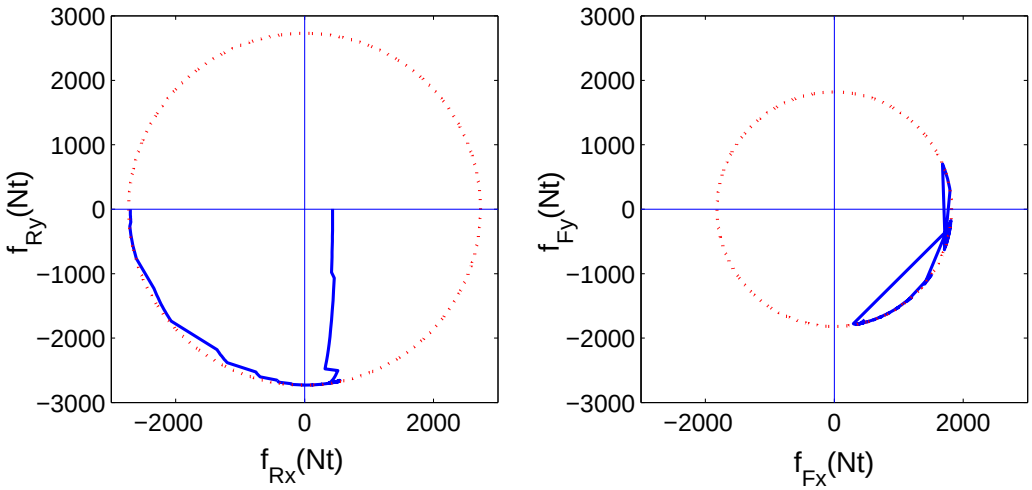

Figure 4.10: 90 deg *corner, minimum time, friction-circle*

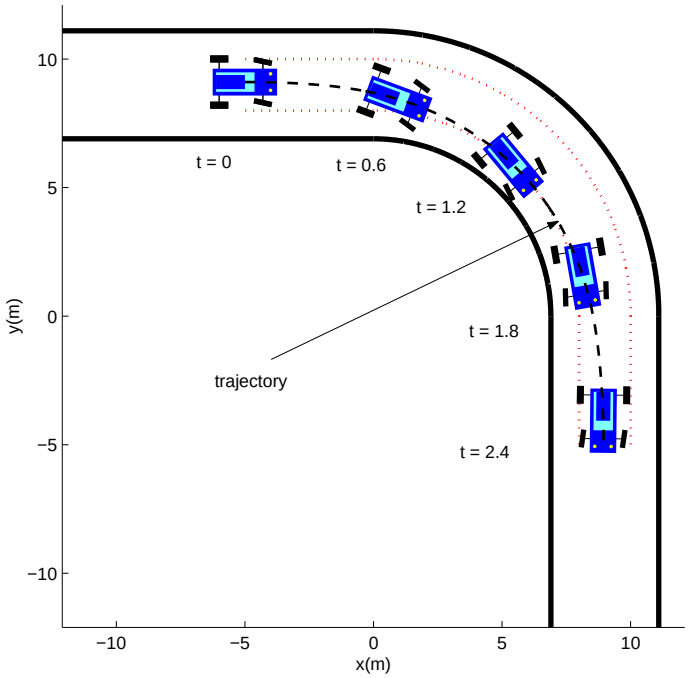

Figure 4.11: 90 deg *corner, minimum time, trajectory*

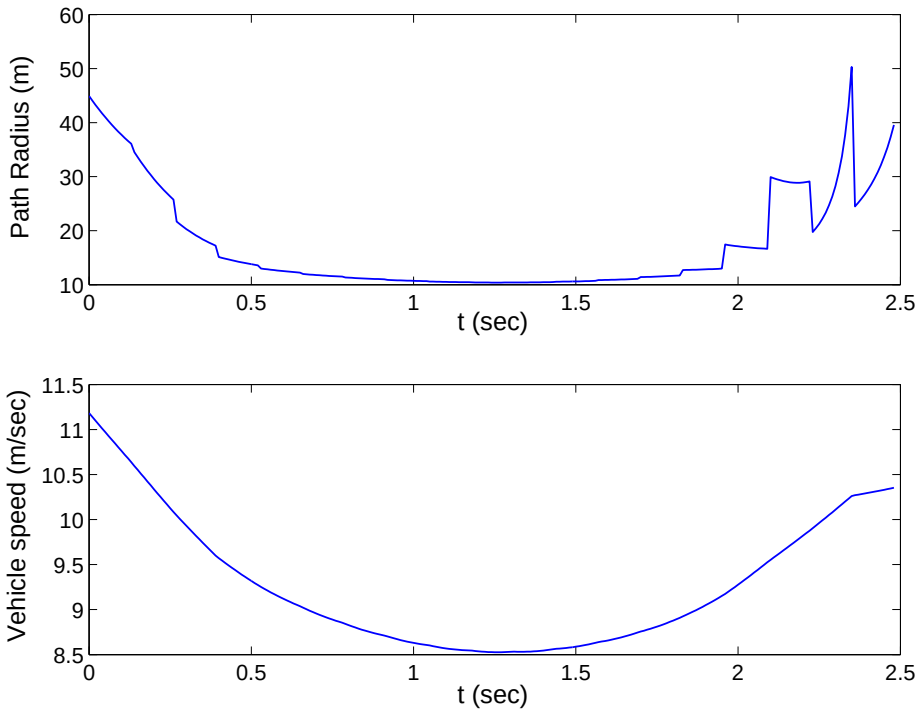

Figure 4.12: 90 deg *corner, minimum time, path radius and vehicle speed*

4.3.2 U-turn

Figures 4.13-4.18 completely describe the optimal solution for the minimum time problem along the U-turn (or 180 deg corner, or "hairpin" turn). The generated optimal states and controls are completely equivalent to those of the 90 deg corner solution.

Trajectory

The trajectory approaches a circular arc which coincides with the inner road edge in the middle of the corner ($0.5\,\text{sec} \leq t \leq 3.5\,\text{sec}$). As expected the steady-state part of the trajectory (approximately constant trajectory radius, vehicle speed and yaw rate) is longer compared to the 90 deg corner. Here too, we observe two transient parts at the beginning and at the end of the corner such that the boundary conditions are satisfied. The radius of the trajectory segments is again a compromise between minimal travel distance and maximum travel velocity. There exists a distinct minimum in the trajectory radius at around 2.25 sec. The vehicle decelerates before this point and accelerates right after (Fig. 4.18).

Control History and Response

The control inputs for the U-turn minimum time problem are also in accordance to the solution for the 90 deg corner. Once again we observe how the cornering maneuver is initiated by steering of the front wheels and how the rear wheels come into play (generate cornering force) as the yaw motion is developed. The tires of the front axle are saturated at all times with accelerating and cornering forces. The tires of the rear axle are also most of the times saturated with friction. Only at the end of the maneuver the rear tire does not generate accelerating friction since the front tire is working at its maximum capacity to stop the yawing motion with maximum lateral friction.

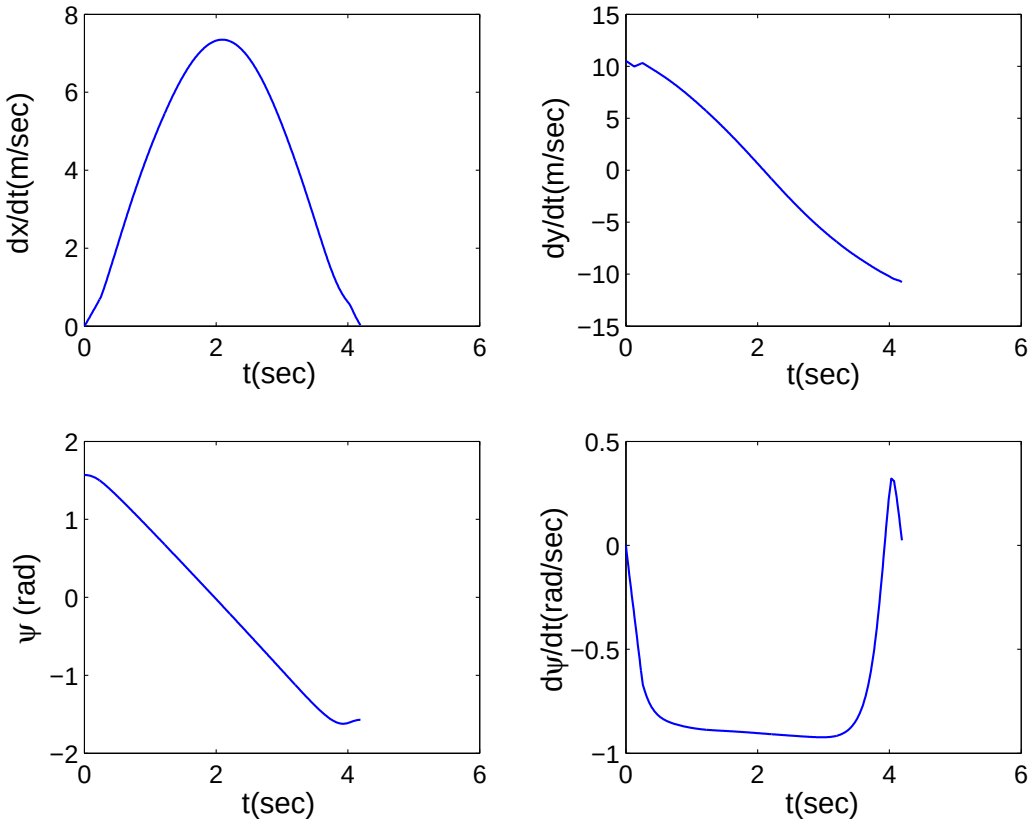

Figure 4.13: *U-turn, minimum time, states*

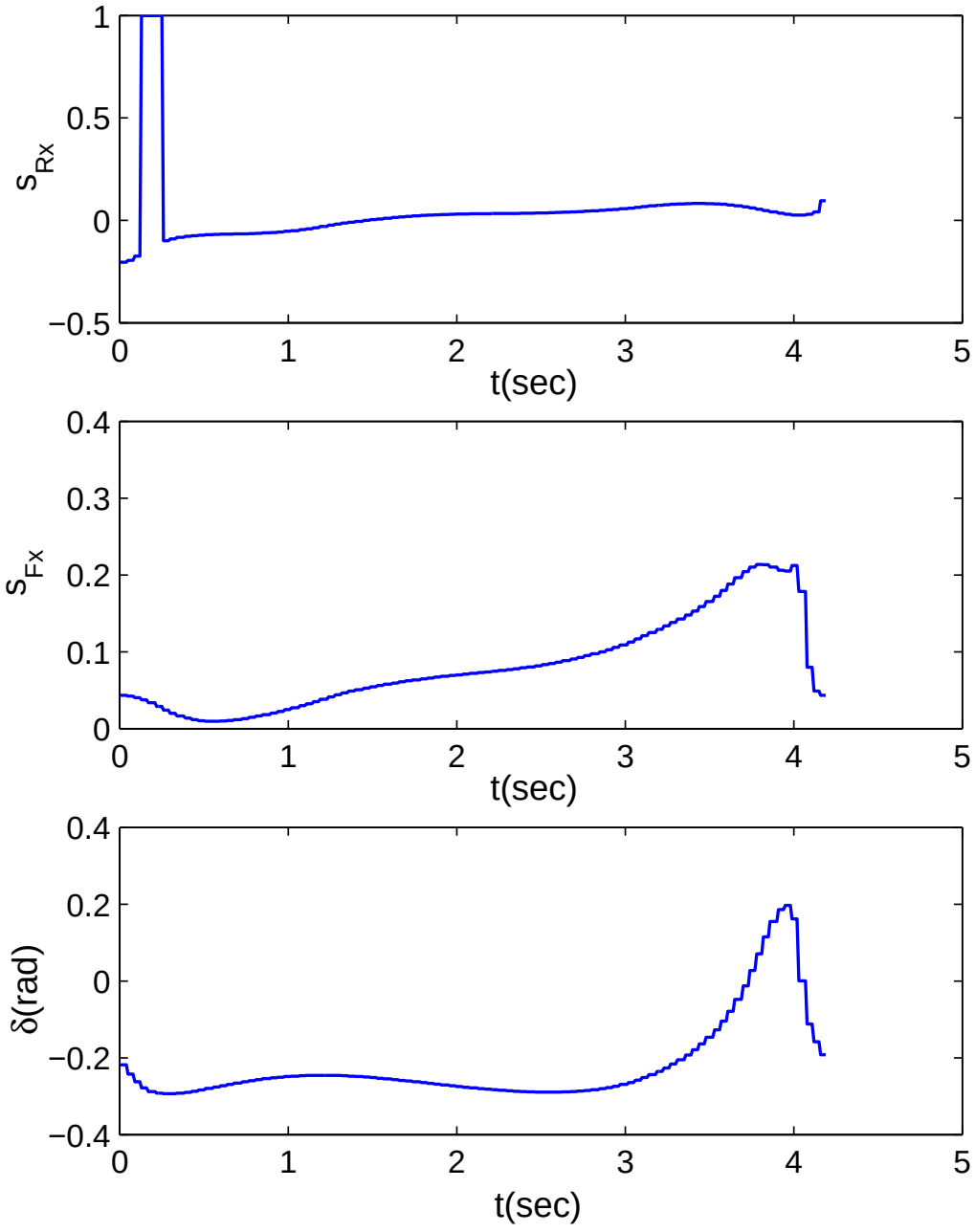

Figure 4.14: *U-turn, minimum time, control*

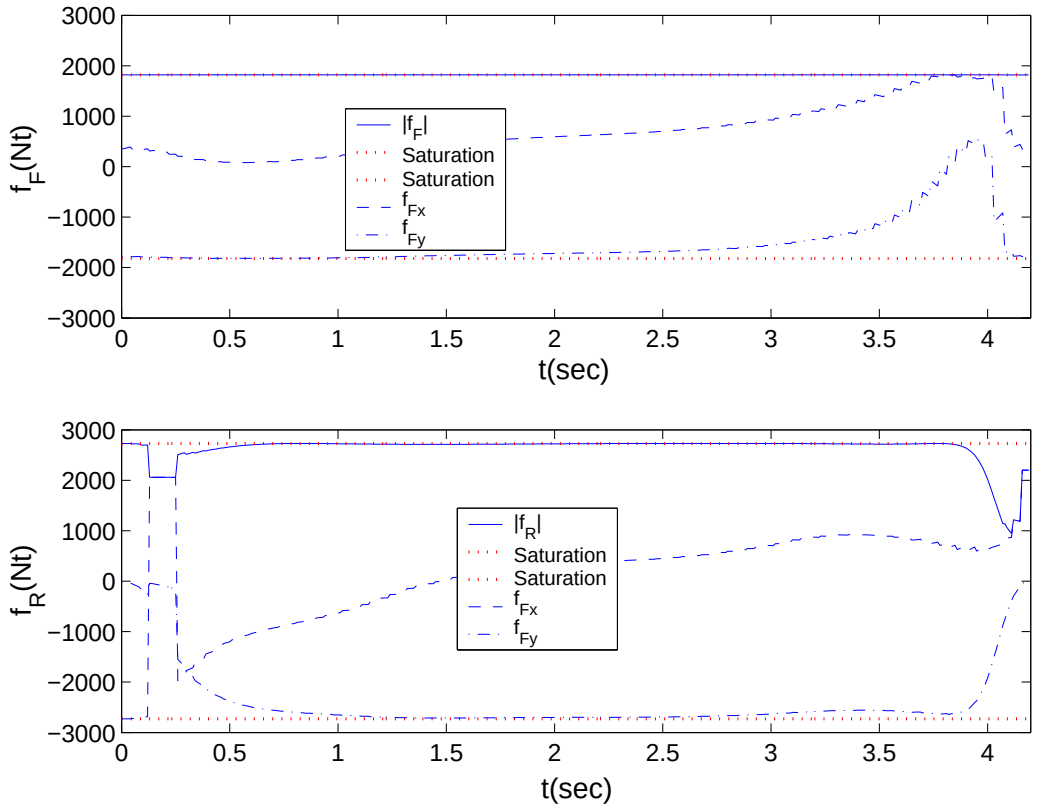

Figure 4.15: *U-turn, minimum time, friction*

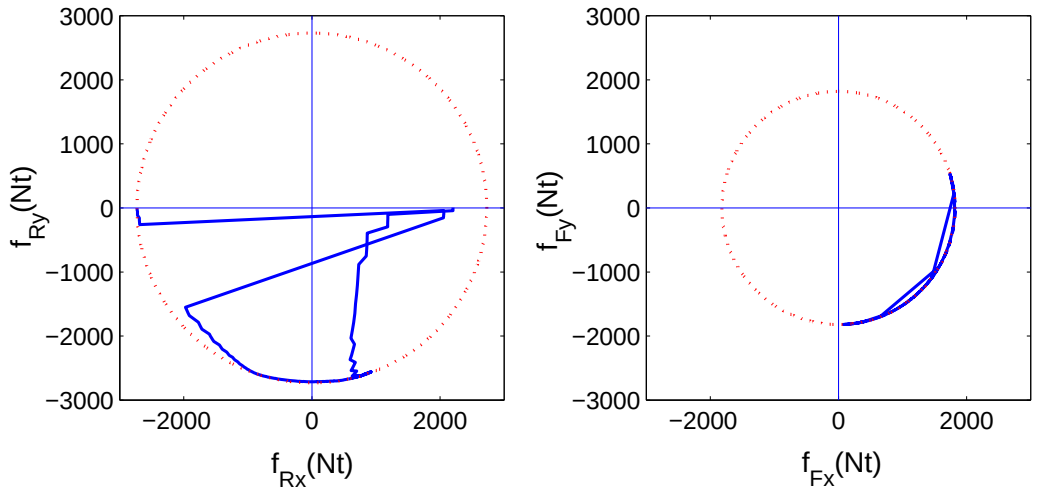

Figure 4.16: *U-turn, minimum time, friction-circle*

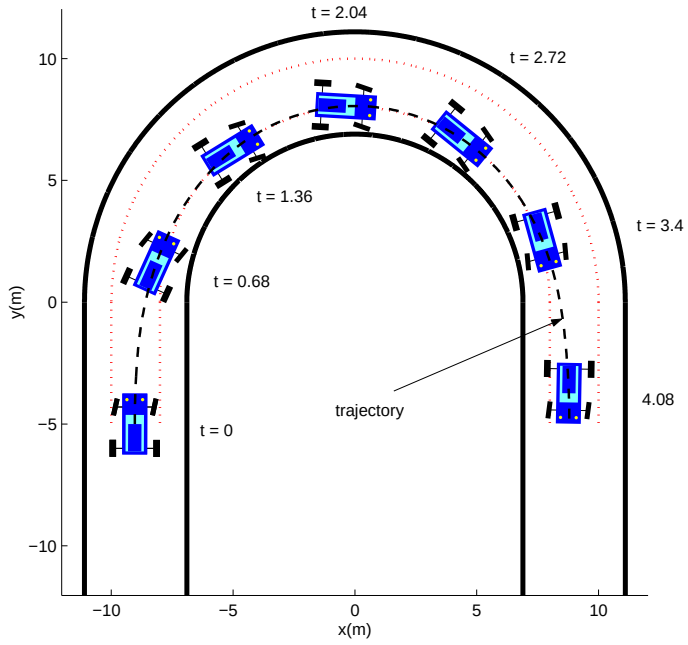

Figure 4.17: *U-turn, minimum time, trajectory*

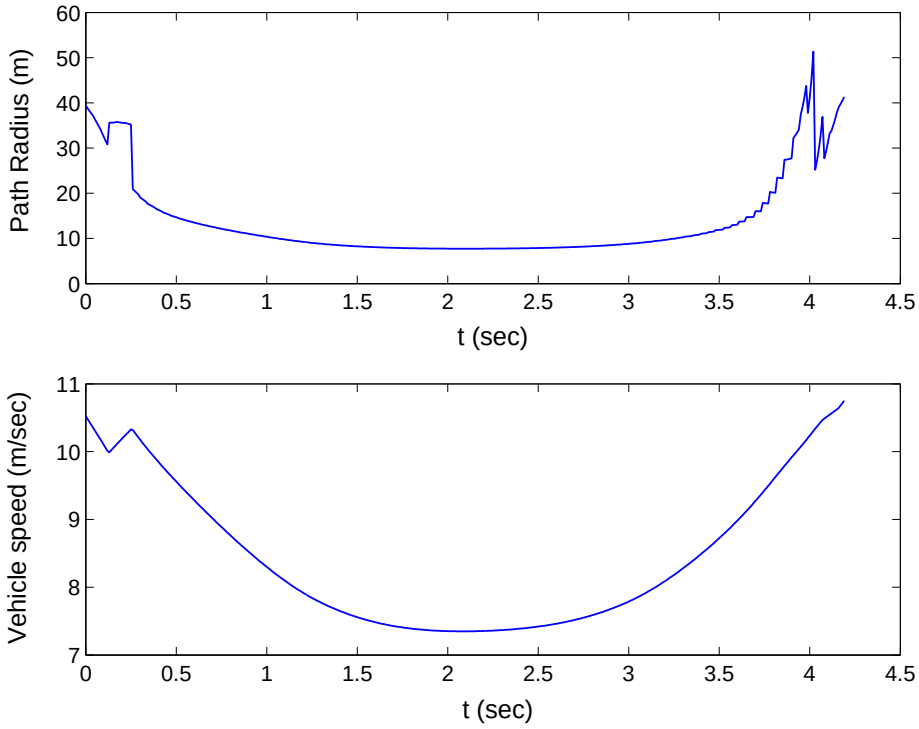

Figure 4.18: *U-turn, minimum time, path radius and vehicle speed*

4.3.3 S-turn

Figures 4.19-4.24 completely describe the optimal solution for the minimum time problem along the S-turn (lane change maneuver). The state constraint in this case consists of two consecutive 90 deg corners of opposite direction.

Trajectory

The trajectory consists of two segments approaching the steady-state cornering, corresponding to each one of the two consecutive 90 deg corners, for $0.5\,\text{sec} \leq t \leq 1.5\,\text{sec}$ and $2.25\,\text{sec} \leq t \leq 3.5\,\text{sec}$. We also observe the associated transient parts of the trajectory in accordance to the results of the optimization scenarios of Sections 4.3.1 and 4.3.2. Once again we may distinguish points of minimum radius at each one of the two steady-state cornering segments at $t = 1$ sec and $t = 3$ sec (Fig. 4.24). The vehicle decelerates before these points and accelerates right after. At $t = 2$ sec we may consider that the two trajectories (corresponding to each of the 90 deg corner) intersect.

Control History and Response

Once again we observe saturation of the tires with friction except from the transit from one direction of cornering to the other (around $t = 2$ sec), and the end of the maneuver as observed in the previous optimization scenarios. We may also observe "noisy" control inputs (front longitudinal slip and steering angle) for the second half of the maneuver at around 2.7 to 3 sec and a jump at the yaw rate of the vehicle. Similarly we observe "noisy" control inputs close to the end of negotiating the first corner at around 1.7 to 2 sec. The trajectory is well defined at the beginning and end due to the specified boundary conditions. Around the middle of the trajectory we have a large transient due to change of direction which results in these noisy control inputs before and after the transient. Such spikes could be avoided by selecting strict optimization tolerances which however makes the optimization algorithm too difficult to converge.

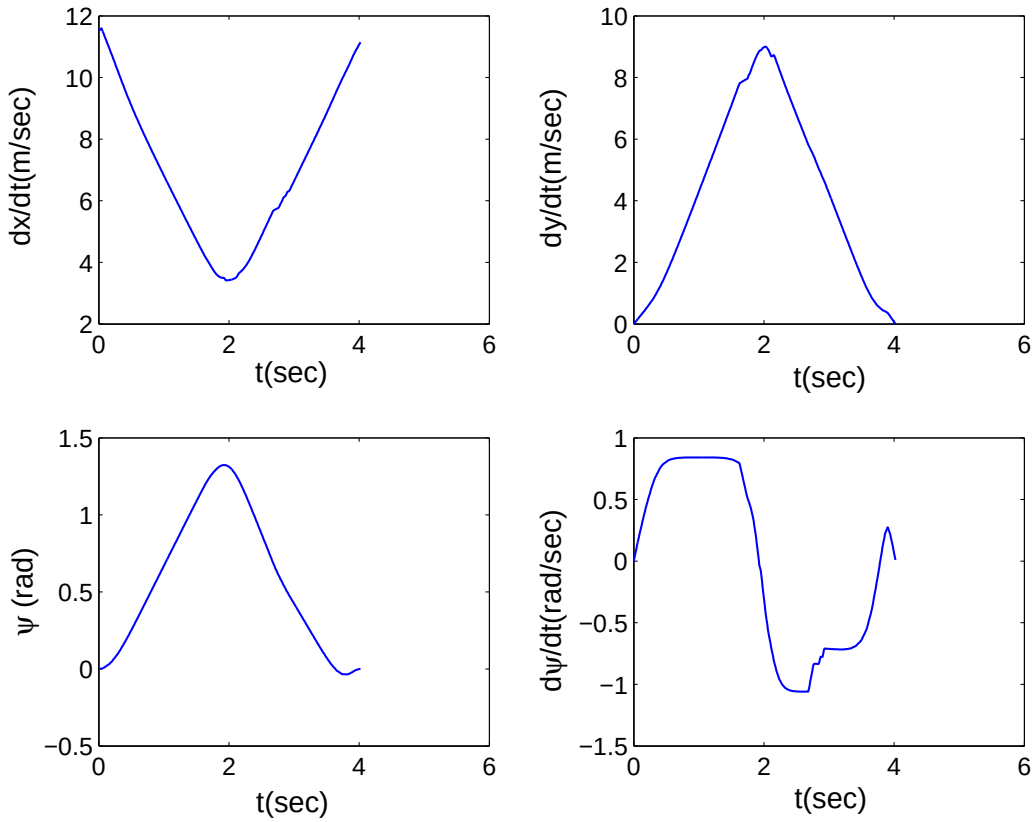

Figure 4.19: *S-turn, minimum time, states*

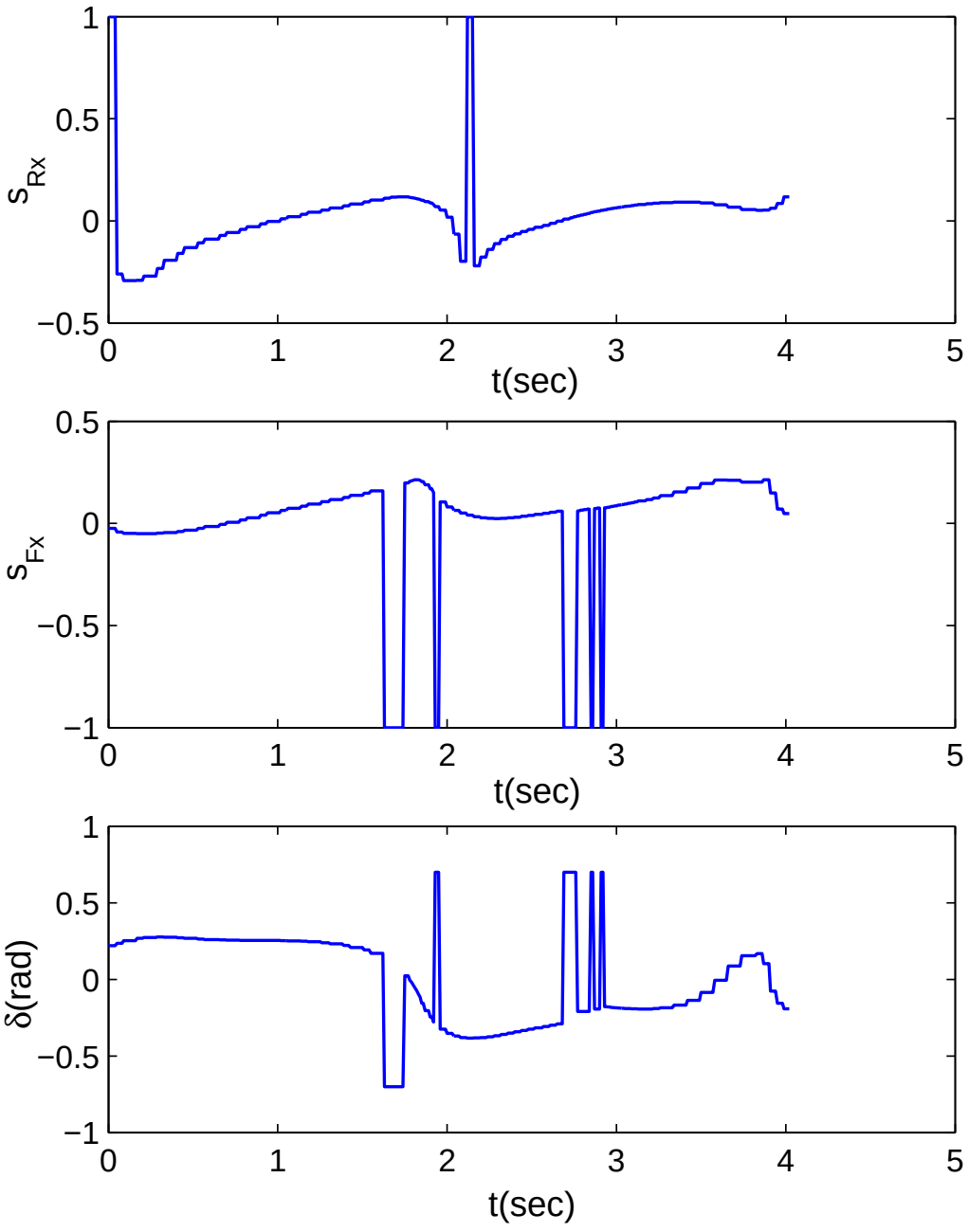

Figure 4.20: *S-turn, minimum time, control*

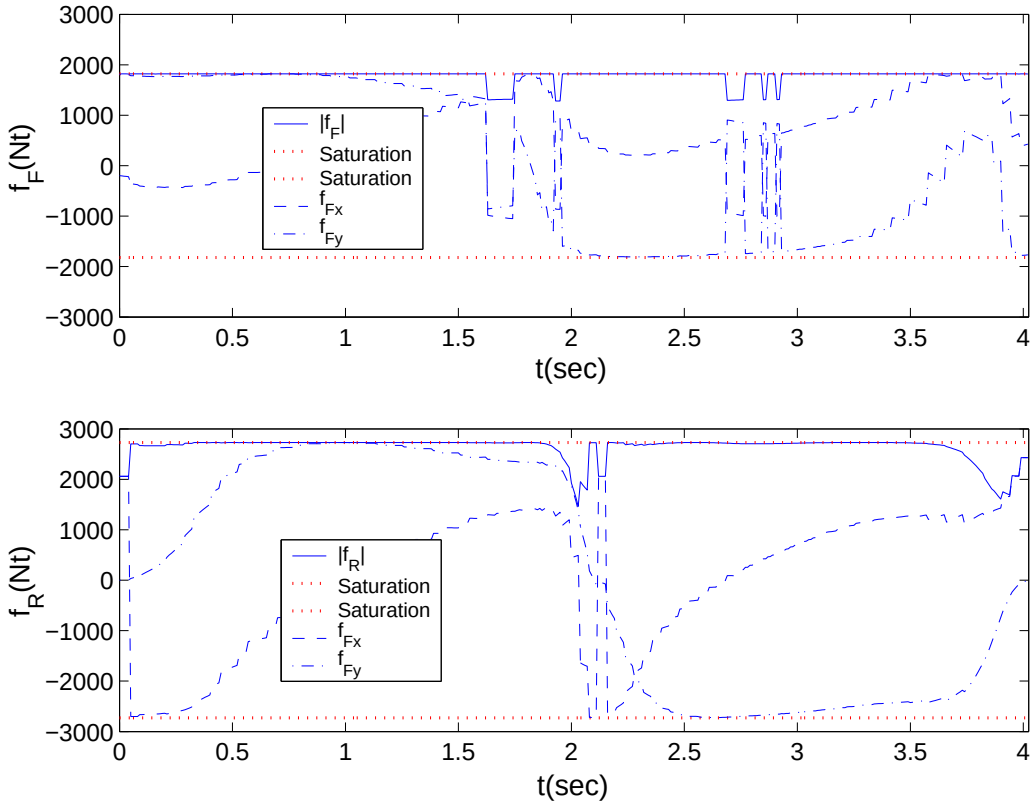

Figure 4.21: *S-turn, minimum time, friction*

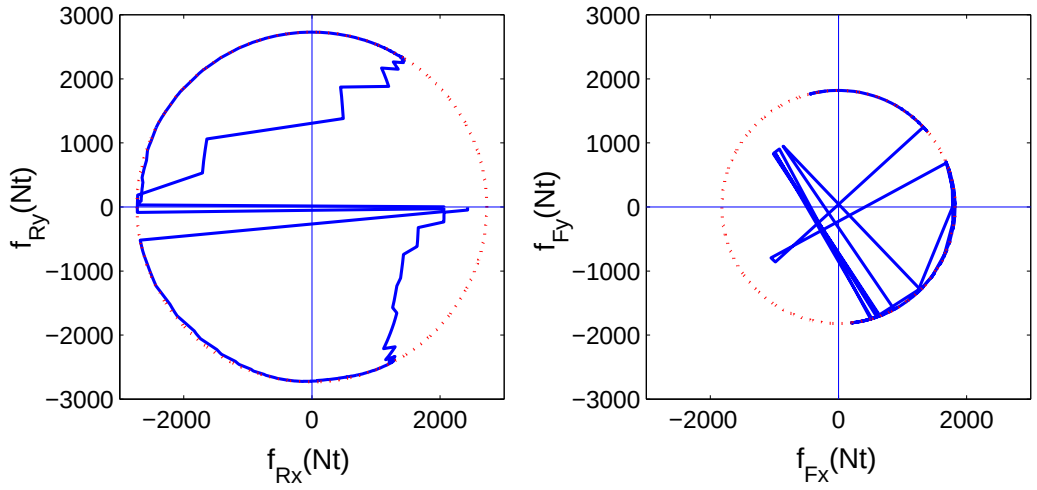

Figure 4.22: *S-turn, minimum time, friction-circle*

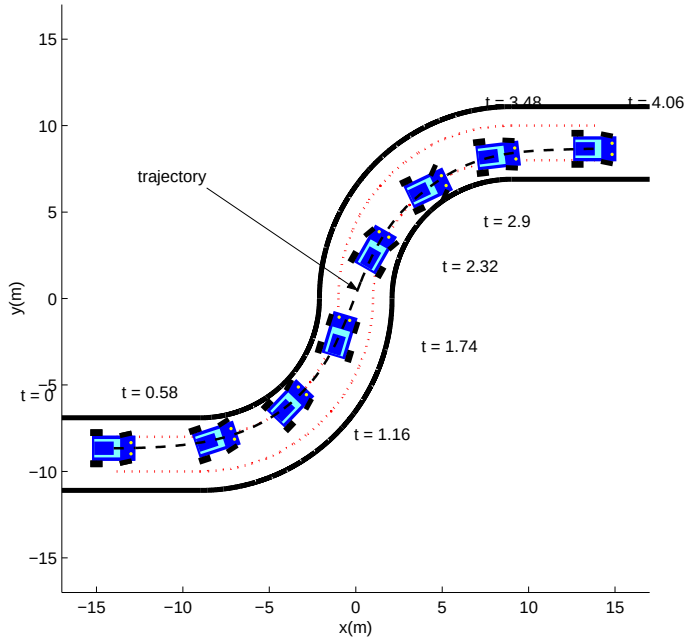

Figure 4.23: *S-turn, minimum time, trajectory*

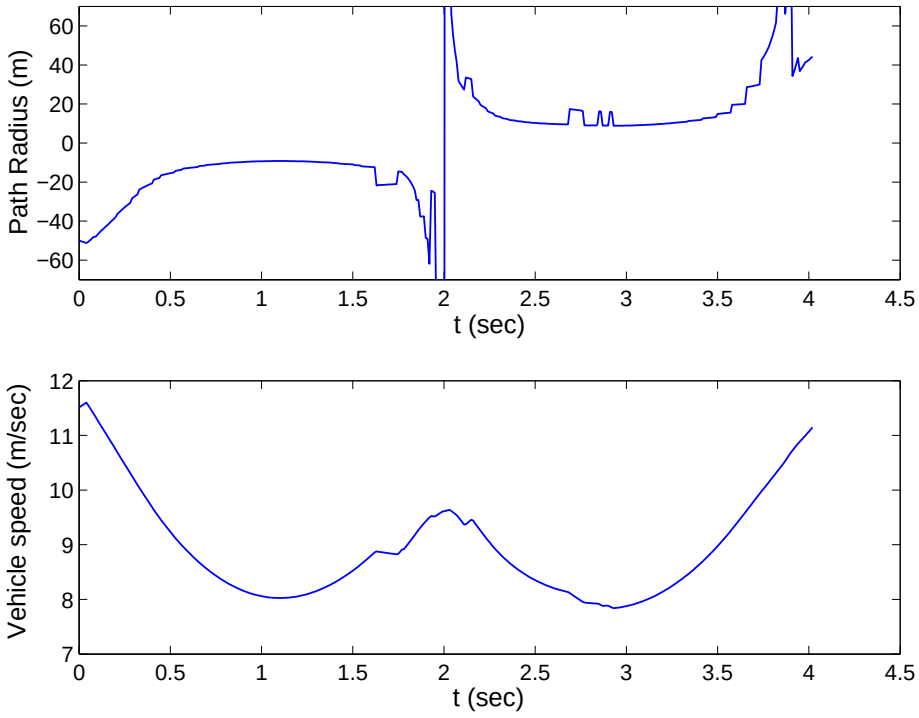

Figure 4.24: *S-turn, minimum time, path radius and vehicle speed*

Chapter 5

Minimum Time vs. Maximum Exit Velocity Cornering

In Section 4.3 we presented solutions to the time minimization problem along several paths using the simplified vehicle model of Section 4.1.4. Having gained experience in the optimization scheme and intuition on the basic vehicle dynamics we now pursue solutions to optimization problems incorporating the comprehensive half-car model (4.1)-(4.3), (4.12) and (4.13). We consider several optimization scenarios and compare different racing styles. At the same time we study the role of suspension dynamics and normal load transfer in limit operation of the vehicle.

In particular, we obtain the numerical solution (trajectory, states and control inputs) of the optimal cornering problem, along the 90 deg corner, for minimum time of travel and maximum exit velocity. Two extreme cases for the vertical position of the C.G. are taken into consideration ($h = 1\,\mathrm{m}$ and $h = 0\,\mathrm{m}$) for each case of the optimization cost in order to investigate the effects of the suspension dynamics and longitudinal load transfer. In the case $h = 0\,\mathrm{m}$ the suspension dynamics are not included in the overall vehicle dynamics and no load transfer occurs. In order to have a fair comparison between the $h = 0\,\mathrm{m}$ and $h = 1\,\mathrm{m}$ cases, we choose a fixed value for the vehicle's initial speed.

5.1 90 deg **Corner - Minimum Time**

Figures 5.1-5.8 completely describe the optimal solution for the minimum time problem along the 90 deg corner. Figures 5.1 and 5.2 show the time histories of the vehicle's states and Fig. 5.3 shows the optimal control inputs (front and rear axle torque and front steering angle). In Fig. 5.4 we show the normal load of each of the front and rear axles. In Fig. 5.5 we may find the time histories of the vehicle speed, the vehicle acceleration component along the vehicle longitudinal axis (that excites the suspension dynamics) and the trajectory radius with respect to time. In Figures 5.6 and 5.7 we have the development of the friction coefficients and friction forces respectively, at each of the front and rear axles. Finally, Fig. 5.8 shows snapshots of the vehicle along its trajectory.

5.1.1 Trajectory

The trajectory for the minimum time case through a 90 deg corner, as it can be seen in Figure 5.8 is in complete accordance to what we saw in Section 4.3.1 corresponding to the solution using the simplified low order half-car model. Once again, the trajectory consists of an approximately steady-state segment tangential to the state constraint, and two transient parts satisfying the prescribed boundary conditions. The vehicle decelerates until the point of minimum radius of its trajectory and accelerates right after. Recall that the radius of the trajectory is a compromise between the shortest distance to travel and the highest average speed through the corner. No significant differences can be observed between the trajectory with $h = 1\,\mathrm{m}$ and the one with $h = 0\,\mathrm{m}$ (Figure 5.8).

5.1.2 Control History and Response

Now lets have another careful look at the response and control inputs plot and derive conclusions on the role of the suspension dynamics.

Figure 5.5 shows that the radius of the trajectory for $h = 0\,\mathrm{m}$ is smaller from the one for $h = 1\,\mathrm{m}$ except from the first $0.5\,\mathrm{sec}$ that the opposite holds. The magnitude

of the velocity, again from Fig. 5.5 is also in accordance to the difference in radius, since higher velocities are possible for higher values of trajectory radii. In fact, in the $h = 0\,\mathrm{m}$ we observe an initial acceleration from the initial speed and then deceleration in the first 0.5 sec. From then on the velocity and trajectory radius are higher for the $h = 1\,\mathrm{m}$.

In the $h = 1\,\mathrm{m}$ case, where the suspension dynamics and load transfer effects are active, the initial acceleration is avoided because this would result in load transfer from the front axle to the rear axle, making the front wheel which initiates cornering produce less friction force. The front wheel is "more important" in the beginning of cornering because it is the one initiating centripetal forces and yawing moments. The rear wheel comes into play (contributes to the cornering forces) after the yaw motion has developed. At the exit of the corner the rear wheel provides yaw damping end helps stop the yawing motion. In both cases we have deceleration until the apex of the corner end then acceleration towards the exit. In the $h = 1\,\mathrm{m}$ case acceleration results in normal load transfer to the rear wheel and thus greater yaw damping by the rear wheel together with less effort from the front wheel to stop the yawing motion. In the $h = 0\,\mathrm{m}$ case acceleration towards the exit does not change the normal load distribution to front and rear axles and the front wheel is saturated with lateral friction in order to stop the yawing motion not allowing higher travel speed. The only way for the $h = 0\,\mathrm{m}$ vehicle to compensate for this loss of speed at the exit is to gain some time at the entry where acceleration does not make the front wheel to lose normal load (first 0.5 sec).

The fact that in the $h = 1\,\mathrm{m}$ case the trajectory radius is higher after $t = 0.5\,\mathrm{sec}$ results in less steering angle δ as we can see in Fig. 5.3. We also observe more torque applied to the rear wheel and less to the front toward the exit of the corner. This is related to the fact that the load transfer makes the rear wheel "heavier" (and respectively the front wheel "lighter") which means that higher torque is needed to accelerate it.

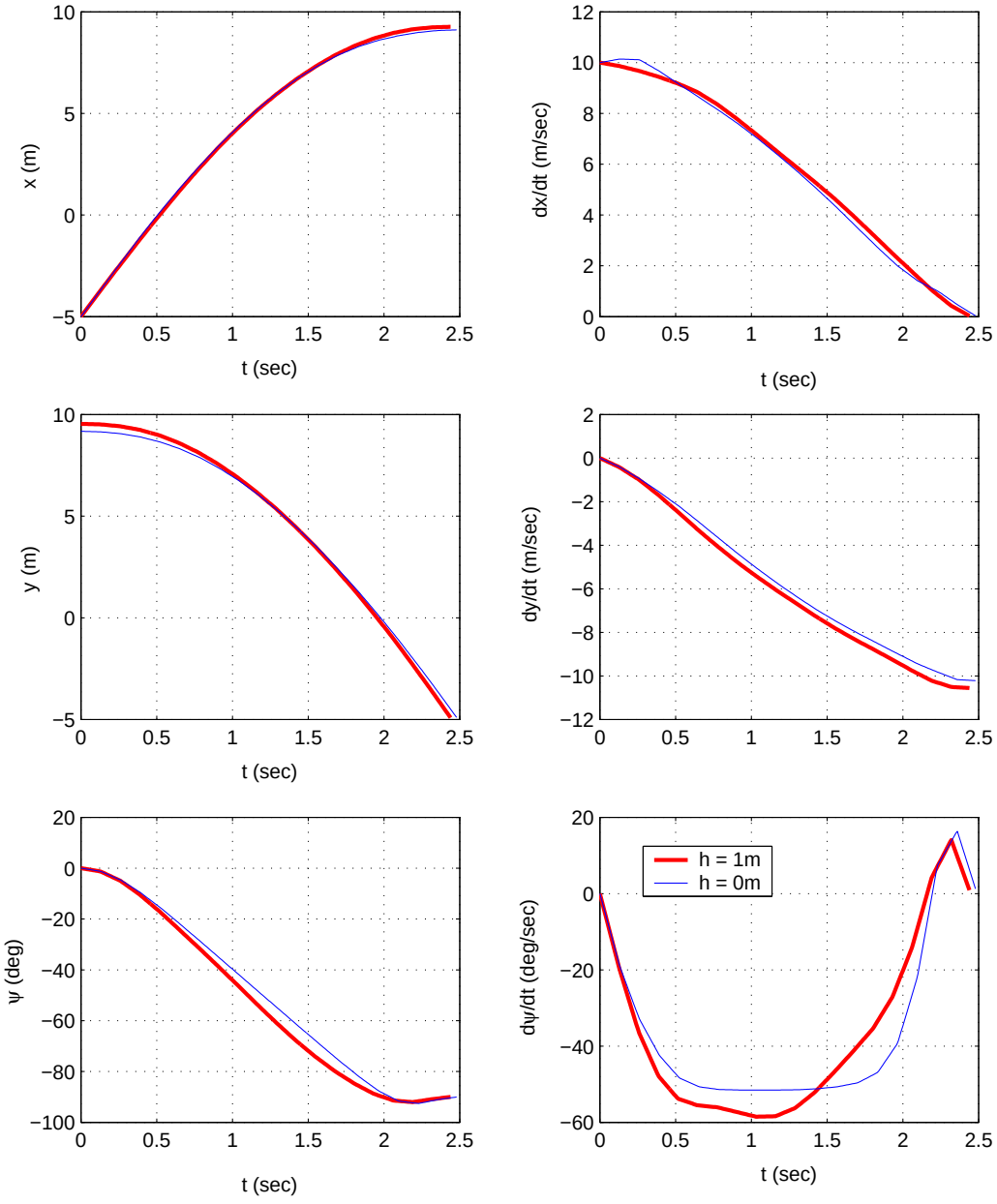

Figure 5.1: 90 deg, *minimum time, states (a)*

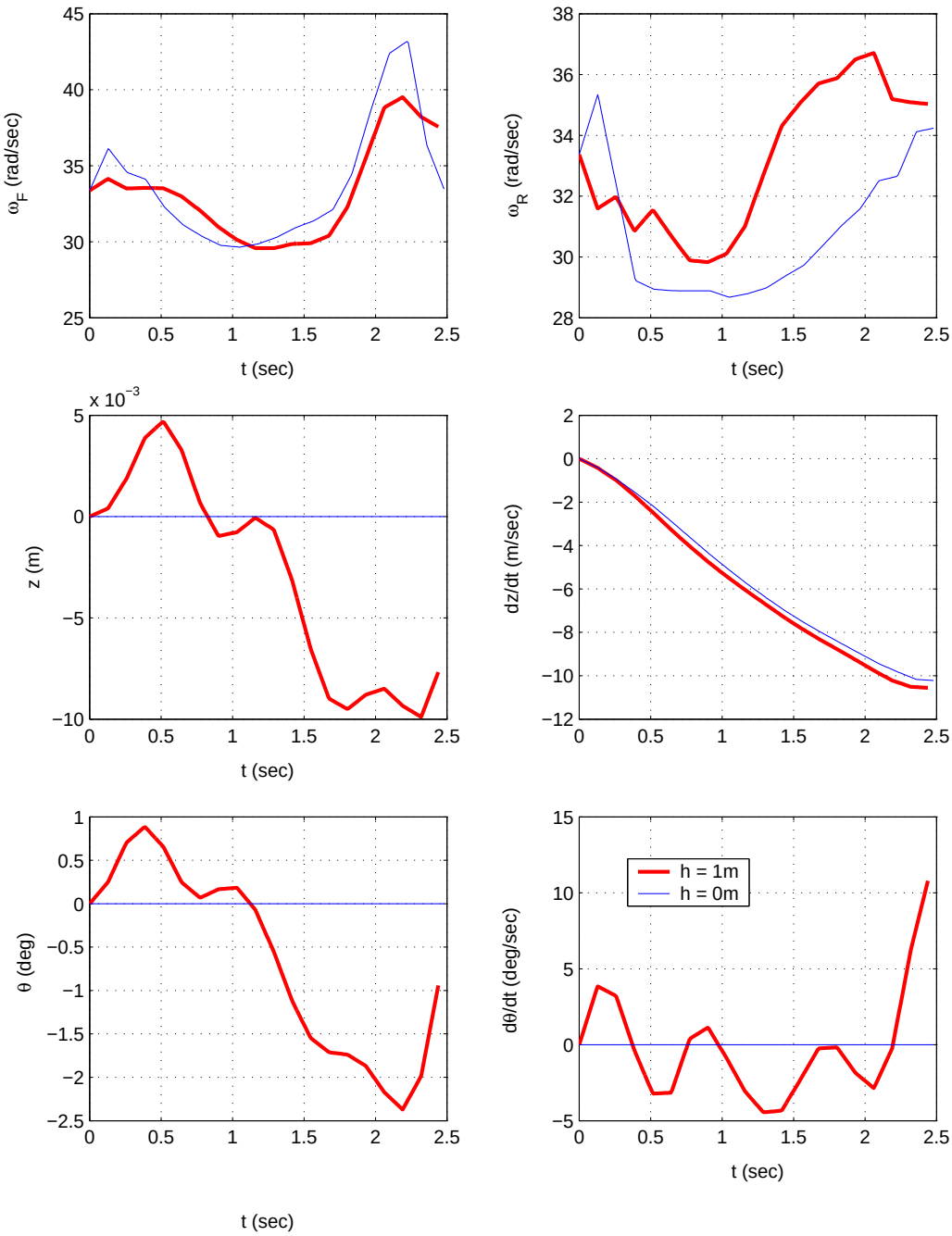

Figure 5.2: 90 deg, *minimum time, states (b)*

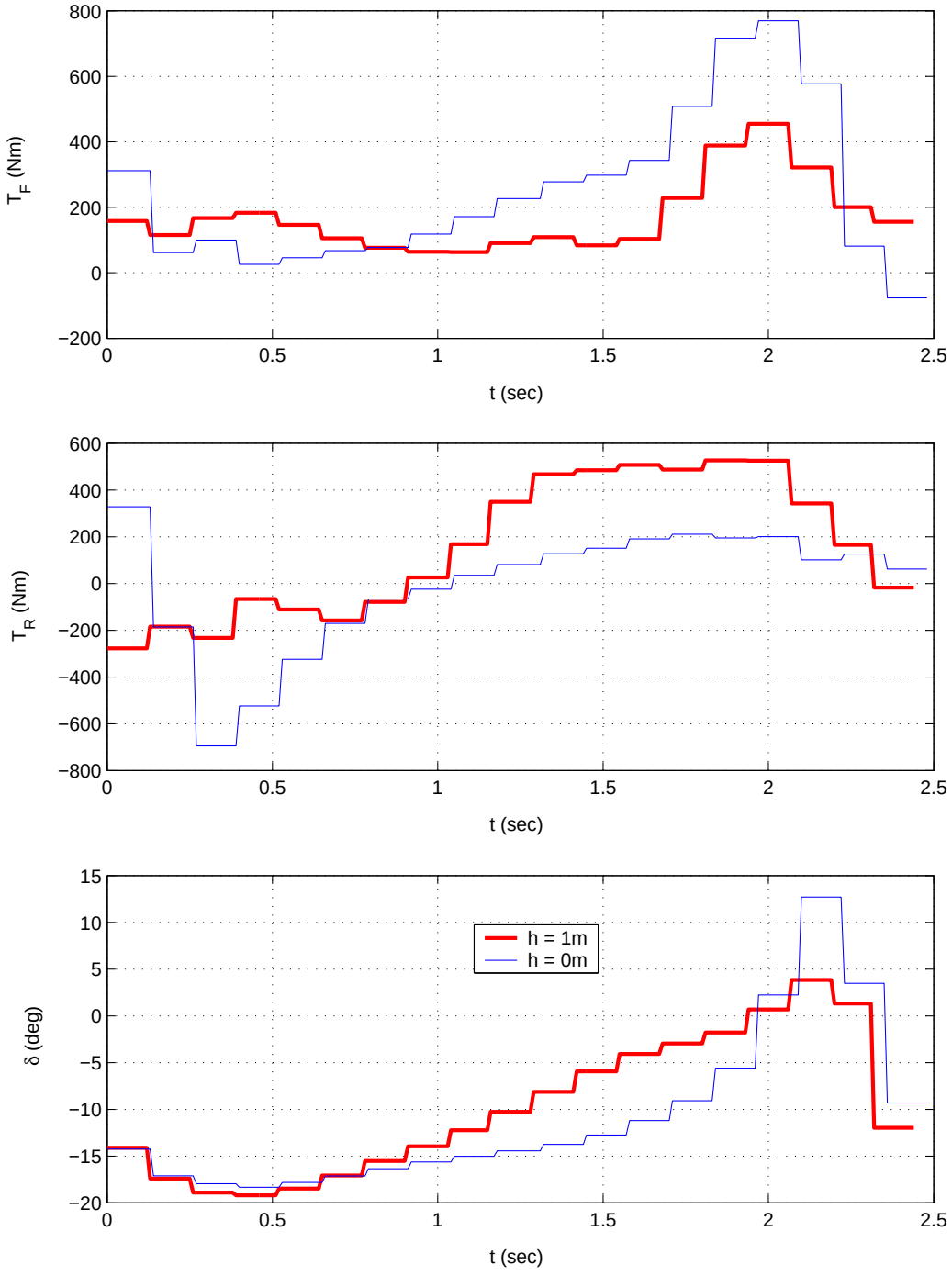

Figure 5.3: 90 deg, *minimum time, control inputs*

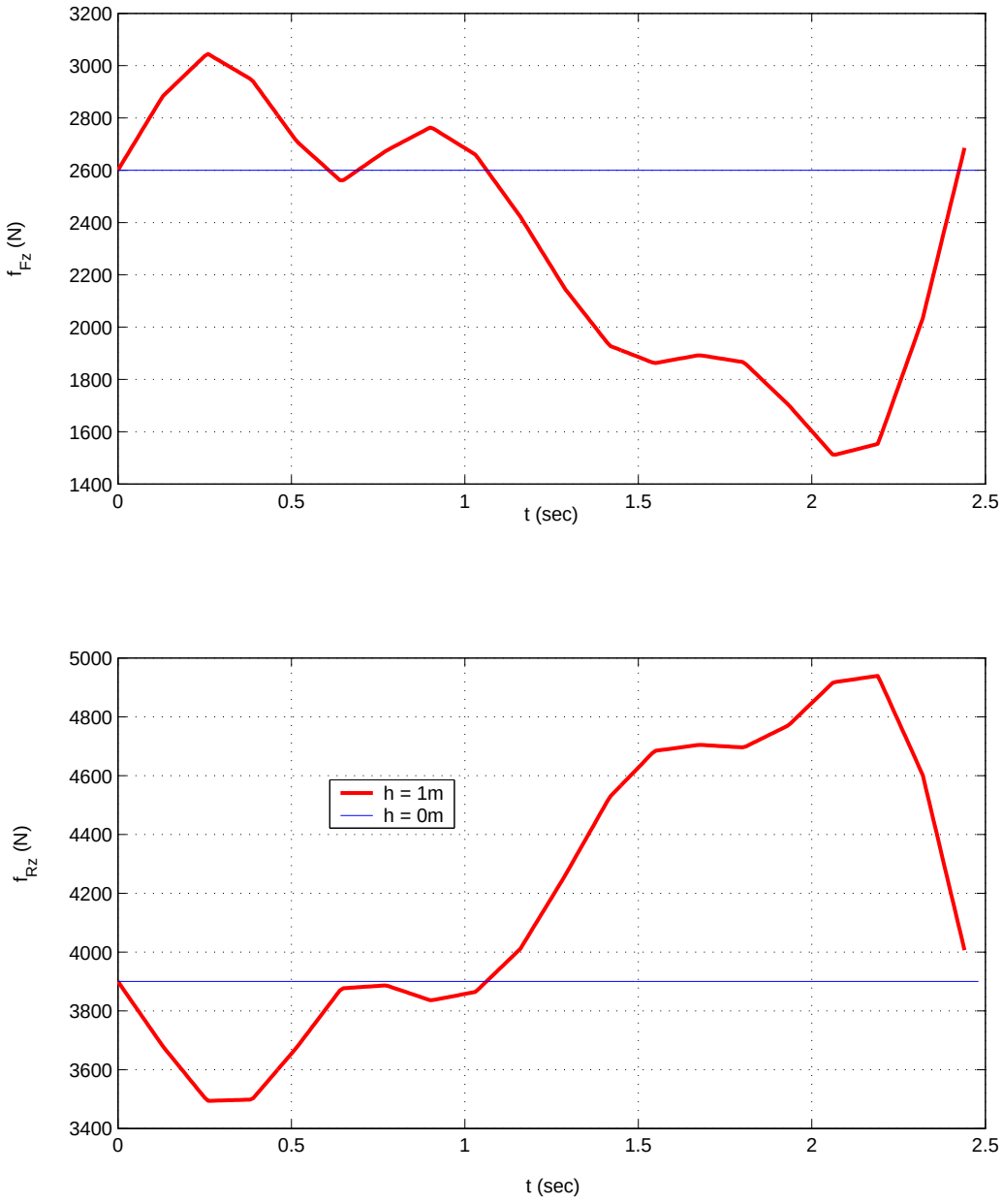

Figure 5.4: 90 deg, *minimum time, normal loads*

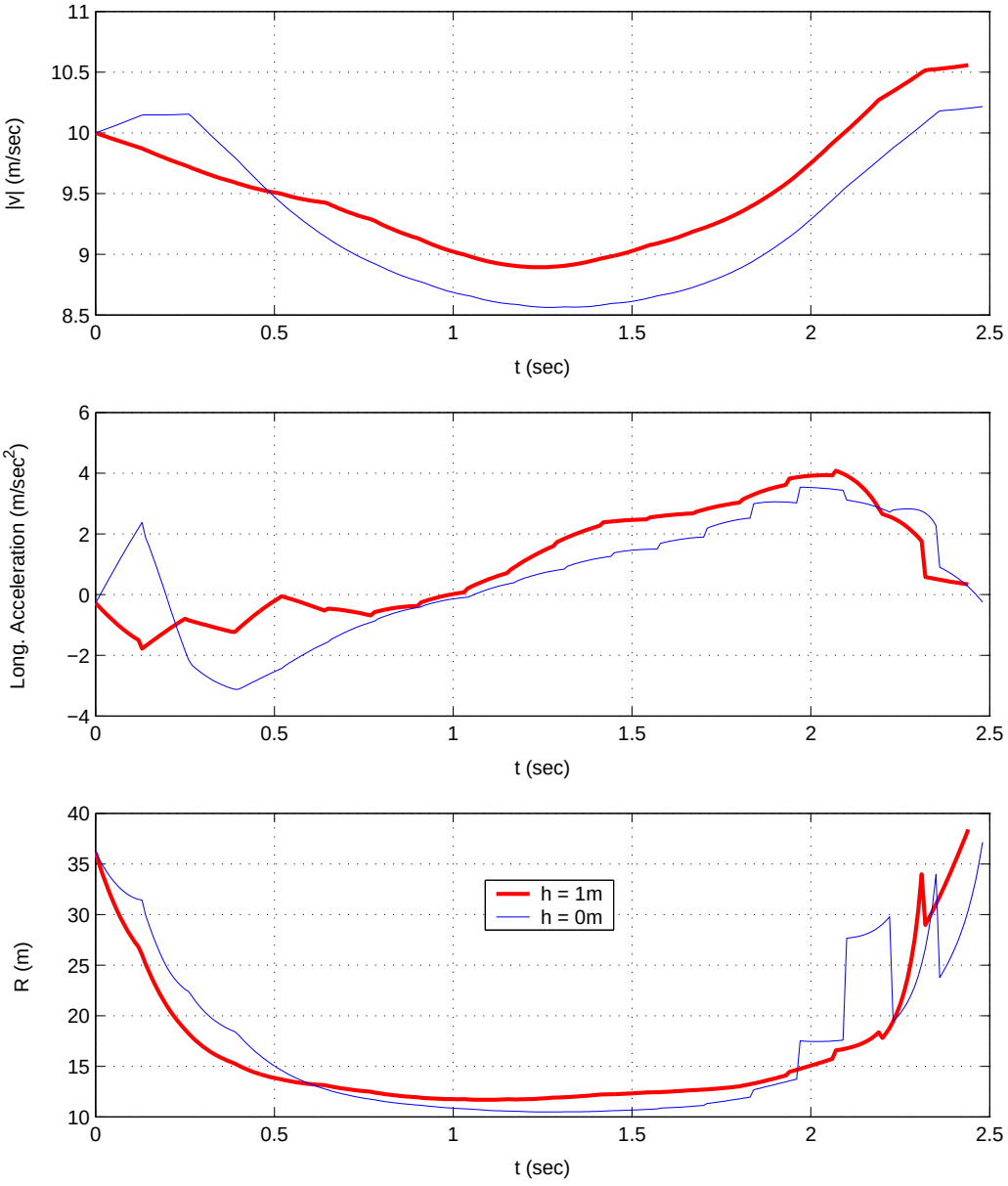

Figure 5.5: 90 deg, *minimum time, absolute velocity - longitudinal acceleration - trajectory radius*

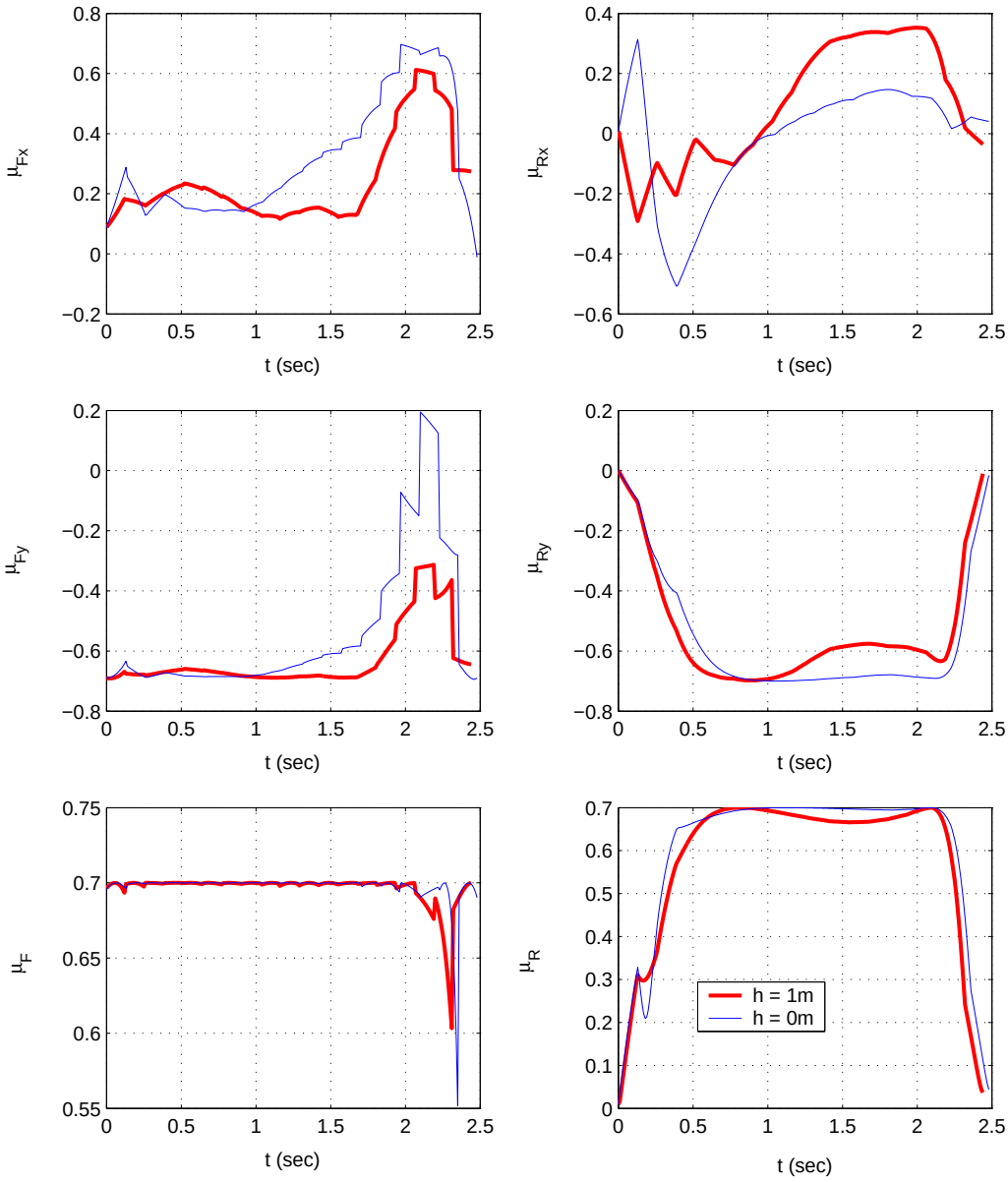

Figure 5.6: 90 deg, *minimum time, friction coefficients*

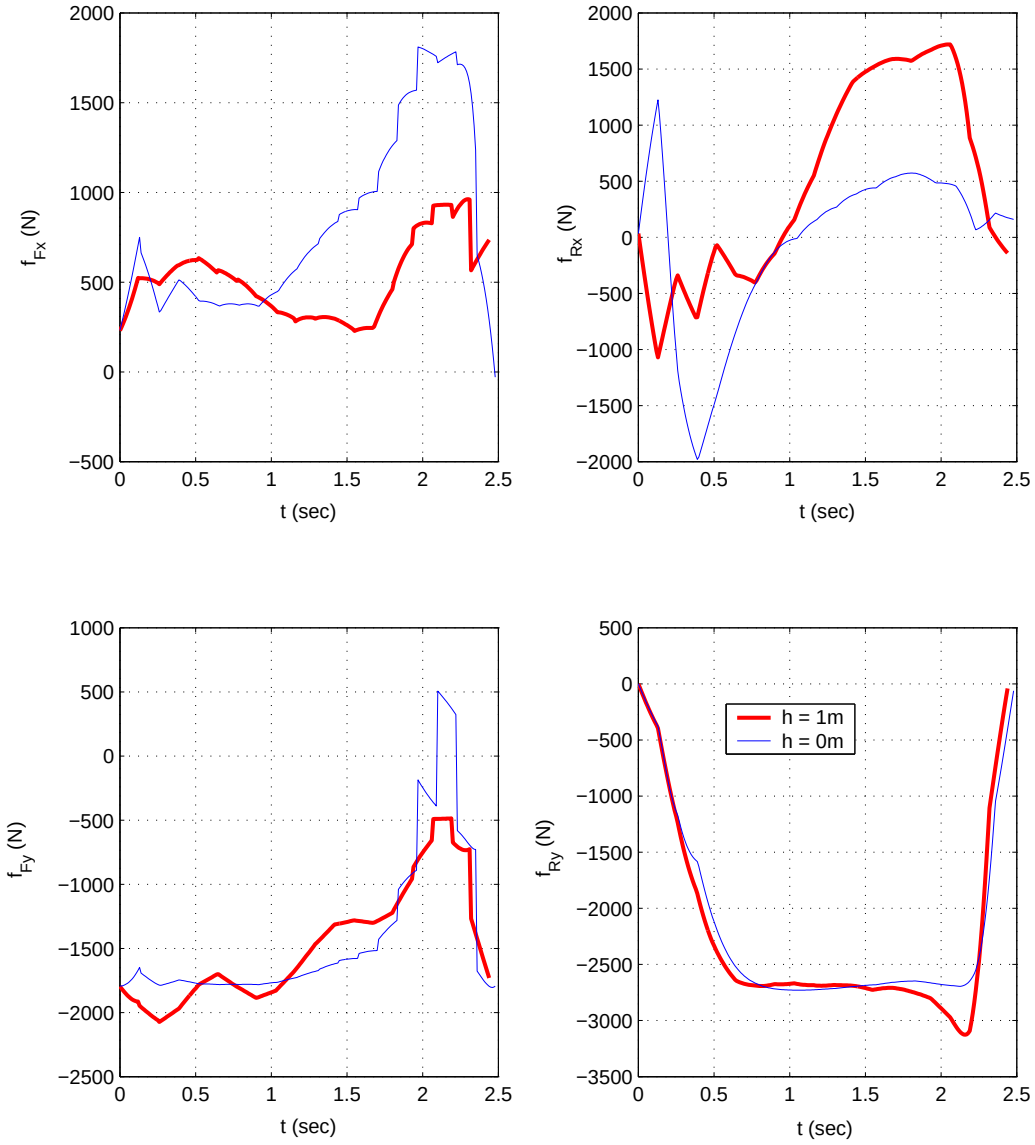

Figure 5.7: 90 deg, *minimum time, friction forces*

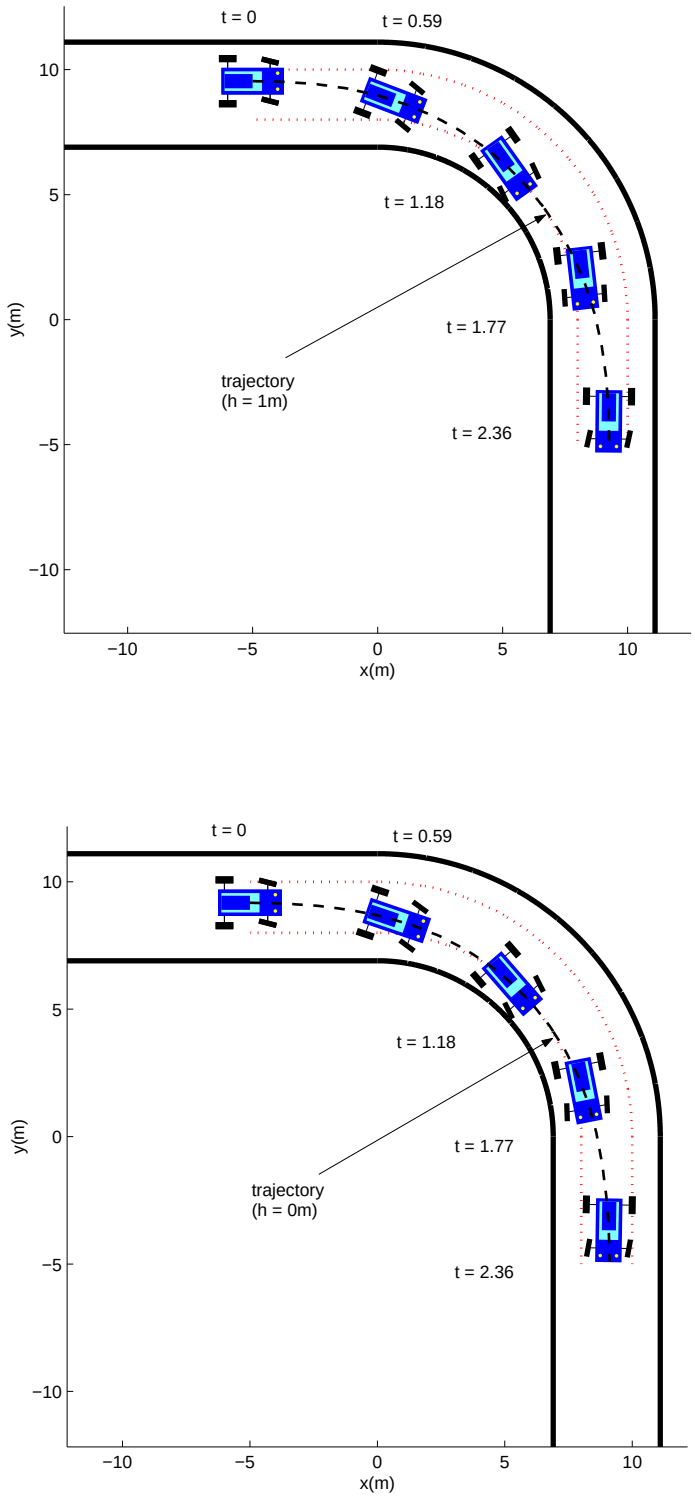

Figure 5.8: 90 deg, *minimum time, trajectories*

5.2 90 deg Corner - Maximum Exit Velocity

Figures 5.9-5.16 completely describe the optimal solution for the maximum exit velocity problem along the 90 deg corner.

5.2.1 Trajectory

The trajectory in the exit velocity maximization problem changes considerably compared to the minimum time solution. The transient - steady state - transient pattern does not appear in this case. We can immediately, however, distinguish the characteristics of the new trajectory independent of the suspension dynamics.

We observe that the trajectory approaches a straight path aligned to the exit, well inside the corner for both $h = 0\,\text{m}$ and $h = 1\,\text{m}$ cases. This part of the trajectory of low curvature requires little cornering effort and thus the vehicle may start accelerating fast, while well inside the corner, maximizing its exit velocity.

We also notice that the vehicle starts well inside the state constraint, turns to the opposite direction of the corner towards the outer edge of the road and then enters the trajectory segment of low curvature. The characteristics of this transition to the low curvature part of the trajectory are more apparent in the $h = 0\,\text{m}$ case, but also present in the $h = 1\,\text{m}$ case.

Recall that in this optimization scenario we are maximizing the exit velocity. Time of travel does not enter the penalty function and thus the trajectory does not have to be of minimal length. We also observe a considerable difference in travel time between the $h = 0\,\text{m}$ and $h = 1\,\text{m}$ cases. This inconsistency is acceptable since minimum time is not the goal.

Nonetheless, in this optimization scenario, we encounter the familiar velocity profile which consists of deceleration followed by acceleration. Only in this case the switching point occurs early in the trajectory, at a point in the transition segment.

5.2.2 Control History and Response

As already mentioned, there is significant difference in travel time between the solutions for the $h = 0\,\mathrm{m}$ and $h = 1\,\mathrm{m}$ cases. The optimization cost (exit velocity) is however very close. The reason for this discrepancy lies on the normal load transfer mechanism. In both cases we observe the pattern of deceleration up to a point and then acceleration right after (Fig. 5.5). In fact some initial acceleration is allowed in the $h = 1\,\mathrm{m}$ case.

Deceleration in the $h = 1\,\mathrm{m}$ case results in load transfer to the front axle (Fig. 5.4) and thus larger friction forces may be generated by the front tires while decelerating. This means that the cornering capacity of the front wheels is larger during deceleration. Recall that cornering is initiated by the front wheels and thus the same radius may be negotiated with higher speed (Fig. 5.5). In fact, the velocity in the $h = 1\,\mathrm{m}$ case is higher at all times, compared to the $h = 0\,\mathrm{m}$ case, which explains the shorter travel time.

Deceleration in the $h = 0\,\mathrm{m}$ case does not change the cornering capacity of the front wheels and thus lower velocity is required for the transit segment. Recall that both vehicles begin at the same velocity. In order for the $h = 0\,\mathrm{m}$ vehicle to decelerate more in the transit segment, it needs more space and thus the longer and curvier trajectory at the beginning.

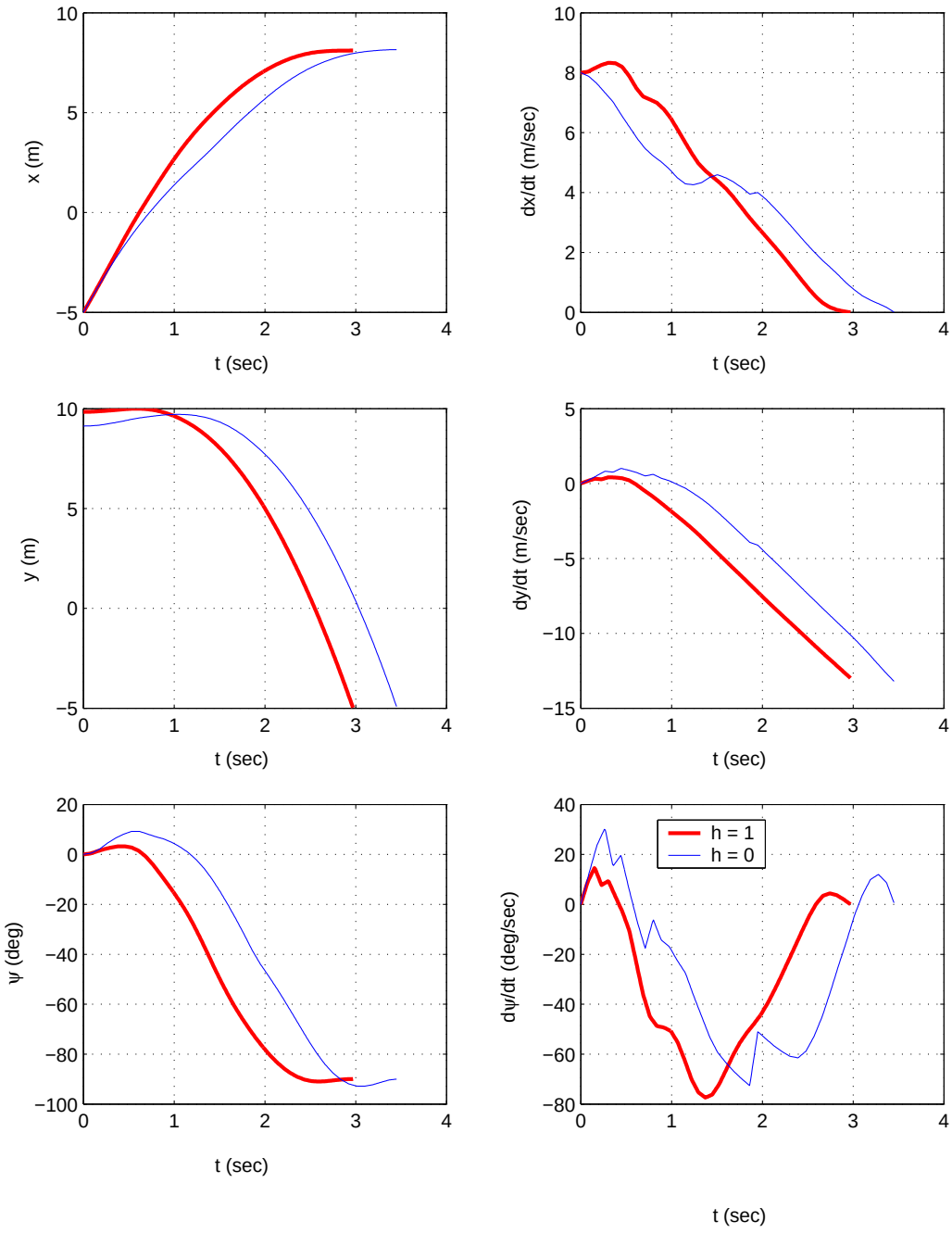

Figure 5.9: 90 deg, *maximum exit velocity, states (a)*

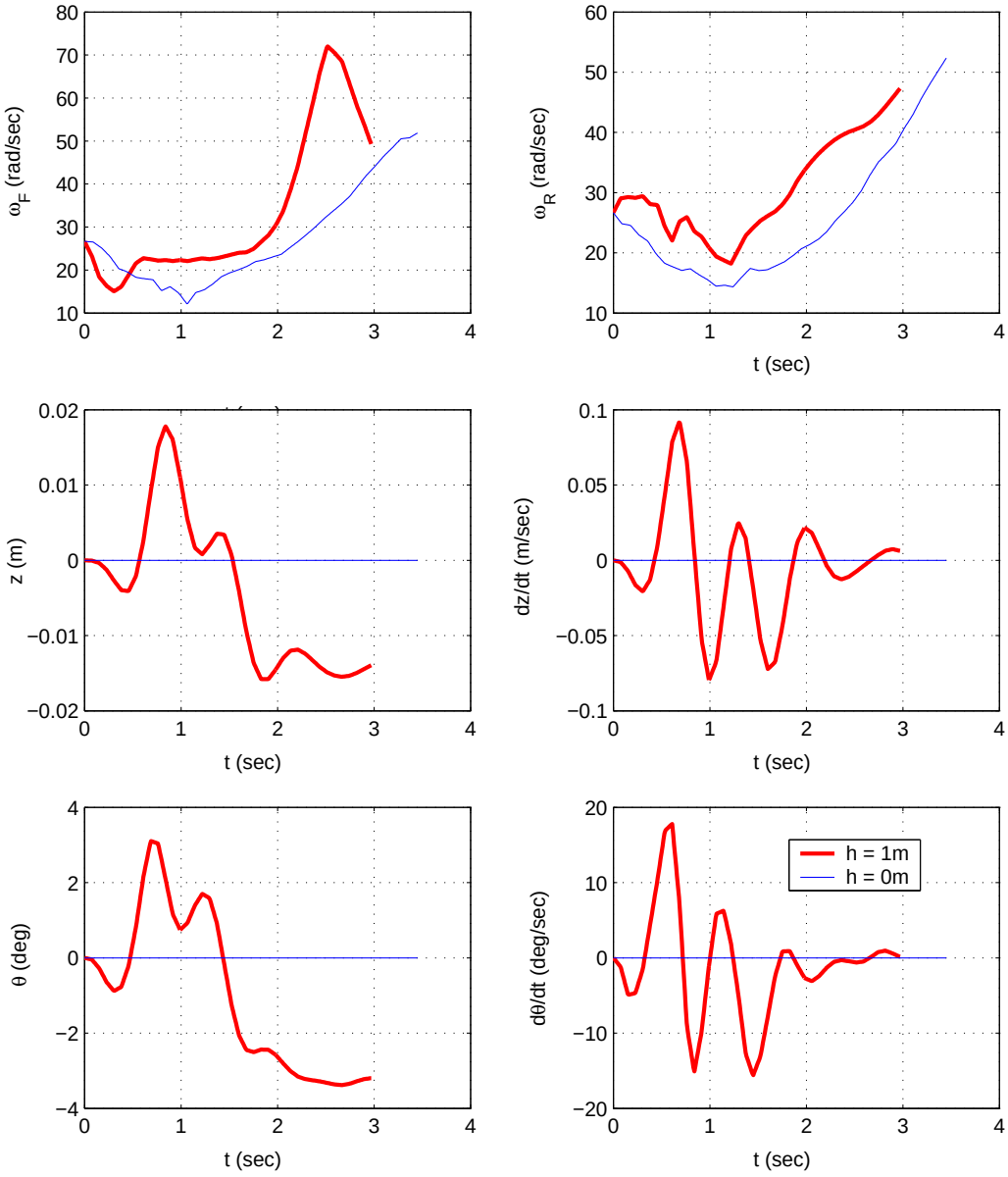

Figure 5.10: 90 deg, *maximum exit velocity, states (b)*

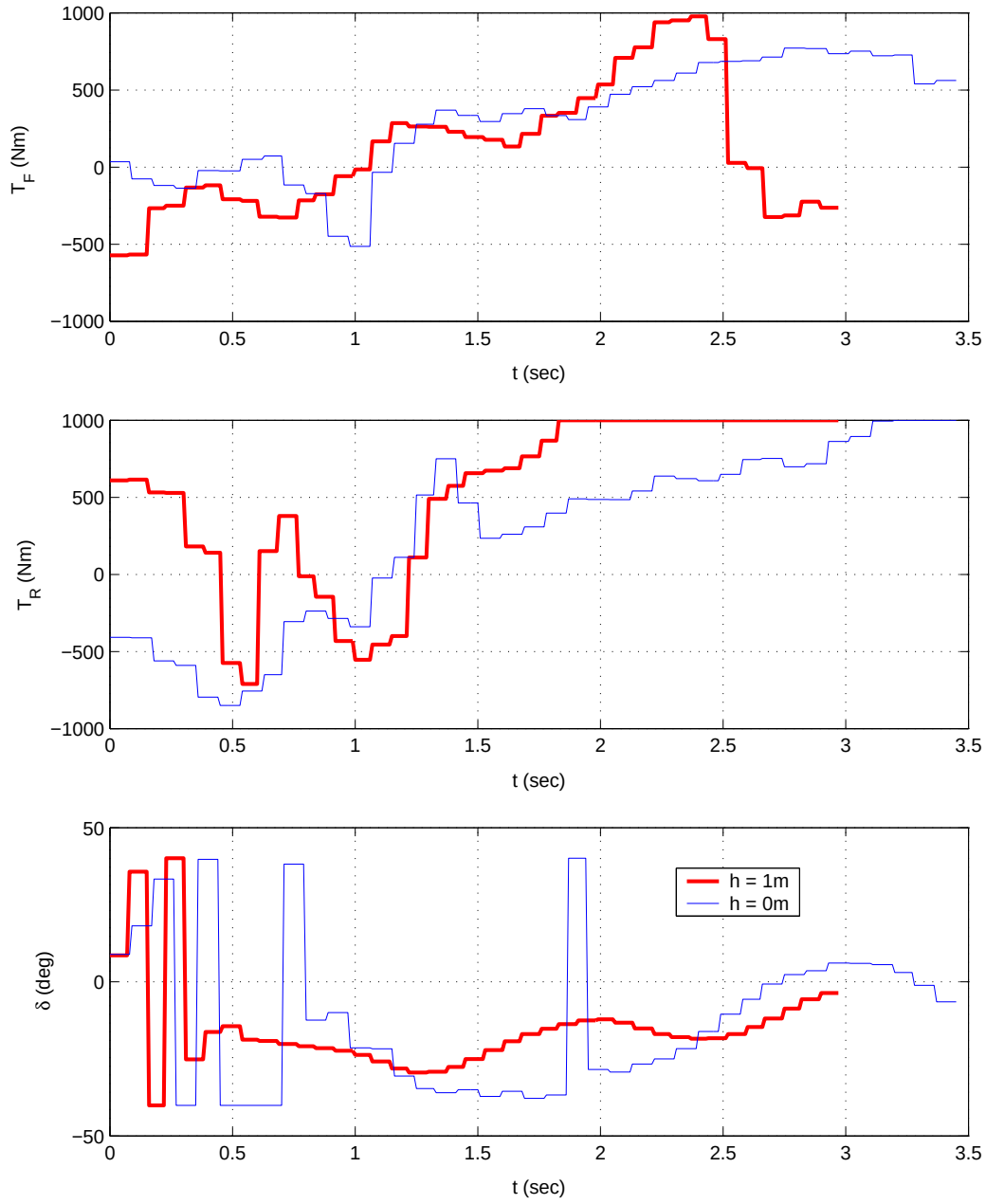

Figure 5.11: 90 deg, *maximum exit velocity, control inputs*

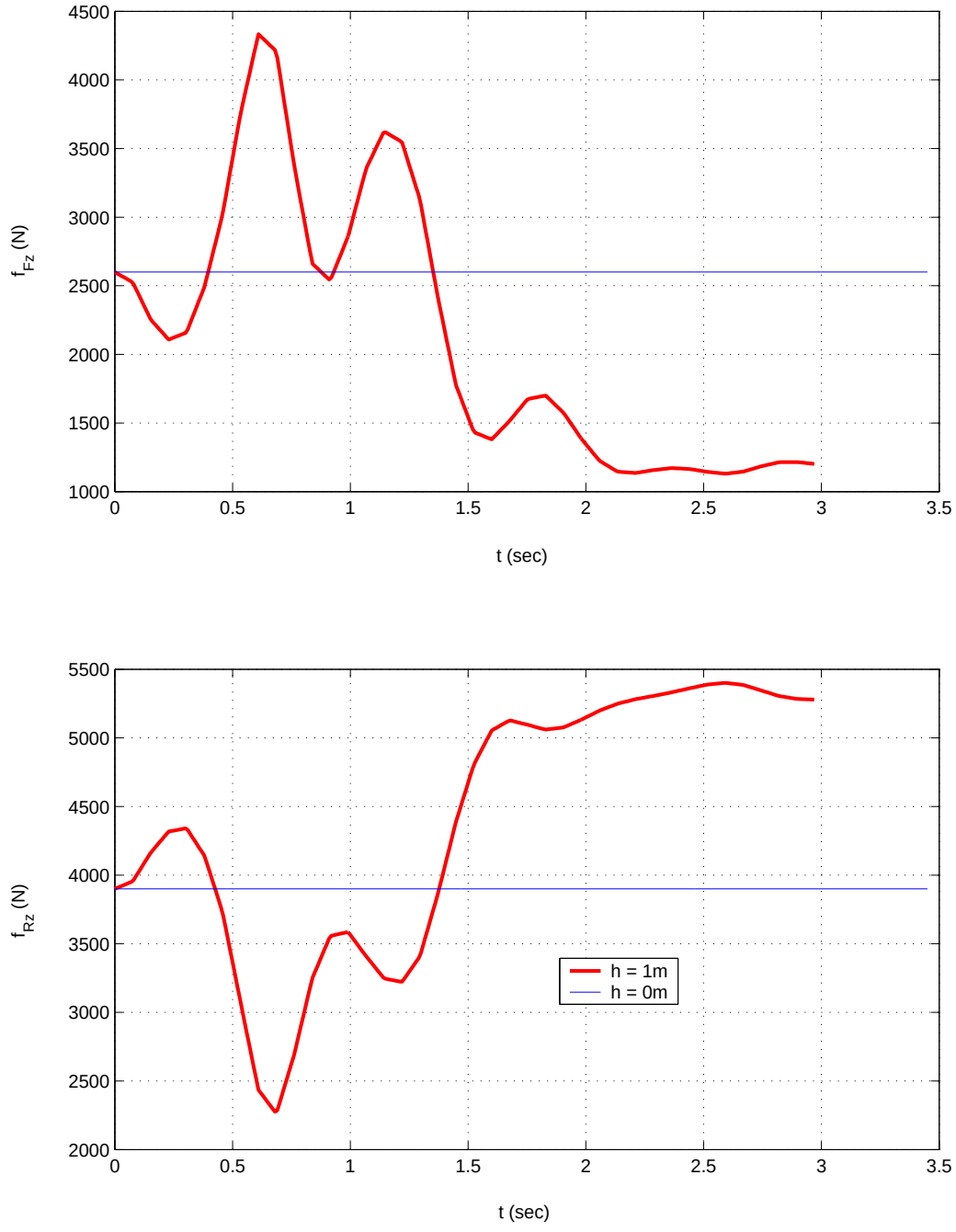

Figure 5.12: 90 deg, *maximum exit velocity, normal loads*

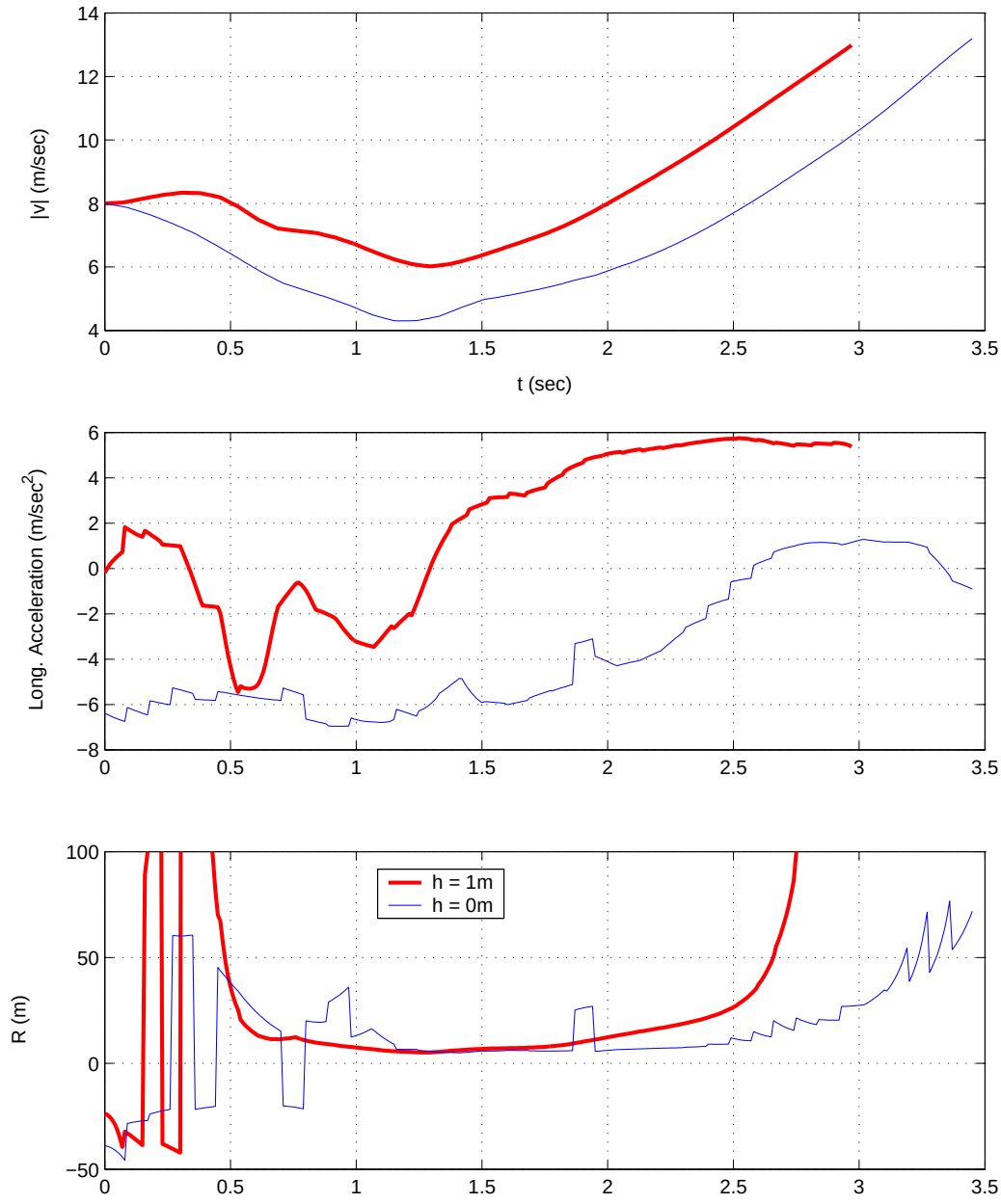

Figure 5.13: 90 deg, *maximum exit velocity, absolute velocity - longitudinal acceleration - trajectory radius*

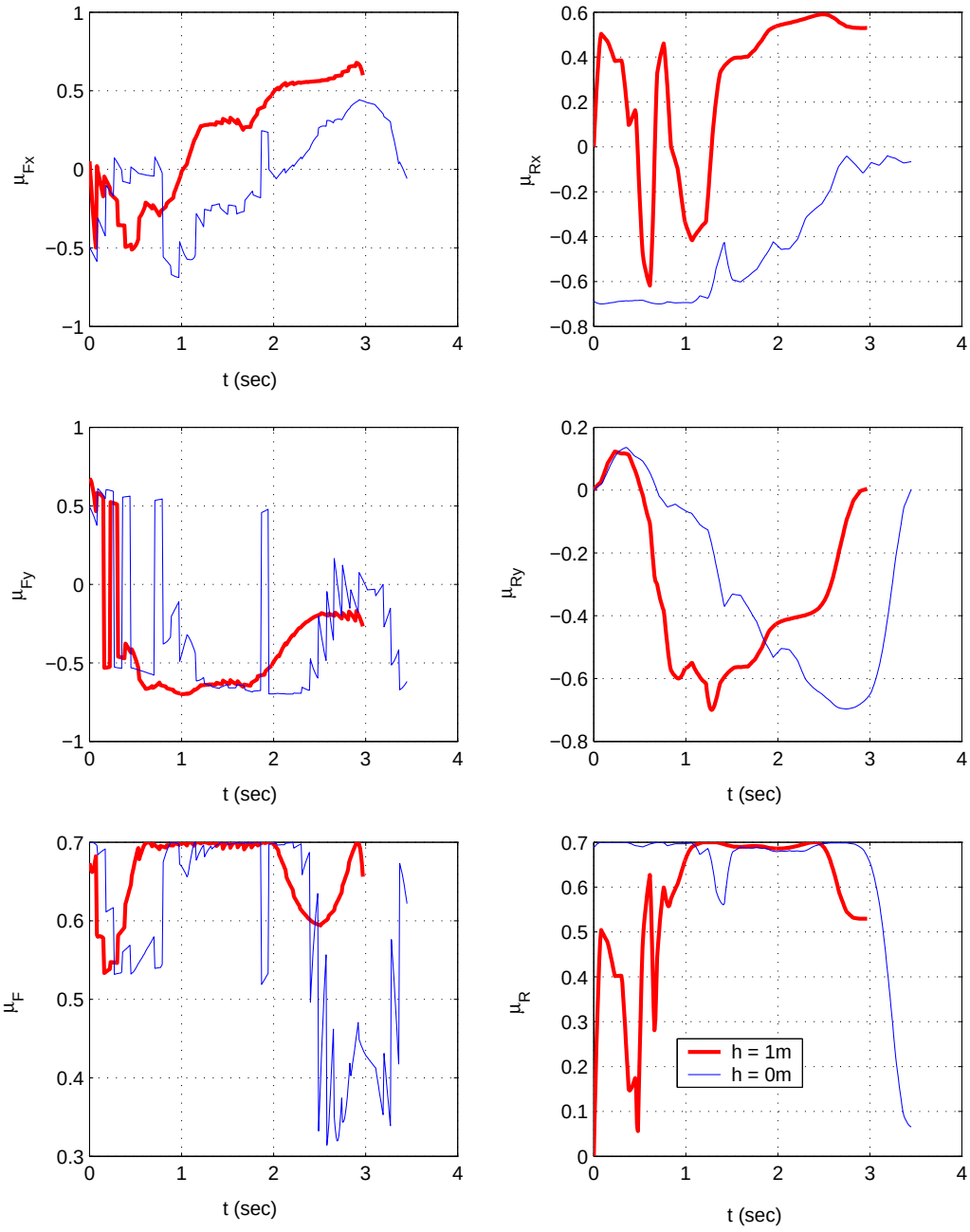

Figure 5.14: 90 deg, *maximum exit velocity, friction coefficients*

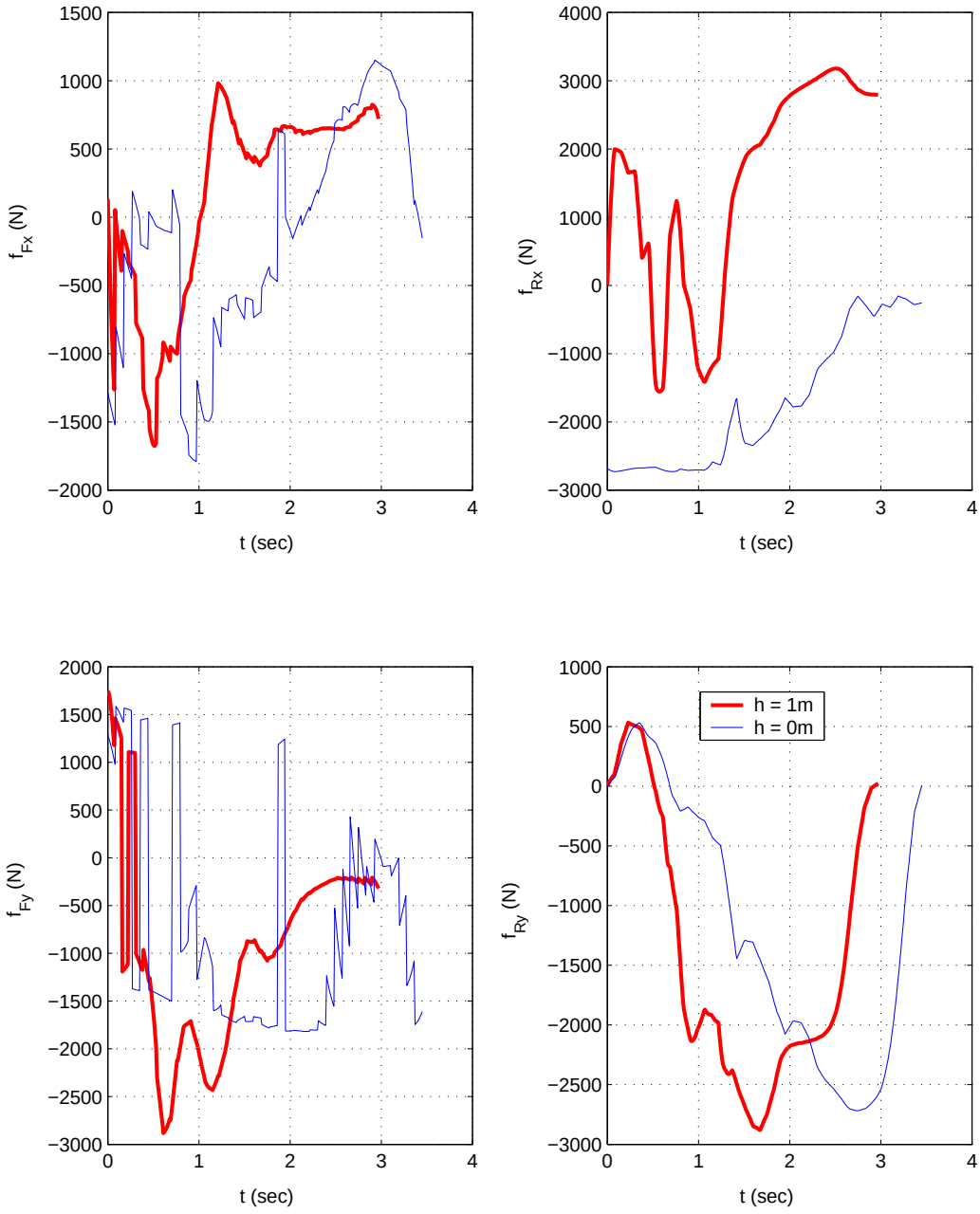

Figure 5.15: 90 deg, *maximum exit velocity, friction forces*

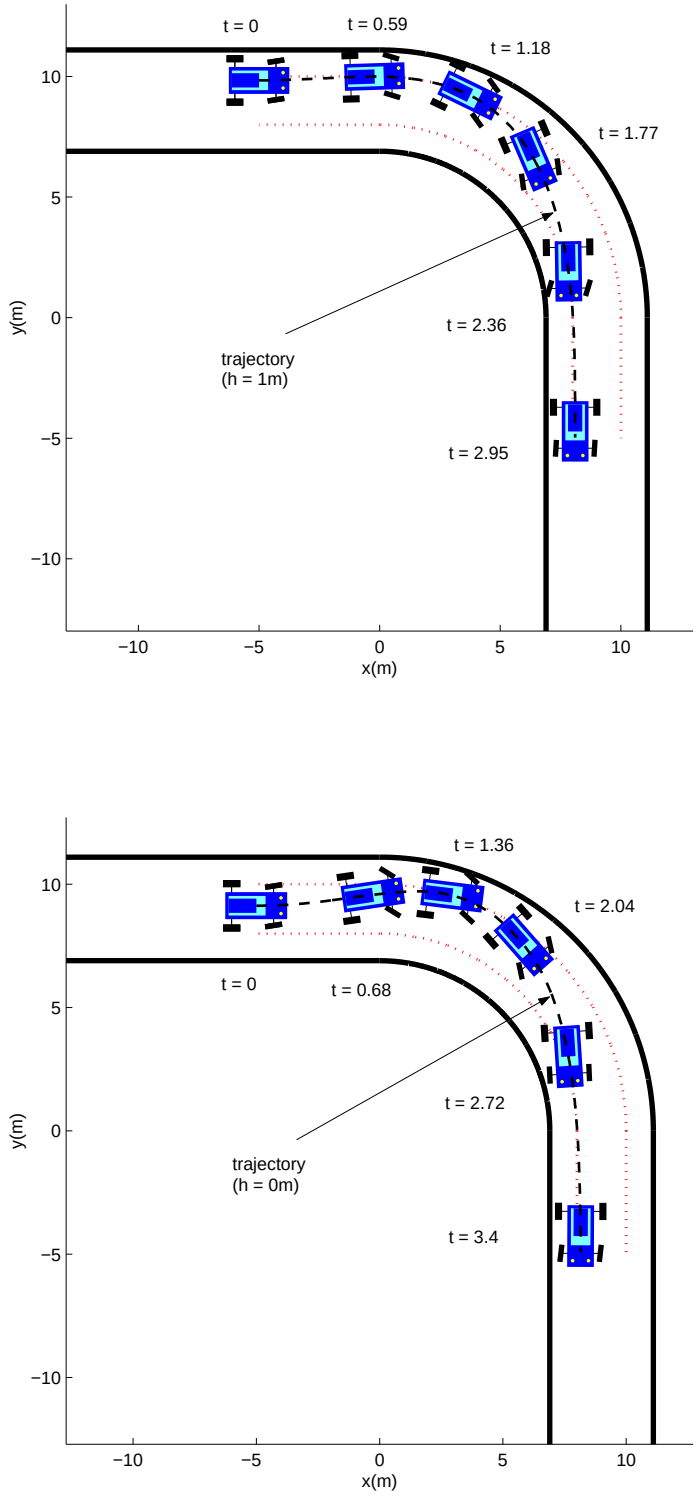

Figure 5.16: 90 deg, *maximum exit velocity, trajectories*

5.3 Minimum Time vs Maximum Velocity

In this section we demonstrate that using the optimal exit velocity solution as seen in Section 5.2 may lead to a better overall time through a course containing the 90 deg than using the optimal time solution of Section 5.1. This can serve as a demonstration of Bellman's Principle of Optimality which states that constructing a solution of optimal subarcs does not guarantee optimality of the overall solution.

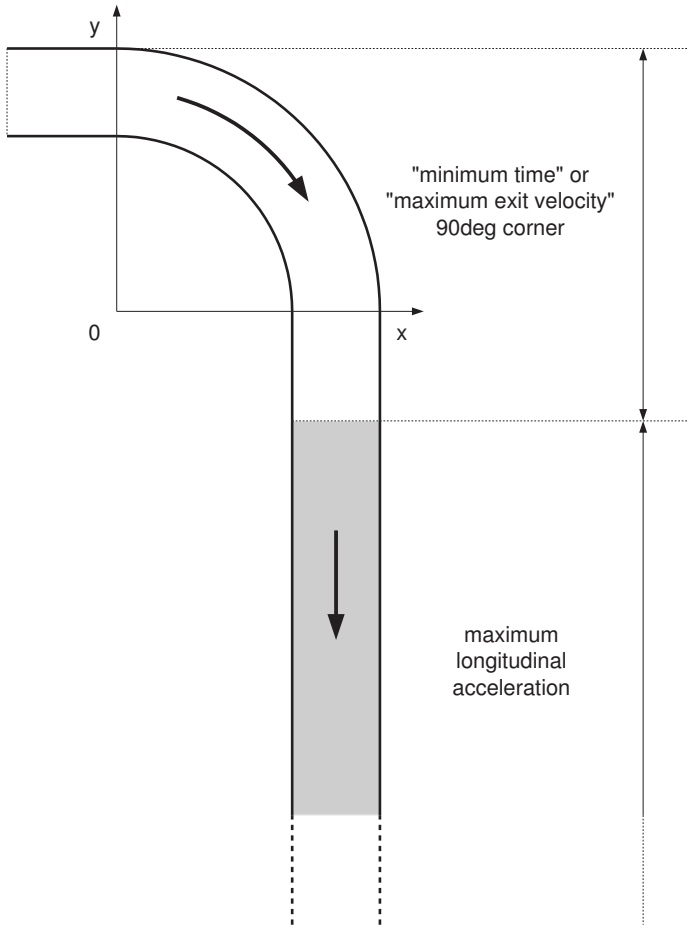

Figure 5.17: *Assume that after a* 90 deg *corner a long straight road segment follows.*

Assume that the course to be negotiated consists of the 90 deg corner followed by a long straight road segment as in Fig. 5.17. The goal is to minimize time from the entry point of the corner to the end of the straight segment. Instead of letting the optimization algorithm to find the optimal solution of this problem we just perform a set of simulations in order to compare the cornering strategies of Sections 5.1 and

5.2. That is, after using the optimal control inputs calculated by the optimization algorithm to negotiate the corner in minimum time and with maximum exit velocity respectively we then apply a closed-loop control to provide maximum longitudinal acceleration throughout the straight segment. The closed-loop controller used in the straight segment is summarized by

$$T_F = -K_1(s_{Fx} - s^*) \tag{5.1}$$

$$T_R = -K_2(s_{Rx} - s^*) \tag{5.2}$$

$$\delta = -K_3\left(\psi + \frac{\pi}{2}\right) \tag{5.3}$$

where, s^* is the total slip quantity that maximizes the friction coefficient between the road and the tire, which can be calculated given the parameters of the "Magic Formula" and K_1, K_2 and K_3 are the controller gains. Equations (5.1) and (5.2) guarantee that maximum longitudinal friction is generated by front and rear wheels, regardless normal load transfer effects. Equation (5.3) stabilizes the yaw angle of the vehicle at $\psi = -\frac{\pi}{2}$. The last equation of the closed loop controller is necessary considering the tolerances involved in the optimization algorithm which may result in small discrepancies of the prescribed boundary conditions at the exit of the corner which may become obvious without stabilization of the yaw angle after some time of full longitudinal acceleration.

At this point we need to clarify that in order to make the comparison between the control strategies of Sections 5.1 and 5.2 fair, we have to assume equal initial velocity of the vehicle at the entry point of the corner. To this end we have performed numerical optimization for minimum time through the corner with the same value of initial velocity as in Section 5.2. The new optimal solution retains exactly the same characteristics as in Section 5.1 and it is omitted for sake of brevity.

In the left plot of Fig. 5.18 we can see the vertical position of the vehicle y versus time. We observe that after $t = 6$ sec the vehicle that had negotiated the corner with maximum exit velocity is ahead of the vehicle that had negotiated the corner in minimum time. This shows that the optimal time solution of one segment of the total trajectory may not be part of the overall optimal time solution.

In order to make the difference more clear we have performed a second set of simulations. In this set we have assumed reduced friction coefficient between tire and road at the straight segment of the road (highlighted area in Fig. 5.17). For example the road may be wet after the corner. The vertical position of the vehicles (using the minimum time and maximum exit velocity trajectories) versus time is shown in the right plot of Fig. 5.18. The control inputs are shown, for the case of the vehicle negotiating the corner with maximum exit velocity, in Fig. 5.19. For the same case, the longitudinal friction coefficient of the front and rear wheels as well as the yaw angle versus time are shown in Fig. 5.20.

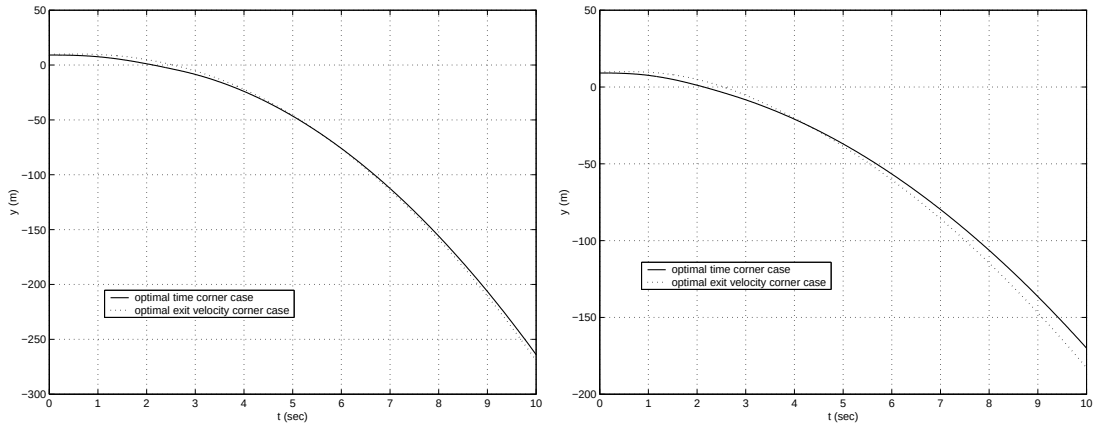

Figure 5.18: *Vertical position of the vehicle with respect to time for both cases of driving through the corner with minimum time and with maximum exit velocity. Left plot: the same friction throughout the whole trajectory. Right plot: the magnitude of friction on the straight segment is reduced to half compared to the one on the corner.*

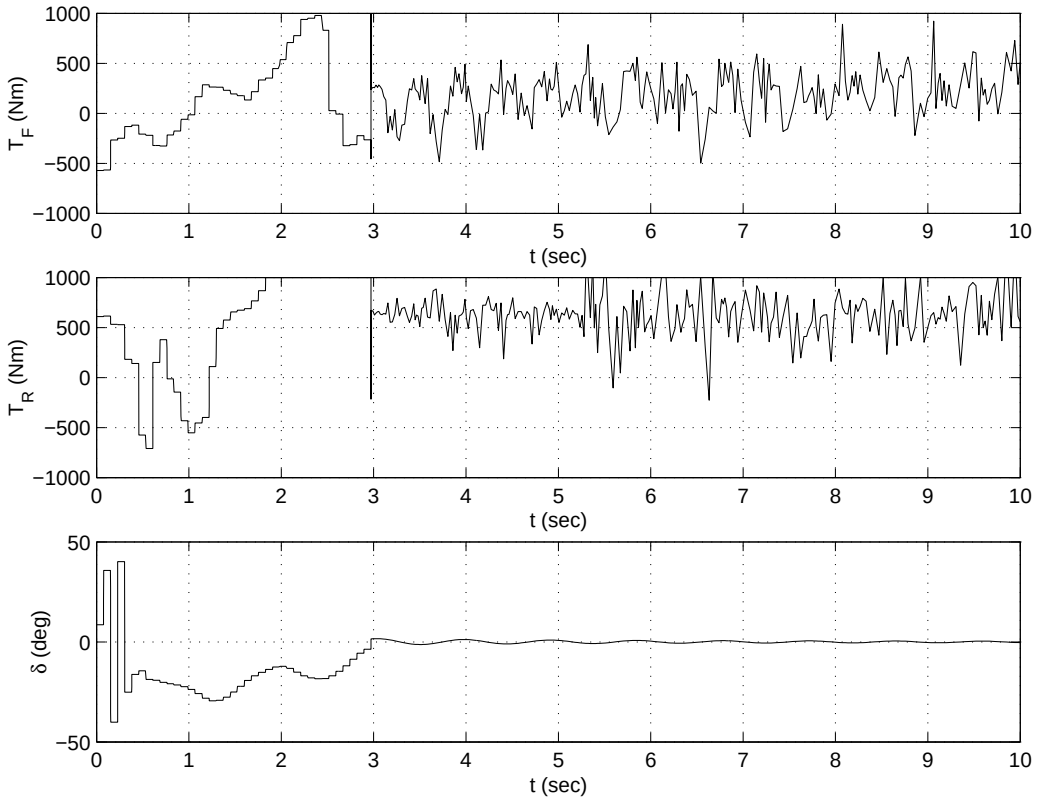

Figure 5.19: *Control inputs for the overall trajectory - corner and straight segment. Maximum exit velocity corner and reduced friction on the straight segment case.*

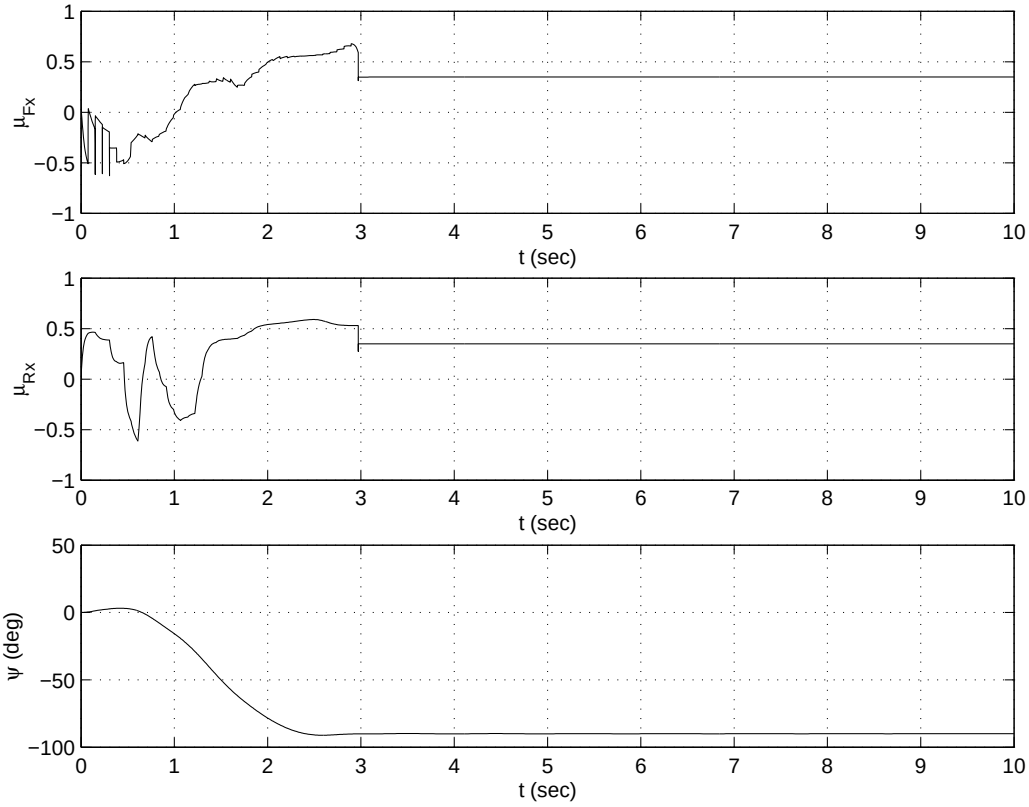

Figure 5.20: *Longitudinal friction coefficient of front and rear wheels and yaw angle with respect to time. Maximum exit velocity corner and reduced friction on the straight segment case.*

5.4 Drifting Through a Corner

A characteristic of rally race driving, which actually makes the sport so appealing to watch and distinguishes it from other types of car racing, such as F1 racing, is that drivers drive through corners inducing drifting, that is driving at high slip vehicle angles β. In such situations drivers manage to balance the oversteering vehicle by steering the front wheels to the opposite direction of the corner (applying 'opposite lock'). In this section we reproduce such a driving behavior as part of an optimal solution through the same 90 deg corner. To this end we choose a more oversteering - less stable vehicle configuration. The goal is again to maximize the exit velocity after the corner.

In order to give the vehicle oversteering behavior the configuration is changed compared to the one used so far. The vehicle's weight balance is chosen 50% on the front axle and 50% on the rear by setting $\ell_F = \ell_R = 1.25\,\mathrm{m}$. This means that less normal load acts on the rear wheel and thus less friction may be generated by it making it easier for the rear tire to loose traction. For simplicity we are using in this case the reduced order vehicle model neglecting the suspension dynamics ($h = 0\,\mathrm{m}$). We present the resulting optimal control inputs and trajectory of the maximum exit velocity problem with the new vehicle configuration (Figures 5.21 and 5.22). Observing the trajectory in Fig. 5.22 we may conclude that it consists of the same parts as the trajectories discussed in Section 5.2, i.e. initially the vehicle turns to the opposite direction of the corner towards the outer edge of the state constraint, then changes direction on a large curvature part of the trajectory that tangentially intersects the outer edge of the corner and finally enters the part of the trajectory of low curvature where it may accelerate towards the exit of the corner. At the transitional phase where the vehicle drives from large curvature to the final part of the trajectory of low curvature we observe considerably high values of slip angle β. At $t = 3.17$ sec the vehicle reaches the maximum slip angle, which one may observe in Fig. 5.22 as the difference between the heading of the vehicle longitudinal axis and the tangent of the trajectory. For 2.9 sec $\leq t \leq$ 3.4 sec we observe that "opposite

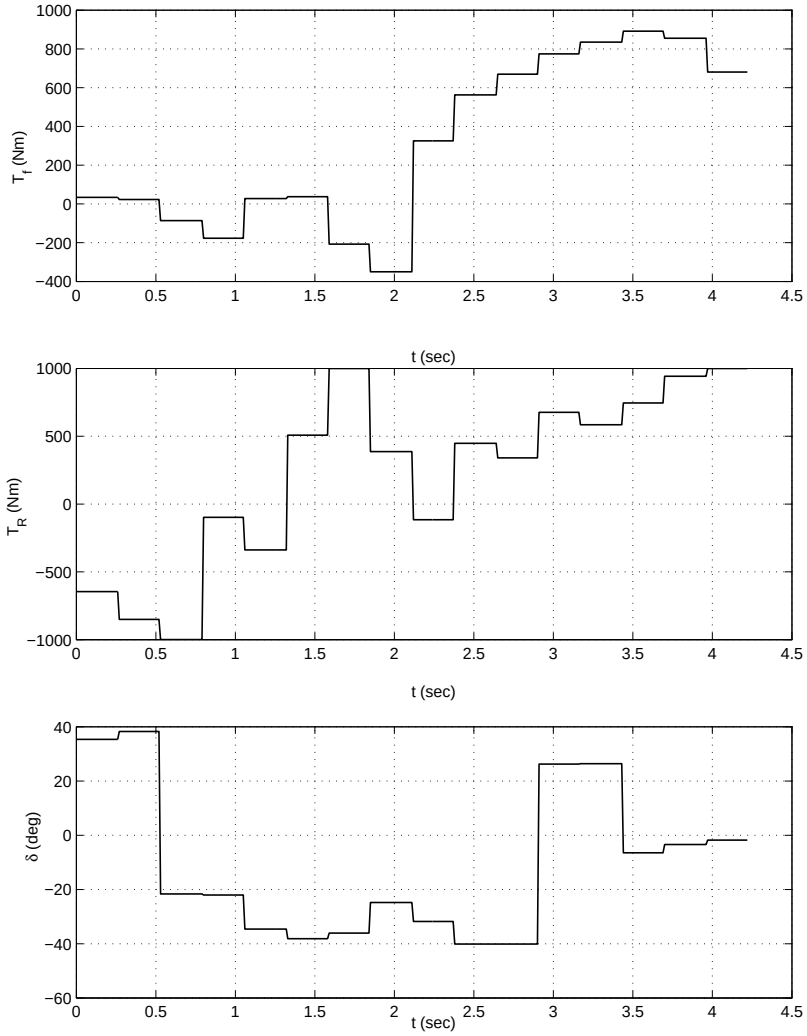

Figure 5.21: *Optimal control inputs for the maximum exit velocity considering an oversteering vehicle.*

lock" is being applied (Fig. 5.21) in order to decelerate the yawing motion of the oversteering vehicle which would lead to instability.

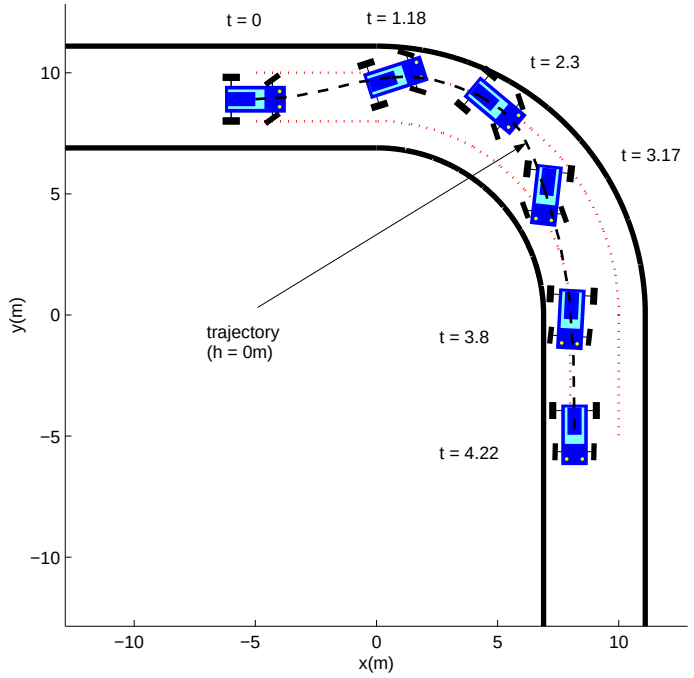

Figure 5.22: *Numerical optimization techniques reproduce driving techniques of expert race drivers, such as cornering with large vehicle slip angles.*

Part III

Semi-Analytic Trajectory Optimization

Chapter 6

Minimum Time Velocity Profile: Optimality and Receding Horizon Implementation

Numerical optimization techniques present little promise of on-line applicability due to the high computational cost and the inability to incorporate unpredictable environments. In addition, convergence of the numerical optimization algorithm also depends on the accuracy of the initial guess of the optimal solution. In this chapter we pursue a semi-analytic approach to generate optimal velocity profiles for minimum time travel along a prescribed path given the acceleration capacity of the vehicle. The semi-analytic nature ensures minimal computational cost and a receding horizon implementation allows application to unpredictable/changing environments. We design a dynamic scheme to determine planning and execution horizons to provide guaranty of convergence of the receding horizon implementation.

6.1 Problem Statement

Consider a vehicle of mass m travelling along a prescribed path, with given acceleration limits and fixed initial and final position and velocity. We seek the velocity profile along the path for minimum travel time. The path is described by its radius $r(s)$ at

each point, which is given as a function of the path length coordinate s, or equivalently by the curvature $k(s)$ along the path (Fig. 6.1). The cartesian coordinates at any point on the path can be calculated using the following standard transformations:

$$k(s) \triangleq \frac{1}{r(s)},\ \phi(s) \triangleq \int_{s_0}^{s} k(\sigma)\mathrm{d}\sigma,$$
$$x(s) = \int_{s_0}^{s} \cos\phi(\sigma)\mathrm{d}\sigma,\ y(s) = \int_{s_0}^{s} \sin\phi(\sigma)\mathrm{d}\sigma. \tag{6.1}$$

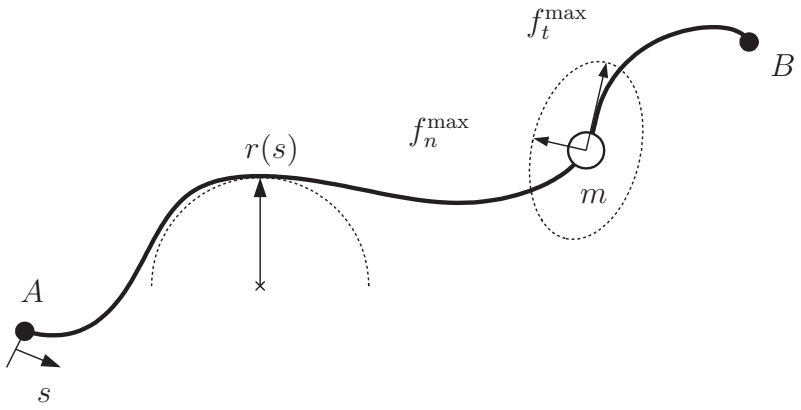

Figure 6.1: *A vehicle of mass m travels along the prescribed path $r(s)$ with given maximum acceleration limits in minimum time.*

The equations of motion are given by

$$m\frac{\mathrm{d}^2 s}{\mathrm{d}t^2} = f_t, \quad m\left(\frac{\mathrm{d}s}{\mathrm{d}t}\right)^2 = f_n r(s), \tag{6.2}$$

where, f_t is the tangential component of the force along the path, and f_n is the normal (centripetal) force such that the vehicle tracks the prescribed path. The force acting on the vehicle is limited within the ellipse

$$\left(\frac{f_t}{f_t^{\max}}\right)^2 + \left(\frac{f_n}{f_n^{\max}}\right)^2 - 1 \leq 0. \tag{6.3}$$

This is shown in Fig. 6.1, where $f_t^{\max}$ is the maximum longitudinal force and $f_n^{\max}$ is the maximum lateral force. We assume that the initial and final vehicle velocities are given, and satisfy

$$\left.\frac{\mathrm{d}s}{\mathrm{d}t}\right|_{t=t_0} < \frac{f_n^{\max} r(s_0)}{m}, \qquad \left.\frac{\mathrm{d}s}{\mathrm{d}t}\right|_{t=t_f} \leq \frac{f_n^{\max} r(s_f)}{m}, \tag{6.4}$$

in order for the initial and final cornering forces to be less than the allowable limit $f_n^{\max}$ and also in order for some accelerating/braking force f_t to be available at t_0. Moreover, it will be assumed that the velocity of the vehicle is always greater than or equal to zero, that is, $\mathrm{d}s/\mathrm{d}t \geq 0$ for all $t \in [t_0, t_f]$. Specifically, the vehicle is not allowed to reverse direction, a natural assumption for a minimum-time problem.

From now on, and unless stated otherwise, we assume uniform acceleration limits $f_t^{\max} = f_n^{\max} = F_{\max}$, i.e., the total force lies within a circle of radius $F_{\max}$.

Consider the following state assignment and change of time scale:

$$\tau \triangleq \beta t, \qquad z_1 \triangleq \alpha\beta s, \qquad z_2 \triangleq \alpha \frac{\mathrm{d}s}{\mathrm{d}t}, \tag{6.5}$$

with $\alpha \triangleq \sqrt{m/F_{\max}}$ and $\beta \triangleq \alpha F_{\max}/m$. The state-space representation of the system may then be written as

$$\dot{z}_1 = z_2, \tag{6.6}$$

$$\dot{z}_2 = \frac{f_t}{F_{\max}}, \tag{6.7}$$

where $\dot{(\,)}$ denotes derivative with respect to τ. The control input in this formulation is f_t, and the maximum overall acceleration limit $F_{\max}/m$ translates to a state-dependent control constraint as follows

$$\left(\frac{f_t}{F_{\max}}\right)^2 + \left(\frac{z_2^2}{R(z_1)}\right)^2 - 1 \leq 0, \tag{6.8}$$

where $R(z_1) \triangleq r(z_1/(\alpha\beta))$.

The control constraint (6.8) can be written as

$$\frac{f_t}{F_{\max}} = u\sqrt{1 - \frac{z_2^4}{R^2(z_1)}}, \quad u \in [-1, +1]. \tag{6.9}$$

In terms of the new control variable u the dynamics of the system is written as

$$\dot{z}_1 = z_2, \qquad \dot{z}_2 = u\sqrt{1 - \frac{z_2^4}{R^2(z_1)}}, \quad u \in [-1, +1]. \tag{6.10}$$

In terms of the original variables, the equation of motion, using the elliptic force envelope constraint (6.3) can be written as

$$m\frac{\mathrm{d}^2 s}{\mathrm{d}t^2} = u\sqrt{(f_t^{\max})^2 - \frac{m}{r(s)}\left(\frac{f_t^{\max}}{f_n^{\max}}\right)^2\left(\frac{\mathrm{d}s}{\mathrm{d}t}\right)^2}, \tag{6.11}$$

where $u \in [-1, +1]$.

Note that the dynamics (6.10) are well defined only for trajectories inside the region $\mathcal{S} \subset \mathbb{R}^2$ of the state space defined by

$$\mathcal{S} \triangleq \{(z_1, z_2) : C_0(z_1, z_2) \triangleq z_2^2 - |R(z_1)| \leq 0\}. \tag{6.12}$$

In addition, controllability is maintained only at the interior of the set $\mathcal{S}$. At the boundary of the set $\mathcal{S}$ controllability is lost. The following lemma states that unless we have a path of constant curvature, the state constraint $C_0(z_1, z_2) \leq 0$ is always inactive for any finite interval of time, hence controllability is maintained for any path of nonzero curvature. In the following, $R'(z_1) = \partial R(z_1)/\partial z_1$.

Lemma 1 *Assume $R'(z_1) \neq 0$ for any $z_1 \in (z_\alpha, z_\beta) \subset [z_{10}, z_{1f}]$, where $z_{10} = z_1(\tau_0)$ and $z_{1f} = z_1(\tau_f)$. Then the manifold $\partial\mathcal{S} = \{(z_1, z_2) : C_0(z_1, z_2) = 0\}$ is not invariant for the system (6.10) for any control u.*

Proof: Invariance of $\partial\mathcal{S}$ with respect to (6.10) implies that

$$-\dot{z}_1 R'(z_1)\ \mathrm{sgn}R(z_1) + 2z_2\dot{z}_2 = 0, \tag{6.13}$$

equivalently,

$$-z_2 R'(z_1)\ \mathrm{sgn}R(z_1) = 0, \tag{6.14}$$

since $\dot{z}_2 = 0$ on $\partial\mathcal{S}$ for any $u \in [-1, +1]$. Since $z_2 > 0$ for all $z_1 \in (z_{10}, z_{1f})$, the last equation is satisfied if and only if $R'(z_1) = 0$. ■

An immediate consequence of Lemma 1 is the fact that $\partial\mathcal{S}$ is invariant under (6.10) only for paths of constant curvature.

Note that the flow of the trajectories of (6.10) in the vicinity of the constraint $C_0(z_1, z_2) = 0$ are given by

$$\begin{aligned}\frac{\mathrm{d}C_0(z_1, z_2)}{\mathrm{d}t} &= \frac{\partial C_0}{\partial z_1}\dot{z}_1 + \frac{\partial C_0}{\partial z_2}\dot{z}_2 \\ &= -\dot{z}_1 R'(z_1)\ \mathrm{sgn}R(z_1) + 2z_2\dot{z}_2 \\ &= -z_2 R'(z_1)\ \mathrm{sgn}R(z_1).\end{aligned}$$

It follows that

$$\frac{\mathrm{d}C_0(z_1, z_2)}{\mathrm{d}t} < 0, \quad \text{if} \quad R'(z_1)\ \mathrm{sgn}R(z_1) > 0 \tag{6.15}$$

and

$$\frac{\mathrm{d}C_0(z_1, z_2)}{\mathrm{d}t} > 0, \quad \text{if} \quad R'(z_1)\ \mathrm{sgn}R(z_1) < 0. \tag{6.16}$$

The following corollary is therefore immediate.

Corollary 1 *The set $\mathcal{S}$ is invariant for the system (6.10) only for paths of monotonically decreasing curvature (increasing radius). Such paths are characterized by the inequality $R'(z_1)\,\mathrm{sgn}R(z_1) > 0$.*

Given a certain path, characterized by its radius $R(z_1)$, the velocity z_2 for which the constraint $C_0(z_1, z_2) = 0$ is satisfied is thus of extreme importance for our problem. We will denote this velocity by $z_{2\mathrm{crit}}(z_1)$. It is given by

$$z_{2\mathrm{crit}}(z_1) \triangleq \sqrt{|R(z_1)|}. \tag{6.17}$$

When $z_2(z_1) = z_{2\mathrm{crit}}(z_1)$ for some $z_1 \in [z_{10}, z_{1f}]$ loss of controllability ensures. Corollary 1 essentially states that for paths of monotonically decreasing curvature loss of controllability can occur only instantaneously. This can also be seen from the following simple argument. Assume, for instance, that at some point $\tau_c \in (\tau_0, \tau_f)$, $z_2(\tau_c) = z_{2\mathrm{crit}}(z_1(\tau_c))$. The tangential component of the acceleration becomes zero and $\dot{z}_2(\tau_c) = 0$. Since the vehicle travels on a path of monotonically decreasing curvature (increasing radius), $|R(z_1(\tau_c^+))| > |R(z_1(\tau_c))|$, while $z_2(\tau_c^+) = z_2(\tau_c)$. It follows that the square root in the rhs of equation (6.10) will take a positive, non-zero value at $\tau = \tau_c^+$ and the system will regain controllability. For a path of monotonically increasing curvature (decreasing radius) on the other hand, the condition $z_2(\tau_c) = z_{2\mathrm{crit}}(z_1(\tau_c))$ at some point $\tau_c \in (\tau_0, \tau_f)$ leads to $\dot{z}_2(\tau_c) = 0$ and $z_2(\tau_c^+) = z_2(\tau_c)$, and since $|R(z_1(\tau_c^+))| < |R(z_1(\tau_c))|$, it follows that $z_2^2(\tau_c^+) \geq |R(z_1(\tau_c^+))|$. The quantity inside the square root at the right-hand-side of (6.10) becomes negative at τ_c^+. The equations are infeasible and a larger centripetal force than the available one $F_{\max}$ is needed for the vehicle to negotiate the path. It follows that for a path of monotonically increasing curvature (characterized by the inequality $R'(z_1)\,\mathrm{sgn}R(z_1) < 0$) we

cannot allow the vehicle to reach $z_{2\text{crit}}(z_1)$. In Section 6.3.2 we discuss this case in great detail and we show that optimal paths necessarily remain in $\mathcal{S}$.

We know turn to the solution of the minimum time problem for system (6.10).

6.2 Optimal Control Formulation

In reference to the system (6.10), and given fixed initial conditions $z_{10} = z_1$, $z_{20} = z_2$ at $\tau = \tau_0$ and final condition $z_{1f} = z_1$, $z_{2f} = z_2$ at $\tau = \tau_f$, we desire the optimal control u that drives the system (6.10) from point A to point B of the cartesian plane (Fig. 6.1) in minimum time τ_f subject to (6.12). We adopt the notation z_1^P and z_2^P for the path length coordinate z_1 and velocity z_2 of a point P of the prescribed path $R(z_1)$. Thus, we have $z_1^A = z_{10}$, $z_2^A = z_{20}$, $z_1^B = z_{1f}$ and $z_2^B = z_{2f}$. Notice that without loss of generality we may assume that $z_2(\tau) > 0,\ \forall\ \tau \in (\tau_0, \tau_f)$.

The cost function to be minimized is written as

$$J = \int_{\tau_0}^{\tau_f} \mathrm{d}\sigma. \tag{6.18}$$

The Hamiltonian for this problem is

$$H(z, \lambda, u) = 1 + \lambda_1 z_2 + \lambda_2 u \sqrt{1 - \left(\frac{z_2^4}{R^2(z_1)}\right)} + \mu C_0(z_1, z_2). \tag{6.19}$$

The system of adjoint equations is

$$\dot{\lambda}_1 = -\frac{\partial H}{\partial z_1} = -\lambda_2 u \frac{z_2^4}{\sqrt{1 - z_2^4/R^2(z_1)}} \frac{R'(z_1)}{R^3(z_1)} + \mu\ \mathrm{sgn} R(z_1) R'(z_1), \tag{6.20}$$

$$\dot{\lambda}_2 = -\frac{\partial H}{\partial z_2} = -\lambda_1 + 2\lambda_2 u \frac{z_2^3}{R^2(z_1)\sqrt{1 - z_2^4/R^2(z_1)}} - 2 z_2 \mu. \tag{6.21}$$

The Kuhn-Tucker conditions imply

$$\mu = 0 \text{ for } C_0(z_1, z_2) < 0 \quad \text{and} \quad \mu \geq 0 \text{ for } C_0(z_1, z_2) = 0. \tag{6.22}$$

The transversality condition implies $H(\tau_f) = 0$, and since the Hamiltonian does not depend explicitly on time it also follows that

$$H(\tau) = 0, \quad \forall\ \tau \in [\tau_0, \tau_f]. \tag{6.23}$$

Consider first the case of an inactive constraint, $C_0(z_1, z_2) < 0$. In this case $\mu = 0$ and Pontryagin's Maximum Principle leads to the optimal control

$$u^* = \text{argmin}_{u\in[-1,+1]} H(z, \lambda, u) = \begin{cases} -1 \text{ for } \lambda_2 > 0, \\ +1 \text{ for } \lambda_2 < 0, \end{cases} \tag{6.24}$$

which implies,

$$u^*(\tau) = -\,\text{sgn}\lambda_2(\tau). \tag{6.25}$$

Therefore λ_2 is the switching function, which determines the value of u^*.

Let us consider the possibility of a singular control interval in the optimal solution, i.e., the existence of a time interval $(\tau_1, \tau_2) \subset [\tau_0, \tau_f]$ such that $\lambda_2(\tau) = 0$, for all $\tau \in (\tau_1, \tau_2)$. Equation (6.20) implies that $\dot{\lambda}_1(\tau) = 0$ for all $\tau \in (\tau_1, \tau_2)$, or equivalently $\lambda_1(\tau) = \lambda_{10} = \text{constant}$ for all $\tau \in (\tau_1, \tau_2)$. Equation (6.21) implies $\dot{\lambda}_2(\tau) = -\lambda_{10}\tau$ for all $\tau \in (\tau_1, \tau_2)$. In addition, $\lambda_2(\tau) = 0$ and $\dot{\lambda}_2(\tau) = 0$ for all $\tau \in (\tau_1, \tau_2)$, and thus we have $\lambda_{10} = 0$ and $\lambda_1(\tau) = \lambda_2(\tau) = 0$ for all $\tau \in (\tau_1, \tau_2)$. Equation (6.19) then gives $H(\tau) = 1$ for $\tau \in (\tau_1, \tau_2)$, which contradicts the condition (6.23) that $H(\tau) = 0$ for all $\tau \in [\tau_0, \tau_f]$.

We have thus proven the following proposition.

Proposition 1 *Assuming that throughout the optimal trajectory $C_0(z_1, z_2) < 0$, there can be no singular subarc.*

This proposition states that to optimally transverse a path in minimum time, the maximum available force must be used at all times and the optimal trajectory is composed only of bang-bang subarcs ($u = +1$ or $u = -1$), assuming that the optimal state trajectory remains inside $\mathcal{S}$.

6.3 Solution for Special Cases of Path Curvature: Inactive Constraint

In the following, we provide solutions to the previous minimum-time problem for several special cases of $R(z_1)$. First, we consider the simplest case when the constraint

(6.12) remains inactive. According to Lemma 1 this occurs only if $R'(z_1) \neq 0$. We distinguish two different cases: paths of decreasing curvature and paths of increasing curvature.

6.3.1 Path of Decreasing Curvature

Consider a path of monotonically decreasing curvature from point A to point B in the cartesian plane denoted by

$$\mathcal{P}_{AB}^{+} = \left\{ (z_1, R(z_1)) : \ R'(z_1)\,\mathrm{sgn}R(z_1) > 0, \ z_1 \in [z_1^A, z_1^B] \right\}. \tag{6.26}$$

From Proposition 1 we know that the optimal path is composed solely of subarcs of maximum acceleration or maximum deceleration.

Equation (6.20) with $R'(z_1)\,\mathrm{sgn}R(z_1) > 0$ yields $\dot{\lambda}_1(\tau) \geq 0$, for all $\tau \in [\tau_0, \tau_f]$. Suppose now that there exists a switching time $\tau_1 \in (\tau_0, \tau_f)$. It follows that $\lambda_2(\tau_1) = 0$. The transversality condition (6.23) implies $\lambda_1(\tau_1) = -1/z_2(\tau_1)$. For any $\tau \in [\tau_0, \tau_1)$ we have that

$$\begin{aligned} -\frac{1}{z_2(\tau)} &\leq \frac{-1 + |\lambda_2|\sqrt{1 - z_2^4/R^2(z_1)}}{z_2(\tau)} = \lambda_1(\tau) \\ &\leq \lambda_1(\tau_1) = -\frac{1}{z_2(\tau_1)} \end{aligned} \tag{6.27}$$

since λ_1 is non-decreasing. Inequality (6.27) implies that $z_2(\tau) \leq z_2(\tau_1)$ for all $\tau \in [\tau_0, \tau_1)$, from which we conclude that τ_1 is a switching point from $u = +1$ to $u = -1$.

Following the same steps as for the switching point τ_1, it is easy to prove that any other switching point $\tau_2 \in (\tau_0, \tau_1)$ has to be from $u = +1$ to $u = -1$. Obviously, there can be no consecutive switching points from $u = +1$ to $u = -1$ without a switching from $u = -1$ to $u = +1$ in between. Thus, we rule out the possibility of existence of a second switching point $\tau_2 \in (\tau_0, \tau_1)$. Finally, suppose that there exists a switching point $\tau_3 \in (\tau_1, \tau_f)$. The transversality condition (6.23) implies $\lambda_1(\tau_3) = -1/z_2(\tau_3)$. Since λ_1 is non-decreasing we have that $\lambda_1(\tau_1) \leq \lambda_1(\tau_3)$ or that $-1/z_2(\tau_1) \leq -1/z_2(\tau_3)$ and finally that $z_2(\tau_1) \leq z_2(\tau_3)$, implying that the vehicle accelerates from τ_1 to τ_3, which contradicts the fact that $u(\tau) = -1$ for $\tau \in (\tau_1, \tau_3)$. It follows that we can have only one switching in the control.

Let now $Z_A^+(z_1)$ be the characteristic constructed by forward integration of (6.10) from (z_1^A, z_2^A) with $u = +1$, and $Z_B^-(z_1)$ be the characteristic constructed by backward integration of (6.10) from (z_1^B, z_2^B) with $u = -1$. We have therefore the following proposition for the optimal trajectory on paths of monotonically decreasing curvature.

Proposition 2 *In the case of a path of monotonically decreasing curvature $\mathcal{P}_{AB}^+$ there can be at most one switching in the control, from $u = +1$ to $u = -1$. In this case the optimal solution is given by*

$$z_2^*(z_1) = \min\left\{Z_A^+(z_1), Z_B^-(z_1)\right\}. \tag{6.28}$$

It is easy to prove the optimality of (6.28) directly, by showing that $z_2^*(z_1)$ in (6.28) maximizes the velocity pointwise for all $z_1 \in [z_1^A, z_1^B]$.

6.3.2 Path of Increasing Curvature

Consider a path of monotonically increasing curvature from point A to point B denoted in the cartesian plane by

$$\mathcal{P}_{AB}^- = \left\{(z_1, R(z_1)) :\ R'(z_1)\,\mathrm{sgn}R(z_1) < 0,\ z_1 \in [z_1^A, z_1^B]\right\}. \tag{6.29}$$

Similar to the case of a path of decreasing curvature, the optimal path is composed only of subarcs of maximum acceleration or maximum deceleration, assuming that the optimal trajectories remain in the interior of $\mathcal{S}$ (Proposition 1). An analysis similar to the one of Section 6.3.1 can be followed to show that, assuming the trajectories remain in $\mathcal{S}$, there can be at most one switch in the control, from $u = +1$ to $u = -1$. Below we show that the optimal trajectory does indeed remain in $\mathcal{S}$.

As before, let $Z_A^+(z_1)$ be the characteristic constructed by forward integration of (6.10) from (z_1^A, z_2^A) with $u = +1$, and $Z_B^-(z_1)$ be the characteristic constructed by backward integration of (6.10) from (z_1^B, z_2^B) with $u = -1$.

Lemma 2 *Assuming $z_2^B \le z_{2\mathrm{crit}}(z_1^B)$, then $Z_B^-(z_1) < z_{2\mathrm{crit}}(z_1)$ for all $z_1 \in [z_1^A, z_1^B)$.*

Proof: The proof involves two steps. First, we construct the locus $\mathcal{M}$ of points in the z_1-z_2 plane having the following property: the slope of any trajectory beginning from any point in $\mathcal{M} \subset \mathcal{S}$ using the control $u = -1$ is less than or equal to the slope of $z_{2\text{crit}}(z_1)$. In the second step we show that for characteristic path starting in $\mathcal{S}\backslash\mathcal{M}$ constructed by backward integration of (6.10) with $u = -1$ remains in $\mathcal{S}$.

To this end, note that the smallest possible slope in the z_1-z_2 plane of any feasible trajectory is achieved using maximum deceleration ($u = -1$). In particular, we have

$$\dot{z}_2 = u\sqrt{1 - \frac{z_2^4}{R^2(z_1)}} \Rightarrow z_2' = \frac{u}{z_2}\sqrt{1 - \frac{z_2^4}{R^2(z_1)}}, \tag{6.30}$$

which for $u = -1$ yields

$$z_{2\text{min}}' = -\frac{1}{z_2}\sqrt{1 - \frac{z_2^4}{R^2(z_1)}}. \tag{6.31}$$

On the other hand, the slope of the $z_{2\text{crit}}(z_1)$ characteristic in (6.17) is

$$z_{2\text{crit}}'(z_1) = \frac{\text{sgn}R(z_1)R'(z_1)}{2\sqrt{|R(z_1)|}} \triangleq \rho(z_1). \tag{6.32}$$

Using (6.31) and (6.32) we may enforce the inequality $z_{2\text{min}}' \leq z_{2\text{crit}}'$ by

$$P(z_2) \triangleq z_2^4 + R^2(z_1)\rho^2(z_1)z_2^2 - R^2(z_1) \leq 0. \tag{6.33}$$

Solving for z_2^2, the roots of $P(z_2)$ are

$$r_{1,2} \triangleq \frac{-R^2(z_1)\rho^2 \mp \sqrt{R(z_1)^4\rho^4 + 4R^2(z_1)}}{2}, \tag{6.34}$$

and for (6.33) to hold, given $z_2 > 0$, we must have

$$z_2 \leq \sqrt{r_2} = \left(\frac{-R^2(z_1)\rho^2(z_1) + \sqrt{R^4(z_1)\rho^4(z_1) + 4R^2(z_1)}}{2}\right)^{1/2}. \tag{6.35}$$

In the limiting case, when $z_{2\text{min}}' = z_{2\text{crit}}'$, we have $z_{2\text{safe}} = \sqrt{r_2}$. An explicit relationship between $z_{2\text{safe}}$ and $z_{2\text{crit}}$ is given by the equation

$$z_{2\text{safe}}^4 - z_{2\text{crit}}^4 + \left(\frac{R'(z_1)^2}{4}\right) z_{2\text{safe}}^2 z_{2\text{crit}}^2 = 0, \tag{6.36}$$

which implies that $z_{2\text{safe}}(z_1) < z_{2\text{crit}}(z_1)$ for all $z_1 \in [z_1^A, z_2^B]$. The set $\mathcal{M}$ is therefore the area underneath the curve $z_{2\text{safe}}(z_1)$. It follows that $\mathcal{M} \subset \mathcal{S}$. The $z_{2\text{crit}}(z_1)$ and $z_{2\text{safe}}(z_1)$ curves for paths of increasing curvature are shown in Fig. 6.2.

To finish the proof, notice that for any trajectory starting in $\mathcal{S}\backslash\mathcal{M}$ (the area between the characteristics $z_{2\text{safe}}(z_1)$ and $z_{2\text{crit}}(z_1)$ in Fig. 6.2) using $u = -1$, we have that $z'_{2\text{min}} > z'_{2\text{crit}}$. Integrating now backwards in time from z_1^B to z_1 ($\mathrm{d}z_1 < 0$) using $u = -1$ one obtains

$$\int_{z_1^B}^{z_1} \mathrm{d}z_{2\text{min}} < \int_{z_1^B}^{z_1} \mathrm{d}z_{2\text{crit}}, \tag{6.37}$$

or $z_{2\text{min}}(z_1) - z_{2\text{min}}(z_1^B) < z_{2\text{crit}}(z_1) - z_{2\text{crit}}(z_1^B)$. Since $z_{2\text{min}}(z_1^B) \leq z_{2\text{crit}}(z_1^B)$ for points in $\mathcal{S}\backslash\mathcal{M}$ it follows that $z_{2\text{min}}(z_1) < z_{2\text{crit}}(z_1)$. See also Fig. 6.3.

We conclude that for an increasing curvature path $\mathcal{P}_{AB}^-$,

$$Z_B^-(z_1) < z_{2\text{crit}}(z_1), \quad z_1 \in [z_1^A, z_1^B), \tag{6.38}$$

given that $z_2^B \leq z_{2\text{crit}}(z_1^B)$. ■

Lemma 2 implies, in particular, that

$$z_2(z_1) = \min\left\{Z_A^+(z_1), Z_B^-(z_1)\right\} < z_{2\text{crit}}(z_1), \quad z_1 \in [z_1^A, z_1^B). \tag{6.39}$$

Hence the constraint (6.12) remains inactive throughout the optimal trajectory. We have therefore shown the following result for the optimal trajectory on paths of monotonically increasing curvature.

Proposition 3 *In the case of a path of monotonically decreasing curvature $\mathcal{P}_{AB}^-$, there can be at most one switching in the control, from $u = +1$ to $u = -1$. In this case the optimal solution is given by*

$$z_2^*(z_1) = \min\left\{Z_A^+(z_1), Z_B^-(z_1)\right\}. \tag{6.40}$$

6.3.3 Numerical Example

Consider a path of increasing magnitude of the radius (decreasing curvature) from point A to point B as in Fig. 6.4(a), described by the following equation

$$R(z_1) = -0.5z_1 - 10. \tag{6.41}$$

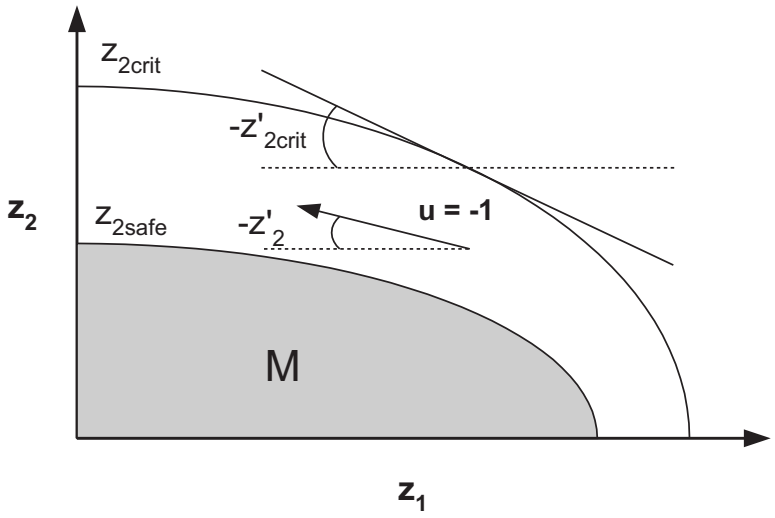

Figure 6.2: *In the area between* $z_{2\text{crit}}$ *and* $z_{2\text{safe}}$ *we can integrate backward in time with* $u = -1$ *without intersecting* $z_{2\text{crit}}$.

Assume that the vehicle starts from point A with zero velocity and reaches point B with zero velocity as well. The switching point SP is determined by the intersection of the characteristic $Z_A^+(z_1)$ in Fig. 6.4(b), created by forward integration of the equations of motion (6.10) with initial conditions (z_1^A, z_2^A) using $u = +1$, with the characteristic $Z_B^-(z_1)$, created by backward integration of the equations of motion with initial conditions (z_1^B, z_2^B) using $u = -1$. Equivalently, the optimal solution $z_2^*(z_1)$ is given by

$$z_2^*(z_1) = \min\left\{Z_A^+(z_1), Z_B^-(z_1)\right\}. \tag{6.42}$$

Figure 6.5 confirms that the optimality conditions hold, i.e. the switching function λ_2 changes sign at the switching point of the control input.

6.4 Solution for Special Cases of Path Curvature: Active Constraint

In this section we consider the case when the constraint (6.12) is active, that is $C_0(z_1, z_2) = 0$. First, observe that when the speed of the vehicle takes the critical

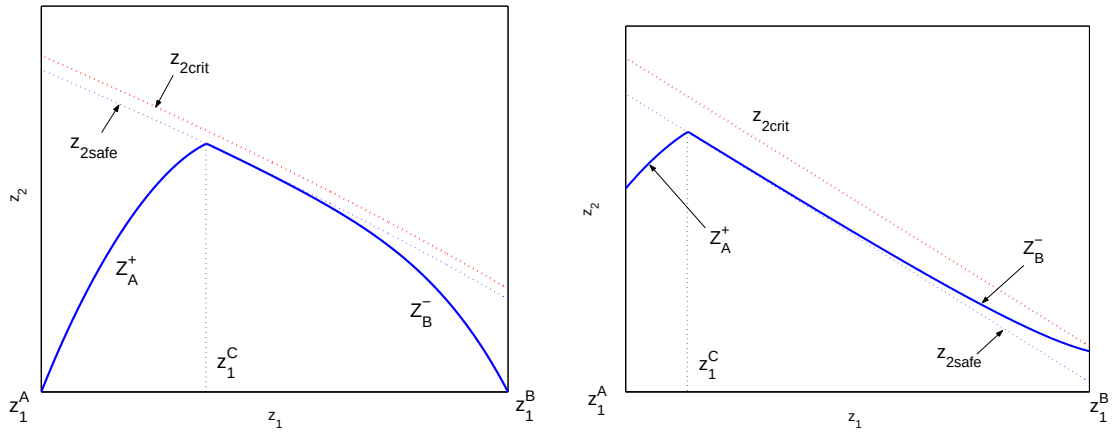

Figure 6.3: *Optimal solution for a path of decreasing curvature near the state constraint.*

value (6.17), equation (6.12) implies that $(z_1, z_2) \in \partial\mathcal{S}$. In this case $f_n = F_{\max}$ and $\dot{z}_2 = 0$ from (6.10). The control input u cannot affect the value of the velocity and loss of controllability ensues. This may also be interpreted as a loss of the ability to generate tangential force f_t, since the whole force capacity $F_{\max}$ is used to produce the required centripetal force f_n. From Lemma 1 it follows that this case is possible only for paths of constant curvature. In the remaining of this section we will therefore consider only paths with $R'(z_1) = 0$.

In order to avoid the difficulty arising from the loss of controllability for the case of a path of constant curvature, we introduce the constraint

$$C_\epsilon(z_1, z_2) \triangleq z_2^2 + \epsilon - |R(z_1)| = 0, \tag{6.43}$$

where $\epsilon > 0$ is a small positive scalar. We investigate optimal paths that satisfy this constraint and the we take $\epsilon \to 0$ to recover the case of $C_0(z_1, z_2) = 0$ at the limit.

An easy calculation shows that the control law that keeps the vehicle on the constraint (6.43) is given by

$$u_{\text{sc}} = \frac{R(z_1)R'(z_1)}{2\sqrt{2|R(z_1)|\epsilon - \epsilon^2}}, \tag{6.44}$$

which, upon $R'(z_1) = 0$ yields $u_{\text{sc}} \equiv 0$ for any $\epsilon > 0$. Hence $\lim_{\epsilon\to 0} u_{\text{sc}} = 0$.

Consider now a path of constant curvature $\mathcal{P}^0_{AF}$. Figure 6.6 shows the characteristic $Z^+_A(z_1)$ constructed by forward integration of (6.10) from (z_1^A, z_2^A) with $u = +1$, the

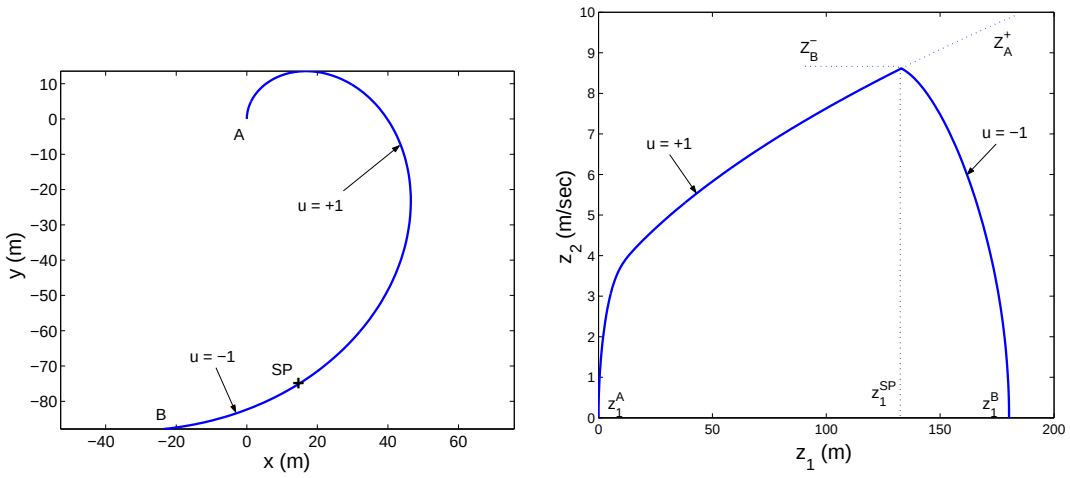

(a) (b)

Figure 6.4: *Optimal velocity profile through a path of increasing radius.*

characteristic $Z^0_{AF}(z_1)$ given by $z_2(z_1) = \sqrt{|R(z_1)| - \epsilon} < z_{2\text{crit}}(z_1)$, for $z_1 \in [z_1^A, z_1^F]$, with $\epsilon > 0$, and the characteristic $Z^-_F(z_1)$ constructed by backward integration of (6.10) from (z_1^F, z_2^F) with $u = -1$. Notice that the characteristic $Z^0_{AF}(z_1)$ is constructed with $u = 0$, which coincides with u_{sc} in (6.44) for $R'(z_1) = 0$. On the characteristic $Z^0_{AF}(z_1)$ the constraint (6.43) remains active, i.e., $C_\epsilon(z_1, Z^0_{AF}(z_1)) = 0$.

Proposition 4 *In the case of a path of constant curvature $\mathcal{P}^0_{AF}$, assuming $\epsilon > 0$, the optimal solution is given by*

$$z_2^*(z_1) = \min\left\{Z^+_A(z_1), Z^0_{AF}(z_1), Z^-_F(z_1)\right\}. \tag{6.45}$$

The trajectory from z_1^A to z_1^B in Fig. 6.6 maximizes point-wise the velocity since it is constructed using maximum acceleration $u = +1$ from a fixed initial velocity $z_2(\tau_0) = z_2^A$. The velocity of the trajectory from z_1^B to z_1^E is equal to the maximum allowable value, $\sqrt{|R(z_1)| - \epsilon}$. Finally, the trajectory from z_1^E to z_1^F on Z^-_F is also of maximum point-wise velocity, since Z^-_F is constructed using maximum acceleration $u = -1$ backward in time starting from a fixed initial velocity $z_2(\tau_f) = z_2^F$. Thus, the overall trajectory of (6.45) maximizes the velocity point-wise, which proves the optimality of the proposed solution.

Let now $\epsilon \to 0$ and assume that at some point $\tau_c \in (\tau_0, \tau_f)$ we have $z_2(\tau_c) = z_{2\text{crit}}(z_1(\tau_c))$, as in (6.17). This point corresponds to $(z_1^C, z_{2\text{crit}})$ in Fig. 6.6. Since

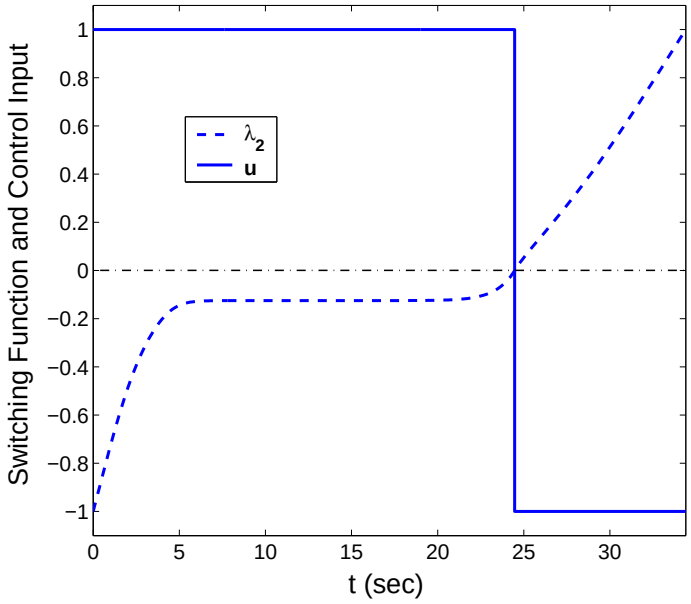

Figure 6.5: *Switching function and control input time history for the path shown in Fig. 6.4(a).*

the square root in equation (6.10) becomes zero, the tangential acceleration becomes zero and hence $\dot{z}_2(\tau_c) = 0$. Since we are on a path of constant curvature, $z_2(\tau) = z_{2\text{crit}}(z_1(\tau))$ for all $\tau \geq \tau_c$ and thus once controllability is lost, it cannot be regained. This means that when the vehicle operates at $(z_1^D, z_{2\text{crit}})$, it cannot switch to $Z_B^-(z_1)$ and the vehicle continues to travel with $z_{2\text{crit}}$. We conclude that in case of a path of constant curvature $\mathcal{P}_{AF}^0$, unless the final velocity $z_2^F = z_{2\text{crit}}(z_1^F)$ we cannot allow $\epsilon = 0$. We have therefore shown the following corollary.

Corollary 2 *Consider the minimum-time problem (6.10), and assume a path of constant curvature, $R(z_1) = c$. If $z_2(\tau_f) \neq \sqrt{|c|}$ an optimal solution does not exist.*

In the sequel we investigate paths composed of concatenations of paths investigated thus far. Such concatenations will allow us to construct the optimal trajectories, along with the corresponding optimal controls, by piecing together the solutions provided by Propositions 1-4.

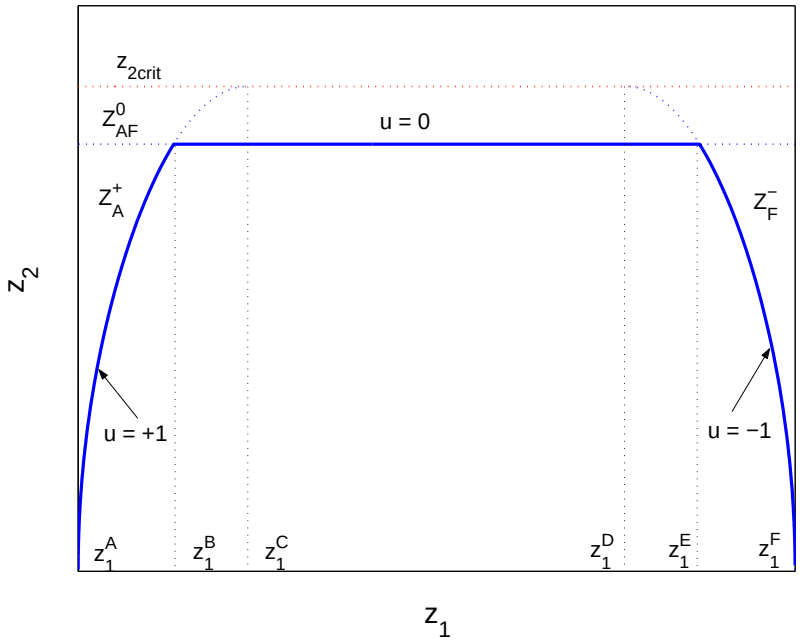

Figure 6.6: *Constant radius path; active constraint case.*

6.5 Path with $\min R(z_1)$

Consider now a path of increasing curvature $\mathcal{P}^{-}_{AC}$ followed by a path of decreasing curvature $\mathcal{P}^{+}_{CB}$ as in Fig. 6.7. We adopt the following notation for the path from point A to point B

$$\mathcal{P}^{\mp}_{ACB} = \mathcal{P}^{-}_{AC} \circ \mathcal{P}^{+}_{CB} = \big\{(z_1, R(z_1)) : R'(z_1)\,\mathrm{sgn}R(z_1) < 0,\ z_1 \in [z_1^A, z_1^C), \\ R'(z_1)\,\mathrm{sgn}R(z_1) > 0,\ z_1 \in [z_1^C, z_1^B])\big\}, \tag{6.46}$$

where "$\circ$" denotes the concatenation operator. The function $R(z_1)$ has a minimum at z_1^C (see Fig. 6.7).

Let $z_2^*(z_1)$ denote the minimum time solution from A to B and z_2^{C*} denote the velocity at point C of the $z_2^*(z_1)$ trajectory. According to Bellman's Principle of Optimality if the solution $A \to B$ is optimal then the first part of this solution, $A \to C$, solves the minimum time problem from A to C with the final condition $z_2(\tau_f) = z_2^{C*}$. Similarly, the second part, $C \to B$, solves the minimum-time problem from C to B with initial condition $z_2(\tau_0) = z_2^{C*}$.

The velocity z_2^{C*} is not known a priori however, and the solution $A \to B$ cannot

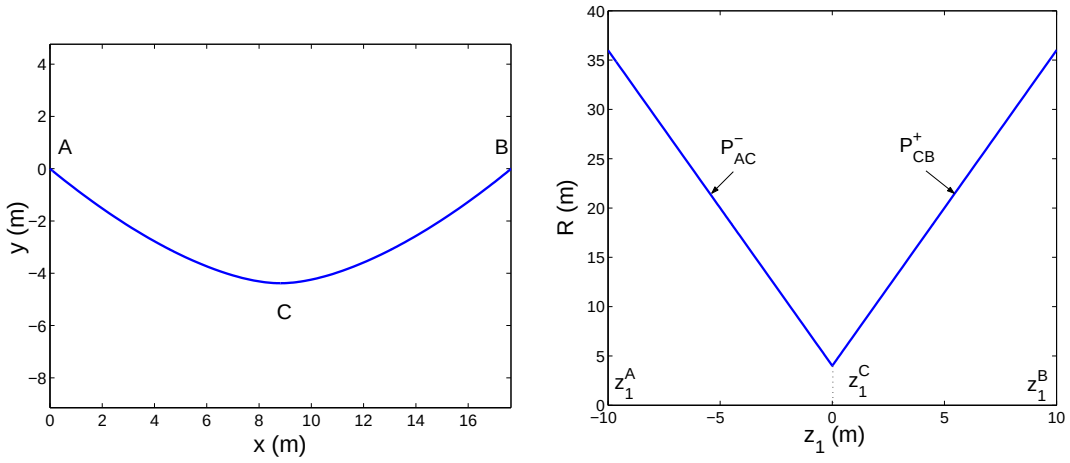

Figure 6.7: *Path with minimum radius at point C, in cartesian coordinates (left); path radius as a function of path length (right).*

be constructed from the solutions $A \rightarrow C$ and $C \rightarrow B$. Nonetheless, we do know the allowable switchings of the control for the subarcs $A \rightarrow C$ and $C \rightarrow B$ from the analysis in Sections 6.3.1 and 6.3.2.

On the part $A \rightarrow C$ we have a path of increasing radius, and according to Section 6.3.1 the possible optimal velocity profiles, summarized in Fig. 6.8(a), are: $u = +1$ (Case 1), $u = -1$ (Case 2) or $u = +1$ that switches once to $u = -1$ (Case 3). Similarly, on the part $C \rightarrow B$ we have a path of decreasing radius and according to Section 6.3.2 the possible optimal velocity profiles, summarized in Fig. 6.8(b), are: $u = +1$ (Case a), $u = -1$ (Case b) or $u = +1$ that switches once to $u = -1$ (Case c). For Bellman's Principle of Optimality to hold, the overall solution from A to B will consist of the subarcs $A \rightarrow C$ and $C \rightarrow B$ that correspond to Cases 1,2,3 and Cases a,b,c (Fig 6.8), respectively. Thus, all the possible optimal velocity profiles for the overall problem from A to B are all the possible combinations of Cases 1,2,3 and Cases a,b,c. These are shown in Fig 6.9. In the following, we discuss each case separately in order to compute the optimal velocity at point C.

Case 1a corresponds to $u = +1$ in both subarcs, $A \rightarrow C$ and $C \rightarrow B$ and the optimal solution $z_2^*(z_1)$ coincides with the characteristic $Z_A^+(z_1)$. Obviously, there is no other path that satisfies the boundary conditions at points A and B. The velocity at point C has to be less than or equal to $z_{2\text{crit}}(z_1^C)$. In this case the optimal velocity

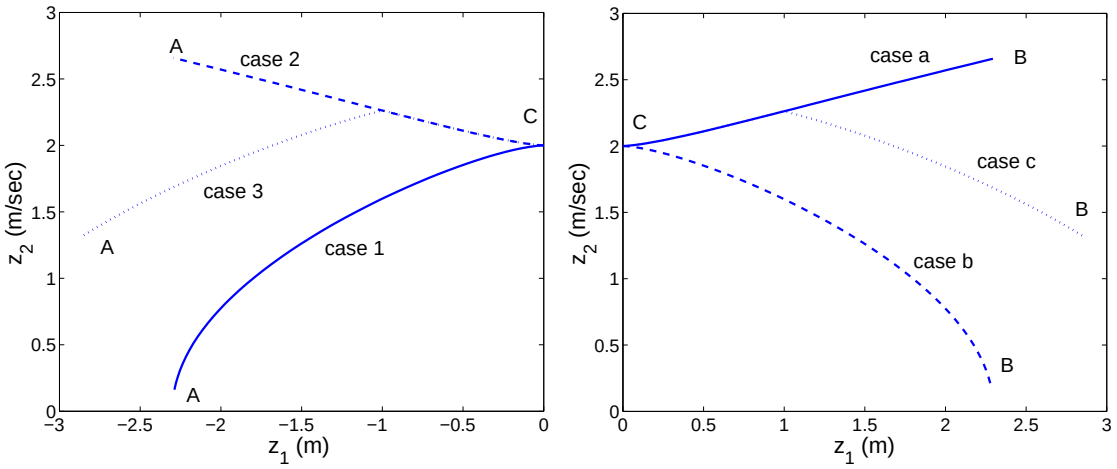

(a) $A \rightarrow C$ (b) $C \rightarrow B$

Figure 6.8: *Possible optimal velocity profiles before (left) and after (right) point C.*

z_2^{C*} is determined by the boundary conditions at A and B.

Case 1b corresponds to $u = +1$ from $A \rightarrow C$ and $u = -1$ from $C \rightarrow B$. Contrary to the previous case, it is now possible to satisfy the boundary conditions at A and B using acceptable control switchings. Consider, for example, the solution using the sequence of characteristics Z_A^+ $(u = +1)$, Z_m $(u = -1)$, Z_n $(u = +1)$, Z_B^- $(u = -1)$ shown in Fig. 6.9, Case 1b. However, it is obvious that the solution using one switching from Z_A^+ to Z_B^- maximizes velocity point-wise between A and B (for the given boundary conditions), and thus this is the optimal solution. Again, the velocity at point C has to be less than or equal to $z_{2\text{crit}}(z_1^C)$.

Case 1c corresponds to $u = +1$ from $A \rightarrow C$ and switching of the control from $u = +1$ to $u = -1$ along the subarc $C \rightarrow B$. This case is similar to the Case 1b. The overall trajectory consists of one switching from acceleration to deceleration. However, this time the switching does not take place at point C due to the different boundary conditions at A and B. Again, the velocity at point C has to be less than or equal to the critical one.

Case 2a corresponds to $u = -1$ from $A \rightarrow C$ and $u = +1$ from $C \rightarrow B$. Assume, as shown in Case 2a of Fig. 6.9, that there are other solutions that consist of admissible switchings, and which satisfy the same boundary conditions at points A and B. In

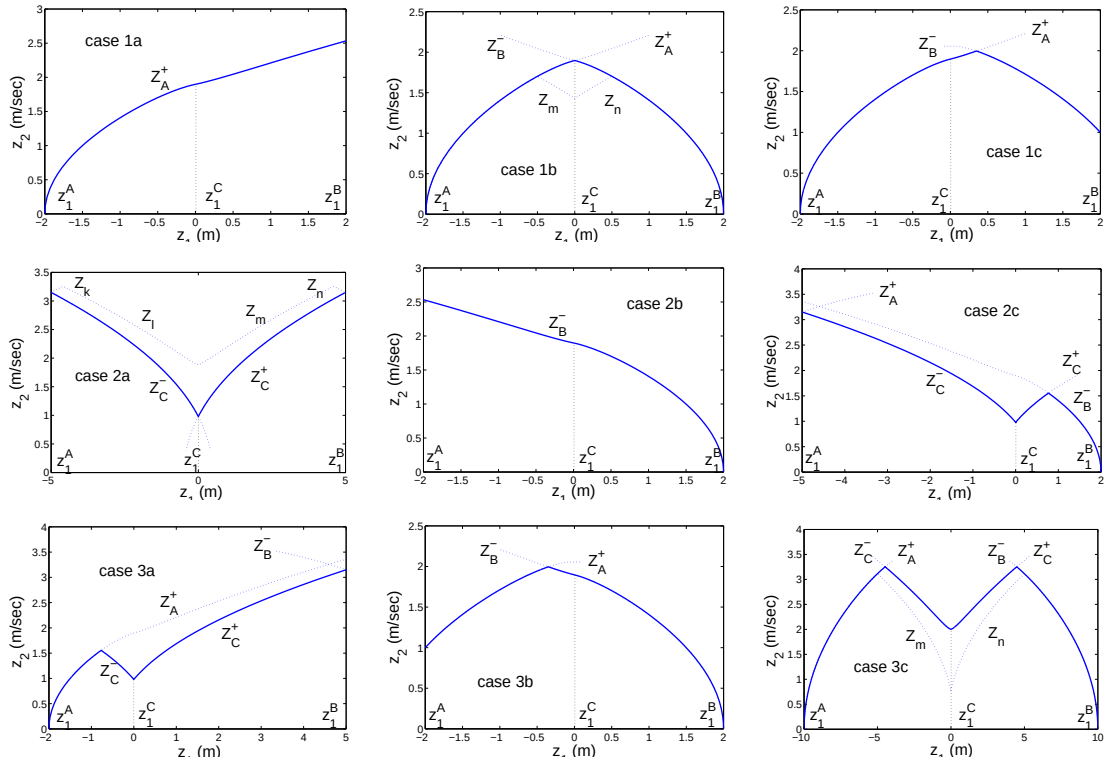

Figure 6.9: *All possible optimal velocity profiles from A to B.*

fact, the solution that corresponds to Case 2a, constructed by the characteristic paths Z_C^- and Z_C^+, is the one with the lowest velocity point-wise between A and B. We conclude that Case 2a will be optimal only if $z_2^{C*} = z_{2\text{crit}}(z_1^C)$, which is acceptable since a path of decreasing curvature follows after point C and controllability is regained immediately.

Case 2b corresponds to $u = -1$ in both subarcs, $A \to C$ and $C \to B$. It is completely equivalent to Case 1a if we reverse the boundary conditions at the points A and B.

Case 2c corresponds to $u = -1$ from $A \to C$ and one switching from $u = +1$ to $u = -1$ in the subarc from $C \to B$. As in Case 2a, unless $z_2^{C*} = z_{2\text{crit}}(z_1^C)$ there are other solutions that satisfy the boundary conditions at points A and B consisting of higher velocities at all points between A and B.

Case 3a corresponds to one switching from $u = +1$ to $u = -1$ along the subarc $A \to C$ and to $u = +1$ along $C \to B$. This case is equivalent to the Case 2c if we switch the boundary conditions of points A and B.

Case 3b corresponds to one switching from $u = +1$ to $u = -1$ along the subarc $A \to C$ and to $u = -1$ from $C \to B$. It is equivalent to Cases 1b and 1c; however, in this case the switching of control occurs before point C.

Case 3c corresponds to one switching from $u = +1$ to $u = -1$ along the subarc $A \to C$ and switching from $u = +1$ to $u = -1$ along the subarc $C \to B$. Unless $z_2^{C*} = z_{2\text{crit}}(z_1^C)$ there are other solutions that satisfy the boundary conditions at points A and B, which all consist of higher velocity at all points.

From the previous analysis we conclude that there are only two possible scenarios for the value of z_2^{C*}. In Cases 1a, 2a, 3a, 2b and 3b we have $z_2^{C*} \leq z_{2\text{crit}}(z_1^C)$ and z_{2C}^* is determined by satisfying the boundary conditions of A and B using allowable control switches. In Cases 2a, 2c, 3a and 3c we have $z_2^{C*} = z_{2\text{crit}}(z_1^C)$ and a control switch from $u = -1$ to $u = +1$ at C.

Next, we propose a methodology to construct the overall optimal solution for a path with curvature switching from increasing to decreasing at a point C. Starting from (z_1^A, z_2^A) we construct the characteristic $Z_A^+(z_1)$ integrating the equations of motion (6.10) forward in time using $u = +1$. Starting from (z_1^B, z_2^B) we construct the characteristic $Z_B^-(z_1)$ integrating the equations of motion (6.10) backward in time using $u = -1$. Starting from $(z_1^C, z_{2\text{crit}}(z_1^C))$ we construct the characteristic $Z_C^-(z_1)$ integrating the equations of motion (6.10) backward in time using $u = -1$. Finally, starting from $(z_1^C, z_{2\text{crit}}(z_1^C))$ we construct the characteristic $Z_C^+(z_1)$ integrating the equations of motion (6.10) forward in time using $u = +1$. The optimal velocity profile is then given by

$$z_2^*(z_1) = \min\left\{ Z_A^+(z_1), Z_C^-(z_1), Z_C^+(z_1), Z_B^-(z_1) \right\}. \tag{6.47}$$

It is easy to show that (6.47) reproduces all the cases of Fig. 6.9.

6.6 Path with $\max R(z_1)$

Consider now a path of decreasing curvature $\mathcal{P}_{AC}^+$ followed by a path of increasing curvature $\mathcal{P}_{CB}^-$. We adopt the following notation for the path from point A to point

B

$$\mathcal{P}^{\pm}_{ACB} = \mathcal{P}^{+}_{AC} \circ \mathcal{P}^{-}_{CB}. \tag{6.48}$$

Clearly, in this case the function $R(z_1)$ has a maximum at z_1^C. All possible scenarios that may appear along the subarcs $A \to C$ and $C \to B$ according to the solutions presented in Sections 6.3.1 and 6.3.2 may be summarized in accordance to Fig. 6.8.

In Section 6.5 we concluded that Cases 2a, 2c, 3a and 3c may appear as the optimal solutions only if the velocity at C is $z_2^{C*} = z_{2\text{crit}}(z_1^C)$. Since C is a point of maximum radius, the critical velocity at point C is larger compared to any other point from A to B. That is,

$$z_{2\text{crit}}(z_1) < z_{2\text{crit}}(z_1^C) \quad \text{for} \quad z_1 \in [z_1^A, z_1^C) \cup (z_1^C, z_1^B]. \tag{6.49}$$

On the other hand, in Cases 2a, 2c, 3a and 3c the velocity at point C is a local minimum. That is, there exists $\delta > 0$ such that $z_2^{C*} < z_2(z_1)$ for $z_1 \in (z_1^C - \delta, z_1^C + \delta)$. For $z_2^{C*} = z_{2\text{crit}}(z_1^C)$ equation (6.49) implies that $z_2(z_1) > z_{2\text{crit}}(z_1)$, for all $z_1 \in (z_1^C - \delta, z_1^C + \delta)$, and the vehicle cannot follow the prescribed path. We conclude that Cases 2a, 2c, 3a and 3c cannot appear as optimal solutions in the case of a path with a point C of maximum radius.

The only possible scenarios are Cases 1a, 1b, 1c, 2b and 3b, where the optimal velocity at C is determined by the initial and final boundary conditions. The optimal solution is finally given by

$$z_2^*(z_1) = \min\left\{Z_A^+(z_1), Z_B^-(z_1)\right\}. \tag{6.50}$$

6.7 General Solution

Assume that the given path from point A to point B is composed of a finite number of segments of constant curvature, of segments of monotonically increasing curvature and segments of monotonically decreasing curvature. Let the total number of segments be $n+1$. The path from point A to point B can then be expressed as

$$\mathcal{P}_{AB} = \mathcal{P}^{i_1}_{AP_1} \circ \mathcal{P}^{i_2}_{P_1P_2} \circ \mathcal{P}^{i_3}_{P_2P_3} \circ \cdots \circ \mathcal{P}^{i_{n+1}}_{P_nB}, \tag{6.51}$$

where $i_k \in \{+,\ -,\ 0\}$, $k = 1, 2, ..., n+1$.

Let $\mathcal{I}^{\mp}$ denote the set of indices corresponding to points of minimum radius of the path $\mathcal{P}_{AB}$, that is, $\mathcal{I}^{\mp} = \{j : i_j = -,\ i_{j+1} = +\}$, $\mathcal{I}^0$ denote the set of indexes corresponding to the first point of a segment of constant curvature, i.e. $\mathcal{I}^0 = \{j : i_j = 0,\ i_{j-1} \neq 0\}$.

The following algorithm provides an ϵ-suboptimal velocity profile for minimum time travel along the path $\mathcal{P}_{AB}$.

ALGORITHM FOR OPTIMAL VELOCITY PROFILE

- From (z_1^A, z_2^A) integrate the equations of motion (6.10) forward in time with $u = +1$ to construct the characteristic $Z_A^+(z_1)$.
- From (z_1^B, z_2^B) integrate the equations of motion (6.10) backward in time with $u = -1$ to construct the characteristic $Z_B^-(z_1)$.
- For each point of minimum radius P_k, $k \in \mathcal{I}^{\mp}$, construct the following characteristics: the characteristic $Z_{P_k}^-(z_1)$ by integrating (6.10) backward in time from $(z_1^{P_k}, z_{2\text{crit}}(z_1^{P_k}))$ using $u = -1$, and the characteristic $Z_{P_k}^+(z_1)$ by integrating (6.10) forward in time from $(z_1^{P_k}, z_{2\text{crit}}(z_1^{P_k}))$ using $u = +1$.
- For each segment $\mathcal{P}^0_{P_\ell P_{\ell+1}}$ of constant radius $R(z_1) = R_\ell$ where $\ell \in \mathcal{I}^0$, construct the following characteristics: the characteristic $Z^0_{P_\ell P_{\ell+1}}(z_1)$ of constant velocity equal to $\sqrt{|R_\ell| - \epsilon}$, for some $\epsilon > 0$, the characteristic $Z_{P_\ell}^-(z_1)$ by integrating backward in time from $(z_1^{P_\ell}, \sqrt{|R_\ell| - \epsilon})$ using $u = -1$, and the characteristic $Z_{P_{\ell+1}}^+(z_1)$ by integrating forward in time from $(z_1^{P_{\ell+1}}, \sqrt{|R_\ell| - \epsilon})$ using $u = +1$.
- The solution to the minimum time problem is given by

$$z_2^*(z_1) = \min\Big\{Z_A^+(z_1), Z_B^-(z_1), Z_{P_k}^-(z_1), \\ Z_{P_k}^+(z_1), Z^0_{P_\ell P_{\ell+1}}(z_1), Z_{P_\ell}^-(z_1), Z_{P_{\ell+1}}^+(z_1)\Big\}, \qquad (6.52)$$

  where $k \in \mathcal{I}^{\mp}$ and $\ell \in \mathcal{I}^0$.

The previous algorithm will give the optimal velocity profile in case $\mathcal{I}^0 = \varnothing$. Otherwise, and in light of Corollary 2, the solution is suboptimal in the sense that it can always be improved by taking $\epsilon \to 0$ but not zero. Proof of optimality can be easily provided by showing that this solution maximizes the velocity pointwise. We demonstrate this fact in the following example.

6.7.1 Example (General Solution)

Consider the path $\mathcal{P}_{AB}$ shown in Fig. 6.10(a). We can identify points of minimum radius at P_1, P_4 and P_9 ($\mathcal{I}^{\pm} = \{1, 4, 9\}$), and intervals of constant radius $\mathcal{P}_{P_5P_6}$ and $\mathcal{P}_{P_7P_8}$ ($\mathcal{I}^0 = \{5, 7\}$). Figure 6.10(b) shows the construction of the necessary characteristics using the rules of the previous section. The minimum time solution is given by (6.52) and it is shown in Fig. 6.11(a).

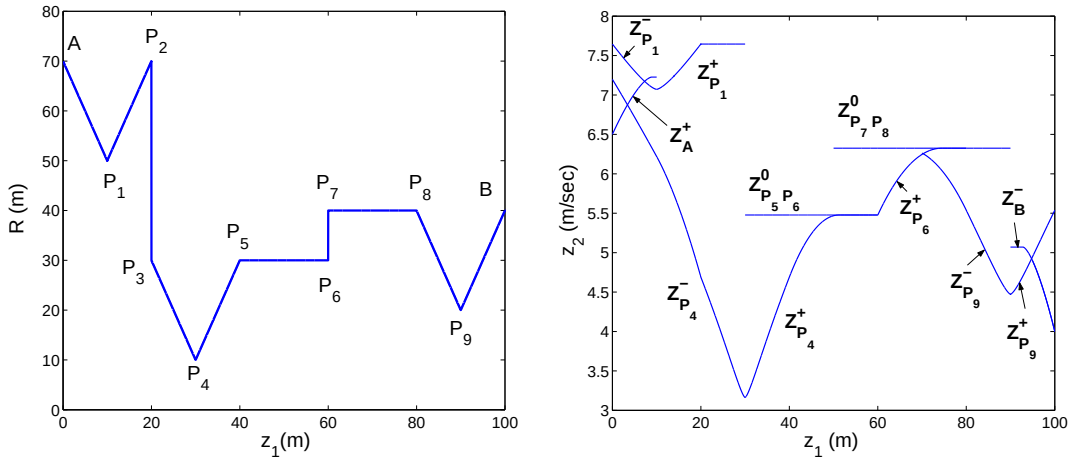

(a) (b)

Figure 6.10: *(a) A general case radius profile path; (b) the free boundary conditions problem solutions for constant radius and* min R *subarcs.*

Consider now the intervals (i) - (viii) along the optimal solution as in Fig. 6.11(b). In the interval (i) we use maximum acceleration $u = +1$ from the starting point A and thus the velocity is maximized point-wise in the interval (i). In (ii) the vehicle decelerates with $u = -1$ towards the critical velocity at P_4. A trajectory passing from a point of higher velocity in (ii) would violate the constraint (6.43) at P_4. After P_4 we have maximum acceleration and thus point-wise maximum velocity in (iii).

The velocity in (iv) is equal to the maximum allowable from (6.43). In (v) we have maximum acceleration and thus maximum velocity as in (iii). Point-wise maximality of the velocity in (vi) and (vii) is shown in accordance to (ii) and (iii) respectively. Considering the problem from B to A, the trajectory in (viii) corresponds to maximum acceleration from the fixed condition at B and thus it maximizes the velocity point-wise.

We conclude that the velocity is maximized point-wise throughout the trajectory from A to B, and thus the trajectory computed using (6.52) is the solution to the minimum time problem.

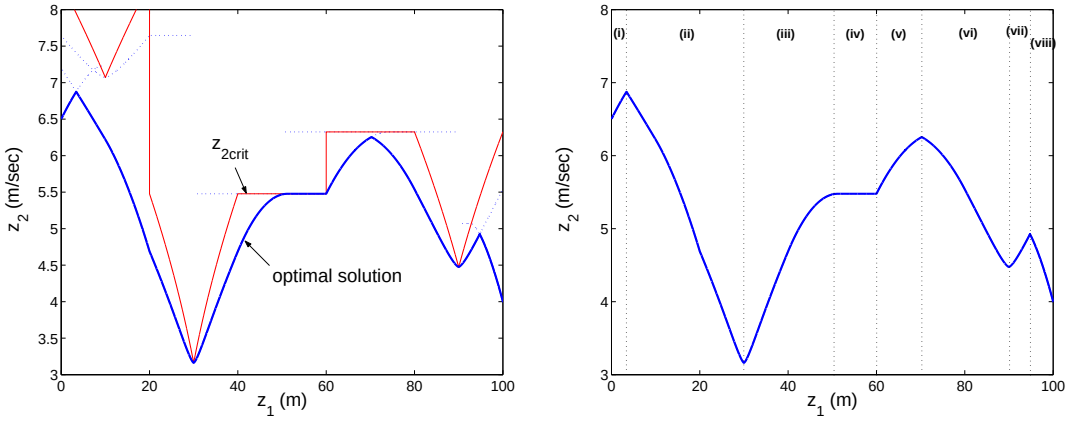

(a) (b)

Figure 6.11: *Optimal velocity profile for the general case path of Fig. 6.10.*

6.8 Application to an F1 circuit

In this section we validate the proposed methodology by applying it to an actual road track. Specifically, we use the previous methodology in order to generate the optimal velocity profile over a F1 circuit, given the acceleration limits of a typical F1 race car. The results are compared to the velocity profiles and lap times achieved by expert F1 race drivers.

Figure 6.12(a), taken from [6], shows the cartesian coordinates of the Silverstone F1 circuit. The data of Fig. 6.12(a) were used to generate the curvature profile

of this trajectory, which is shown in Fig. 6.12(b). By matching the performance

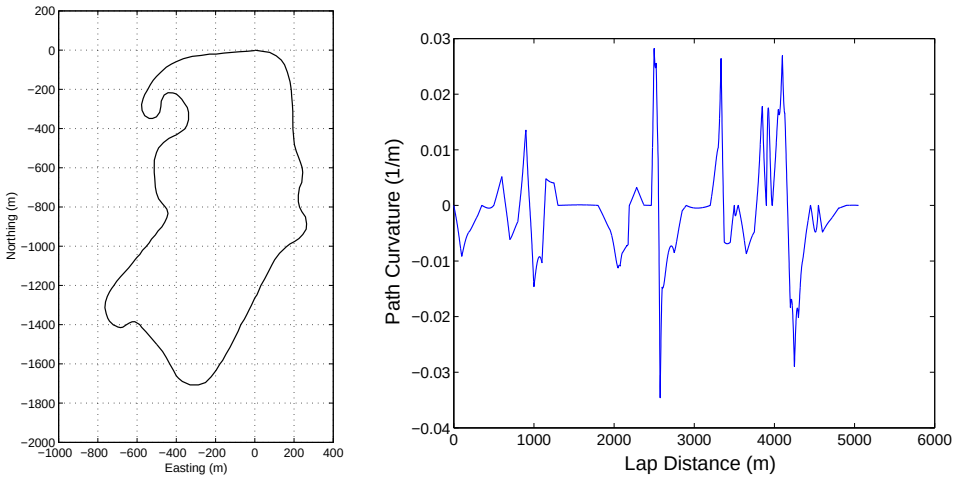

(a) (b)

Figure 6.12: *A trajectory followed by an F1 race car in the Silverstone F1 circuit [6] and its curvature profile.*

characteristics of the vehicles in [68], [6] we can approximate the acceleration limits of a typical F1 race car as follows

$$f_t^{\max}/m = \begin{cases} +16 - 0.0021v^2 \text{ m/sec}^2 \text{ for } u = +1, \\ -18 - 0.0021v^2 \text{ m/sec}^2 \text{ for } u = -1, \end{cases}$$

and

$$f_n^{\max}/m = 30 \text{ m/sec}^2.$$

The optimal velocity profile along the trajectory of Fig. 6.12 is calculated using the methodology of Section 6.7. The results are shown in Fig. 6.13(b). Figure 6.13(a), taken from [6], shows the velocity measurements for three laps of an F1 car along the Silverstone circuit. The optimally calculated lap time using the proposed approach is 82.7 sec. The measured lap times corresponding to the data of Fig. 6.13(a) are 86.063 sec, 90.891 sec and 85.805 sec respectively for each lap. Note that the record time for the Silverstone circuit belongs to K. Raikkonen (78.233 sec, McLaren Mercedes, 2004).

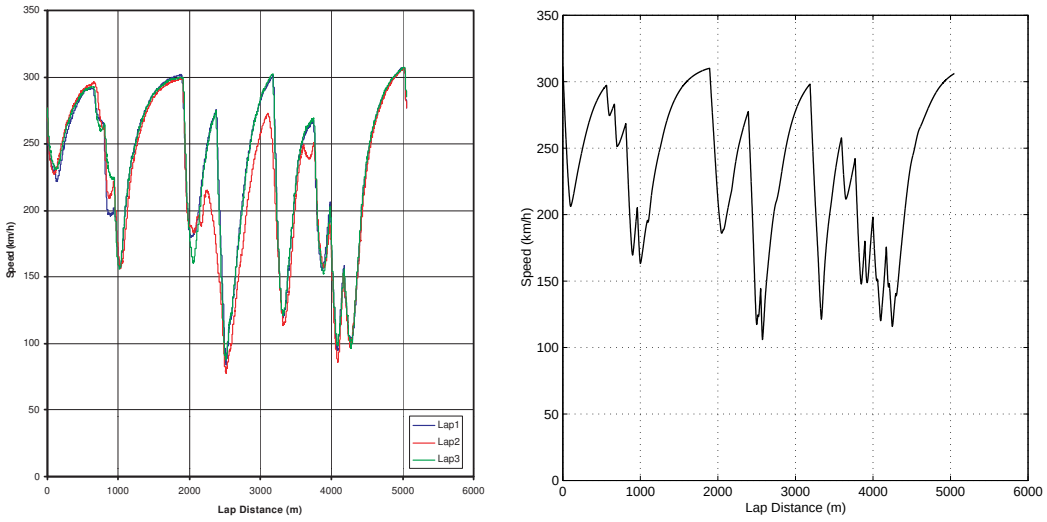

(a) (b)

Figure 6.13: *Velocity profiles through the Silverstone circuit: (a) achieved by human driver, (b) computed optimal.*

6.9 Receding Horizon Implementation

When the environment is changing the optimal profile needs to be generated on-line. One way to achieve this is for the trajectory optimization to be implemented in a receding horizon scheme rather than executed in one shot, from the start point to the end point. In [78] numerical optimization along with a receding horizon scheme was used for trajectory planning of an autonomous vehicle maneuvering through obstacles. By including the distance between the end of the horizon and the final destination point in the total cost, it was shown that the vehicle reaches the final point. In [79] an extension of the previous optimization scheme was proposed in order to avoid the entrapment of the vehicle in concave obstacles. The main idea is that the cost function is estimated off-line for the whole area where the vehicle may move. Areas that may lead to entrapment are penalized and the estimated cost is taken into consideration in the total cost. Finally, in [80] the receding horizon strategy of [78] was combined with a "safety algorithm". The "safety algorithm" computes an "escape plan" from the end of the horizon to a "safe" state (such as the vehicle coming to a stop), for each optimization step. If such an "escape plan" is not feasible, then the last optimization

step is not executed and the "escape plan" of the previous step is executed instead.

In this work we have assumed that the geometry of the trajectory is computed separately and it is provided to the velocity optimizer beforehand. Therefore, during a receding horizon implementation we assume that it is the job of the path planner to provide a feasible path that ensures obstacle avoidance and guarantees that the vehicle will reach its final destination. This can be achieved by following the same strategy as in [78],[79] and [80]. However, guarantees that the velocity will not exceed the critical value at any point, and that there exists an "escape plan" at the end of each optimization step, will have to be provided before the velocity optimizer is implemented in a receding horizon scheme. Below we propose a dynamic scheme to adaptively choose the planning and execution horizons to provide such guaranties.

6.9.1 Receding Horizon Scheme

Figure 6.14 shows a schematic that demonstrates how the receding horizon scheme works. The *Planning Horizon* (PH_i) is the distance from the current position up to the point which the i^{th} optimization step is performed. The *Execution Horizon* (EH_i) is a fraction of PH_i and it is the distance up to the point which the planned optimization will actually be executed. When the vehicle reaches the *Replanning Horizon* RH_i, which is a fraction of EH_i, the optimization is performed again up to the new planning horizon PH_{i+1}.

Let the vehicle be at the starting point ($s = s_0$ in Fig. 6.14). The optimization methodology is applied up to PH_1. After the optimization is completed, the vehicle may start executing the optimal trajectory up to EH_1. The shadowed area (i) in Fig. 6.14 shows the portion of the first optimization that is actually executed. When the vehicle reaches RH_1 the optimization is applied again from the current position RH_1 to the new planning horizon PH_2. The portion of the second optimization that will be actually executed is from EH_1 to EH_2 and it is shown as the shadowed area (ii) in Fig. 6.14. The process will end when the final destination is within the execution horizon. The distance between RH_i and EH_i is chosen such that enough time is allowed for the computation of the optimal trajectory from RH_i to PH_{i+1} before EH_i

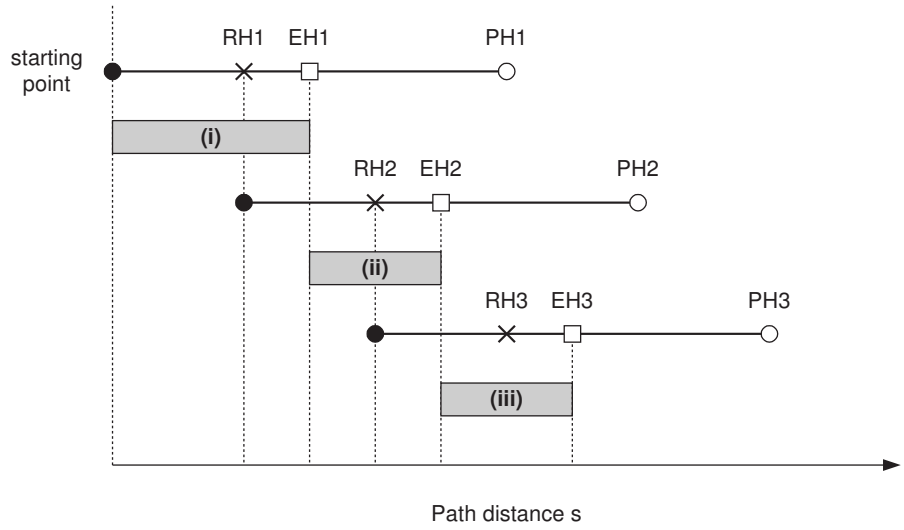

Figure 6.14: *Optimization with receding horizon.*

is reached. If the computation is instantaneous RH_i and EH_i can coincide. As already mentioned, the semi-analytical nature of the proposed algorithm results in minimal computational cost and thus from now on we will assume that the replanning and execution horizons coincide.

6.9.2 Robustness guarantees

In this section we propose an implementation scheme for the receding horizon optimization of the velocity profile along a given path. In particular, we propose a dynamic scheme to determine planning and execution horizons in the z_1 domain and guarantee the existence of an "escape plan" in the end of each executed subarc.

We propose the following formula to determine the planning horizon of the i^{th} optimization step

$$\mathrm{PH}_i = \max\{Tv_i, \mathrm{PH}_{\min}\}, \tag{6.53}$$

where v_i is the vehicle velocity at the position of the execution horizon of the previous optimization step EH_{i-1}, $v_i = z_2(\mathrm{EH}_{i-1})$, T is a constant "reaction" time, and $\mathrm{PH}_{\min}$ is the minimum planning horizon (typically for $v_i = 0$). This is not unlike the way a human driver chooses a planning horizon, that is, the larger the velocity, the longer

the "look ahead" distance needs to be. At the initial point A on the path, for the first optimization step $i = 1$ we have

$$\mathrm{EH}_0 = z_1^A. \tag{6.54}$$

The optimal solution from the current position EH_{i-1} to PH_i is calculated using (6.52) and is denoted by ${}^i z_2^*(z_1)$.

Next, we construct the characteristic from $(z_1 = \mathrm{PH}_i, z_2 = 0)$ integrating backwards in time using $u = -1$. This characteristic is denoted by ${}^i z_2^{\mathrm{esc}}(z_1)$ and is referred to as *escape trajectory* of the i^{th} optimization step. We choose the execution horizon for the i^{th} optimization step as follows:

$$\mathrm{EH}_i = \left\{ z_1 : \ {}^i z_2^*(z_1) = \ {}^i z_2^{\mathrm{esc}}(z_1), \ z_1 \in [\mathrm{EH}_{i-1}, \mathrm{PH}_i] \right\}. \tag{6.55}$$

In the case when

$$\{(z_1, {}^i z_2^*(z_1)), z_1 \in [\mathrm{EH}_{i-1}, \mathrm{PH}_i]\} \bigcap \{(z_1, {}^i z_2^{\mathrm{esc}}(z_1)), z_1 \in [\mathrm{EH}_{i-1}, \mathrm{PH}_i]\} = \varnothing \tag{6.56}$$

we need to increase T in (6.53) to determine a longer planning horizon until we can find the intersection point of the optimal solution and the escape trajectory (6.55).

At the end of each executed subarc EH_i we optimize up to the new planning horizon PH_{i+1}. The vehicle can decelerate enough to negotiate any corner outside PH_i since we have guaranteed that the vehicle starting from EH_i can come to a complete stop at PH_i. In case an obstacle exists after PH_i the vehicle can follow the escape trajectory to avoid collision. The Receding Horizon optimization scheme terminates when the end point B is within the execution horizon, namely $z_1^B \leq \mathrm{EH}_i$ for some i.

The proposed implementation is summarized in the block diagram of Fig. 6.14. The first optimization step using the above Receding Horizon scheme on the general case path of Section 6.7.1 is shown in Fig. 6.16. Let the planning horizon PH_1 from (6.53) be at 30m as in Fig. 6.16. The execution horizon EH_1 is determined by the intersection of ${}^1 z_2^*$ and ${}^1 z_2^{\mathrm{esc}}$. Observe that the solution generated by this implementation coincides with the infinite horizon solution of Section 6.7.1. If we randomly choose

PH_x and EH_x as in Fig. 6.16 we run the risk of reaching unacceptably high velocities. For example, the critical velocity at P_1 does not allow the vehicle to decelerate enough and negotiate the sharp turn at P_2. In this case notice that there is no intersection point between the optimal solution and the escape trajectory (characteristic ${}^{x}z_2^{\mathrm{esc}}$) and thus we need to increase T and choose a longer initial planning horizon.

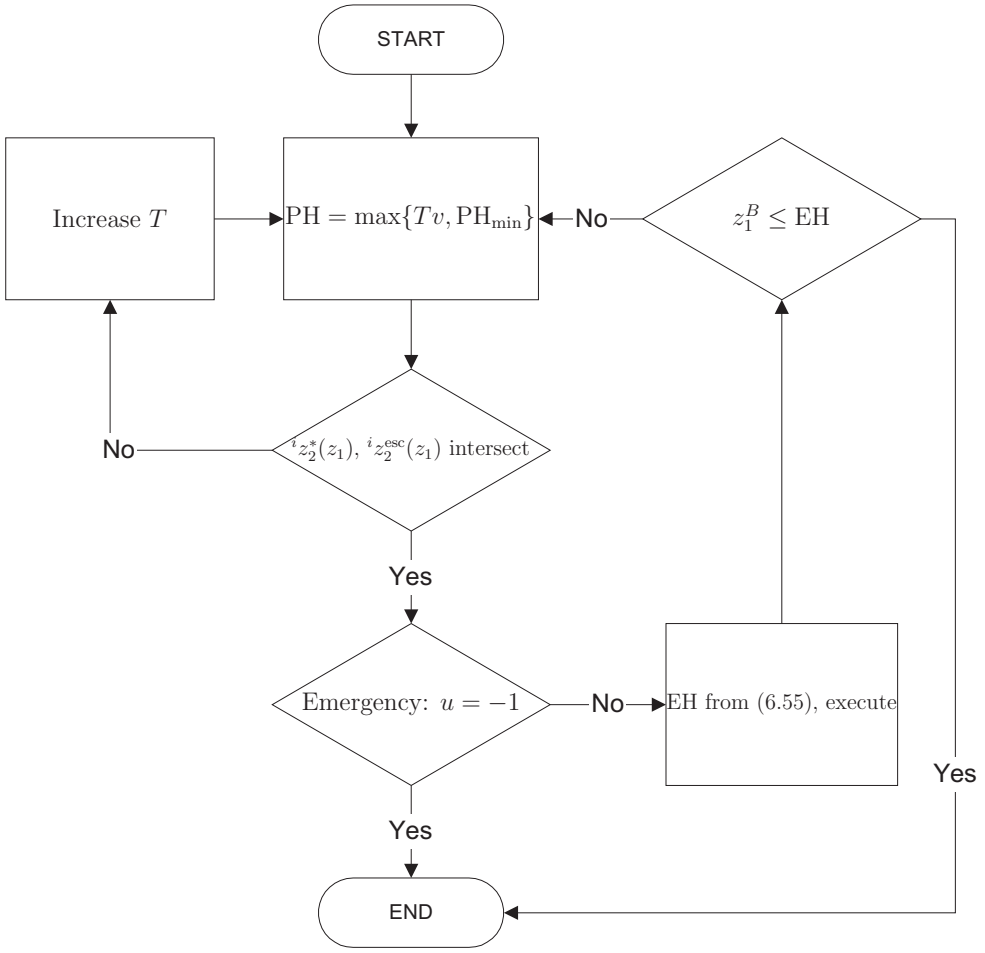

Figure 6.15: *Receding Horizon implementation block diagram.*

6.9.3 Numerical Example (Receding Horizon Implementation)

In this section we apply the proposed receding horizon algorithm to the F1 car trajectory of Section 6.8. We have chosen $T = 5$ sec, which for this example is enough

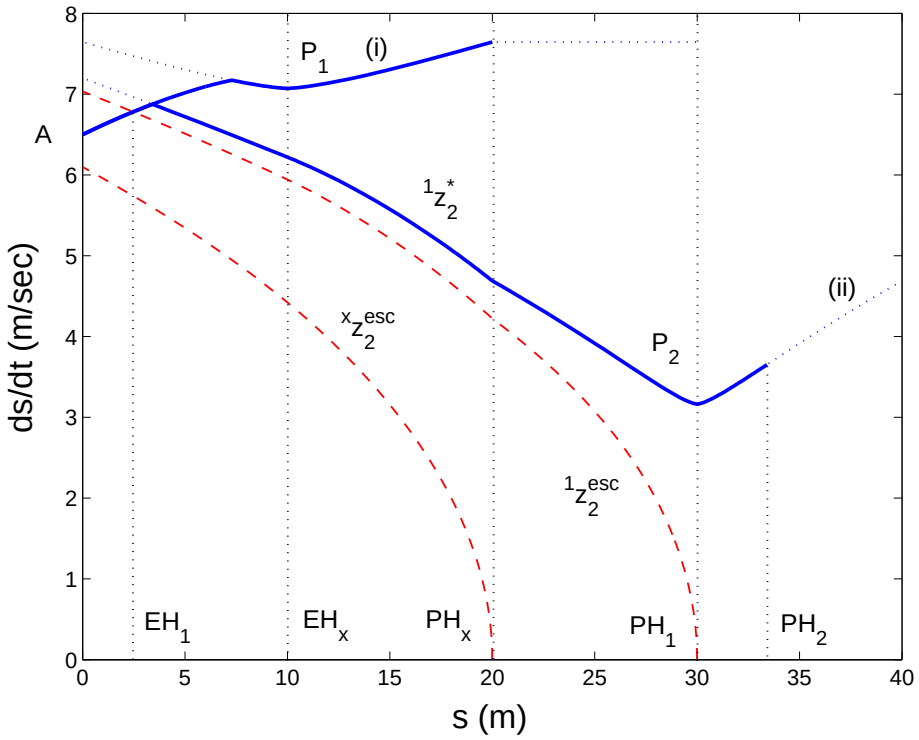

Figure 6.16: *Dynamic scheme for determination of* EH_i.

for the "emergency stop" characteristic to intersect the optimal solution within the planning horizon for each iteration. The minimum planning horizon was chosen as $\mathrm{PH}_{\min} = 200$ m.

In Fig. 6.17 the results of the first five steps of the receding horizon scheme are shown, along with the planning and execution horizons of each step. The solution (solid line) is compared with the infinite-horizon solution of the optimal velocity generator of Section 6.8 (dotted line). The two solutions coincide, thus confirming the validity of the proposed receding horizon scheme.

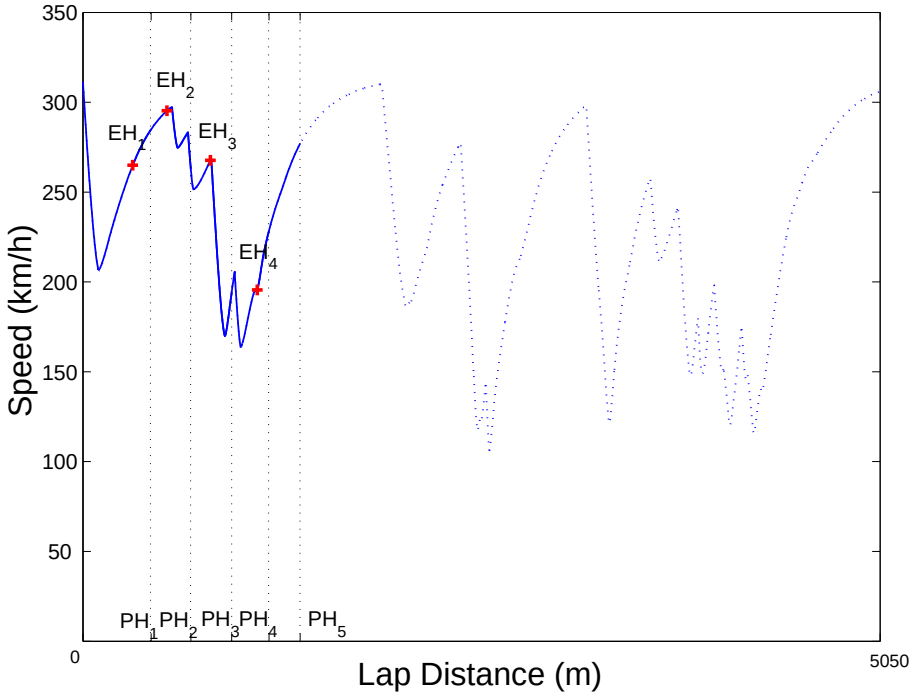

Figure 6.17: *Optimization with receding horizon for the Silverstone circuit.*

Chapter 7

Optimal Velocity Profile: Extension to a Half-Car Model

The analytic approach to the complex optimization problem of maneuvering of a wheeled vehicle subject to saturation constraints presented in the previous chapter compromises in the fidelity of the dynamical model used. To this end, in this chapter we extend the methodology described in the Section 6.7 to a half-car model in order to derive the missing attitude information of the vehicle's orientation. Care is taken such that we maintain stability of the yaw dynamics.

7.1 Acceleration Envelope of the Half-Car Model

7.1.1 The Half-Car Model

The equations of motion of a half-car model along a prescribed path as in Fig. 7.1, are given below

$$m\ddot{x} = (f_{Fx} + f_{Rx})\cos\psi - (f_{Fy} + f_{Ry})\sin\psi, \tag{7.1}$$

$$m\ddot{y} = (f_{Fx} + f_{Rx})\sin\psi + (f_{Fy} + f_{Ry})\cos\psi, \tag{7.2}$$

$$I_z\ddot{\psi} = f_{Fy}\ell_F - f_{Ry}\ell_R. \tag{7.3}$$

In these equations m is the vehicle's mass, I_z is the polar moment of inertia of

the vehicle about its center of mass (C.M.), x and y are the cartesian coordinates of the C.M. in the inertial frame of reference, ψ is the yaw angle of the vehicle, and f_{ij} $(i = F, R,\, j = x, y)$ denote the friction forces of the front and rear wheels, respectively, along the longitudinal and lateral body axes. Note that the speed v of the vehicle is given by $v = \sqrt{\dot{x}^2 + \dot{y}^2}$.

The tangential and centripetal forces at the center of mass, f_t and f_n respectively, are given by

$$f_t = (f_{Fx} + f_{Rx}) \cos\beta + (f_{Fy} + f_{Ry}) \sin\beta, \tag{7.4}$$

$$f_n = -(f_{Fx} + f_{Rx}) \sin\beta + (f_{Fy} + f_{Ry}) \cos\beta. \tag{7.5}$$

The path angle ϕ and the vehicle slip angle β (see Fig. 7.1) are given by

$$\phi = \arctan\left(\dot{y}/\dot{x}\right), \qquad \beta = \phi - \psi, \tag{7.6}$$

respectively.

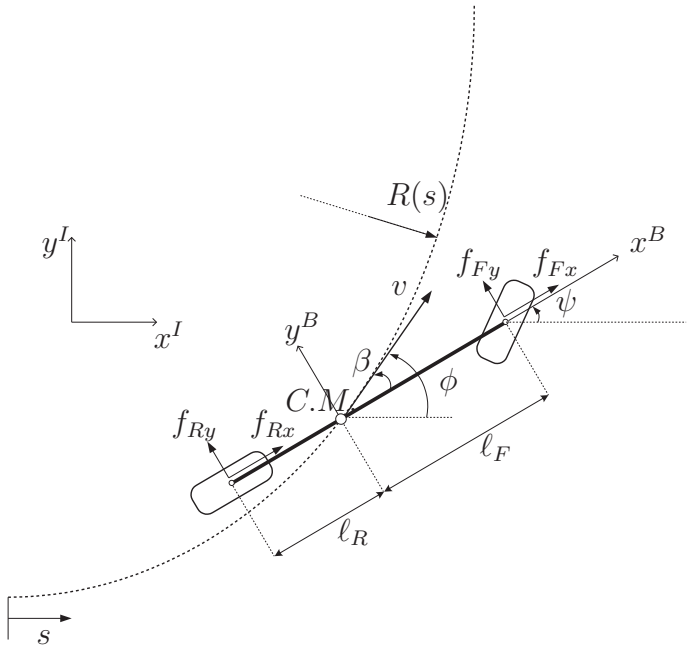

Figure 7.1: *A half-car model of a vehicle driving along a prescribed path* $R(s)$.

7.1.2 Construction of the GG-diagram

The equations of motion (7.1)-(7.3) are expressed in terms of the friction forces generated by the front and rear tires f_{ix} and f_{iy}, $(i = F, R)$, in the vehicle frame. In the sequel, we neglect power limitations due to the engine/transmission driveline. Such an assumption is more realistic when the vehicle operates on surfaces of low friction coefficient, such as wet road or dirt, where the adhesion limits of the tires are considerably reduced and dominate the overall acceleration capacity of the vehicle.

The tire friction forces are calculated using Pacejka's "Magic Formula" model [1] as follows.

$$f_{ij}^{\text{tire}} = -\frac{s_{ij}}{s_i} F_i, \qquad i = F, R \ \text{ and } \ j = x, y, \tag{7.7}$$

where f_{ij}^{tire} are the components of the front and rear wheel friction forces along the longitudinal and lateral tire axes respectively, s_{ix} is the longitudinal slip and s_{iy} is the lateral slip of the ith wheel[1]. In particular, we have that

$$f_{Rj} = f_{Rj}^{\text{tire}}, \tag{7.8}$$

$$f_{Fx} = f_{Fx}^{\text{tire}} \cos\delta - f_{Fy}^{\text{tire}} \sin\delta, \tag{7.9}$$

$$f_{Fy} = f_{Fx}^{\text{tire}} \sin\delta + f_{Fy}^{\text{tire}} \cos\delta, \tag{7.10}$$

where δ is the steering angle of the front wheel.

The total friction force of the front and rear wheel, F_i, is computed using

$$F_i = F_{iz} D \sin(C \text{atan}(B s_i)), \qquad i = F, R, \tag{7.11}$$

where F_{iz} is the normal load at the front and rear axles, and the total slip s_i is computed from

$$s_i \triangleq \sqrt{s_{ix}^2 + s_{iy}^2}, \qquad i = F, R. \tag{7.12}$$

The friction force at each wheel lies within a circle of radius equal to the maximum friction force $F_i^{\max}$, which is the maximum value of F_i in (7.11) attained at $s_i^{\max}$. This is shown in Fig. 7.2.

[1]The components f_{ij}^{tire} should not be confused with f_{ij} used in equations (7.1)-(7.3).

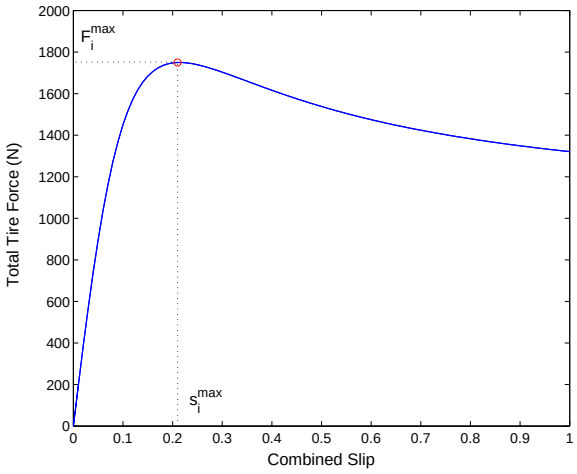

Figure 7.2: *Total friction force of the ith wheel with respect to the combined slip as given by the Magic Formula.*

We assume in the sequel that we can control the longitudinal slip s_{ix}, of the front and rear wheels independently, as well as the steering angle δ of the front wheel. This is a realistic assumption for modern vehicles equipped with variable ratio torque distribution systems such as Acura's SH-AWD and BMW's XDrive. Using the standard definition for the longitudinal slip [1], we may assume that $s_{ix} \in [-1, +1]$.

The expressions for the lateral slip of the front and rear wheels can be computed from

$$s_{Ry} \triangleq \frac{v \sin\beta - \dot{\psi}\ell_R}{v\cos\beta}, \tag{7.13}$$

$$s_{Fy} \triangleq \frac{v \sin(\beta-\delta) + \dot{\psi}\ell_F \cos\delta}{v\cos(\beta-\delta) + \dot{\psi}\ell_F \sin\delta}. \tag{7.14}$$

Notice that the rear lateral slip s_{Ry} is completely determined, for any given operating condition of the vehicle. Thus, for a given triplet $(v,\, \beta,\, \dot{\psi})$ – and assuming that we can control s_{Rx} – the rear friction force f_R lies on a characteristic curve $\mathcal{F}_R(s_{Ry})$ as in Fig. 7.3(a). That is,

$$f_R(s_{Ry}) \in \mathcal{F}_R(s_{Ry}) \triangleq \left\{ (f_{Rx}, f_{Ry}) :\ f_{Rj} = \frac{s_{Rj}}{s_R} F_R(s_R),\ s_{Rx} \in [-1,1],\ j = x, y \right\} \tag{7.15}$$

The front lateral slip s_{Fy}, however, depends also on the steering angle δ, which is one of the control variables. Figure 7.4 demonstrates that for any operating condition

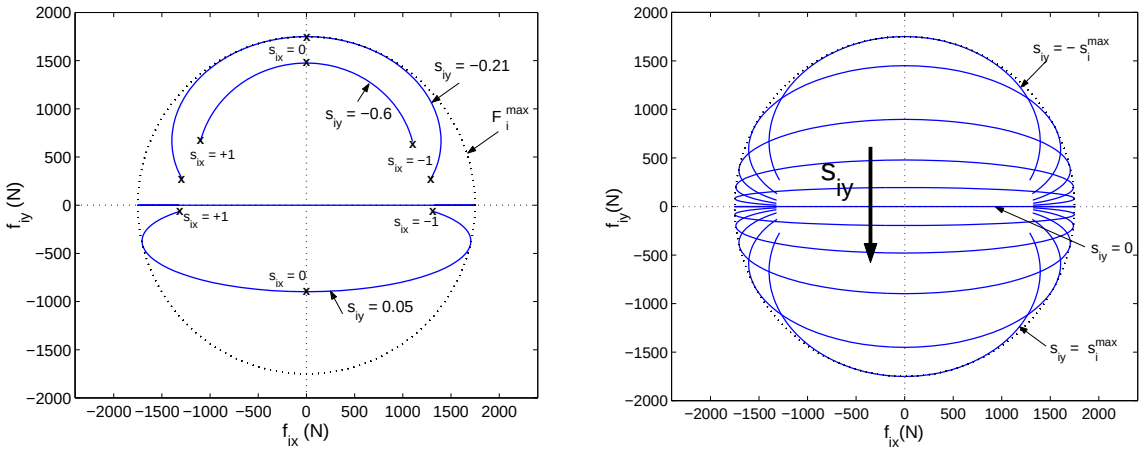

(a) (b)

Figure 7.3: *(a) Tire friction characteristic curves for fixed lateral slip s_{iy} and longitudinal slip $s_{ix} \in [-1, +1]$ $(i = F, R)$. (b) The whole friction circle can be constructed by tire friction characteristics for all $s_{iy} \in [-s_i^{\max}, s_i^{\max}]$.*

we may generate any front wheel lateral slip, $s_{Fy} \in [-s_F^{\max}, +s_F^{\max}]$ using a steering angle δ within a realistic range of $\delta \in [-\pi/4, +\pi/4]$. Figure 7.3(b) shows that the whole friction circle can be constructed by characteristics of s_{Fy} in the interval $[-s_F^{\max}, +s_F^{\max}]$. Thus, given any operating condition of the vehicle, and assuming that we can control independently the front longitudinal slip and steering angle, the front friction force f_F may be chosen anywhere inside the front wheel friction circle $\mathcal{F}_F$

$$f_F \in \mathcal{F}_F \triangleq \left\{ (f_{Fx}, f_{Fy}) : \sqrt{f_{Fx}^2 + f_{Fy}^2} \leq F_F^{\max} \right\}. \tag{7.16}$$

In Fig. 7.3 we consider the case of a neutrally balanced vehicle (the C.M. is in the middle of the wheelbase) with same tires in the front and rear wheels. For a neutrally balanced vehicle $F_{Fz} = F_{Rz}$ in (7.11) and $F_F^{\max} = F_R^{\max}$. Thus,

$$\mathcal{F}_R(s_{Ry}) \subset \mathcal{F}_F \quad \text{and} \quad \mathcal{F}_F = \bigcup_{s_{Ry} \in [-s_R^{\max}, s_R^{\max}]} \mathcal{F}_R(s_{Ry}). \tag{7.17}$$

We conclude that assigning s_{Rx}, s_{Fx} and δ as the control variables is equivalent to choosing f_R and f_F from (7.15) and (7.16), respectively. Hence, in the sequel we treat f_R and f_F, as the control to be determined to control the vehicle in lieu of s_{Rx}, s_{Fx} and δ.

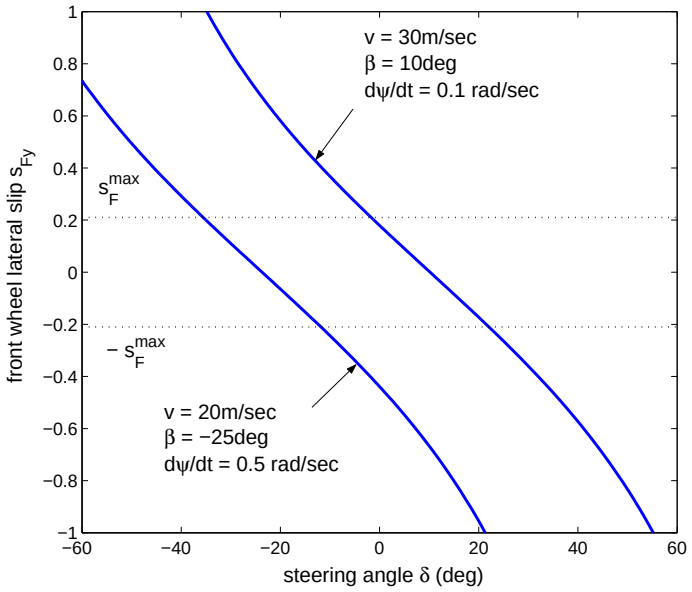

Figure 7.4: *Front lateral slip with respect to steering angle for given operating condition of the vehicle.*

The resultant force envelope $\mathcal{F}_{GG}(s_{Ry})$ at the center of mass of the vehicle, referred to as the GG-diagram in the vehicle dynamics literature [2], is constructed for each operating condition of the vehicle (v, β, $\dot{\psi}$), equivalently s_{Ry}, by adding the available front and rear tire friction forces, as in Fig. 7.5. $\mathcal{F}_{GG}(s_{Ry})$ is essentially the Minkowski sum[2] [82] of the front friction circle $\mathcal{F}_F$ and the rear wheel friction characteristic curve $\mathcal{F}_R(s_{Ry})$. That is,

$$\mathcal{F}_{GG}(s_{Ry}) = \mathcal{F}_F \oplus \mathcal{F}_R(s_{Ry}) \triangleq \{f_{GG} = f_F + f_R,\ f_F \in \mathcal{F}_F,\ f_R \in \mathcal{F}_R(s_{Ry})\}, \quad (7.18)$$

where $f_{GG} = (f_{GGx}, f_{GGy})$ is the resultant force at the center of mass expressed in the vehicle frame.

The optimal control strategy of Section 6.7 dictates that for minimum time travel the vehicle should use the maximum available acceleration or deceleration at each instant of time. For the case of the point mass model of Section 6.7 this corresponds to $u = \pm 1$. The maximum available acceleration for the half-car model is given by the boundary of $\mathcal{F}_{GG}(s_{Ry})$ denoted by $\partial\mathcal{F}_{GG}(s_{Ry})$. Notice that for any $f_{GG}(s_{Ry}) \in$

[2]Efficient algorithms to compute the Minkowski sum of two sets in the plane can be found in any good book on computational geometry; see, for instance, [81].

$\partial\mathcal{F}_{GG}(s_{Ry})$ there exists unique pair $f_F(s_{Ry}) \in \partial\mathcal{F}_F$ and $f_R(s_{Ry}) \in \mathcal{F}_R(s_{Ry})$, such that $f_{GG}(s_{Ry}) = f_F(s_{Ry}) + f_R(s_{Ry})$. In other words, one can define the following one-to-one mapping

$$\mathcal{M} : \partial\mathcal{F}_F \times \mathcal{F}_R(s_{Ry}) \mapsto \partial\mathcal{F}_{GG}(s_{Ry}) \tag{7.19}$$

defined by

$$f_{GG}(s_{Ry}) = \mathcal{M}(f_F(s_{Ry}), f_R(s_{Ry})), \tag{7.20}$$

along with its inverse

$$(f_F(s_{Ry}), f_R(s_{Ry})) = \mathcal{M}^{-1}(f_{GG}(s_{Ry})). \tag{7.21}$$

This is shown in Fig. 7.6. An extension of the optimal control strategy described in Section 6.7 now becomes evident. Given an operating condition of the vehicle (v, β, $\dot{\psi}$) and the geometry of the path $R(s)$, we can calculate the necessary centripetal force f_n from (6.2) such that the vehicle follows the path. We can also determine the tangential and normal directions to the path with respect to the orientation of the vehicle (these are denoted by e_t and e_n respectively in Fig. 7.5). The calculated f_n lies along the normal direction e_n and may be produced by only two possible total forces f_{GG}^+ and f_{GG}^- on $\partial\mathcal{F}_{GG}$ (Fig. 7.5). The force f_{GG}^+ produces an accelerating tangential force f_t, which corresponds to $u = +1$, and f_{GG}^- produces a braking force that corresponds to $u = -1$. From (7.21) we can determine the friction forces at the front and rear wheels $f_F = (f_{Fx}, f_{Fy})$, $f_R = (f_{Rx}, f_{Ry})$ given $f_{GG}^{\pm}$ (Fig. 7.6). We can now use these forces to integrate the equations of motion (7.1)-(7.3). The schematic in Fig. 7.7 describes the procedure to determine the forces f_F and f_R, equivalently s_{Fx}, s_{Rx} and δ, given the state of the system.

7.2 Direct Implementation of the Point Mass Control Strategy

In this section we implement the control strategy of Section 6.7 to the half-car model along a path with a point of minimum radius.

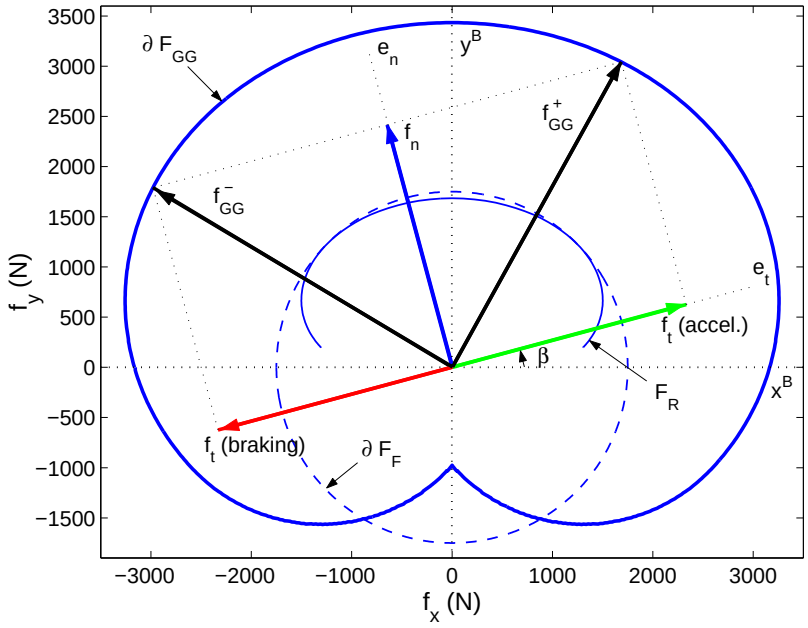

Figure 7.5: *GG-diagram for a given operating condition of the vehicle.*

Consider the path of Fig. 7.8(a) with radius profile as shown in Fig. 7.8(b). The radius profile takes its minimum value at point P_1. According to the methodology of Section 6.7 the velocity of the vehicle is equal to v_{crit} at $s_{P_1} = 0$ in order for the generated centripetal force to match the total acceleration capacity of the vehicle. The vehicle uses maximum deceleration ($u = -1$) before the point P_1 and maximum acceleration ($u = +1$) after the point P_1.

Our first task is to determine the critical velocity $v_{\text{crit}}(s_{P_1})$ of the half-car model at P_1. For this value of the velocity the centripetal force on the vehicle matches the vehicle's acceleration capacity ($f_n \in \partial F_{GG}$). As demonstrated in Section 7.1.2 the acceleration capacity F_{GG} of the half-car model depends on v, β and $\dot{\psi}$. For consistency, we enforce

$$\beta(s_{P_1}) = 0, \qquad \dot{\psi}(s_{P_1}) = v(s_{P_1})/R(s_{P_1}). \tag{7.22}$$

The conditions (7.22) imply that the vehicle satisfies the steady-state cornering requirement [2, 22], at the point of minimum radius P_1.

It follows from conditions (7.22) that the lateral slip of the rear wheel at P_1 is

$$s_{Ry}(s_{P_1}) = -\ell_R/R(s_{P_1}). \tag{7.23}$$

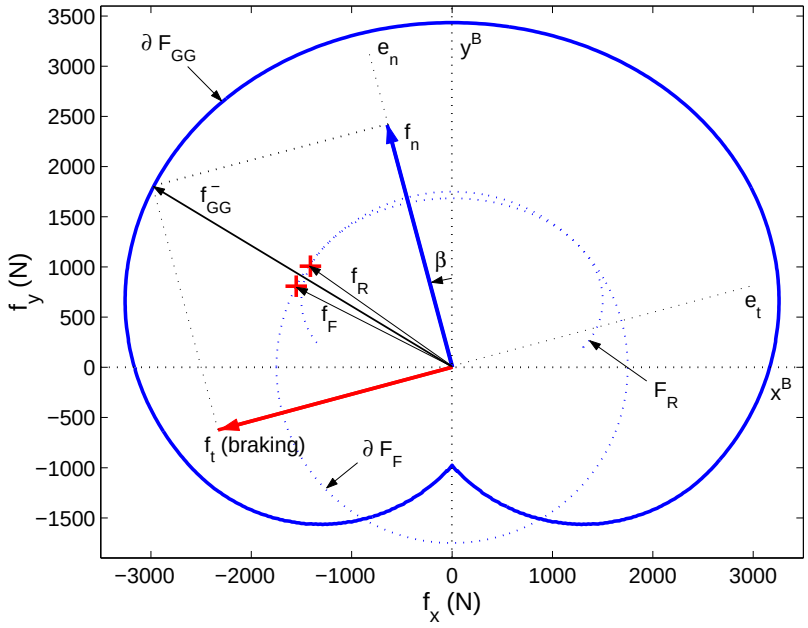

Figure 7.6: *Using $\mathcal{M}^{-1}$ we can calculate the front and rear axle forces f_F and f_R when the vehicle operates at the limit of its acceleration capacity: Maximum deceleration case f_{GG}^-.*

At P_1 the rear tire force along the normal direction e_n coincides with the lateral friction force f_{Ry}, since $\beta = 0$. Notice also from Fig. 7.3(a), that $f_{Ry}(s_{P_1})$ is maximized when $f_{Rx}(s_{P_1}) = 0$. Recall that we may use any front tire force within the friction circle of radius $F_F^{\max}$. In order to maximize the contribution of the front tire to the centripetal force we therefore choose $|f_{Fy}(s_{P_1})| = F_F^{\max}$ and $f_{Fx}(s_{P_1}) = 0$. It follows that the velocity of the half-car model at the point of minimum radius P_1 is given by

$$v_{\text{crit}}(s_{P_1}) = \sqrt{\frac{|R(s_{P_1})|(F_F^{\max} + |f_{Ry}(s_{P_1})|)}{m}}. \tag{7.24}$$

We can now construct the trajectory according to the optimal control strategy of Section 6.7: We integrate the equations (7.1)-(7.3) forward in time using f_{GG}^+ and backwards in time using f_{GG}^- from Section 7.1.2, and with initial conditions (7.22) and (7.24). The vehicle trajectory is shown in Fig. 7.9.

The resulting velocity profile is shown in Fig. 7.10(a) and the vehicle slip angle β is shown in Fig. 7.10(b). The longitudinal, lateral and total friction forces, f_{ix}, f_{iy} and f_i, of the front and rear tires are shown in Figs 7.11(a) and 7.11(b) respectively.

In both accelerating and braking phases, we notice an increase in the magnitude

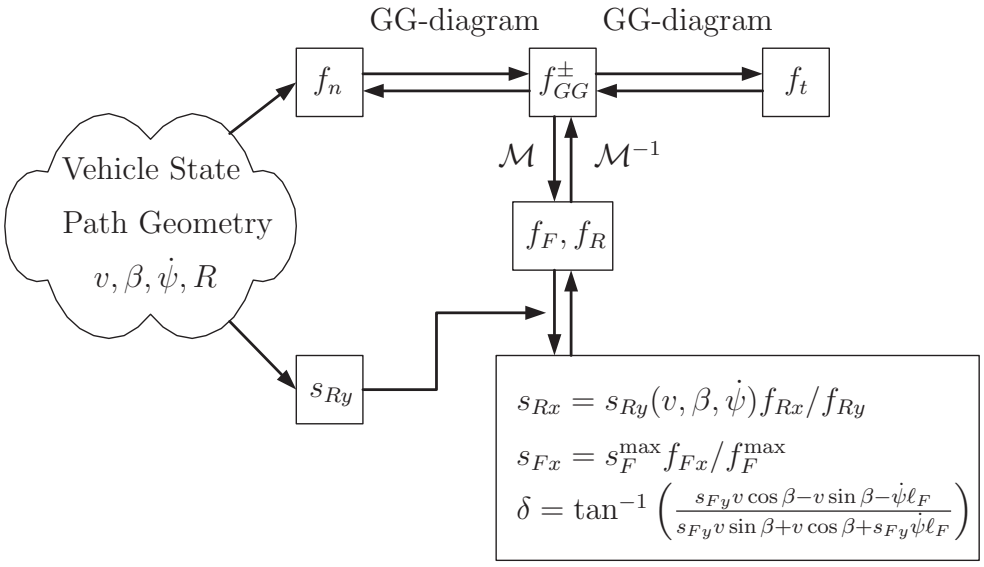

Figure 7.7: *From the operating condition of the vehicle and path geometry, we can calculate the required centripetal force. Using the GG-diagram we can then calculate the maximum acceleration/deceleration $f_{GG}^{\pm}$, and from $\mathcal{M}^{-1}$ we can calculate the corresponding front and rear tire forces f_F, f_R. The equivalent control inputs s_{Rx}, s_{Fx} and δ can finally be calculated from f_F, f_R.*

of the vehicle slip angle β and in particular, an oversteering tendency of the vehicle. Oversteer occurs when the "destabilizing" yaw moment of the front tire $\ell_F f_{Fy}$ is greater than the "restoring" yaw moment of the rear tire $\ell_R f_{Ry}$ [2]. Oversteer appears as a "nose-in" spin of the vehicle (Fig. 7.9), i.e. when the vehicle slip angle develops in a direction such as $\beta\,\mathrm{sign}(R) < 0$.

Using $\ell_F = \ell_R$ and $\mathcal{F}_R \subset \mathcal{F}_F$ for our vehicle configuration, the tendency to oversteer near the point of minimum radius is easily seen using the fact that at point P_1 we have $\beta = 0$, $f_{Ry} = f_R \in \mathcal{F}_R$ and $f_{Fy} = f_F \in \partial\mathcal{F}_F$. Hence near P_1 we have $|\ell_R f_{Ry}| \leq |\ell_F f_{Fy}|$ as it can be confirmed in Fig. 7.11.

In the following we propose a methodology to implement the optimal strategy of Section 6.7 to the half-car model in a stable manner, that is, by eliminating excessive oversteer.

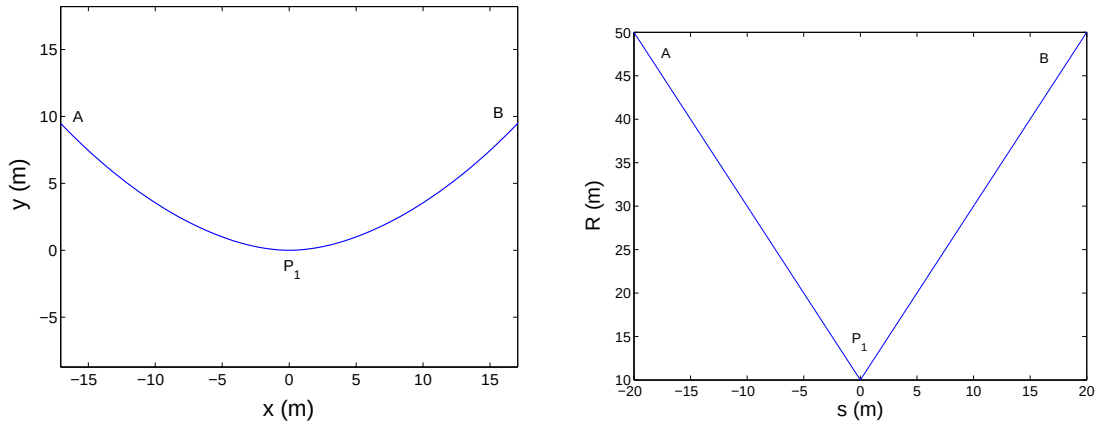

(a) (b)

Figure 7.8: *(a) A path with a point of minimum radius. (b) Radius profile of the path.*

7.3 Eliminating Oversteer

Vehicle yaw stability characteristics vary with the various possible configurations of the vehicle, e.g., weight distribution, front-rear-all wheel drive, etc. [2]. In this section we investigate in great detail the onset of yaw instability when implementing the minimum-time strategy of Section 6.7 to the half-car model. For demonstration purposes we consider a neutrally balanced vehicle, with the same tire characteristics and an inherent oversteering behavior as described earlier.

We propose a control scheme in which the optimal $f_{GG}^{\pm}$ strategy is interrupted momentarily by a control law that tends to reduce the magnitude of the vehicle slip angle. The objective of the proposed stabilizing control law is therefore to: (i) guarantee that the vehicle remains on the prescribed path, and (ii) generate a yaw moment to oppose oversteer.

7.3.1 Stabilizing Control

Consider the control strategy such that the friction forces at the front and rear axles are parallel to the normal direction to the path, i.e.

$$f_i^T e_t = 0, \qquad i = F, R. \tag{7.25}$$

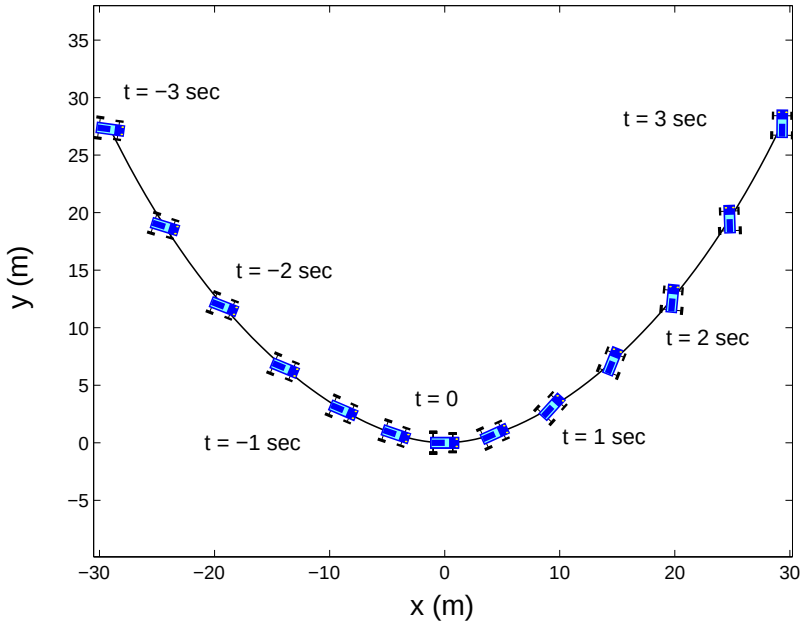

Figure 7.9: *Direct implementation of the point mass strategy to the half-car model. Vehicle trajectory.*

The forces generated by the front and rear tires contribute only to the centripetal acceleration of the vehicle and thus

$$f_F + f_R = f_n = \frac{mv^2}{R(s)}, \tag{7.26}$$

whereas the speed remains constant,

$$\dot{v} = 0. \tag{7.27}$$

The control strategy (7.25)-(7.26) is demonstrated in Fig. 7.12. Recall that for any given operating condition of the vehicle (v, β, $\dot{\psi}$), the rear tire force $f_{Ry}(s_{Ry})$ lies on the characteristic curve $\mathcal{F}_R(s_{Ry})$. Given (7.25) the rear tire friction force is determined uniquely as in Fig. 7.12. In the same figure we also notice that the front tire force is uniquely determined so that condition (7.26) is satisfied.

Next, we derive the switching condition that determines the instances when the control strategy (7.25)-(7.26) must be activated. We also show why this strategy will lead to a reduction of yaw instability.

Differentiating twice with respect to time equation (7.6) that relates the vehicle

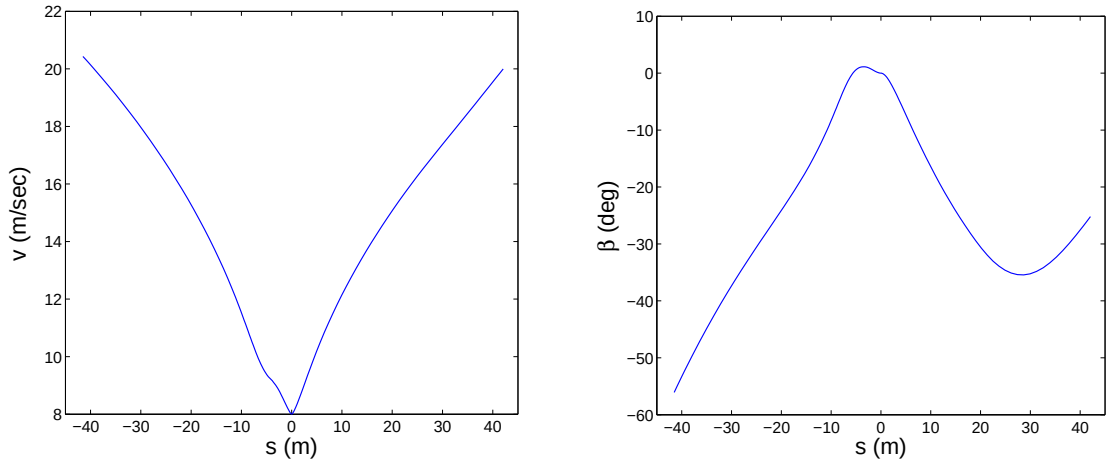

(a) (b)

Figure 7.10: *Direct implementation of the point mass strategy to the half-car model: (a) velocity profile (b) vehicle slip angle.*

slip angle β, the vehicle yaw angle ψ and the path angle ϕ, we obtain

$$\dot{\beta} = \dot{\phi} - \dot{\psi} = \phi' v - \dot{\psi} = \frac{v}{R} - \dot{\psi}, \tag{7.28}$$

$$\ddot{\beta} = -\frac{R'}{R^2} v^2 + \frac{1}{R}\dot{v} - \frac{1}{I_z}(\ell_F f_{Fy} - \ell_R f_{Ry}). \tag{7.29}$$

Condition (7.25) implies

$$\frac{s_{Rx}}{s_{Ry}} = -\tan\beta, \qquad s_R = |s_{Ry}|\sqrt{1+\tan^2\beta}. \tag{7.30}$$

Hence, the total rear tire force under the conditions (7.25)-(7.26) is given by

$$|f_R| = F_R^{\text{stable}} = F_{Rz} D \sin(C\text{atan}(B s_R)), \tag{7.31}$$

with s_R from (7.30). The components of the rear and front tire forces along the vehicle y-axis can be computed by

$$f_{Ry} = f_R \cos\beta = \text{sign}(R) F_R^{\text{stable}} \cos\beta \tag{7.32}$$

$$f_{Fy} = f_F \cos\beta = \left(\frac{mv^2}{R} - \text{sign}(R) F_R^{\text{stable}}\right)\cos\beta. \tag{7.33}$$

Using $\dot{v} = 0$ and (7.32), (7.33), equation (7.29) can be written as

$$\text{sign}(R)\ddot{\beta} = -\frac{\text{sign}(R) R'}{R^2} v^2 - \frac{1}{I_z}\left(\frac{\ell_F m v^2}{|R|} - (\ell_F + \ell_R) F_R^{\text{stable}}\right)\cos\beta. \tag{7.34}$$

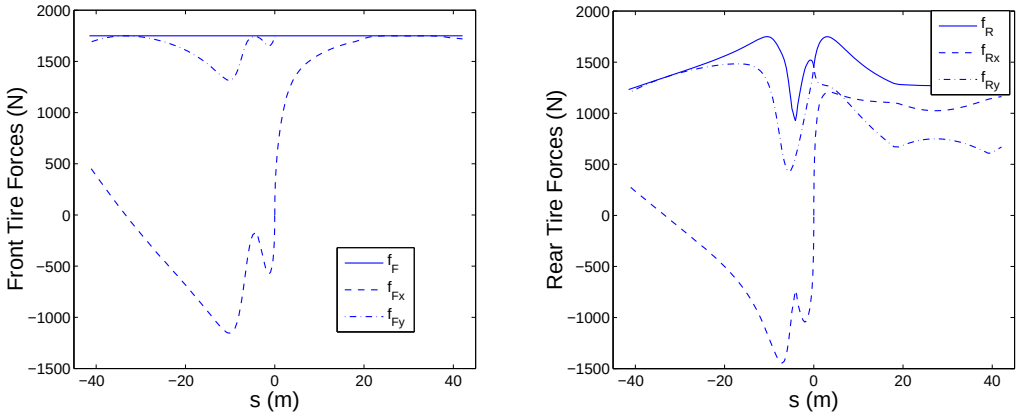

(a) (b)

Figure 7.11: *Direct implementation of the point mass strategy to the half-car model. Front and rear tire forces.*

The condition for a yaw acceleration to oppose oversteer along a curved path is

$$\text{sign}(R)\ddot{\beta} > 0. \tag{7.35}$$

Substituting (7.34) in (7.35) we get

$$v < \sqrt{\frac{R^2(\ell_F + \ell_R)F_R^{\text{stable}} \cos\beta}{I_z \text{sign}(R)R' + \ell_f |R| m \cos\beta}} \triangleq v_s \tag{7.36}$$

In summary, we have that switching from $f_{GG}^{\pm}$ to (7.25), (7.26) when $v < v_s$ results in a yawing acceleration that reduces oversteer.

We also notice that the vehicle acceleration capacity is considerably reduced when $|s_{Ry}| > s_R^{\max}$. Observe, for instance, the characteristic curve $\mathcal{F}_R(-0.6)$ in Fig. 7.3(a) which lies entirely inside the friction circle. From the definition (7.13) we conclude that eliminating oversteer will also reduce the magnitude of s_{Ry}. In order to avoid operating at rear lateral slip magnitudes greater than $s_R^{\max}$ we may enforce switching from $f_{GG}^{\pm}$ to (7.25), (7.26) when

$$v \geq v_s - \epsilon \qquad \text{or} \qquad |s_{Ry}| \geq s_R^{\max}, \tag{7.37}$$

where ϵ is a small positive scalar.

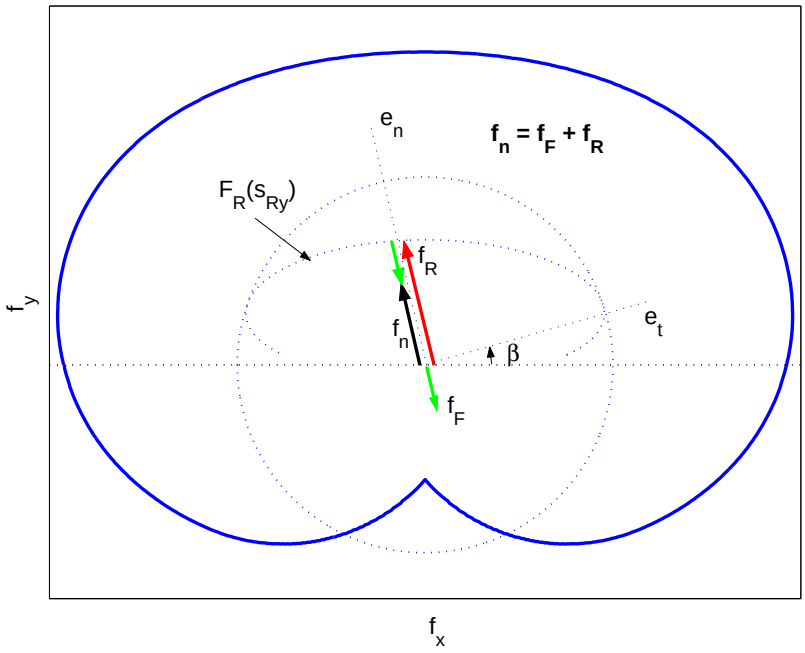

Figure 7.12: *The front and rear wheel friction forces are uniquely determined in the oversteer elimination mode.*

7.3.2 Example 1: Single Corner

We consider again the reference path of Fig. 7.8. The vehicle trajectory is generated by first integrating equations (7.1)-(7.3) forward in time accelerating with initial conditions (7.22) and $v(s_{P_1}) = \min\{v_{\text{crit}}(s_{P_1}), v_s(s_{P_1}) - \epsilon\}$ and backward in time decelerating with the same initial conditions. Figure 7.13 shows the velocity profile using the previous strategy. In the same figure we have superimposed the velocity profile of the direct implementation of Section 7.2, as well as the corresponding $v_s(s)$ profile. We notice that we achieve velocity profiles close to the one from the direct implementation of Section 7.2. The $v_s(s)$ profile is discontinuous at the point of minimum radius $s_{P_1} = 0$ due to the discontinuity of $R'(s)$ at $s_{P_1} = 0$ (Fig. 7.8(b)). Finally, we notice intervals of constant velocity around $s = -12$m and $s = 10$m, which correspond to switching of the control from $f_{GG}^{\pm}$ to (7.25)-(7.26) due to increase of the rear lateral slip s_{Ry}.

Figure 7.14 shows the slip angle of the vehicle β along the path, as well as the vehicle slip angle profile corresponding to the direct implementation of Section 7.2. For comparison, we also plot the slip angle profile for the case when only the first

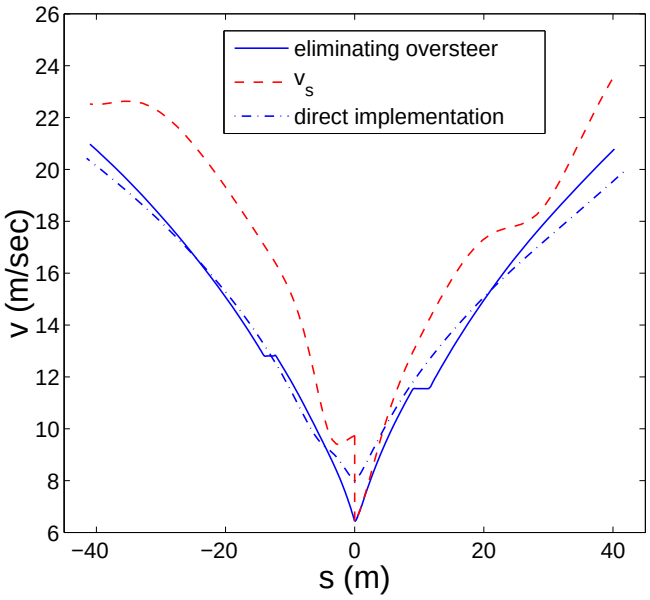

Figure 7.13: *Stable implementation of the optimal control strategy to the half-car model: velocity profile.*

of the inequalities in (7.37) is used for switching (this is the dashed line denoted by (i) in the figure). It is clear that the vehicle slip angle along the path is significantly reduced compared to the direct implementation scheme.

The longitudinal, lateral and total friction forces, f_{ix}, f_{iy} and f_i of the front and rear tires are shown in Figs. 7.15(a) and (b), respectively. We can identify the switching intervals from $f_{GG}^{\pm}$ to (7.25)-(7.26) as the intervals where $|f_F| < f_F^{\max}$. We can identify the switchings around $s = -12\,\mathrm{m}$ and $s = 10\,\mathrm{m}$, as we did from the velocity profile of Fig. 7.13, that are due to the increase of s_{Ry}. Close to the origin we observe high frequency switching from $f_{GG}^{\pm}$ to (7.25)-(7.26) due to the velocity v being close to v_s (see also Fig. 7.13).

Figure 7.16 shows the vehicle trajectory. We observe that excessive oversteer has been eliminated. At the same time we have achieved a velocity profile that is close to the profile generated by direct implementation of the optimal control strategy of Section 6.7. In fact, we observe that at certain intervals the velocity from the stable implementation scheme is higher than the one resulting from the direct implementation. As already mentioned, excessive oversteer and the increase of the vehicle slip

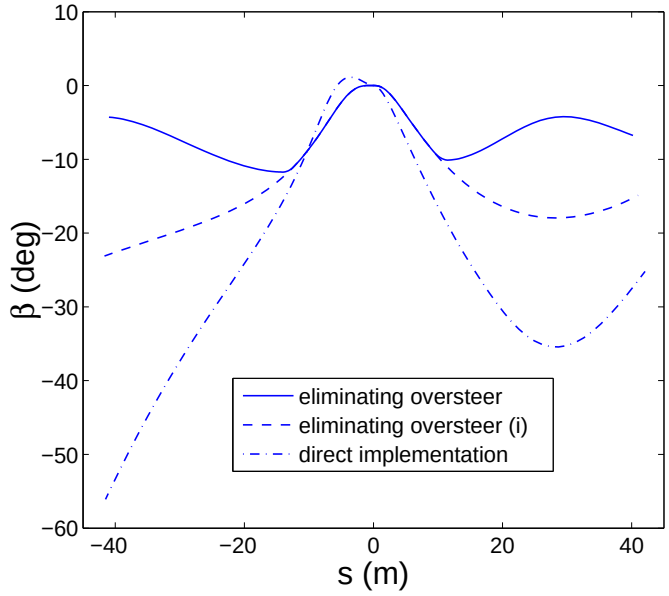

Figure 7.14: *Stable implementation of the optimal control strategy to the half-car model: vehicle slip angle.*

results in reduction of the acceleration capacity. Hence, a stable implementation has the added benefit that it may also lead to a solution that is closer to the optimal one.

7.3.3 Example 2: S-Turn

Consider the path of Fig. 7.17(a). Figure 7.17(b) shows the corresponding curvature profile. Consider fixed initial and final velocities $v_0 = v_f = 5$m/sec at points A and B of the path respectively.

According to the methodology of Section 6.7 we construct the following trajectories:

- Starting from point A with initial yaw states satisfying (7.22) and velocity v_0 we integrate forward in time equations (7.1) - (7.3). The control switches from f_{GG}^{+} to (7.25), (7.26) when (7.37) holds. The resulting velocity profile $V_A^{+}(s)$ is shown in Fig. 7.18 and the vehicle slip angle $\beta_A^{+}(s)$ in Fig. 7.19.
- Starting from point B with initial yaw states satisfying (7.22) and velocity v_f we

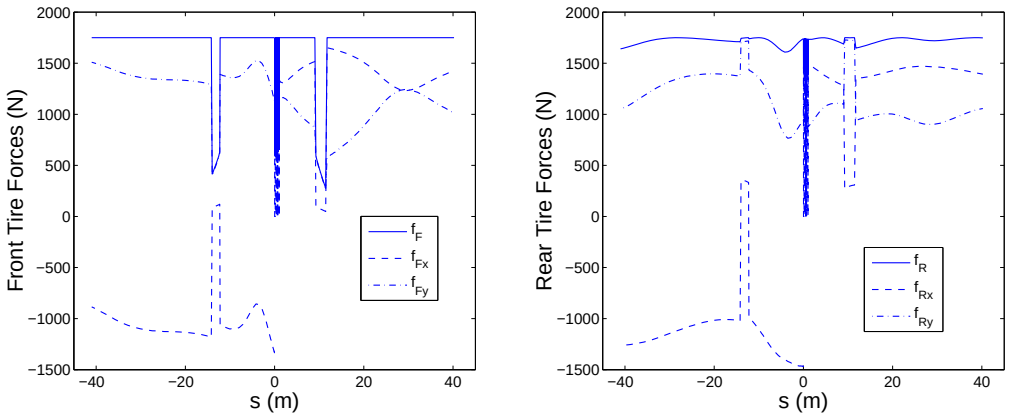

(a) (b)

Figure 7.15: *Stable implementation of the optimal control strategy to the half-car model: front and rear tire forces.*

integrate backwards in time equations (7.1) - (7.3). The control switches from f_{GG}^{-} to (7.25), (7.26) when (7.37) holds. The resulting velocity profile $V_B^{-}(s)$ is shown in Fig. 7.18 and the vehicle slip angle $\beta_B^{-}(s)$ in Fig. 7.19.

- Starting from point P_1 with initial yaw states satisfying (7.22), and initial velocity

$$v(s_{P_1}) = \min\{v_{\text{crit}}(s_{P_1}), v_s(s_{P_1}) - \epsilon\}, \tag{7.38}$$

we integrate forward in time equations (7.1) - (7.3). The control switches from f_{GG}^{+} to (7.25), (7.26) when (7.37) holds. The corresponding velocity profile is $V_{P_1}^{+}(s)$ and the vehicle slip angle is $\beta_{P_1}^{+}(s)$ in Figs. 7.18 and 7.19 respectively.

- Starting from point P_1 with initial conditions (7.22), (7.38) we integrate backwards in time equations (7.1) - (7.3). The control switches from f_{GG}^{-} to (7.25), (7.26) when (7.37) holds. The corresponding velocity profile is $V_{P_1}^{-}(s)$ and the vehicle slip angle is $\beta_{P_1}^{-}(s)$ in Figs. 7.18 and 7.19 respectively.

- Finally, we construct the velocity and vehicle slip angle profiles for P_2, $V_{P_2}^{\pm}(s)$ and $\beta_{P_2}^{\pm}(s)$ in Figs. 7.18 and 7.19 respectively, similar to the characteristics corresponding to point P_1.

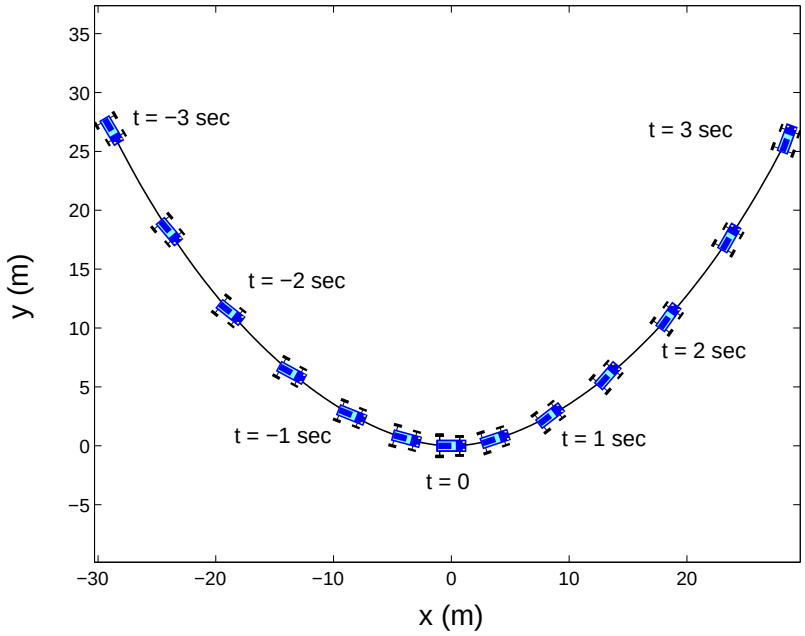

Figure 7.16: *Stable implementation of the optimal control strategy to the half-car model: vehicle trajectory.*

The switching points for the overall trajectory are chosen by trial and error, in the area of intersection of the velocity profiles aiming to generate a velocity profile

$$V_o(s) \simeq \min_s \{V_A^+(s), V_{P_1}^-(s), V_{P_1}^+(s), V_{P_2}^-(s), V_{P_2}^+(s), V_B^-(s)\}. \tag{7.39}$$

The first switching from acceleration f_{GG}^+ to deceleration f_{GG}^-, for instance, is adjusted from IP_{A1} (the point of intersection of V_A^+ and $V_{P_1}^-$) to the point SP_{A1} in Fig. 7.18. Switching control exactly at IP_{A1} results in a solution $V_e(s)$ that diverges from (7.39). The velocity profile $V_o(s)$ along the whole path is shown in Fig. 7.18 and the corresponding vehicle slip angle $\beta_o(s)$ is shown in Fig. 7.19. The trajectory of the vehicle along the path is shown in Fig. 7.20.

7.4 Zero Vehicle Slip Implementation

In this section we present an alternative extension of the methodology of Section 6.7 to produce the (sub)optimal velocity profile for the case of the half-car model. This time we impose the additional constraint that the vehicle tracks the given path with zero slip angle in order to completely eliminate yaw instability.

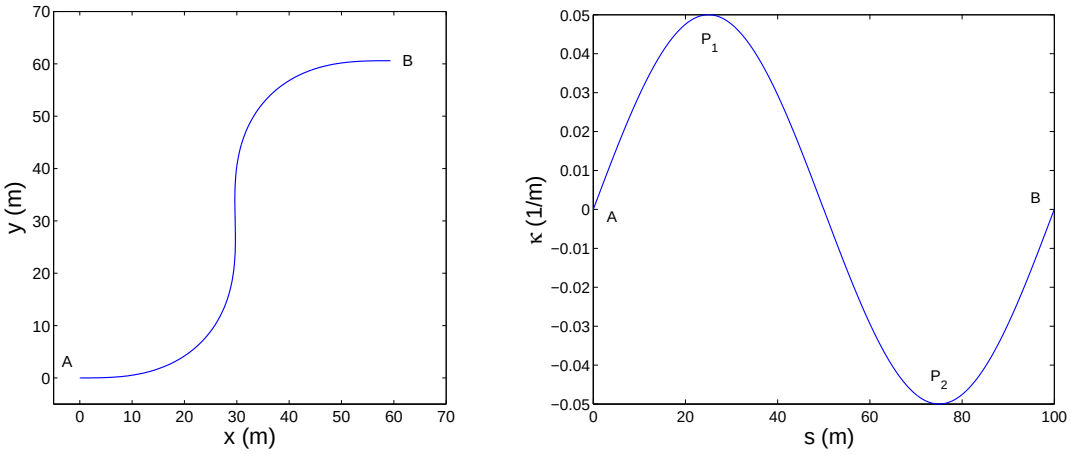

(a) (b)

Figure 7.17: *(a) S-turn. (b) Curvature profile of the S-turn.*

For exact tracking of the curvature profile $\kappa(s)$ with vehicle slip angle $\beta = 0$ the centripetal force on the vehicle is

$$f_n = \kappa m v^2 = f_{Fy} + f_{Ry}. \tag{7.40}$$

For $\beta = 0$ the path angle ϕ coincides with the yaw angle ψ of the vehicle. That is, for $\beta = 0$

$$\psi(s) = \phi(s), \qquad \psi'(s) = \phi'(s) = \kappa(s), \qquad \psi''(s) = \phi''(s) = \kappa'(s). \tag{7.41}$$

Notice also that $\ddot{\psi} = \psi'' v^2 + \psi' v' v$. The yaw dynamics (7.3) can then be written as

$$I_z \psi'' v^2 + I_z \psi' v' v = \ell_F f_{Fy} - \ell_R f_{Ry}, \tag{7.42}$$

or, using (7.40),

$$I_z \psi'' v^2 + I_z \psi' v' v = \ell_F \kappa m v^2 - (\ell_F + \ell_R) f_{Ry}. \tag{7.43}$$

Consider now the longitudinal dynamics

$$m\dot{v} = f_t \Rightarrow m v v' = f_t. \tag{7.44}$$

Equation (7.43) can be written as

$$I_z \kappa' v^2 + I_z \kappa \frac{f_t}{m} = \ell_F \kappa m v^2 - (\ell_F + \ell_R) f_{Ry}$$

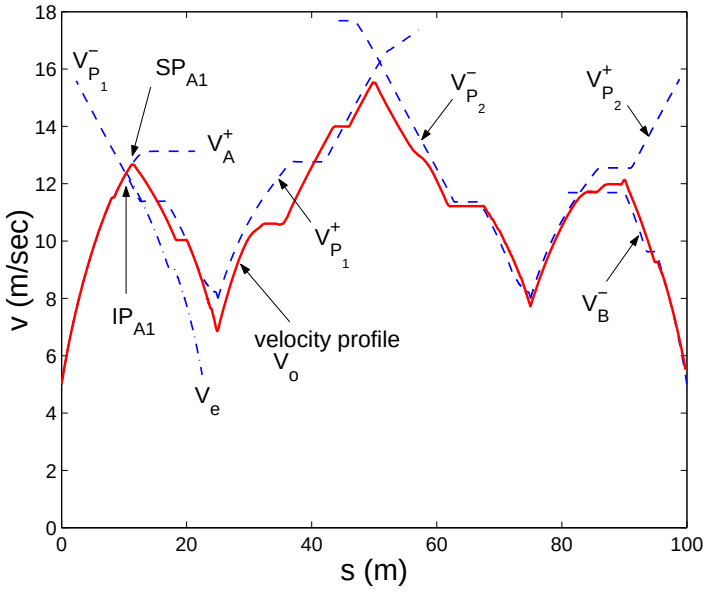

Figure 7.18: *Stable implementation for the S-turn example: velocity profile.*

or

$$f_t = \frac{m(\ell_F \kappa m v^2 - I_z \kappa' v^2)}{I_z \kappa} - \frac{m(\ell_F + \ell_R)}{I_z \kappa} f_{Ry}. \tag{7.45}$$

This equation provides an expression for the necessary tangential force f_t for the vehicle to track $\kappa(s)$, while maintaining $\beta = 0$, given the rear lateral force f_{Ry}. The map $f_t(f_{Ry})$ in (7.45) is linear and it is shown in Fig. 7.21.

The rear tire lateral slip when $\beta = 0$ is given by

$$s_{Ry} = -\frac{\dot{\psi}\ell_R}{v} = -\frac{\psi' v \ell_R}{v} = -\kappa \ell_R, \tag{7.46}$$

whereas the rear lateral force f_{Ry} changes with $s_{Rx} \in [-1, +1]$ as in Fig. 7.3. Accordingly, we can use (7.45) to find the range of all possible values for f_t.

For a given operating condition of the vehicle v, $\dot{\psi}$ and $\beta = 0$ (equivalently, a given value of s_{Ry}), each value of $s_{Rx} \in [-1, +1]$ corresponds to unique values of f_{Rx} and f_{Ry} from (7.7) and a unique value of f_t from (7.45). The front tire longitudinal force f_{Fx} is given by

$$f^+_{Fx}(f_{Rx}, f_{Ry}) = f_t(f_{Ry}) - f_{Rx}, \qquad s_{Rx} \in [-1, 0], \tag{7.47}$$

$$f^-_{Fx}(f_{Rx}, f_{Ry}) = f_t(f_{Ry}) - f_{Rx}, \qquad s_{Rx} \in (0, +1]. \tag{7.48}$$

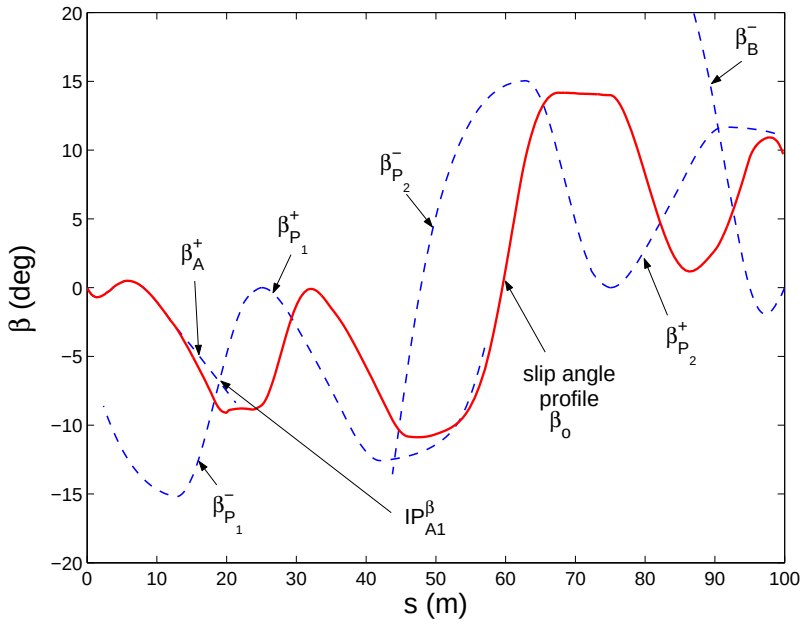

Figure 7.19: *Stable implementation for the S-turn example: vehicle slip angle.*

The front longitudinal forces $f_{Fx}^{\pm}(f_{Rx}, f_{Ry})$ from (7.47) and (7.48), for $s_{Rx} \in [-1, +1]$ are shown in Fig. 7.21.

Finally, in order for the front tire friction force to remain inside the front tire friction circle we have to ensure that

$$|f_{Fx}| \leq \sqrt{(f_F^{\max})^2 - f_{Fy}^2} = \sqrt{(f_F^{\max})^2 - (f_{Ry} - \kappa m v^2)^2} \triangleq f_{Fx}^{\max}. \tag{7.49}$$

The bounds $\pm f_{Fx}^{\max}$ from (7.49) are shown in Fig. 7.21.

An extension of the methodology of Section 6.7 to a half-car model tracking a prescribed path $\kappa(s)$ with vehicle slip angle $\beta = 0$ now becomes evident.

The maximum available accelerating front longitudinal force f_{Fx} is given by the intersection of f_{Fx}^{+} from (7.47) with $f_{Fx}^{\max}$ from (7.49). This defines f_{Ry}^{+} as in Fig. 7.21, which provides the maximum available accelerating force of the vehicle f_t^{+}. The control f_t^{+} corresponds to the maximum acceleration $u = +1$ for the point mass model of Section 6.7. If there is no intersection of f_{Fx}^{+} from (7.47) with $f_{Fx}^{\max}$ from (7.49) the maximum available acceleration f_t^{+} is given for $s_{Rx} = -1$ as in Fig. 7.22(a).

Equivalently, the maximum available decelerating front longitudinal force f_{Fx} is given by the intersection of f_{Fx}^{-} from (7.48) with $-f_{Fx}^{\max}$ from (7.49). This defines f_{Ry}^{-}

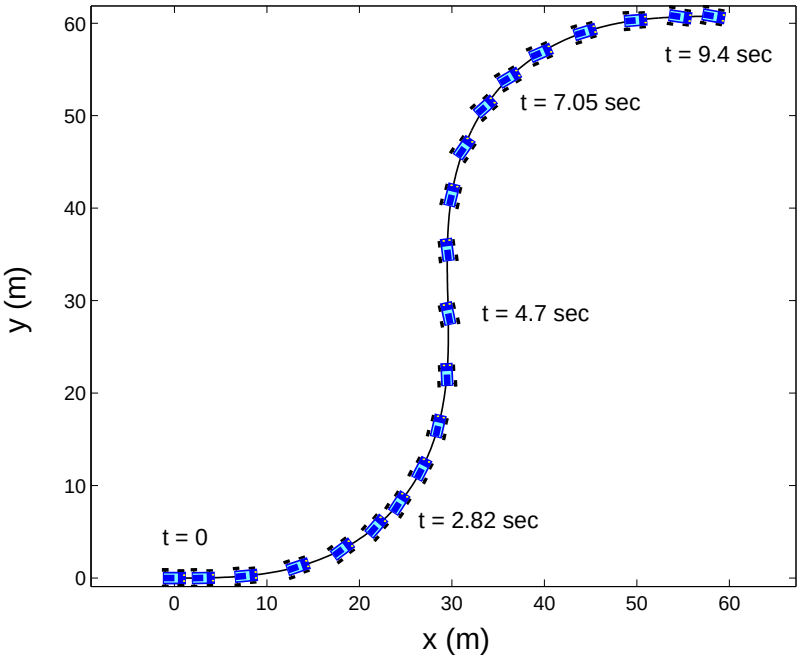

Figure 7.20: *Stable implementation for the S-turn example: vehicle trajectory.*

and f_t^-. The control f_t^- corresponds to the maximum deceleration $u = -1$ for the point mass model of Section 6.7. If there is no intersection of f_{Fx}^- from (7.48) with $-f_{Fx}^{\max}$ from (7.49) the maximum available deceleration f_t^- is given for $s_{Rx} = 0$ as in Fig. 7.22(b).

As the velocity decreases, f_t from (7.45) becomes negative for all $s_{Rx} \in [-1, +1]$ (Fig. 7.23(a)). This implies that there is no available accelerating force $f_t > 0$. Hence, the vehicle cannot switch from deceleration to acceleration without violating $\beta = 0$.

Equivalently, as velocity increases, f_t from (7.45) becomes positive for all $s_{Rx} \in [-1, +1]$ (Fig. 7.23(b)). This implies that there is no available decelerating force $f_t < 0$. Hence, the vehicle cannot switch from acceleration to deceleration without violating $\beta = 0$. In order to avoid such problematic cases we switch from $f_t^{\pm}$ to the following control

$$f_t = 0, \quad \text{when} \quad f_t^- \geq 0 \quad \text{or} \quad f_t^+ \leq 0. \tag{7.50}$$

In other words, the vehicle stops accelerating when there is no available decelerating force $f_t < 0$ from (7.45). Similarly the vehicle stops decelerating when there is no available accelerating force $f_t > 0$ from (7.45).

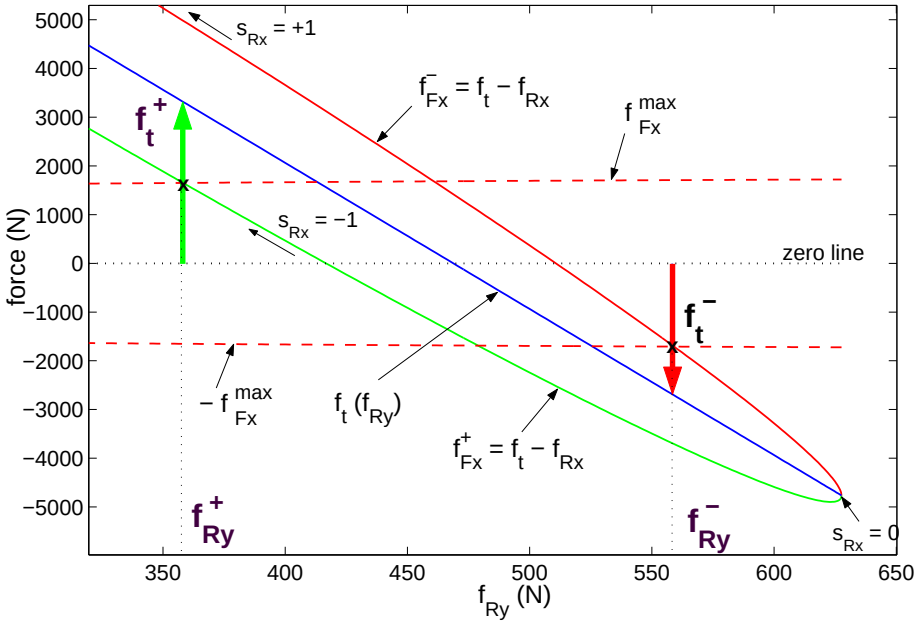

Figure 7.21: *Force diagram for tracking with* $\beta = 0$.

7.4.1 Numerical Example

Consider the S-turn example of Fig. 7.17. First we need to derive the optimal values of the states at the points P_1 and P_2, which are the points of minimum magnitude of the path radius. Clearly, $\beta(s_{P_1}) = \beta(s_{P_2}) = 0$. Moreover, from equations (7.41) we get

$$\dot{\psi}(s_{P_i}) = \psi'(s_{P_i})v(s_{P_i}) = \kappa(s_{P_i})v(s_{P_i}), \qquad i = 1, 2. \tag{7.51}$$

To maximize the centripetal force at P_1 and P_2 we enforce $s_{Rx}(s_{P_i}) = 0$ in order to maximize f_{Ry}. The rear lateral force is calculated from (7.7), given $s_{Ry} = -\kappa\ell_r$. The initial velocity $v(s_{P_i})$ is finally calculated from (7.45) by setting $f_t = 0$.

The resulting velocity profile is shown in Fig. 7.24. The figure reveals that–as expected–the zero-slip implementation of Section 7.4 is conservative compared to the approach of Section 7.3.3. On the other hand, continuity of the β and $\dot{\beta}$ is a-priori guaranteed using this approach. Figure 7.25 shows the calculated vehicle trajectory.

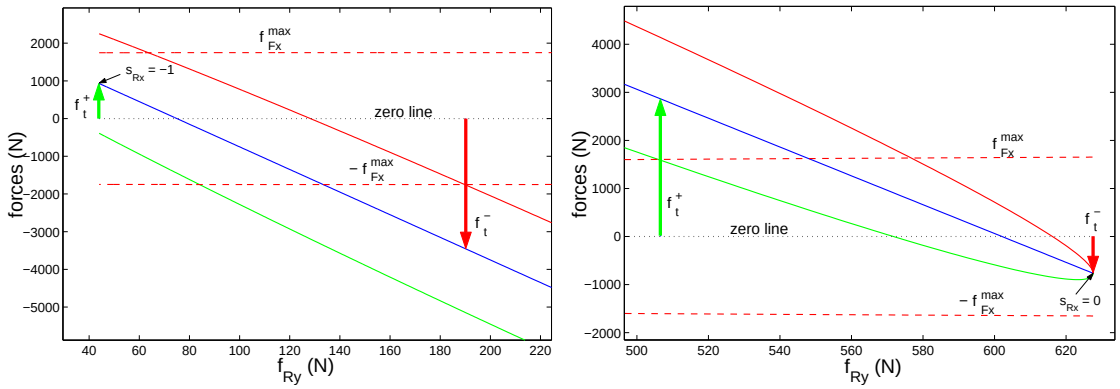

(a) (b)

Figure 7.22: *(a)* f_t^+ *for* $s_{Rx} = -1$. *(b)* f_t^- *for* $s_{Rx} = 0$.

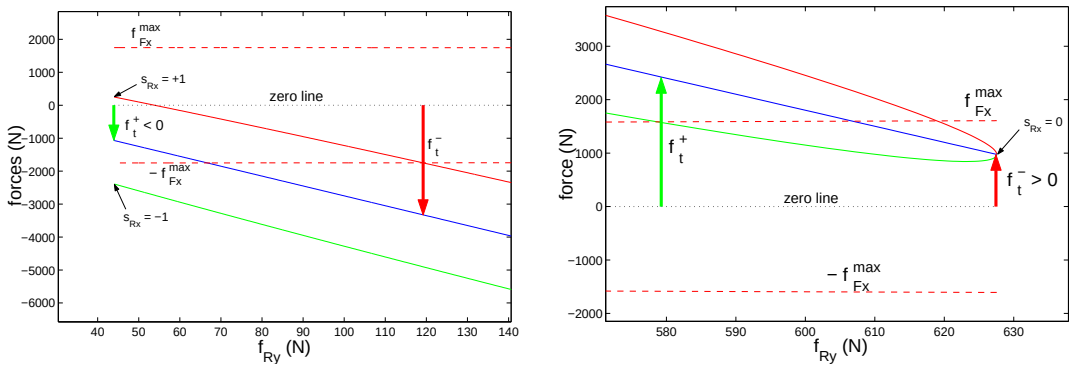

(a) (b)

Figure 7.23: *(a) Negative maximum acceleration* f_t^+ *(b) Positive maximum deceleration* f_t^-.

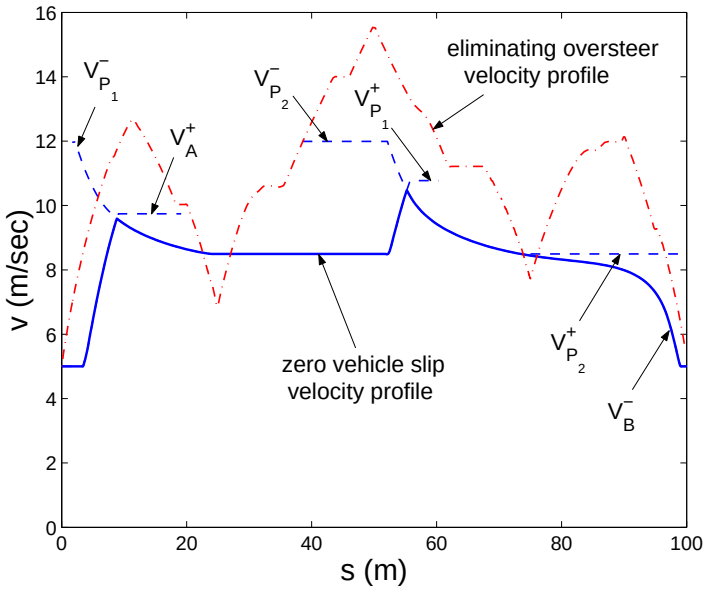

Figure 7.24: *Zero-slip implementation to S-turn: velocity profile.*

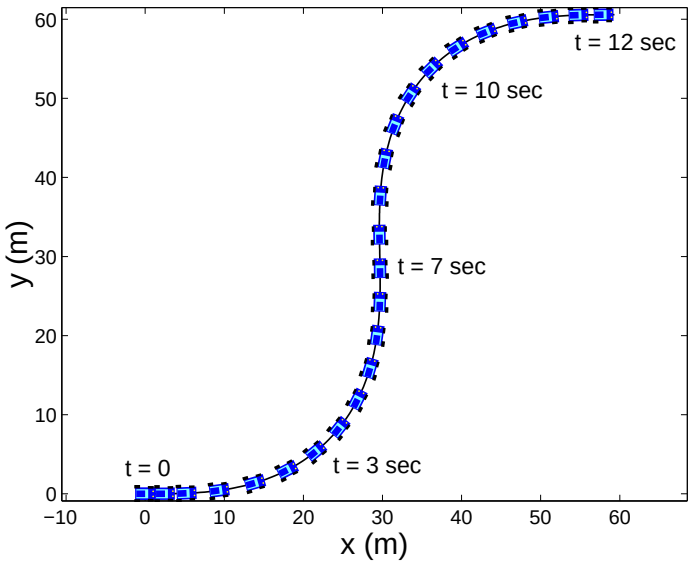

Figure 7.25: *Zero-slip implementation to S-turn: vehicle trajectory.*

Chapter 8

Conclusion

The main objective of this work was to develop methodologies for path planning of autonomous ground vehicles that take advantage of the full acceleration capacity of the vehicle, minimizing time of travel and exposure to danger during a mission. It is envisioned that autopilot agents for autonomous vehicles may be developed that operate similar to expert race drivers. In this chapter we summarize the conclusions of this work and discuss possible extensions of the results presented and plans for future research.

Interpretation of the results of any optimization process requires good understanding of the physics governing the system in consideration. In this case, vehicle dynamics is a subject well established in the literature and most of the modeling issues have been addressed using classical mechanics. Tire friction modeling, however, still remains an open problem in the literature mainly because of lack of understanding of the physics involved in the dry friction generation mechanism. In this work we have presented the development of a new dynamic tire friction model, namely the LuGre tire friction model, that provides physical interpretation of friction as a force due to the elastic deformation of the tire at the contact area with the road. Its dynamic formulation allows the study of effects such as transient behavior and hysteresis that are empirically observed but cannot be incorporated by the widely used empirical, steady-state, static tire models. In addition, singularities at low vehicle speeds are avoided. The derivation involved application of a point contact dynamic

friction model on the contact patch of a tire resulting in an infinite order distributed system. We developed several low-order approximate expressions that were validated by comparison to the exact dynamics of the friction model. We derived an exact expression of the dynamics of finite order by applying the Method of Moments. We also presented identification of the new model's parameters and proof of its validity by comparison to both existing empirical models and experimental data. This work towards the development of the LuGre dynamic tire friction model has resulted in numerous publications [83, 84, 34, 75, 85, 86, 87].

Next, we formulated the problem of trajectory optimization for ground wheeled vehicles as a problem in optimal control. Our first approach to finding the optimal solution was in accordance to the current trends in the literature, that is we used a numerical optimization scheme. In contrast to these current trends, however, we formulated the problem as one with "free final time" avoiding singularities for high vehicle slip angles. We demonstrated that such a mode of operation where the vehicle travels with high slip angle may appear in the optimal solution. Convergence of the optimization algorithm depends on the complexity of the problem and the accuracy of the initial guess. The complexity of the model incorporated in our optimization scenarios was increased with our intuition in vehicle dynamics and our ability to generate "good" initial guesses. We examined several optimization scenarios for different road formations as well as a case study of minimum time versus maximum exit velocity cornering. In the later case we also examined the role of longitudinal load transfer and suspension dynamics in limit operation of the vehicle. Numerical optimization schemes provide a powerful tool for off-line analysis of vehicle dynamics, limit operation and trajectory optimization. It allows the study of several vehicle parameters in limit operation which would be extremely difficult using straightforward simulation. In this work we demonstrated optimality of travelling with high vehicle slip angles, similarly to rally racing techniques, by changing the longitudinal position of the C.G. and the cornering capacity of the tires.

Numerical optimization schemes present little promise as far as on-line applicability due to the high computational cost, the inability to incorporate unpredictable

environments and the dependence on the initial guess. In this work we provided rigorous proof of optimality of a semi-analytical methodology to generate optimal velocity profiles for minimum time travel along a prescribed path given the acceleration capacity of the vehicle. The semi-analytic nature ensures minimal computational cost. In addition we designed a receding horizon implementation providing guarantees of existence of an "escape" maneuver to incorporate unpredictable environments. We finally extended the semi-analytical methodology from a point mass model to the half-car model in order to recover the fidelity of the vehicle model (low order model with no wheel and suspension dynamics) used in the previous numerical optimization approach. The semi-analytical methodology satisfies the essential criteria for on-line applicability. In addition, it provides a powerful tool to generate "good" initial guesses for a numerical optimization scheme, when even higher model fidelity is required. The results in trajectory optimization of this work were presented in the following publications [88, 89, 90, 91].

8.1 Extensions of Current Results

In this section we discuss possible extensions and improvements of the results of this work towards the development of methodologies to generate reference signals for an "expert" autopilot for ground wheeled vehicles.

Convergence of the numerical optimization algorithm depends mainly on the complexity of the problem, namely the order of the dynamical model used, and the accuracy of the initial guess. In this work we were able to overcome this difficulty by first introducing a low order model, neglecting wheel and suspension dynamics in order to obtain preliminary results. Next, we used these preliminary solutions to construct initial guesses for a new formulation of the problem including a higher order system. This procedure may be used to further increase the fidelity of the model allowing us to study more details of the overall vehicle dynamics. For instance the solutions obtained in this work using a half-car model with wheel and suspension dynamics can be used to construct initial guesses for a new formulation incorporating the full,

four wheel, vehicle model (Fig. 8.1). In this case we can study the role of additional effects such as roll motion and lateral weight transfer.

In order to pursue an analytic solution to the trajectory optimization problem initially we had to compromise in the fidelity of the vehicle model introducing the simplified point mass characterization. We were, however, able to provide the necessary extensions to analytically construct a sub-optimal solution using a vehicle model of level of detail comparable to the one used in the numerical optimization approach. This was achieved by construction of the acceleration envelope of the vehicle using the knowledge of the friction capacity of the tires. The friction capacity of the tires depends linearly on the normal load of the axles. Thus, we can further extend the analytical approach to a vehicle model including suspension dynamics and load transfer effects by characterizing the acceleration envelope of the vehicle as a function of the normal load distribution to front and rear axles.

The semi-analytic methodology developed here is more appropriate for online applications compared to numerical optimization techniques. It may also provide a tool to generate initial guesses for the numerical optimization scheme. In this way we may further increase the level of detail of the vehicle model used in the numerical optimization and study higher order effects.

The main difference in the formulation of the optimal control problem in the numerical and analytical approach is that in the latter we assumed a fixed path to be followed. The geometry of the path was an additional parameter for optimization in the numerical scheme. We can combine the analytic methodology with another optimization scheme that determines (for example numerically) the optimal geometry of the path to be followed. For example the path may be of minimum distance or minimum average curvature. In fact, in the analysis of the results of the numerical optimization scheme we concluded that the geometry of the path compromises between minimum distance and minimum curvature for minimum time travel and thus a combined cost seems necessary. Numerical optimization of the path's geometry is expected to require little computational cost since the complex vehicle dynamics are not taken into consideration in the calculations.

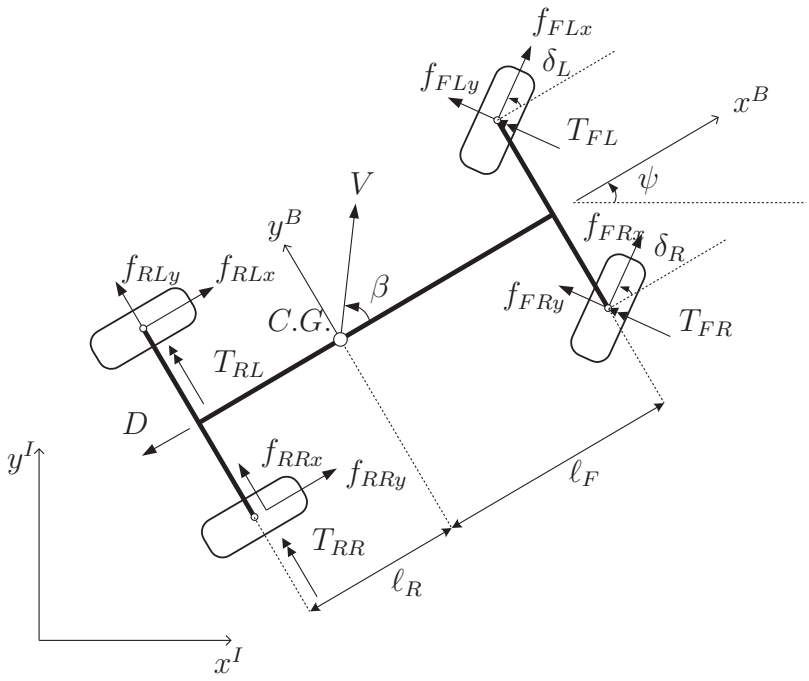

Figure 8.1: *The 4-wheel (full-car) model can be used to study the effects of roll motion and lateral load transfer in the optimal solution.*

8.2 Future Work: Next Generation of Active Safety Systems for Passenger Vehicles

Under normal operating conditions of an automobile, where the tires operate in the linear range away from their saturation limit, the driver maintains control of the vehicle through steering, accelerating and braking. The tires provide the interface between the vehicle and the road, and when operating in their linear range they produce friction forces according to the driver's commands. In such cases accident avoidance depends on the level of concentration, good health, reflexes etc of the driver.

In limit operation of the vehicle, that is in high speeds and when the tires are operating near their adhesion limits the average driver is very likely to loose control of the vehicle when performing an emergency maneuver such as hard braking and/or obstacle avoidance, thus leading to an accident. This loss of controllability ensues due to the tires reaching their saturation limit and thus no additional friction forces to perform the maneuver are available. To this end the automotive industry has

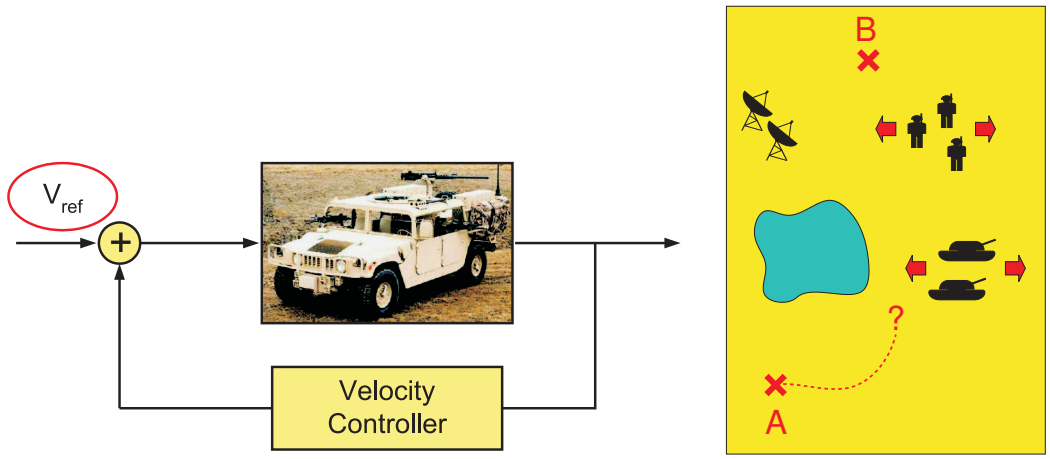

Figure 8.2: *The semi-analytic methodology to generate reference velocity signals for minimum time travel along a prescribed path can be combined with a path planner that will optimize the geometry of the path to be followed.*

focused its interest towards developing systems to assist drivers in such situations aiming to increase the chances of preventing an accident in the first place, rather than minimizing the effects on the passengers after an accident occurs. This extension of the vehicle's overall safety is referred to as "Active Safety". The results have been very impressive in the last few decades with the development of such systems as the anti-lock braking system (ABS) or, more recently, the electronic stability program (ESP) (Fig. 8.3). While it is commonly acknowledged that the above mentioned active safety systems have greatly increased safety of modern automobiles, we will demonstrate in this section that there still remains a lot of room for improvement, motivated by the results presented in this work.

Anti-Lock Braking System: The ABS system is designed to assist the driver in emergency braking. Sudden application of the brakes typically result in locking of the wheels (especially in wet/icy road) at which point the tires capacity to produce lateral forces is considerably reduced and thus loss of lateral (cornering) control of the vehicle occurs (Fig. 8.3 (a)). The ABS system reduces the brake pressure on the wheels before locking occurs, assisting the driver to maintain cornering authority on the vehicle. The latest trend in the research literature of ABS systems [92, 93, 94, 95, 96] is to optimize the system's operation by designing controllers that aim to maximize the

(a) (b)

Figure 8.3: *The latest advances in active passenger vehicle safety has led to the development of systems such as (a) the anti-lock braking (ABS) (photo from [7]), that allows the driver to maintain steering control during emergency braking and (b) the electronic stability program (ESP) (photo from [8]) that helps the vehicle retain controllability in high speed cornering maneuvers (right vehicle with ESP system, left vehicle without ESP).*

braking tire friction force, and thus minimize the braking distance. In fact, there is formal proof of optimality of this strategy in [97] which however considers a quarter car model, i.e. the longitudinal dynamics only of the vehicle. Maximization of the braking force is achieved by driving the longitudinal slip of the braking wheels to the value s_x^* as in Fig.8.4(a). Considering the friction ellipse envelope (Fig.8.4(b)) where the tire friction force lies (also recall equation (7.7)) we observe that the more longitudinal (braking) force we demand from the wheel, the less lateral (cornering) force is left available. And thus, maximizing the braking force results in reduced available cornering authority which arises a contradiction with the initial purpose of the ABS systems, that is maintaining steering control during emergency braking.

In the velocity generation methodology presented in the previous chapter we introduced a characterization of the acceleration envelope of the vehicle using the GG-diagram (Fig.8.5(a)). The GG-diagram takes into consideration the contribution of front and rear axle forces and provides the maximum available traction/braking forces for a given velocity of the vehicle in a corner, i.e. for given centripetal force in demand. It is envisioned the a new approach to optimal ABS systems may be developed where measurements of the steering angle will provide information on the intentions of the driver about the desired path he decides to follow during an emergency. The

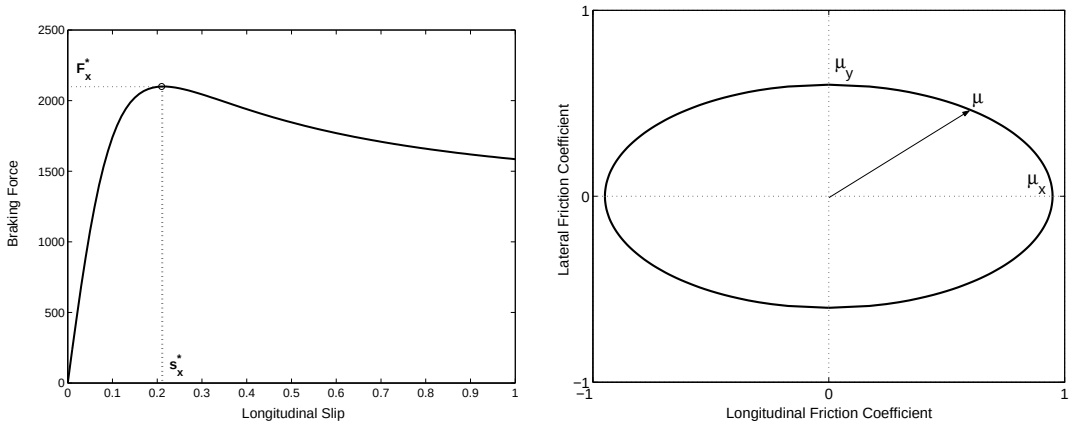

(a) (b)

Figure 8.4: *Current research in ABS systems tend towards maximizing the longitudinal (braking) force of each wheel. Taking into consideration the friction ellipse concept as the force envelope where tire friction lies we conclude that a conflict of interest arises with the initial purpose of the ABS systems, which is maintaining steering control during emergency braking.*

braking (ABS) controller then will allow only the maximum available braking forces such that the centripetal force in demand for the maneuver remains available. Similar ideas may apply for a TCS system with the traction (acceleration) forces.

Electronic Stability Program: The ESP is one of the latest active safety systems introduced to commercial passenger vehicles. It is a vehicle yaw control system that aims to assist the driver maintain control of the vehicle during cornering in cases where the wheels of the front or rear axle are close to the adhesion limit, via independent braking of the wheels. Intuitively, one would expect that yaw control of the vehicle would be pursued via steering control. In fact there is significant research on active steering for vehicle stability with interesting results as in [46], [45]. However, as it is shown in [98], [99] the effect of steer angle control is reduced near the limit of the tire adhesion. Alternative approaches to yaw control [98], [100], [99], [101] include independent wheel braking for the generation of the desired control yaw moment leading to the development of the ESP system.

In a nutshell ESP works as follows (Fig.8.5(b)). Consider the following critical situations. In the case where the wheels of the front axle loose traction the vehicle understeers, that is the cornering radius cannot be further reduced and the vehicle

looses the ability to trace the desired course. Even worse, in the case where the wheels of the rear axle loose traction the vehicle oversteers, that is starts to spin uncontrollably in the inward direction of the corner. ESP is a vehicle yaw control system that aims to assist the driver avoid such undesired and dangerous situations via independent braking of the wheels. When steering input from the driver and estimated vehicle slip angle compared indicate that the vehicle understeers, braking is applied to the inner rear wheel resulting in an inward yaw moment. When oversteer is sensed braking is applied to the front outer wheel resulting in a stabilizing outward yaw moment.

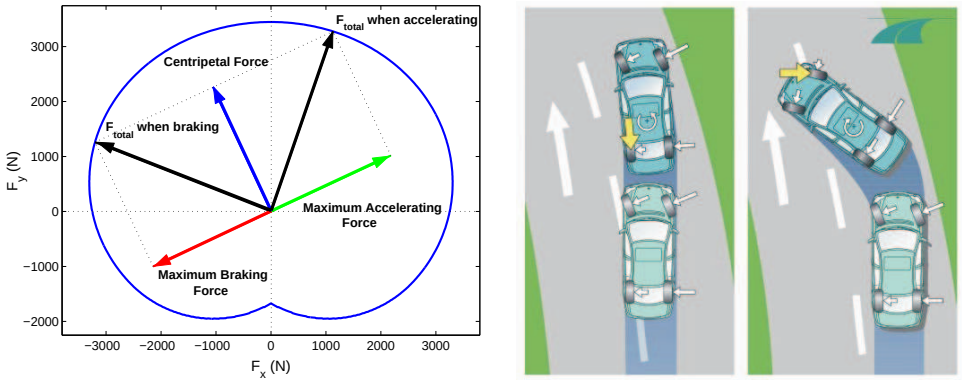

(a) (b-i) (b-ii)

Figure 8.5: *(a) The acceleration envelope for a given operating point of a bicycle model (GG-diagram) that provides the maximum acceleration/braking forces; (b) ESP system: Independent wheel braking produces stabilizing yaw moment when the tires of the front (b-i) or the rear (b-ii) axle reach the adhesion limit (*`www.whnet.com/4x4/esp.html`*).*

At this point we realize that the full available force capacity from all four wheels is not being used by the ESP system. In case of oversteer the wheels of the rear axle are saturated with friction and thus no control forces may be generated. Braking force is being applied to the front outer wheel to generate stabilizing yaw moment while the front inner wheel is not being used by the control system (braking of this wheel would result to destabilizing yaw moment). We are thus motivated to explore the benefits of combining an active steering system in conjunction with ESP. Counter steering of the front wheels in the oversteer case would get the front inner wheel to contribute

to the stabilizing maneuver. Note that the front inner wheel is not saturated by the ESP system and thus may contribute significantly to the total control yaw moment. A "drive by wire" system such as the active steering as a supplement to ESP is very realistic given the configuration of modern passenger vehicles. A steering angle sensor is already being used by the ESP (Fig. 8.6(a)) while the majority of commercial vehicles already use electric or hydraulic actuators for power steering assist systems. Thus no additional hardware need to be developed in order for such a system to be put into practice.

Expert Auto-Pilots: With the addition of various sensors, the sensing capability of the vehicle control systems is increased. Both the driver's intention and the external environmental information of a driving vehicle can now be determined, detected and even measured (Fig 8.6(b),(c)). The reader is referred to the numerous results in applications of vision systems in lane and obstacle detection for automobiles [102, 103, 104, 105, 106, 107]. The Lane Departure Warning system for example, available in Mercedes-Benz' and Freightliner's line of heavy trucks, involves a video camera looking in front onto the road. The system produces a rumbling sound if the vehicle changes lanes without the prior use of a blinker; left and right lane crossings are encoded acoustically by a stereo speaker. It is meant to alert those drivers which are swerving off the lane, possibly because they have fallen asleep.

There is a benefit to extend the driver's intention driven strategy in traditional active stability controls to including the environment information driven strategy. For instance, a vehicle driven on an emergency situation might be put into an imminent crash if it keeps on its un-safe path (for instance, an approaching guest vehicle is in the path); a vehicle of a drunken driver or a drowsy driver or a distracted driver (who is responding to a wireless phone) might drive out of a lane or off the road.

In those cases, the driver's intention is either wrong or irresponsible, and the environmental information obtained from the vehicle equipped sensors might be used to either override the driver's intention leading to danger, or take over the responsibility to avoid the hazards from the irresponsible or improper action of the driver. This is an on-demand prevention, override or takeover and it can be allowed only if the

hazards are and the driver's lack of proper action are reliably identified.

With such a benefit in mind, our future research plans include integrating the environmental sensors with other active control systems which not only respond to the driver's intension but also respond to the detected hazard information. In order to achieve this, a reference driver model is required that will be based on the optimization scheme described in this work. It is envisioned that "expert" auto-pilot software agents will be developed that will completely eliminate human intervention during emergencies.

(a) (b) (c)

Figure 8.6: *(a) Components in Bosch's ESP system. They include (A) active wheel speed sensors; (B) steering angle sensor; (C) combined yaw rate sensor/lateral accelerometer; (D) attached electronic control unit (ECU); (E) motor; (F) pressure sensor, and (G) hydraulic unit. (Photo from [9]); (b) Stereo (binocular) camera set up of an automobile machine vision system (Photo from [10]); (c) Vision based lane and obstacle detection results of the GOLD (Generic Obstacle and Lane Detection) system developed at the university of Parma (Photo from [11]).*

Bibliography

[1] E. Bakker, L. Nyborg, and H. Pacejka, "Tyre modelling for use in vehicle dynamics studies," 1987. SAE Paper No. 870421.

[2] W. Milliken and D. Milliken, *Race Car Vehicle Dynamics*. Warrendale PA USA: Society of Automotive Engineers (SAE) International, 1995.

[3] J. Harned, L. Johnston, and G. Scharpf, "Measurement of the tire brake force characteristics as related to wheel slip (antilock) control system design," *SAE paper # 690214*, pp. 909–925, 1987.

[4] A. Zomotor, *Fahrwerktechnik: Fahrverhalten*. Vogel Buchverlag Würzburg, 1987.

[5] P. Fancher, J. Bernard, C. Clover, and C. Winkler, "Representing truck tire characteristics in simulations of braking and braking-in-a-turn maneuvers," *Vehicle System Dynamics Supplement*, vol. 27, pp. 207–220, 1997.

[6] Anonymous, "RT3000 inertial and GPS measurement system, report from Silverstone F1 test," Technical Report, Oxford Technical Solutions, Oxfordshire, UK, 2002.

[7] "www.tcmi.com.ph/altisbut4.htm." last accessed March 22, 2006.

[8] "www.whnet.com/4x4/esp.html." last accessed March 22, 2006.

[9] "www.edmunds.com/ownership/safety/articles/45992/article.html." last accessed March 22, 2006.

[10] "www.gavrila.net/computer_vision/smart_vehicles/smart_vehicles.html." last accessed March 22, 2006.

[11] "http://vislab.ce.unipr.it/gold/." last accessed March 22, 2006.

[12] K. Park, H. Chung, and J. Lee, "Point stabilization of mobile robots via state space exact feedback linearization," in *Proceedings of the 1999 IEEE International Conference on Robotics and Automation*, (Detroit, MI), pp. 2626–2631, May 1999.

[13] H. Tanner and K. Kyriakopoulos, "Discontinuous backstepping for stabilization of nonholonomic mobile robots," in *Proceedings of the 2002 IEEE International Conference on Robotics and Automation*, (Washington, DC), pp. 3948–3953, May 2002.

[14] P. Tsai, L. Wang, F. Chang, and T. Wu, "Point stabilization control of a car-like mobile robot in hierarchical skew symmetry chained form," in *Proceedings of the 2004 IEEE International Conference on Networking, Sensing and Control*, (Taipei, Taiwan), pp. 1346–1351, March 21-23 2004.

[15] K. Do, Z. Jiang, and J. Pan, "A global output-feedback controller for simultaneous tracking and stabilization of unicycle-type mobile robots," *IEEE Transactions on Robotics and Automation*, vol. 20, pp. 589–594, June 2004.

[16] Y. Miyazaki, A. Ohya, and S. Yuta, "Obstacle avoidance behavior of autonomous mobile robot using fiber grating vision sensor," in *Proceedings of the 26th Annual Conference of the IEEE Industrial Electronics Society*, (Nagoya, Japan), pp. 1925–1930, October 22-28 2000.

[17] M. Lim, J. Lim, and S. Oh, "High-speed wall following and obstacle avoidance of wheeled mobile robots using behavior specifications," in *Proceedings of the 2001 IEEE International Symposium on Computational Intelligence in Robotics and Automation*, (Banf, Alberta, Canada), pp. 143–148, July 29 - August 1 2001.

[18] A. Fujimori and S. Tani, "A navigation of mobile robots with collision avoidance for moving obstacles," in *Proceedings of the 2002 IEEE International Conference on Industrial Technology*, (Bangkok, Thailand), pp. 1–6, December 11-14 2002.

[19] Z. Feng, T. Danolg, and W. Yingzi, "Obstacle avoidance for mobile robots based on relative coordinates," in *Proceedings of the 2003 IEEE International Conference on Robotics, Intelligent Systems and Signal Processing*, (Changsha, Hunan, China), pp. 616–621, October 8-13 2003.

[20] J. Wang, Z. Qu, Y. Guo, and J. Yang, "A reduced-order analytical solution to mobile robot trajectory generation in the presence of moving obstacles," in *Proceedings of the 2004 IEEE International Conference on Robotics and Automation*, (New Orleans, LA), pp. 4301–4307, April 26 - May 1 2004.

[21] J. Wong, *Theory of Ground Vehicles*. New York: John Wiley and Sons, Inc., 1978.

[22] T. Gillespie, *Fundamentals of Vehicle Dynamics*. Warrendale PA USA: Society of Automotive Engineers (SAE) International, 1992.

[23] M. Burckhardt, "ABS and ASR, sicherheitsrelevantes," *Radschupf-Regel*, 1987.

[24] M. Burckhardt, "Fahrwerktecknik: Radschlupfregelsysteme," *Vogel-Verlag*, 1993.

[25] U. Kiencke and A. Daiss, "Estimation of tyre friction for enhanced ABS-systems," in *Proceedings of AVEC 1994*, (Tsukuba, Japan), November 24-28 1994.

[26] H. Pacejka and E. Bakker, "The magic formula tyre model," in *Proceedings of 1st International Colloquium on Tyre Models for Vehicle Dynamics Analysis*, (Delft, The Netherlands), October 21-22 1991.

[27] A. Van Zanten, W. Ruf, and A. Lutz, "Measurement and simulation of transient tire forces," *SAE paper # 890640*, 1989.

[28] P. Bliman and M. Sorine, "A system-theoretic approach of systems with hysteresis application to friction modelling and compensation," in *Proceedings of 2nd European Control Conference*, (Gröningen, The Netherlands), 1993.

[29] P. Bliman, T. Bonald, and M. Sorine, "Hysteresis operators and tyre friction models. application to vehicle dynamic simulation," in *Proceedings of ICIAM 95*, (Hamburg, Germany), July 3-7 1995.

[30] M. Sorine and J. Szymanski, "A new dynamic multi d.o.f. tire model," in *Transportation Systems 2000*, (Braunschweig, Germany), 2000.

[31] J. Szymanski, "Modèles réduits du contact pneu-sol et applications à l' automobile," Technical Report, Renault, Technocentre Renault, Guyancourt, France, 1999.

[32] J. Deur, J. Asgari, and D. Hrovat, "A dynamic tire friction model for combined longitudinal and lateral motion," in *Proceedings of the ASME-IMECE World Conference*, (New York, USA), November 2001.

[33] X. Claeys, C. Canudas de Wit, J. Yi, R. Horowitz, L. Alvarez, and L. Richard, "A new 3d dynamic tire/road friction model for vehicle simulation and control," in *Proceedings of the ASME-IMECE World Conference*, (New York, USA), November 2001.

[34] C. Canudas de Wit, P. Tsiotras, E. Velenis, M. Basset, and G. Gissinger, "Dynamic friction models for road/tire longitudinal interaction," *Vehicle System Dynamics*, vol. 39, no. 3, pp. 189–226, 2003.

[35] P. Bliman and M. Sorine, "Easy-to-use realistic dry friction models for automatic control," in *Proceedings of 3rd European Control Conference*, (Rome, Italy), pp. 3788–3794, September 1995.

[36] C. Canudas de Wit, H. Olsson, K. J. Åström, and P. Lischinsky, "A new model for control of systems with friction," *IEEE Transactions on Automatic Control*, vol. 40, no. 3, pp. 419–425, 1995.

[37] C. Canudas de Wit and P. Tsiotras, "Dynamic tire friction models for vehicle traction control," in *Proceedings of 38th IEEE Conference on Decision and Control*, (Phoenix, Arizona, USA), pp. 3746–3751, 1999.

[38] J. Deur, "Modeling and analysis of longitudinal tire dynamics based on the LuGre friction model," Technical Report, Ford Motor Company, Scientific Research Laboratory MD 1170, Dearborn, MI 48121-2053, USA, 2001.

[39] M. Villela, "Nonlinear modeling and control of automobiles with dynamic wheel-road friction and wheel torque inputs," 2004. M.S. thesis, School of Electrical and Computer Engineering, Georgia Institute of Technology.

[40] M. Villela and D. Taylor, "Input-output linearization of an automobile model with 2D LuGre friction," in *Proceedings of the American Control Conference*, (Portland, OR), pp. 429–434, June 8 - 10 2005.

[41] C. Canudas-de Wit, M. Petersen, and A. Shiriaev, "A new nonlinear observer for tire/road distributed contact friction," in *Proceedings of the* 42^{th} *IEEE Conference on Decision and Control*, (Maui, Hawaii, to appear), December 9-12 2003.

[42] C. Canudas de Wit, R. Horowitz, and P. Tsiotras, "Model-based observers for tire/road contact friction prediction," in *New Directions in Nonlinear Observer Design* (H. Nijmeijer and T. Fossen, eds.), vol. 244 of *Lecture Notes in Control and Information Science*, pp. 23–42, London: Springer-Verlag, 1999.

[43] J. Bernard and M. Pickelmann, "An inverse linear model of a vehicle," *Vehicle System Dynamics*, vol. 15, pp. 179–186, 1986.

[44] J. Ackermann, J. Guldner, and V. Utkin, "A robust nonlinear control approach to automatic path tracking of a car," in *Control '94*, vol. 1, pp. 196–201, March 21-24 1994.

[45] J. Ackermann, J. Guldner, W. Sienel, R. Steinhauser, and V. Utkin, "Linear and nonlinear controller design for robust automatic steering," *IEEE Transactions on Control Systems Technology*, vol. 3, no. 1, pp. 132–143, 1995.

[46] J. Ackermann, "Robust control prevents car skidding," *IEEE Control Systems Magazine*, vol. 17, pp. 23–31, 1997.

[47] C. Chen and H. Tan, "Steering control of high speed vehicles: Dynamic look ahead and yaw rate feedback," in *Proceedings of the* 37^{th} *IEEE Conference on Decision and Control*, (Tampa, FL), December 1998.

[48] K. Unyelioglu, C. Hatipoglu, and U. Özguner, "Design and stability analysis of a lane following controller," *IEEE Transactions on Control Systems Technology*, vol. 5, no. 1, pp. 127–134, 1997.

[49] U. Özguner, K. Unyelioglu, and C. Hatipoglu, "An analytical study of vehicle steering control," in *Proceedings of the* 4^{th} *IEEE Conference on Control Applications*, (Albany, NY), pp. 125–130, September 28-29 1995.

[50] O. Mokhiamar and M. Abe, "Active wheel steering and yaw moment control combination to maximize stability as well as vehicle responsiveness during quick lane change for active vehicle handling safety," *Proceedings of the Institution of Mechanical Engineers, Part D: Journal of Automobile Engineering*, vol. 216, no. 2, pp. 115–125, 2002.

[51] R. Sharp and V. Valtetsiotis, "Optimal preview car steering control," *Vehicle System Dynamics Supplement*, vol. 35, pp. 101–117, 2001.

[52] C. Hatipoglu, U. Özguner, and K. Unyelioglu, "On optimal design of a lane change controller," in *Proceedings of the Intelligent Vehicles '95 Symposium*, (Detroit, MI), pp. 436–441, September 25-26 1995.

[53] S. Drakunov and R. DeCarlo, "Sliding mode control design for automated steering via Lyapunov approach," in *Proceedings of the* 34^{th} *IEEE Conference on Decision and Control*, (New Orleans, LA), December 1995.

[54] P. Hingwe and M. Tomizuka, "Experimental evaluation of a chatter free sliding mode control for lateral control in AHS," in *Proceedings of the American Control Conference*, (Albuquerque, NM), June 4-6 1997.

[55] J. Zhang, S. Xu, and A. Rachid, "Path tracking control of vehicles based on Lyapunov approach," in *Proceedings of the American Control Conference*, (Anchorage, AK), May 8-10 2002.

[56] J. Zhang, S. Xu, and A. Rachid, "Automatic path tracking control of vehicles based on Lyapunov approach," in *Proceedings of the 2001 IEEE Intelligent Transportation Systems Conference*, (Oakland, CA), August 25-29 2001.

[57] S. Xu and J. Zhang, "Nonlinear automatic steering control of vehicles based on Lyapunov approach," in *Proceedings of the IEEE* 5^{th} *International Conference on Intelligent Transportation Systems*, (Singapore), September 3-6 2002.

[58] J. Zhang, A. Rachid, and S. Xu, "Velocity controller design for automatic steering of vehicles," in *Proceedings of the American Control Conference*, (Arlington, VA), June 25-27 2001.

[59] B. d'Andrea Novel and M. Ellouze, "Tracking with stability for a vehicle braking in a corner," in *Proceedings of the* 40^{th} *IEEE Conference on Decision and Control*, (Orlando, FL), December 2001.

[60] I. Haskara, C. Hatipoglu, and U. Özguner, "Combined decentralized longitudinal and lateral controller design for truck convoys," in *Proceedings of the IEEE Conference on Intelligent Transportation System 1997*, (Boston, MA), pp. 123–128, November 9-12 1997.

[61] E. Lim and J. Hedrick, "Lateral and longitudinal vehicle control coupling for automated vehicle operation," in *Proceedings of the American Control Conference*, (San Diego, CA), June 2-4 1999.

[62] R. S. Sharp, D. Casanova, and P. Symonds, "A mathematical model for driver steering control, with design, tuning and performance results," *Vehicle System Dynamics*, vol. 33, pp. 289–326, 2000.

[63] H. Hatwal and E. Mikulcik, "Some inverse solutions to an automobile path tracking problem with input control of steering and brakes," *Vehicle System Dynamics*, vol. 15, pp. 61–71, 1986.

[64] J. Trom, M. Vanderploeg, and J. Bernard, "Application of inverse models to vehicle optimization problems," *Vehicle System Dynamics*, vol. 19, pp. 97–110, 1990.

[65] J. Sridhar and H. Hatwal, "A comparative study of four wheel steering models using the inverse solution," *Vehicle System Dynamics*, vol. 21, pp. 1–18, 1992.

[66] T. Fujioka and M. Kato, "Numerical analysis of minimum-time cornering," in *Proceedings of AVEC 1994*, (Tsukuba, Japan), November 24-28 1994.

[67] J. Hendrikx, T. Meijlink, and R. Kriens, "Application of optimal control theory to inverse simulation of car handling," *Vehicle System Dynamics*, vol. 26, pp. 449–461, 1996.

[68] D. Casanova, R. S. Sharp, and P. Symonds, "Minimum time manoeuvring: The significance of yaw inertia," *Vehicle System Dynamics*, vol. 34, pp. 77–115, 2000.

[69] D. Casanova, R. S. Sharp, and P. Symonds, "On minimum time optimisation of formula one cars: The influence of vehicle mass," in *Proceedings of AVEC 2000*, (Ann-Arbor, MI), August 22-24 2000.

[70] D. Metz and D. Williams, "Near time-optimal control of racing vehicles," *Automatica*, vol. 25, no. 6, pp. 841–857, 1989.

[71] M. Gadola, D. Vetturi, D. Cambiaghi, and L. Manzo, "A tool for lap time simulation," in *Proceedings of SAE Motorsport Engineering Conference and Exposition*, (Dearborn, MI), 1996.

[72] M. Lepetic, G. Klancar, I. Skrjanc, D. Matko, and B. Potocnic, "Time optimal path planning considering acceleration limits," *Robotics and Autonomous Systems*, vol. 45, pp. 199–210, 2003.

[73] H. Pacejka and R. Sharp, "Shear force developments by pneumatic tires in steady state conditions: A review of modelling aspects," *Vehicle Systems Dynamics*, pp. 121–176, 1991.

[74] M. Sorine, "Applications of hysteresis models: Contact friction in tires, muscle contraction," in *IEEE CDC 98 Workshop #2*, (Tampa, Florida), 1998.

[75] E. Velenis, P. Tsiotras, and C. Canudas-de Wit, "Extension of the lugre dynamic tire friction model to 2d motion," in *Proceedings of the 10th IEEE Mediterranean Conference on Control and Automation - MED2002*, (Lisbon, Portugal), July 9-12 2002.

[76] S. Yamazaki, O. Furukawa, and T. Suzuki, "Study on real time estimation of tire to road friction," *Vehicle System Dynamics*, vol. 27, pp. 225–233, 1999.

[77] P. Gill, W. Murray, M. Saunders, and M. Wright, *User's Guide for NPSOL (version 4.0)*. Dept. of Operations Research, Stanford University, CA, 1986. Report SOL 86-2.

[78] T. Schouwenaars, B. De Moor, E. Feron, and J. How, "Mixed integer programming for multi-vehicle path planning," in *Proceedings of the 2001 European Control Conference*, (Porto, Portugal), pp. 2603–2608, September 2001.

[79] J. Bellingham, A. Richards, and J. How, "Receding horizon control of autonomous aerial vehicles," in *Proceedings of the American Control Conference*, (Anchorage, AK), pp. 3741–3746, May 8-10 2002.

[80] T. Schouwenaars, E. Feron, and J. How, "Safe receding horizon path planning for autonomous vehicles," in *Proceedings of the 40th Allerton Conference on Communication, Control and Computing*, (Monticello, IL), October 2002.

[81] J. O'Rourke, *Computational Geometry in C, Second Edition*. New York: Cambridge University Press, 1998.

[82] S. Skiena, *The Algorithm Design Manual*. New York: Springer-Verlag, 1997.

[83] C. Canudas-de Wit, P. Tsiotras, and E. Velenis, "Dynamic friction models for longitudinal road/tire interaction: Theoretical advances," in *Proceedings of the 21st IASTED Conference on Modelling, Identification and Control*, (Innsbruck,Austria), pp. 48–53, February 18-21 2002.

[84] C. Canudas-de Wit, P. Tsiotras, E. Velenis, M. Basset, and G. Gissinger, "Dynamic friction models for longitudinal road/tire interaction: Experimental results," in *Proceedings of the 21st IASTED Conference on Modelling, Identification and Control*, (Innsbruck,Austria), February 18-21 2002.

[85] E. Velenis, P. Tsiotras, C. Canudas-de Wit, and M. Sorine, "A dynamic tire friction model for combined longitudinal and lateral vehicle motion," *Vehicle System Dynamics*, vol. 43, no. 1, pp. 3–29, 2005.

[86] P. Tsiotras, E. Velenis, and M. Sorine, "A lugre tire friction model with exact aggregate dynamics," in *Proceedings of the American Control Conference*, (Boston, MA), pp. 1457–1462, June 30 - July 2 2004.

[87] P. Tsiotras, E. Velenis, and M. Sorine, "A lugre tire friction model with exact aggregate dynamics," *Vehicle System Dynamics*, vol. 42, no. 3, pp. 195–210, 2004.

[88] E. Velenis and P. Tsiotras, "Minimum time vs maximum exit velocity path optimization during cornering," in *2005 IEEE International Symposium on Industrial Electronics*, (Dubrovnic, Croatia), pp. 355–360, June 20 - 23 2005.

[89] E. Velenis and P. Tsiotras, "Optimal velocity profile generation for given acceleration limits: Theoretical analysis," in *Proceedings of the American Control Conference*, (Portland, OR), pp. 1478–1483, June 8 - 10 2005.

[90] E. Velenis and P. Tsiotras, "Optimal velocity profile generation for given acceleration limits: Receding horizon implementation," in *Proceedings of the American Control Conference*, (Portland, OR), pp. 2147–2152, June 8 - 10 2005.

[91] E. Velenis and P. Tsiotras, "Optimal velocity profile generation for given acceleration limits: The half-car model case," in *2005 IEEE International Symposium on Industrial Electronics*, (Dubrovnic, Croatia), June 20 - 23 2005.

[92] S. Drakunov, U. Özguner, P. Dix, and B. Ashrafi, "ABS control using optimum search via sliding modes," *IEEE Transactions on Control Systems Technology*, vol. 3, no. 1, pp. 79–85, 1995.

[93] J. Yu, "A robust adaptive wheel-slip controller for antilock brake system," in *Proceedings of 38th IEEE Conference on Decision and Control*, (San Diego CA), pp. 2545–2546, March 1997.

[94] T. Johansen, J. Kalkkuhl, J. Ludemann, and I. Petersen, "Hybrid control strategies in ABS," in *Proceedings of the American Control Conference*, (Arlington, VA), June 25 - 27 2001.

[95] C. Lin and C. Hsu, "Self-learning fuzzy sliding-mode control for antilock braking systems," *IEEE Transactions on Control Systems Technology*, vol. 11, no. 2, pp. 273–278, 2003.

[96] J. Yi, L. Alvarez, X. Claeys, and R. Horowitz, "Emergency braking control with an observer-based dynamic tire/road friction model and wheel angular velocity measurement," *Vehicle System Dynamics Supplement*, vol. 39, no. 2, pp. 81–97, 2003.

[97] P. Tsiotras and C. Canudas de Wit, "On the optimal braking of wheeled vehicles," in *Proceedings of American Control Conference*, (Chicago IL), June 28-30 2000.

[98] M. Yamamoto, "Active control strategy for improved handling and stability," *SAE Transactions*, vol. 100, no. 6, pp. 1638–1648, 1991.

[99] K. Koibuchi, M. Yamammoto, Y. Fukada, and S. Inagaki, "Vehicle stability control in limit cornering by active brake," *SAE Special Publications, Investigations and Analysis in Vehicle Dynamics and Simulation*, no. 1141, pp. 163–173, 1996.

[100] S. Inagaki, I. Kshiro, and M. Yamamoto, "Analysis on vehicle stability in critical cornering using phase-plane method," in *Proceedings of AVEC 1994*, (Tsukuba Research Center), October 24-28 1994.

[101] A. T. van Zanten, R. Erhardt, and G. Landesfeind, K. Pfaff, "Vehicle stabilization by the vehicle dynamics control system ESP," in *IFAC Mechatronic Systems*, (Darmstadt, Germany), pp. 95–102, 2000.

[102] C. Taylor, J. Malik, and J. Weber, "A real-time approach to stereopsis and lane-finding," in *IEEE Intelligent Vehicles Symposium*, pp. 207–212, 1996.

[103] A. Takahashi and Y. Ninomiya, "Model-based lane recognition," in *IEEE Intelligent Vehicles Symposium*, pp. 162–166, 1996.

[104] J. Goldbeck and B. Huertgen, "Lane detection and tracking by video sensors," in *IEEE International Conference on Intelligent Transportation Systems*, pp. 74–79, 1999.

[105] S. Ernst, C. Stiller, J. Goldbeck, and C. Roessig, "Camera calibration for lane and obstacle detection," in *IEEE International Conference on Intelligent Transportation Systems*, pp. 356–361, 1999.

[106] R. Aufrere, R. Chapuis, and F. Chausse, "A fast and robust vision based road-following program," in *IEEE International Conference on Intelligent Transportation Systems*, pp. 346–351, 2000.

[107] K. Huh, J. Park, D. Hong, D. Cho, and J. Park, "Vision-based lane detection for passenger cars: configuration aspects," in *Proceedings of the American Control Conference*, (Boston, MA), pp. 792–797, June 30 - July 2 2004.